



UNIVERSITY OF  
**LEICESTER**

DEPARTMENT OF PHYSICS AND ASTRONOMY

Radio and Space Plasma Physics Group

---

**In-situ Spectroscopy on Mars: ChemCam  
Activities and Preparations for the Raman  
Laser Spectrometer on ExoMars**

---

Peter Henry Edwards

*Submitted in accordance with the requirements for the degree of Doctor of Philosophy.*

Under the supervision of Ian Hutchinson at the University of Leicester.

September 2017

The candidate confirms that the work submitted is her own and that appropriate credit has been given where reference has been made to the work of others.

This copy has been supplied on the understanding that it is copyright material and that no quotation from the thesis may be published without proper acknowledgement.

## Abstract

This thesis aims to perform appropriate preparatory work for the Raman Laser Spectrometer (RLS) on ExoMars. In order to test the prototype instrumentation it is important to select analogue samples as close as possible to the drill core that ExoMars will analyse. Work with 200 thousand spectra from the first 1000 sols of ChemCam operation on the Mars Science laboratory detected the presence of a basalt – trachybasalt igneous compositional trend, rich in alkali feldspar. These studies informed analogue sample selection at a Martian analogue site in the Utah desert as part of the MURFI rover trials. A flight representative Raman spectrometer was used in the field to acquire spectra. These were used to select a collection of analogues for further studies with RLS prototype instruments. These samples were chosen to be representative of the diverse mineralogy of the analogue site, this included; quartz, gypsum, anhydrite, celestine, barite and calcite. Work to fully characterise these samples used grain scale 532nm and 785nm Raman microscopes and an X-ray diffractometer instrument in order to determine the full composition for comparison with the capabilities of RLS. Nine of these samples were then analysed with the RLS Engineering Qualification Model to give as representative a view of RLS mission operation as possible. These studies found that whilst the RLS data was lower in spectral resolution and SNR compared to the laboratory instrumentation, it still possessed clear Raman bands enabling identification of all but two samples. These two samples were further analysed with the UK RLS prototype where additional Raman observation points produced clear bands allowing for the identification of the remaining samples. Recommendations for RLS operation and further testing include increasing the number of observation points on each sample and further testing with phyllosilicate analogues of the possible ExoMars landing site Marwth Vallis and Oxia Planum.

## Acknowledgments

There are too many people to thank for help from the last 4 years. As such I have probably missed many deserving people out, and for that I am very sorry. Ian, I always feel better after meetings with you. Thank you for many late nights proof reading chapters and being hugely supportive throughout the whole of my PhD. Rich, for many great Laphroaig fuelled conversations, valuable proof reading advice and countless times you have helped me in the lab. John, for supporting me whilst applying for the PhD, advice about geology and inclusion as a MSL collaborator. Mel, for keeping me company in the desert, guiding me through the final days of the thesis and often helping me with instrumentation. Hannah, for a ridiculous number of grammar improvements and helping me so much through these last few days. Liam, you have always been really helpful and encouraging, particularly when I was just starting the PhD. Arthur, great to share offices with you these last 4 years, I enjoyed our many discussions about football. Cedric, for many fine cooked meals, looking after me in Liege and valuable advice about Raman Spectroscopy. Emma, you have been super supportive these through this writing up period, thank you for always being so encouraging, watching crystal maze with me and making sure I have valuable nights off. You have made the last few months so much more bearable! Oli, Josh and Ben – Guys, thanks for being great housemates, sorry I haven't been around whilst writing, really looking forward to seeing you all more! Mum and Dad, you are all round great parents. Thanks to the Spanish RLS team for making me feel so welcome at INTA, including me in the EQM campaign and assisting with the analysis of my samples. The MSL Team for including me as a collaborator and providing data from the Curiosity rover. UKSA for funding my PhD and organising the MURFI field trial.

## Contents

Abstract.....	ii
Acknowledgments .....	iii
List of Figures .....	viii
List of Tables .....	xiii
List of Abbreviations .....	xiv
Preface .....	xvi
Publications.....	xvi
Conference abstracts .....	xvi
Personal Contributions .....	xviii
<b>Chapter 1: Planetary Exploration.....</b>	<b>1</b>
1.1 Planetary Exploration.....	1
1.2 Geology .....	4
1.3 Astrobiology .....	7
1.4 Mars .....	10
1.4.1 The Martian Environment .....	14
1.4.3 Gale Crater.....	19
1.4.4 Mars as a Candidate for Supporting Life .....	20
1.5 Europa .....	21
1.5.1 History of Europa Exploration .....	21
1.5.2 The European Environment.....	22
1.5.3 Europa as a Candidate Supporting for Life .....	23
1.6 Venus.....	24
1.6.1 History of Venus Exploration .....	24
1.6.2 The Venusian Environment .....	25
1.6.3 Venus as a Candidate for Supporting Life .....	26
1.7 Analytical Science Requirements.....	27
<b>Chapter 2: Analytical Science techniques.....</b>	<b>30</b>
2.1 Introduction .....	30
2.1.1 Mars Science Laboratory .....	32

2.1.2 ExoMars .....	34
2.2 Laser Induced Breakdown Spectroscopy .....	36
2.2.1 LIBS Method .....	36
2.2.2 LIBS detection capability .....	37
2.2.3 ChemCam on MSL .....	38
2.2.4 LIBS Planetary Science Results .....	41
2.3 Raman Spectroscopy.....	42
2.3.1 Raman Method.....	42
2.3.2 Raman Detection Capability .....	45
2.3.3 ExoMars Raman Laser Spectrometer .....	46
2.3.4 SHERLOC on MARS 2020 .....	47
2.3.5 CIRS .....	48
2.3.6 SuperCam on MARS 2020.....	49
2.4 X-Ray Fluorescence and Alpha Particle X-Ray Spectroscopy .....	49
2.4.1 APXS Method.....	50
2.4.2 XRF Method .....	50
2.4.3 APXS Detection Capability .....	51
2.4.4 XRF Detection Capability .....	51
2.4.5 Viking and Venera missions XRF.....	51
2.4.6 MER and MSL APXS .....	52
2.4.7 PIXL on MARS 2020.....	53
2.4.8 Planetary Science Results from APXS and XRF.....	53
2.5 X-Ray Diffraction .....	54
2.5.1 XRD method.....	55
2.5.2 XRD detection capability .....	55
2.5.3 CheMin on MSL .....	55
2.5.4 Planetary Science Results from X-ray Diffraction.....	56
2.6 Infra-Red Imaging Spectroscopy .....	57
2.6.1 Infra-Red spectroscopy method.....	57
2.6.2 Micro Omega on ExoMars.....	58
2.7 Mössbauer Spectroscopy.....	58
2.8 Gas Chromatography Mass Spectroscopy .....	59

2.9 Combined instrumentation .....	60
2.9.1 Raman/LIBS.....	61
2.9.1.1 RLS Raman/LIBS .....	61
2.9.1.2 <i>SuperCam</i> .....	62
2.9.2 XRF/XRD.....	63
2.9.3 Raman/IR .....	64
2.9.4 LIBS/XRD .....	64
2.10 Future missions.....	65
<b>Chapter 3: ChemCam analysis at Mars</b> .....	66
3.1 Introduction .....	66
3.2 ChemCam data acquisition .....	67
3.3 Geology .....	69
3.3.1 Basalt .....	69
3.3.2 Trachybasalts.....	69
3.3.3 Alkali and sub alkaline basalts .....	70
3.3.4 Feldspar .....	71
3.3.5 Normative compositions .....	71
3.3.6 Martian Geology.....	72
3.4 ChemCam results from the first 1000 sols at Gale Crater .....	75
3.4.1 Igneous rock classification.....	75
3.4.2 Possible feldspar mineral detections .....	88
3.4.3 Igneous trend modelling .....	92
3.4.4 CIPW Normative and AFM compositions .....	94
3.5 Discussion .....	95
3.5.1 Terrestrial and experimental analogues for Martian samples.....	97
3.6 Conclusions .....	99
<b>Chapter 4: MURFI field trials – Raman Spectroscopy</b> .....	101
4.1 Introduction .....	101
4.2 Importance of analogue studies .....	102
4.3 MURFI 2016 .....	102

4.3.1 Mission Goals.....	103
4.3.2 Rover platform.....	103
4.3.3 Landing site.....	104
4.3.4 Mission operation.....	107
4.3.5 CSA joint operations and AEGIS Tests .....	108
4.4 Analogue Samples.....	109
4.4.1 Sample Preparation .....	110
4.4.2 Instrumentation.....	110
4.5 Results.....	114
4.5.1 Silicate field studies .....	114
4.5.2 Sulphate field studies .....	115
4.5.3 Feldspar field studies.....	118
4.5.4 Carbonate field studies.....	118
4.5.5 Raman Microscope and XRD sample mineralogical identification .....	120
4.5.6 Phyllosilicate samples.....	141
4.6 Discussion .....	145
4.6.1 Comparison between mission representative spectrometers and lab instrumentation.....	145
4.6.2 XRD analyses.....	147
4.6.3 Challenges for Raman identification .....	147
4.7 Conclusion.....	152
<b>Chapter 5: Raman Laser Spectrometer Engineering Qualification Model tests ....</b>	<b>154</b>
5.1 Introduction .....	154
5.2 Raman Laser Spectrometer.....	154
5.2.1 Instrument design.....	156
5.2.2 RLS Engineering Qualification Model .....	157
5.2.3 RLS UK Breadboard Instrument.....	158
5.2.4 Spectral acquisition and processing .....	159
5.3 Samples .....	162
5.3.1 Preparation .....	163
5.4 Results.....	163

5.4.1 Sulphates .....	163
5.4.2 Feldspar .....	166
5.4.3 Silicates .....	168
5.4.4 Phyllosilicate .....	169
5.5 Discussion.....	170
5.5.1 Spectra comparison.....	170
5.5.2 Recommendations for RLS .....	174
5.6 Conclusion.....	175
<b>Chapter 6: Conclusion.....</b>	<b>177</b>
References.....	181
Appendix 1 Technology Readiness Levels.....	231
Appendix 2 Geological definitions .....	232

## List of Figures

### Chapter 1

- 1.1 Galilean moons composite image Io, Europa, Ganymede and Callisto. Image Credit: NASA/JPL/DLR
- 1.2 Image of Voyager probe (Murray 1989)
- 1.3 3 generations of NASA rovers, Pathfinder 1997, Spirit/Opportunity 2004, and Curiosity 2012 Image Credit: NASA/ JPL-Caltec
- 1.4 MSL MastCam image southern facing view of The Kimberley a sedimentary outcrop in Gale Crater, Mars Image acquired on Sol 580. Image Credit NASA/ JPL (Grotzinger, Gupta, et al. 2015)
- 1.5 The Syctonemin molecular structure, a useful biomarker for life adapted to high UV radiation conditions, such as those on Mars
- 1.6 Artist's impression of Mariner 4 Image Credit NASA/JPL
- 1.7 Artist's impression of the Spirit rover airbag landing system Image Credit NASA/JPL
- 1.8 Artist's impression of Viking lander with instruments labelled (Soffen & Snyder 1976)

- 1.9 Cumberland drill hole, samples were analysed on board the Curiosity rover whilst remote analysis took place of the drill tailings. Image acquired by the MastCam Camera on Sol 279 Image Credit NASA/JPL
- 1.10 Mars showing atmospheric weather. Mars Global Surveyor, Mars Orbiter Camera Image (Wang & Ingersoll 2002) Image Credit: NASA/JPL-Caltech/MSSS
- 1.11 Topographical surface map of Mars from Mars Global Surveyor. White indicates higher altitude and dark blue lower. Mars Orbital Laser Altimetry instrument obtained the data (Smith et al. 2001) Image Credit NASA/JPL
- 1.12 Warrego Vallis, Mars, The drainage shows evidence of fluvial activity from rainfall and surface runoff. Image Credit NASA/JPL (Carr 2012)
- 1.13 Jupiter's Icy moon Europa. Image Credit: NASA/JPL/DLR taken by the solid state imaging television camera on board the Galileo spacecraft
- 1.14 Design of Venera 9 and 10 Image Credit (Keldysh 1977)
- 1.15 Mariner 10 image of Venus. Image Credit NASA

## **Chapter 2**

- 2.1 Mosaic of MSL images from the MAHLI camera on the robotic arm to create a self-portrait of the rover on Sol 1126 Image Credit NASA/JPL
- 2.2 Artist's impression of the ExoMars rover Image Credit ESA
- 2.3 LIBS Experimental setup Image Credit: (Cremers and Radziemski 2013)
- 2.4 The ChemCam Mast Unit Image Credit: NASA/JPL
- 2.5 The unnormalised LIBS spectra from single shot at an observation point from each of four ChemCam targets
- 2.6 RMI images before and after LIBS 5 x 1 Raster of observation points Image Credit NASA/JPL
- 2.7 Energy level diagram of Rayleigh and Raman scattering
- 2.8 Raman spectra of a celestine sample obtained with the RLS EQM
- 2.9 RLS instrument design. ICEU - Instrument Control and Excitation Unit (Red). SPU – Spectrometer unit (Green). IOH – Internal optical head (Yellow). Image Credit (Rull et al. 2017)
- 2.10 MARS 2020 instrument layout showing position of SHERLOC on the robotic arm Image Credit NASA
- 2.11 MastCam image of the MSL APXS instrument on the robotic arm. Image Credit NASA/JPL
- 2.12 PIXL instrument design Image Credit NASA/JPL
- 2.13 XRD diffractogram for MSL at Rocknest showing evidence for olivine Image Credit NASA/JPL
- 2.14 MAHLI image of John Klein drillhole on sol 270 ChemCam laserspots are visible next to a light vein. Image Credit NASA/JPL
- 2.15 Combined Raman LIBS RLS instrument design

- 2.16 Artist's impression of SuperCam in action with the green 532nm Raman laser and the 106nm LIBS laser Image Credit NASA/JPL

### **Chapter 3**

- 3.1 Representative MSL ChemCam igneous targets (Edwards et al. 2017)
- 3.2 TAS (Total Alkali Silica) plot
- 3.3 Representative specimen of trachybasalt from Mt. Dore, Auvergne, France. University of Leicester Geology department collection.
- 3.4 Example of a feldspar ternary plot with terrestrial feldspar locations marked.
- 3.5 Mosaic of HIRISE images marking the first 1000 sols of MSL Curiosity rover's progress since landing with some of the various targets or target sites of interest marked – sedimentary units and some key igneous locations. (Edwards et al. 2017)
- 3.6 Collage of example end-member trachybasalt and basalt igneous samples. (Edwards et al. 2017)
- 3.7 Histograms showing the compositional distribution of both Igneous and Sedimentary ChemCam targets. (Edwards et al. 2017)
- 3.8 Harker contour plots showing the distribution of ChemCam data over different combinations of oxides.
- 3.9 TAS plot of the sedimentary and igneous samples from the first 1000 sols of MSL mission.
- 3.10 Tetrahedral plots of ChemCam single shot data for (a) Sedimentary outcrops and (b) Sedimentary compared to Igneous.
- 3.11 RMI image of Noriss\_2 target (Trachybasalt group), showing white felsic mineral grains.
- 3.12 Ternary plot of detected possible feldspars, dashed line indicates Shergottite felsic compositions terrestrial feldspar compositions from (Gasda et al. 2016)
- 3.13 MER image of Humphrey a Spirit APXS target, image credit: NASA
- 3.14 AFM plot showing a trend analogous to terrestrial tholeiites.
- 3.15 TAS Diagram showing the four major trends from (Whitaker et al. 2005)

### **Chapter 4**

- 4.1 MURFI 2016 Rover Q14 Platform supplied by Oxford University Robotics Institute
- 4.2 Red brown / Light layering Image taken during MURFI mission
- 4.3 UAV image Mission operations area, Brown-red and white soil layers are visible, Image Credit Steve Kay
- 4.4 Images of key samples
- 4.5 The mortar and pestle used for crushing the samples
- 4.6 Rockhound Raman spectrometer
- 4.7 Advantage 532 nm spectrometer
- 4.8 The 532 nm Labram Raman microscope used at the University of Liege

- 4.9 Silicate Raman spectra Rockhound and Advantage
- 4.10 Sulphate Raman spectra Rockhound and Advantage
- 4.11 Feldspar Raman spectra Rockhound
- 4.12 Carbonate Raman spectra Rockhound
- 4.13 MURFI drill core sample Rockhound
- 4.14 Samples Milkybar (Left) and Cross (Right) scale bar indicates 1 cm
- 4.15 Spectra of both materials in the Cross samples. 785nm, 532nm and Barite and Calcite reference samples from the University of Liege are shown.
- 4.16 XRD diffractogram with calcite and barite peaks fitted
- 4.17 Carotene spectra detected on the surface on the Cross sample.
- 4.18 Galliger sample with two clear different types of material
- 4.19 Galliger Raman spectra showing comparison to Celestine and Quartz
- 4.20 XRD Diffractogram of Galliger White material with Celestine Reference peaks
- 4.21 Barclay sample
- 4.22 Raman Spectra of Barclay sample showing the gypsum hydration bands.
- 4.23 Stanford sample
- 4.24 Anhydrite spectra from Stanford sample
- 4.25 XRD Diffractogram of Stanford sample showing Anhydrite, Quartz and Calcite
- 4.26 Image of the Justineau sample
- 4.27 Two types of material detected within the Justineau sample Barite reference samples from the University of Liege
- 4.28 Image of Melanie sample
- 4.29 Feldspar spectra from the Melanie sample compared to a labradorite reference spectra
- 4.30 XRD diffractogram of Melanie sample showing evidence of Albite and Quartz
- 4.31 Moon sample
- 4.32 Moon sample spectra compared to reference Quartz spectra
- 4.33 Talc sample 532nm spectra
- 4.34 Montmorillonite sample spectra
- 4.35 Biotite sample spectra
- 4.36 Background fluorescence
- 4.37 Sample Cross measured with 785 nm Raman with a laser spot covering the colour change within the sample, demonstrating the mineralogical matrix effects from two mineralogically distinct materials
- 4.38 Comparison of both the powdered and unpowdered versions of the Galliger sample, unpowdered sample refers to the Red material on the surface of the sample.
- 4.39 Comparison between 532 nm and 785 nm wavelengths spectra have been normalised with no fluorescence subtraction.

## **Chapter 5**

- 5.1 EQM SPU component
- 5.2 The RLS UKBB setup, laser is on the left, spectrometer on the right and optical head and sample stage in the centre
- 5.3 CCD Image showing the order of the Raman spectra from an EQM measurement
- 5.4 Uncalibrated PET spectra from RLS EQM
- 5.5 Calibration conversion from the PET CCD image for the RLS EQM
- 5.6 The samples selected for EQM in Spain analysis prepared in the University of Liege.
- 5.7 Sulphate sample Raman spectra acquired with the RLS EQM
- 5.8 Sample 2 Raman spectra acquired with the RLS EQM
- 5.9 Sample 2 Raman spectra acquired with the RLS UKBB
- 5.10 Feldspar sample Raman spectra acquired with the RLS EQM
- 5.11 Spectra of Sample 6 with the RLS UKBB
- 5.12 Silicate samples Raman spectra acquired with the RLS EQM
- 5.13 Raman spectra acquired with the RLS EQM for Talc sample
- 5.14 Comparison of the locations of the main sulphate bands in the EQM data
- 5.15 Hydration bands in the high spectral range from the EQM

## List of Tables

### **Chapter 1**

- 1.1 Instrumentation on Mars lander missions
- 1.2 Instrumentation on Venus lander missions

### **Chapter 2**

- 2.1 Comparison of different analytical science techniques with example instruments
- 2.2 Table of key biomarkers detectable with Raman Spectroscopy from Edwards et al. (2014).
- 2.3 Combined instrumentation techniques and their uses for planetary science

### **Chapter 4**

- 4.1 Feldspar classifications of possible detected feldspars in order of quantity.
- 4.2 Table of representative feldspar compositions.
- 4.3 Mean basalt and trachybasalt end member alongside Sedimentary compositions showing the CIPW norms for the Basalt and Trachybasalt groups.

### **Chapter 5**

- 5.1 Table of Cross sample band locations
- 5.2 Table of Galliger sample band locations
- 5.3 Table of Barclay sample band locations
- 5.4 Table of Stanford sample band locations
- 5.5 Table of Justineau sample band locations
- 5.6 Table of Melanie sample band locations
- 5.7 Table of Moon sample band locations
- 5.8 Table of talc band positions
- 5.9 Table of montmorillonite band locations
- 5.10 Table of biotite band locations

## List of Abbreviations

AEGIS	Automated Exploration for Gathering Increased Science
ALD	Analytical Laboratory Drawer
APXS	Alpha Particle X-ray Spectroscopy
AUPE	Aberystwyth University PanCam Emulator
CCAM	ChemCam
CCD	Charged Coupled Device
CIRS	Compact Integrated Raman Spectrometer
CIVA-M	Comet Infrared Visible Analyser (2 <sup>nd</sup> experiment)
CLUPI	Close Up Imager
CSA	Canadian Space Agency
DAN	Dynamic Albedo of Neutrons
DPSS	Diode-Pumped Solid-State Laser
EDM	Entry and Descent Module
EET	Elephant Moraine
EQM	Engineering Qualification Model
ESA	European Space Agency
FWHM	Full Width Half Maximum
GCMS	Gas Chromatography Mass Spectroscopy
HRC	High Resolution Camera
ICA	Independent Component Analysis
ICEU	Instrument Control and Excitation Unit
iOH	internal Optical Head
IR	Infrared
INTA	Instituto Nacional de Técnica Aeroespacial
ISEM	Infrared Spectrometer for Exomars
JAXA	Japan Aerospace Exploration Agency
JUICE	JUperiter ICy moons Explorer
LIBS	Laser Induced Breakdown Spectroscopy
MA_MISS	Mars Multispectral Imager for Subsurface Studies
MAHLI	Mars Hand Lens Imager
MARDI	Mars Descent Imager
MER	Mars Exploration Rover
MOC	Mission Operations Centre
MOMA	Mars Organic Molecule Analyzer
MSL	Mars Science Laboratory
MURFI	Mars Utah Rover Field Investigation
NASA	National Aeronautics and Space Administration
NIR	Near Infrared
PET	Polyethylene terephthalate

PIXL	Planetary Instrument for X-ray Lithography
PLS	Partial Least Squared
QMS	Quadrupole Mass Spectrometer
QUE	Queen Alexandra Range
RAD	Radiation Assessment Detector
RADAR	RADio Detection And Ranging
REMS	Rover Environmental Monitoring Station
RLS	Raman Laser Spectrometer
RMI	Remote Micro Imager
RTG	Radioisotope Thermal Generator
SAM	Sample Analysis at Mars
SHERLOC	Scanning Habitable Environments with Raman & Luminescence for Organics and Chemicals
SNR	Signal to Noise Ratio
SPU	Spectrometer Unit
TAS	Total Alkali Silica
TEC	ThermoElectric Cooler
TRL	Technology Readiness Level
UKBB	UK Breadboard
UKSA	UK Space Agency
UAV	Unmanned Aerial Vehicle
UV	Ultra Violet
WISDOM	Water Ice Subsurface Deposit Observation on Mars
XRD	X-Ray Diffraction
XRF	X-Ray Fluorescence

## Preface

The work presented in Chapter 3 is based on *Basalt-Trachybasalt Samples from Gale Crater, Mars* by Peter H. Edwards et al, published on 14 September 2017 in Meteoritics and Planetary Science. Subsections of the chapter feature work presented by *Identification and Characterization of Feldspars in Gale Crater, Mars, using ChemCam*, by P. J. Gasda et al. (in preparation).

Chapter 4 of this document is based on Raman Spectroscopy on the UKSA MURFI rover trials, a publication by P. H. Edwards et al. in preparation.

## Publications

- **Peter H. Edwards**, Melissa McHugh, Ian Hutchinson, Hannah Lerman, Howell Edwards, Steve Banham, Cedric Malherbe, Steve Kay, Matt Balme, Mike Curtis Rouse, "Raman Spectroscopy on the UKSA MURFI rover trials" (in prep.)
- **Peter H. Edwards**, John C. Bridges, Ryan Anderson, Darby Dyar, Martin Fisk, Lucy Thompson, Patrick Gasda, Justin Filiberto, Susanne P. Schwenzer, Walter Goetz, Diana Blaney, Ian Hutchinson, Roger Wiens, "*Basalt-Trachybasalt Samples from Gale Crater, Mars*", Meteoritics and Planetary Science (In Press)
- P. J. Gasda, R. C. Wiens, J. C. Bridges, **P. H. Edwards**, V. Sautter, A. Cousin, S. Maurice, O. Gasnault, E. Carlson, S. Clegg, D. M. DeLapp, R. E. Mcinroy S. K. Sharma, A. K. Misra, E. Hellebrand, and the MSL team, "*Identification and Characterization of Feldspars in Gale Crater, Mars, using ChemCam*", (in prep.)
- J Frydenvang, PJ Gasda, JA Hurowitz, JP Grotzinger, RC Wiens, HE Newsom, KS Edgett, J Watkins, John C Bridges, S Maurice, MR Fisk, JR Johnson, W Rapin, NT Stein, SM Clegg, SP Schwenzer, CC Bedford, **P Edwards**, N Mangold, A Cousin, RB Anderson, V Payre, D Vaniman, DF Blake, NL Lanza, S Gupta, J Van Beek, V Sautter, P-Y Meslin, M Rice, R Milliken, R Gellert, L Thompson, BC Clark, DY Sumner, AA Fraeman, KM Kinch, MB Madsen, IG Mitrofanov, I Jun, F Calef, AR Vasavada "*Diagenetic silica enrichment and late-stage groundwater activity in Gale crater, Mars*", Geophysical Research Letters, 44, 10, 4716-4724 (2016)
- JC Bridges, SP Schwenzer, Richard Leveille, Frances Westall, RC Wiens, N Mangold, T Bristow, **P Edwards**, G Berger, "*Diagenesis and clay mineral formation at Gale Crater, Mars*", Journal of Geophysical Research: Planets, 120, 1, 1-19 (2015)

## Conference abstracts

- MR Balme, MC Curtis-Rouse, S Banham, D Barnes, R Barnes, A Bauer, C Bedford, J Bridges, FEG Butcher, P Caballo, A Caldwell, A Coates, C Cousins, J Davis, J Dequaire, **P Edwards**, P Fawdon, K Furuya, M Gadd, A Griffiths, PM Grindrod, M Gunn, S Gupta, R Hansen, JK Harris, J Holt, B Huber, C Huntly, I Hutchinson, L Jackson, S Kay, S Kybert, HN Lerman, M McHugh, W McMahan, J-

- P Muller, G Paar, LJ Preston, S Schwenzer, R Stabbins, Y Tao, C Traxler, S Turner, L Tyler, S Venn, H Walker, J Wright, B Yeomans, *“UK Space Agency “Mars Utah Rover Field Investigation 2016”(MURFI 2016): overview of mission, aims and progress”*, Lunar and Planetary Science Conference, 48 (2017)
- **Peter H. Edwards**, Ian Hutchinson, Sally Morgan, Melissa McHugh, Cédric Malherbe, Hannah Lerman and Richard Ingley, *“Preparations for ExoMars: Learning lessons from Curiosity”*, EPSC (2016)
  - J. C. Bridges, **P. H. Edwards**, J. Filiberto, S. P. Schwenzer, P. Gasda, R. Wiens, *“Basalt-Trachybasalt Fractionation In Gale Crater, Mars.”* MetSoc 2016
  - PJ Gasda, DM Delapp, RE McInroy, RC Wiens, JC Bridges, **PH Edwards**, E Carlson, V Sautter, A Cousin, S Maurice, S Clegg, MSL Team, *“Identification of Fresh Feldspars in Gale Crater Using ChemCam”*, Lunar and Planetary Science Conference, 47 (2016)
  - Bridges, J. C.; **Edwards, P. H.**; Anderson, R.; Dyar, M. D.; Fisk, M.; Thompson, L.; Gasda, P.; Schwenzer, S. P. ; Goetz, W.; Blaney, D.; Filiberto, J. and Wiens, R. C. (2016). *“Igneous differentiation on Mars: Trachybasalts in Gale Crater”*. Lunar and Planetary Science Conference, 47 (2016)
  - Justin Filiberto, John Bridges, Rajdeep Dasgupta, **Peter Edwards**, Susanne P Schwenzer and Roger C Wiens, *“Formation Conditions of Basalts at Gale Crater, Mars from ChemCam Analyses”* , AGU Fall Meeting Abstracts (2015)
  - **P. H. Edwards**, Ian B Hutchinson, Richard Ingley and John C Bridges, *“Analytical science techniques available for planetary science”*, SciX (2015)
  - J Bridges, **P Edwards**, MD Dyar, MR Fisk, SP Schwenzer, O Forni, RC Wiens, *“Comparing MSL ChemCam Analyses to Shergottite and Terrestrial Rock Types”* , AGU Fall Meeting Abstracts (2014)
  - J Bridges, SP Schwenzer, RJ Leveille, F Westall, RC Wiens, N Mangold, T Bristow, **P Edwards**, *“Smectite Formation in Gale Crater, Mars and in the Nakhlite Martian Meteorites”*, AGU Fall Meeting Abstracts (2014)
  - MR Fisk, MD Dyar, J Bridges, RB Anderson, ME Schmidt, O Gasnault, N Mangold, RL Tokar, RC Wiens, R Gellert, DF Blake, SP Schwenzer, **P Edwards**, *“Hypotheses on the Source of Potassium Enrichment in Some Gale Crater Rocks”*, AGU Fall Meeting Abstracts (2014)
  - **P. Edwards**, J.C. Bridges, M.D. Dyar, M. Fisk, S.P. Schwenzer, O. Forni , R.C. Wiens, *“Comparing MSL ChemCam Analyses to Shergottite and Terrestrial Rock Types”*, AGU Fall Meeting Abstracts (2014)
  - JC Bridges, SP Schwenzer, R Leveille, F Westall, RC Wiens, N Mangold, T Bristow, **P Edwards**, G Berger, *“Clay and magnetite formation at Yellowknife Bay, Mars”*, 77th Annual Meeting of the Meteoritical Society (2014)
  - **P. Edwards**, J.C. Bridges, I. Hutchinson, R. Ingley, *“ChemCam Analyses on Mars”*, Fermor Meeting 2014: Comparative Planetology, (2014)

## Personal Contributions

### **Chapter 1**

All work in this chapter is my own and is included after discussions with supervisors.

### **Chapter 2**

All work in this chapter is my own and is included after discussions with supervisors.

### **Chapter 3**

MSL data provided by the MSL Science and Operations teams.

### **Chapter 4**

Participated in fields work, selected samples, performed lab characterisation. Geological overview produced from discussions with Dr Steve Banham. Field campaign organised by UKSA. Lab assistance from Cedric Malherbe.

### **Chapter 5**

Assistance from Melissa McHugh setting up the UKBB  
Worked with the Spanish RLS team for EQM measurement campaign

# Chapter 1: Planetary Exploration

## 1.1 Planetary Exploration

Humans have long sort to explore their environment. For the majority of history this exploration has been confined to Earth, with only telescopes allowing us to gaze beyond gravitational constraint towards the stars and planets. However in the 20<sup>th</sup> century, with the dawn of rocketry and space exploration, further limits of exploration became possible.

Planetary exploration can take many different forms. The first method was to examine celestial bodies remotely from Earth, initially by eye, but then later, with the aid of telescopes. Today, terrestrial telescopes are capable of visually mapping some planetary surfaces and can even provide spectral analysis of light passing through atmospheres (Goldstein et al. 1991). The first use of a telescope for astronomy was Galileo's discovery of four moons in orbit around Jupiter (Figure 1.1), when in 1610 he identified Io, Europa, Ganymede and Callisto (Stevenson 2001). To improve the images obtained by



*Figure 1.1 Galilean moons composite image Io, Europa, Ganymede and Callisto. Image Credit: NASA/JPL/DLR*

our telescopes even further, the interference of the atmosphere can be bypassed via the use of measurements from orbital telescopes such as the famous Hubble Space Telescope. These space based missions allow for detailed images of not just distant stars but also planetary bodies within our solar system (Clarke et al. 1998). Different spectral ranges can be used to remotely examine objects. For example, the XMM Newton (Jansen et al. 2001), Chandra (Santos-Lleo et al. 2009) and Swift Gamma Ray Burst Explorer (Gehrels et al. 2004) missions carry X-ray optics and detectors while the future James Webb Space Telescope (Gardner et al. 2006) will study infrared characteristics.

Remote observations from Earth's local environment are limited in their capabilities. The next step is to launch a probe on a trajectory to encounter the orbit of another planetary body. The probe could then either perform a fly-by or manoeuvre into a stable orbit. This allows spacecraft to record measurements of features remotely, such as the thickness and composition of the atmosphere or the surface topography (with spectral mapping of the likely geological makeup). This method allows for a much more detailed view of a planetary system than remote telescopic observations, but still relies on remote observations rather than in-situ measurements. The amount of fuel (and thus launch weight) is considerably greater for a mission which seeks to obtain a stable orbit compared to a flyby, so many of the earliest missions were designed to intercept the orbit of the planet with minimal trajectory adjustments. A range of missions have followed this path, with the first successful planetary flyby achieved by Mariner 2 in 1962 with an encounter with the planet Venus. Measurements of the planetary temperature and magnetic field strength were performed along with investigations of interplanetary space (Neugebauer & Snyder 1966). Perhaps the most effective flyby missions were the probes Voyager 1 and 2 (see Krimigis et al. 2003), which visited multiple planets, imaging them and their moons, taking advantage of the favourable alignment of the planets in the solar system (allowing for multiple gravity assists to reduce fuel costs). The recent New Horizons mission performed a flyby of Pluto in 2015 and will head out into the Kuiper belt for an extended mission of additional flybys of outer solar system objects (Stern et al. 2016).

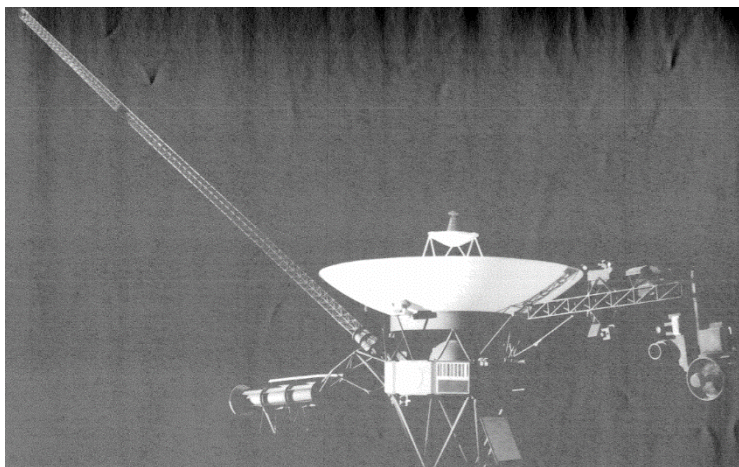


*Figure 1.2 Image of Voyager probe (Murray 1989) One of two probes which performed flybys of most of the solar system planets via the use of gravity assists from one to the other*

It wasn't until 1971 that NASA's Mariner 9 mission became the first artificial satellite around another body, when it successfully achieved Mars orbit (McCauley et al. 1972; Sagan & Fox 1975). The main advantage of an orbital mission over a flyby

is the increased useful mission lifetime. When Mariner 9 reached Mars there was an unusually large atmospheric dust storm preventing clear imaging of the surface (Withers et al., 2015) and if the mission had been a flyby, there would only have been a small chance of performing comprehensive imaging of the surface. Instead, Mariner 9 was able to obtain over 7000 images of the Martian planetary surface over nearly a year of operation (McCauley et al. 1972). Many orbiters have been very successful, particularly the Galileo (active 1995 – 2003) (Young 1998; Greeley et al. 1998; Kivelson et al. 2000) and Cassini (active 2004 – 2017) (Lange 2008; Lopes et al. 2007; Lebreton & Matson 2003) missions, which have provided detailed observations of the Jupiter system and Saturn and its moons .



*Figure 1.3 3 generations of NASA rovers, Pathfinder 1997, Spirit/Opportunity 2004, and Curiosity 2012 Image Credit: NASA/JPL-Caltec*

One of the most technically challenging methods utilised by space agencies to explore planets, is to deploy a stationary lander or a mobile robotic rover on the surface of a planet in order to acquire in-situ data. Achieving a safe landing can be a challenging task, with many missions failing during transit or crashing during to landing. However, the benefits of being able to utilise contact and short range analytical techniques are enormous, some of these are detailed in Chapter 2, Sections 2.2 to 2.8. After numerous attempts which impacted into the lunar surface, the Soviet Union successfully landed a probe in 1966, with the Lunar 9 mission (Biesbroek & Janin 2000). This was followed shortly after by NASA’s Surveyor 1 (Jaffe 1967). Since then, landers have visited the

surface of Venus, Mars, Titan, comets and asteroids (Keldysh 1977; Klein 1979; Lebreton and Matson 2003a). To increase the operational range of a mission, rovers (Figure 1.3) have been developed that are capable of travelling over a planetary surface, expanding the area of operations for one mission (Rice 2014; Biesbroek & Janin 2000). This is demonstrated by the two Mars Exploration Rovers and Curiosity, which all achieved successful campaigns on Mars; these missions are detailed further in Chapter 2, Section 2.1. The rovers aim to simulate the capability of a human geologist working on the planetary surface. Future crewed missions could perform much the same study in a fraction of the time, however there are numerous financial and logistical challenges that need be solved before human missions to another planet can be completed.

Fundamentally, the questions planetary exploration seeks to answer are of geology, biology and chemistry. Astrobiology is the study of the origins, evolutions, diversity and distribution of life in the universe. Many space missions to other planets, such as the recent NASA Mars Science Laboratory (MSL) rover Curiosity (Grotzinger et al. 2012; Grotzinger, Crisp, et al. 2015), seek to characterise the environment to determine whether it is, or ever has been, habitable for life. This involves examining a wide range of features, including the search for liquid water, measurements of the atmosphere and the radioactive nature of the surroundings.

Aside from the search for life, the geological and chemical characterisation of a planetary body is of scientific interest. The investigation of the geological history of both a small scale landing site and that sites context within the whole planet. This can provide evidence of whether conditions may have once been able to support ancient life in the distant past. Most planets underwent significant changes between their initial formation and the environments that are detected now (Carr & Head 2010; Chassefiere 1997; Craddock & Howard 2002).

## 1.2 Geology

Geology is the study of solid earth, including rocks, soils and the internal structure of a planetary body. There are a number of key features of interest about a planetary environment from a geological point of view. At the most basic level this includes: the

elemental composition in the immediate area and the molecular structure of the elemental compounds. This leads to determining the types of mineral that are present, which, in turn, formed rocks (which in a geological sense are defined as “naturally occurring solid aggregate of one or more minerals or mineraloids”). These rocks are classified by formation method into three different types; igneous, sedimentary and metamorphic (Blatt et al. 2006; Pettijohn 1957; Winkler 1967).

Igneous rocks are formed from magma or lava cooling from a source region that has undergone temperature, pressure or compositional change. This process can happen either on the surface (extrusive) or underground (intrusive). The rate of cooling and conditions the sample underwent can inform our understanding of the geological history of the area. This is discussed in greater detail in Chapter 3. Igneous rocks are typically identified by their lack of surrounding “cement”, as they are “float rocks”, loose from the local material and are often coarse-grained. Basalt is a key igneous rock for many planetary systems (Le Maitre 1989; Lissauer and Pater 2013; Wilson 2007).

In contrast, sedimentary rocks are generally formed on the surface of a planetary body or within water, via the deposition of older rocks. This sediment is formed as a consequence of various erosion processes or weathering of a source region. So, the presence of sedimentary rocks is informative of the surrounding areas and their past environmental processes, particularly providing evidence of aqueous processes. They generally have a layered appearance and are composed of multiple elements cemented together as a conglomerate, sandstone or mudstone, rather than as individual mineral grains (Lissauer & Pater 2013; Le Deit et al. 2016; Blatt et al. 2006). Figure 1.4 shows a sedimentary outcrop encountered by NASA’s Mars Science Laboratory rover, Curiosity.



*Figure 1.4 MSL MastCam image southern facing view of The Kimberley a sedimentary outcrop in Gale Crater, Mars Image acquired on Sol 580. Image Credit NASA/JPL (Grotzinger, Gupta, et al. 2015)*

Finally, metamorphic rocks are formed by the application of heat and/or pressure to a different classification of rock. These conditions cause it to change in form, leading to a largely different chemical and physical composition. Metamorphic rocks generally rely on tectonic processes and so they would not be present on planets such as Mars which are thought to lack any tectonic activity (Karlsson et al. 1992; Banerdt & Smrekar 2013; Mezger et al. 2012).

Classification of rocks, particularly the differentiation between igneous and sedimentary is a valuable distinction when determining the geology of an area of investigation. By investigating the chemical and molecular composition of a rock, alongside visual classification, geologists can determine much about a locality's makeup and formation history. The more targets investigated, the more representative the conclusions that are drawn will be. Few scientific instruments provide a full coverage of all chemical, molecular and morphology information, so combinations of instruments are necessary, as discussed in Chapter 2. Because of this, it can sometimes be challenging to assess the mineralogy purely from the chemical makeup (see Chapter 3) and likewise, techniques which determine the mineralogy can be simplified by utilising information on elemental composition.

Knowledge of rock and mineral types allows us to determine hydration levels and investigate evidence of aqueous processes, which is of great interest to astrobiologists. Mineral hydration is a process where water bonds with the crystal structure of a mineral.

Many minerals have hydrous and anhydrous forms. These minerals typically form wherever water has been in the past (Lissauer & Pater 2013; Vaniman et al. 2014). Likewise, knowledge of the kind of tectonic and fractionation processes which formed a rock has numerous implications as regards the composition and makeup of not just the target material but many other samples in the wider area (Cox et al. 1979).

It is also important to consider a much wider view, by investigating the methods with which global processes govern a planet's formation and geography, choosing landing sites for further investigation and providing a greater context for other work. Whilst many geological questions can be answered with remote sensing techniques, a major goal from a geological point of view is to return samples to laboratories on Earth to allow for a much more thorough investigation, without the limits placed on the techniques by the requirements of miniaturising and automating that are necessary for a planetary mission. This has already been accomplished for Earth's Moon, both robotically and by sample return via the Apollo missions (Biesbroek & Janin 2000; Shkuratov et al. 2013). Future missions will seek to replicate this, returning samples from Mars and other planetary bodies (Venkatapathy et al. 2016; Murchie et al. 2014; Mattingly & May 2011). To best prepare for planetary missions, analogues to the expected samples which are chemically and mineralogically similar based on spectral observations from orbiting satellites. These are necessary for tests with mission instrumentation during the preparation phase of the mission.

### **1.3 Astrobiology**

A key science goal of many planetary missions is the search for evidence of extinct or extant life. This involves searching for evidence of whether the environment was, or is, habitable for life processes. On Earth life exists in nearly every natural environment, thriving in harsh environments. By understanding the limits of where life can survive on Earth, it is possible to determine which environments on other planets or moons could potentially be habitable.

Conditions on Earth are very favourable to life. The planet has a thick atmosphere that is primarily composed of nitrogen (78.09%), oxygen (20.95%), argon (0.93%) and carbon dioxide (0.04%) (McEwan & Phillips 1975). This atmosphere protects life against the hazards of space; radiation and meteor impacts. Radiation from the Solar energetic particles and Galactic Cosmic Rays (Guo et al. 2015), are absorbed before they can sterilise the surface. Meteors are much more likely to burn up due to heat from re-entry whilst passing through an atmosphere. Heavy meteor bombardment from space creates a challenging environment for life to grow. The early Earth's atmosphere would likely have been much richer in carbon dioxide, which would have reduced as plant life grew and photosynthesis developed (Kasting 1993). Water is vital for all life on Earth and is generally accepted to be the origin point for the beginnings of life on Earth (Brack 1993; Lane et al. 2010). Water's presence on Earth is almost always accompanied by microbial life (Rothschild & Mancinelli 2001). Temperature is also a key factor; water is most beneficial when in liquid form, and when considering suitable conditions, a "goldilocks zone" or habitable zone is often referred to and relates to the range from the sun where water would be present in liquid form (Kasting 1993). This is not a complete restriction however, as gravitational heating near a gas giant can replace the sun's heat. From a biochemical perspective most living organisms are only viable due to the catalysing effects of many highly-specialised proteins, which are destroyed at high temperatures (Schulze-Makuch & Irwin 2002; Rampelotto & Henrique 2010). A strong magnetic field is also thought to be, if not necessary, very beneficial for the formation of life. It seems likely that it played a key role in preventing water and atmospheric loss that would otherwise arise from interactions with the solar wind (Chassefiere 1997). By examining the extremes of conditions where life survives on Earth it is possible to constrain the search for life in the solar system:

- Temperature, it is possible to find *Planococcus halocryophilus* in permafrost at temperatures as low as  $-15^{\circ}\text{C}$  (Mykytczuk et al. 2013) or hyperthermophiles at  $100^{\circ}\text{C}$  (Stetter 1999),
- pH level, Acidic environments with bacteria capable of growth at pH 0 (Edwards 2000) and alkaline environments pH 9.6 (Lefèvre et al. 2011),

- Deep below the surface of the Earth in hot low oxygen environments (Kerr 1997) and around vents at the bottom of the deepest part of ocean trenches (Gold 1992; Baross & Hoffman 1985),
- Halophiles surviving in the areas of high salt concentration (Marshall et al. 2007),
- Radiation resistant extremophiles near nuclear reactors (Gabani & Singh 2013).

Any astrobiological life would likely be microscopic, too small for conventional optical cameras to image. One solution is to instead search for biomarkers, evidence that life processes leave behind. Whilst some biomarkers can be bioinorganic, there are some which can only be produced by life. One example is scytonemin (see Figure 1.5), which is a pigment produced by Cyanobacteria (some of the earliest terrestrial life) to protect themselves from UV rays (Edwards et al. 2000; Varnali et al. 2009). This is exactly the sort of adaption that lifeforms would need to utilise in order to survive on a planet like Mars, which lacks a magnetic field to protect the surface from solar radiation. However detection of pigments is considered unlikely with current equipment. Instead geological evidence of habitability is the goal of many missions, these bioinorganic molecules such as whewellite, aragonite, mellite and vaterite would if detected be unambiguous evidence for life (Edwards et al. 2014).

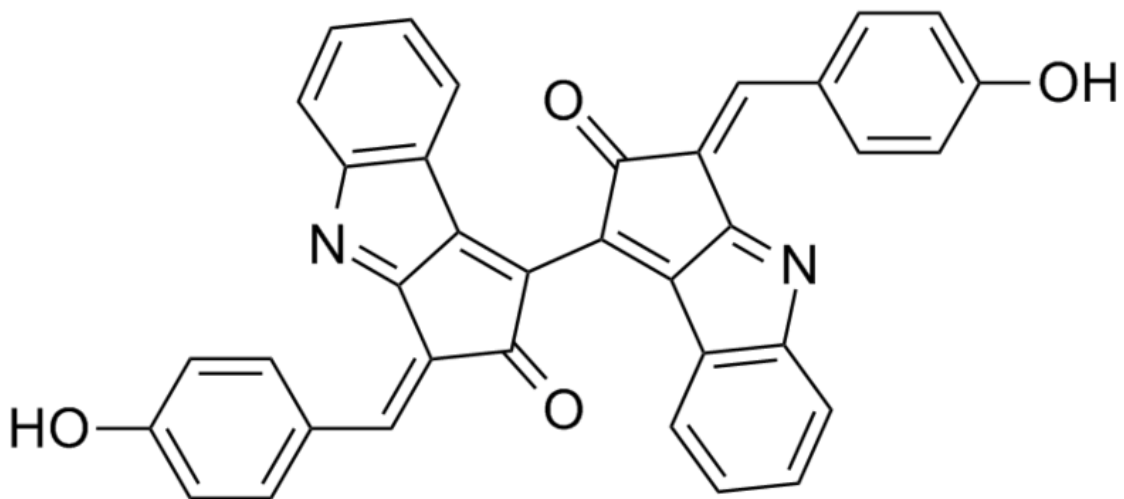


*Figure 1.5 The Scytonemin molecular structure, a useful biomarker for life adapted to high UV radiation conditions, such as those on Mars*

## 1.4 Mars

As one of the neighbouring planets to Earth, Mars has long been observed from Earth, with the first recorded observations by the ancient Egyptians 4 millennia ago (Symons et al. 2012). In the 1600's Galileo performed the first telescopic study of Mars and by the 19<sup>th</sup> century, different albedo features on the surface could be differentiated (Sagan & Fox 1975). Around this time, discussion of the possibility of life on Mars began to be discussed with Percival Lowell erroneously believing he had identified canals on the surface (Sagan & Fox 1975).



Figure 1.6 Artist's impression of Mariner 4 Image Credit NASA/JPL

From the 1960s, both NASA and the Soviet Union sought to send probes on fly-by and hard impact trajectories to Mars. NASA's Mariner 4 performed the first successful fly-by (Chapman et al. 1969) (Figure 1.6), with Mariner 9 the first spacecraft to achieve a stable Martian orbit (McCauley et al. 1972). These missions revealed a red desert world bearing little resemblance to the canalled world suggested by Percival Lowell (Sagan & Fox 1975).

The Martian atmosphere, whilst much less protective than that on Earth (around one hundredth of the pressure (Hess et al. 1979)), still provides more coverage than airless bodies such as the Moon receive. The atmosphere is thick enough that parachutes can be a major component in slowing down a landing probe. This allows for more of the spacecraft launch weight to be devoted to scientific instrumentation, rather than a larger, powered landing system that would be purely responsible for a soft landing.

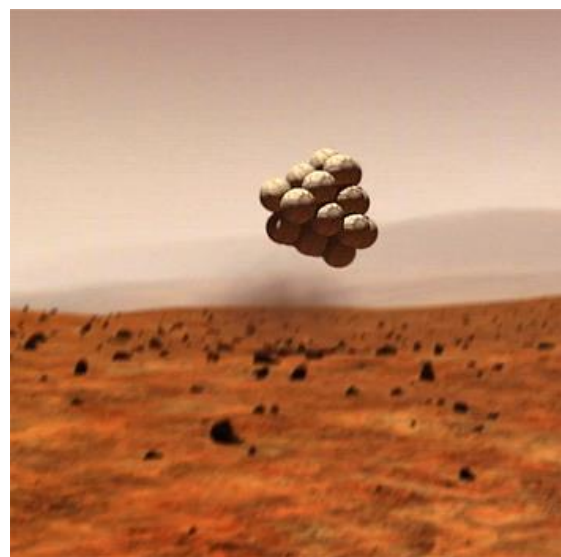


Figure 1.7 Artist's impression of the Spirit rover airbag landing system Image Credit NASA/JPL

However, some form of

additional landing system is required in alongside the parachute, typical systems include:

- Inflatable airbags, as used in the Pathfinder and MER rovers (Figure 1.7) (Braun & Manning 2006),
- Powered sky crane system such as used for Curiosity and planned for MARS 2020 which lowers the rover gently down to the surface from a rocket powered autonomous craft (Prakash et al. 2008)
- A landing platform which undergoes a powered descent before lowering a ramp for the rover to depart, such as that that ExoMars will use (Vago et al. 2013) .

In the early 1970's, numerous Soviet Mars probes were intended to land on the Martian surface (Perminov et al. 1999). The Mars 2 and Mars 3 missions failed during descent or shortly after landing, but some of the later probes recorded atmospheric data (Barlow 2008). NASA's two Viking landers (Figure 1.8) provided the first long term in-situ analysis of the Martian environment. These missions acquired the first colour images of the Martian surface and performed experiments seeking to investigate the possibility of life on Mars (Klein et al. 1976).

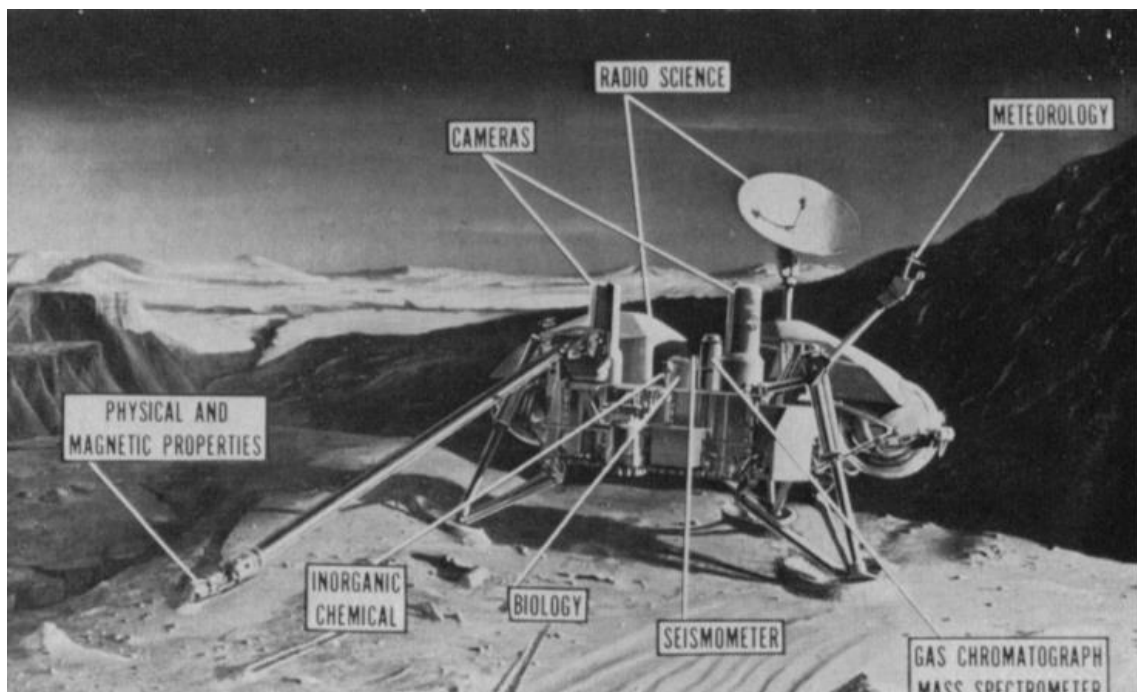


Figure 1.8 Artist's impression of Viking lander with instruments labelled (Soffen & Snyder 1976)

Since the Viking landers, there have been numerous other attempted missions, however many have failed before reaching the planet's surface because of the difficulties associated with performing a remote landing in the challenging Martian conditions. The entire landing process must be completely autonomous as the probe will be too distant to send instructions to in time to react to any difficulties, the probe will be completely reliant on sensors, which if any give inaccurate data could cause a loss of mission. Numerous orbiters have comprehensively mapped Mars both visually and in other spectral ranges, investigating Mars' geology, atmosphere and residual magnetic field (McSween et al. 2009; Mustard et al. 2008; Bandfield et al. 2000). NASA currently has 3 active orbiters (2001 Mars Odyssey, Mars reconnaissance orbiter and MAVEN), whilst ESA also has Mars Express and the ExoMars Trace Gas Orbiter (which arrived in October 2016). The Indian space agency ISRO has their Mangalyaan orbiter.

NASA has sent 4 robotic rovers; Pathfinder (Golombek 1997), Spirit (S. W. Squyres, Arvidson, et al. 2004), Opportunity (Squyres et al. 2006) and the most recent, Curiosity (Grotzinger, Crisp, et al. 2015). See Table 1.1 for instruments on these Mars missions. These rovers deployed a variety of analytical instrumentation, used for investigating and characterising the Martian surface environment (see Figure 1.9). The techniques used by these missions are examined in detail in Chapter 2, with a particular focus on the Curiosity rover. Many of these missions lasted well beyond their original planned lifetimes (Zurek et al. 2016) and have greatly increased the understanding of the Martian environment. Studies performed with data returned by the Curiosity and Spirit rovers are detailed in Chapter 3. Numerous other missions are planned for the next launch windows (which occur roughly every 2 years) in 2018 and 2020 from space agencies including: NASA, ESA, ISRO, the United Arab Emirates and the Chinese



*Figure 1.9 Cumberland drill hole, samples were analysed on board the Curiosity rover whilst remote analysis took place of the drill tailings, the methods used are described in Chapter 2. Image acquired by the MastCam Camera on Sol 279  
Image Credit NASA/JPL*

National Space Administration. Some of these future missions are detailed in Chapter 2, Section 10.

Viking <sup>1</sup>	Pathfinder <sup>2</sup>	MER <sup>3</sup>	MSL <sup>4</sup>	ExoMars <sup>5</sup>	MARS 2020 <sup>6</sup>
Biology experiments <sup>7</sup>	Imager for Mars Pathfinder <sup>12</sup>	Pancam <sup>15</sup>	Mastcam <sup>22</sup>	PanCam <sup>31</sup>	Mascam-Z <sup>40</sup>
GCMS <sup>8</sup>	APXS <sup>13</sup>	Mini- TES <sup>16</sup>	ChemCam <sup>23</sup>	ISEM <sup>32</sup>	SuperCam <sup>41</sup>
XRF <sup>9</sup>	Meteorology package <sup>14</sup>	Microscopic Imager <sup>17</sup>	REMS <sup>24</sup>	WISDOM <sup>33</sup>	MEDA <sup>42</sup>
Seismometer <sup>10</sup>		APXS <sup>18</sup>	SAM <sup>25</sup>	ADROM <sup>34</sup>	PIXL <sup>43</sup>
Meteorology instrument <sup>11</sup>		Mossbauer Spectrometer <sup>19</sup>	CheMin <sup>26</sup>	CLUPI <sup>35</sup>	SHERLOC <sup>44</sup>
		Rock abrasion tool <sup>20</sup>	APXS <sup>27</sup>	MA_MISS <sup>36</sup>	RIMFAX <sup>45</sup>
		Magnetic properties instrument <sup>21</sup>	MAHLI <sup>28</sup>	MOMA <sup>37</sup>	
			RAD <sup>29</sup>	MicrOmega <sup>38</sup>	
			DAN <sup>30</sup>	RLS <sup>39</sup>	

Table 1.1 Instrumentation on Mars lander missions

**1.** (Klein 1979) **2.** (Golombek 1997) **3.** (Squyres et al. 2003) **4.** (Grotzinger et al. 2012) **5.** (Vago et al. 2013) **6.** (MARS 2020 Reference) **7.** Gas exchange/ labelled release **8.** Gas Chromatography Mass Spectroscopy **9.** X-ray Florescence **10.** Seismometer **11.** Weather sensors **12.** Imager **13.** Alpha Particle X-ray Spectrometer **14.** Weather sensor **15.** Imaging system, **16.** Infrared Spectrometer **17.** Imager **18.** Alpha Particle X-ray Spectrometer **19.** Mossbauer spectrometer **20.** Sample preparation **21.** Magnetism sensor **22.** Imaging system **23.** Laser Induced Breakdown Spectroscopy (LIBS) **24.** Weather sensors **25.** Mass spectroscopy **26.** X-ray Diffraction **27.** Alpha Particle X-ray Spectrometer **28.** Robotic arm camera **29.** Radiation sensor **30.** Neutron spectrometer **31.** Imaging system **32.** Infrared spectrometer **33.** Ground penetrating Radar **34.** Neutron spectrometer **35.** Close-up imager **36.** IR- spectrometer in the drill **37.** Mars Organic molecule analyser **38.** Visual/ IR spectroscopy **39.** Raman spectroscopy **40.** Imaging system **41.** Raman/LIBS **42.** Weather sensor **43.** X-ray Fluorescence **44.** UV-Raman **45.** Subsurface Radar

### 1.4.1 The Martian Environment

Mars bears some similarities to Earth. It is a rocky planet but much smaller (50% of Earth's diameter) and lower in mass (10% of Earth's mass), with only a third of the gravity of its larger neighbour.

The planet lacks all but a residual magnetic field (12 nT) (Bisikalo et al. 2017; Connerney et al. 2001) which has led to a

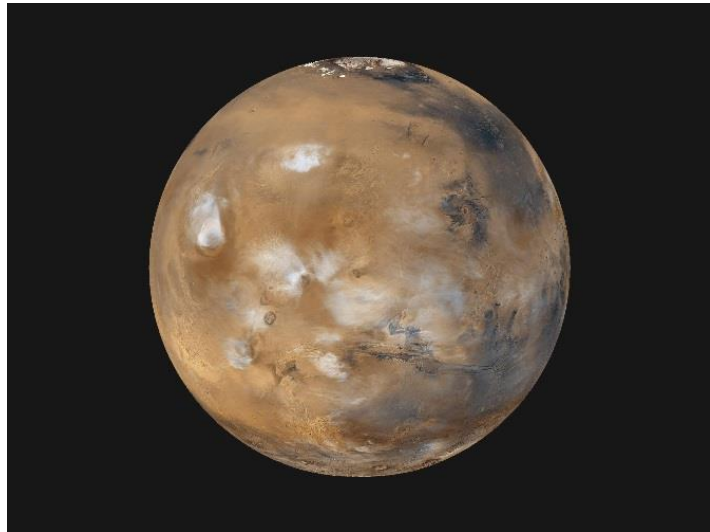


*Figure 1.10 Mars showing atmospheric weather. Mars Global Surveyor, Mars Orbiter Camera Image (Wang & Ingersoll 2002) Image Credit: NASA/JPL-Caltech/MSSS*

significant atmospheric reduction from solar wind compared to its ancient past (Dehant et al. 2007). The atmosphere is also very different from that on Earth (Figure 1.10). It is currently composed mainly of carbon dioxide (95.97%) argon (1.93%), nitrogen (1.89%) oxygen (0.15%) and carbon monoxide (0.0557%). In addition, compared to the terrestrial atmosphere, the pressure is very low at 6mbar (Barlow 2008; Hess et al. 1979).

The temperature typically varies between 150K and 250K (White 1979) with an average of 202K (Haberle et al. 2014; Vasavada et al. 2017). The majority of the Martian surface is very different from most terrestrial environments. The rocky, silica rich environment is marked with many impact craters and covered by an iron oxide dust, which gives it a distinctive red colouration with significant brighter and darker regions (Ruff & Christensen 2002; Greeley & R. 1985). This dust can often be displaced by large storms, which can obscure much of the planet's surface from orbital observations (Withers et al. 2015; McCauley et al. 1972; Zurek 1982).

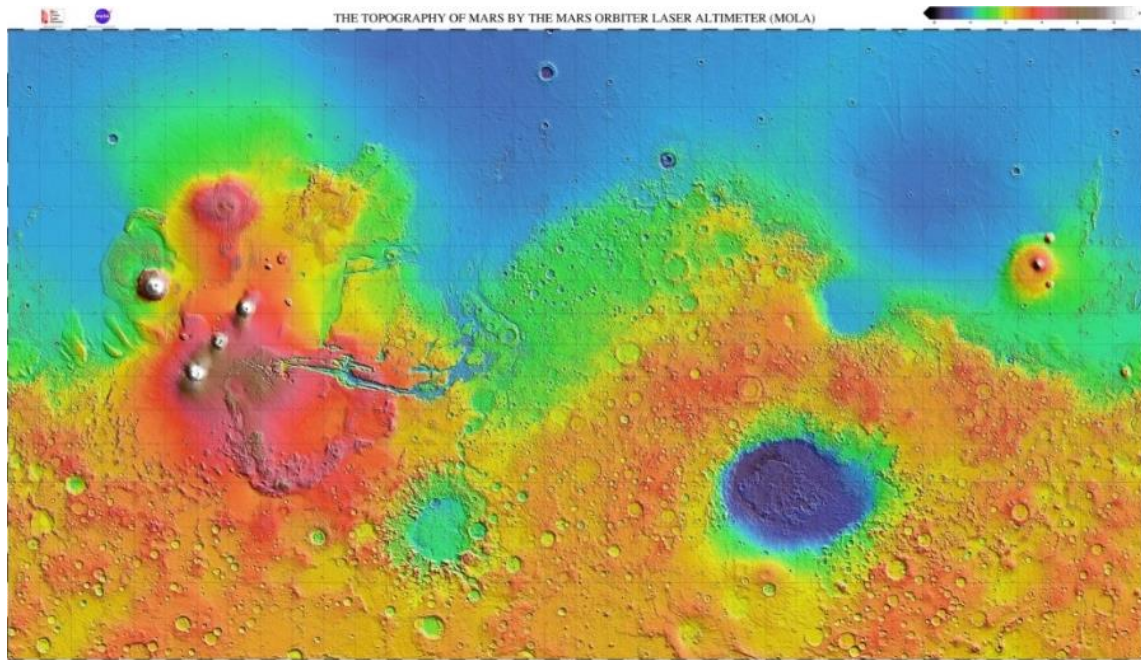


Figure 1.11 Topographical surface map of Mars from Mars Global Surveyor. White indicates higher altitude and dark blue lower. Mars Orbital Laser Altimetry instrument obtained the data (Smith et al. 2001) Image Credit NASA/JPL

There is a clear hemispherical dichotomy between the north and south Martian terrain (Tanaka et al. 1988; Squyres & Kasting 1994). The southern highlands are considerably older and much more cratered than their northern counterpart. In contrast, the North is relatively smoother and younger. This is demonstrated by the topographical map shown in Figure 1.11. This feature may be due to one large impact or perhaps multiple smaller ones (Wilhelms & Squyres 1984; Breuer et al. 1993). It is important for different missions to explore both of these environments to enable comparison. The science goals of a mission will determine the landing area on which to focus. Some missions aim to investigate the boundary between the two areas in order to examine their interactions. The study of Martian history is typically split between 3 main geological epochs; The Noachian, Hesperian and Amazonian (Carr & Head 2010).

#### 1.4.2.1 Noachian

The first main Martian geological age, the Noachian period, was characterised by heavy meteorite impacts. The formation of the large Hellas crater is generally considered to be the starting point at between 4.1 to 3.8 Gyr ago (Carr & Head 2010) which coincides with the Late Heavy Bombardment, a period of heavy meteorite activity in the early solar system (Wetherill & W. 1975). This early period marked the formations of many of the

Martian craters visible today, with erosion and valley formations also dominant processes. The huge impacts that were required to have produced craters such as Hellas would also have distributed ejecta material over much of the Martian surface (Segura et al. 2002). Whilst volcanism would likely have occurred it would have been focused in the Tharsis region and impacts would likely have been the primary motivator for surface change (Phillips et al. 2001). Many of the rocks in the heavily cratered highlands are basaltic in origin but lower in calcium or pyroxene (Bibring et al. 2006; Poulet et al. 2009). A representative example of this type of terrain is the Columbia Hills region visited by Spirit MER rover (McSween & Ruff 2006; Squyres et al. 2007). There is evidence that Noachian rocks underwent chemical alteration indicative of aqueous processes, suggesting hydrothermal fluids due to the detection of igneous minerals in Noachian environments (Bibring et al. 2006), with indications of weathering and deeper hydrated minerals within alluvial fans that would have formed prior to these minerals (Carr & Head 2010). Many of these craters also show evidence of erosion, much more so than the newer geography elsewhere on Mars. The later Hesperian craters are generally smaller and contain the primary impact features. This indicates that erosion process dropped off from the end of the Noachian to the start of the Hesperian (Craddock & Howard 2002; Golombek et al. 2006). Valleys are common throughout the Noachian terrain draining into local lows. Evidence from these valleys indicate precipitation and surface run off occurred throughout the Noachian (Craddock & Howard 2002; Irwin & Howard 2002; Hynek & Phillips 2003). Many of the lower craters have inlet and outlet channels indicating past flowing water (Fassett & Head 2008b) along with valleys and lakebeds (Szabó et al. 2015; S. W. Squyres, Grotzinger, et al. 2004). It is unclear whether the Noachian age included Martian oceans. There are two possible shorelines at Hellas (Moore 2001a) and northwest Arabia (Howard et al. 2005). However, if they had existed much of the evidence would now be gone (Head et al. 2002).

There is evidence from the presence of water (Fassett & Head 2008b), phyllosilicates (Murchie et al. 2007; Leroi et al. 2009) and chlorine rich deposits (Osterloo et al. 2008) that the Noachian climate was quite different from Mars today, with periods of warmth during and towards the end of the period, with a thicker atmosphere allowing for liquid

water on the surface (Jakosky & Phillips 2001; Carr 1999; Craddock & Howard 2002). Isotopic ratios can be used to estimate the pressure and composition of the early Martian atmosphere as potentially between 0.5 – 1 bar in pressure (Carr 1999; Craddock & Howard 2002). Early greenhouse gases could have led to a much warmer surface (Sagan 1997). The warmer temperature and pressure could have allowed for liquid water on the surface and even rainfall and a water cycle (Craddock & Howard 2002).

Mars lacks significant carbon deposits (Bibring et al. 2006) to act as sinks for the carbon which would have composed a thick early CO<sub>2</sub> atmosphere. This indicates that a different warming system than the CO<sub>2</sub> - H<sub>2</sub>O greenhouse trend would have taken place. An explanation for this is the possible presence of other gases such as SO<sub>2</sub> and CH<sub>4</sub> or other largescale effects such as huge impacts or volcanism (Carr & Head 2010). However, it is unlikely that such impacts would contain enough potential precipitation to erode valley networks, also the largest impact sites show less valley systems than other locations. As such, it seems likely that Mars did possess a warmer environment for at least part of the Noachian, which it subsequently lost (Squyres & Kasting 1994; Paige 2005; Craddock & Howard 2002).

#### *1.4.2.2 Hesperian*

The Noachian was followed by the Hesperian period (named after Hesperia Planum). Unlike the Noachian in the Hesperian bombardment from space was not the dominant factor, instead volcanism played a primary role. It lasts from the end of the Late Heavy Bombardment at around 3.7 Gyr to 3 Gyr (Hartmann & Neukum 2001). Hesperian volcanism saw a resurfacing of approximately 30% of the Martian surface (Head et al. 2002). This period saw the formation of large lava planes, less valley formation, but larger canyons with outflowing into the lakes or seas. The lower rates of erosion during this period indicate much less aqueous erosion than occurred during the Noachian (Carr & Head 2010). These were detected by high quantities of olivine in Hesperian terrain (Bandfield et al. 2000) as olivine will likely breakdown when encountering hydrous conditions. Spirit data of the basaltic flow at the Hesperian Gusev crater shows little alteration in the rocks (Greeley et al. 2005). Erosion rates in the Hesperian dropped between 2 to 5 orders of magnitude and never returned to the rates seen in the

Noachian (Golombek et al. 2006). It was during this period that the large Martian volcano, Olympus Mons was formed. Despite the reduced valley formation there are still some of Hesperian age, particularly on volcanoes (Gulick 1998; Gulick 2001; Fassett & Head 2006). However, the relative rarity of these valleys compared to the Noachian terrain indicates that conditions had changed so that valleys were only formed sporadically (Fassett & Head 2008b). Some of these valleys may have been formed by ice melting on the summits of volcanoes, rather than as a consequence of more significant climate change. The outflow channels identified from this period are likely of fluvial origin (Head et al. 2002). As these outflow channels appear to have formed rapidly, they are unlikely to be produced gradually by precipitation and instead their source is probably a large sudden release of water. There are a number of possible sources for this water: groundwater aquifers, lakes or ice. Various evidence of all these phenomena has been identified in the Martian environment. If these outflow channels were caused by sudden flooding then large bodies of water would be left at the bottom in the northern lowlands. Some possible shorelines for these bodies of water have been identified (Clifford 2001; Parker et al. 1989; Parker et al. 1993) and Hellas (Moore 2001a) but they remain controversial. The Dorsa Argentea Formation in the south, measured as Hesperian (Tanaka et al. 1987), is thought to be the site of a huge icecap in the Hesperian period over double the size of the current Martian polar icecaps (Head & Pratt 2001).

#### *1.4.2.3 Amazonian*

The most recent and current Martian age is the Amazonian, from 3Gyrs to now, making it by far the longest of the time periods considered. Changes over this time period are generally smaller than in the other earlier ones with less impacts, volcanism and barely any erosion (Golombek et al. 2006). The decline in volcanism has seen a change in the eruption rate amounting to 10 times less than the Hesperian (Greeley & Schneid 1991), although eruption does still occur sporadically. Due to the lack of these major processes, features such as wind and ice dominate those geological changes which do occur.

Ice, in particular, had a major impact on the Amazonian landscape, possibly due to frozen water left from the Hesperian (Kargel et al. 1995). Ice deposits on the Martian surface are generally seasonal, although in some areas, it is thicker or present below the

surface (Rennó et al. 2009; Smith et al. 2009). To the present day, Mars possesses polar icecaps of frozen carbon dioxide which are clearly visible from orbit (Kieffer et al. 2006; Farmer et al. 1976). The poles vary in size on a seasonal basis with summer causing sublimation, cloud formation and pressure changes (Hess et al. 1979). Compared to other regions on Mars, ice is particularly thick in the Polar Regions, 3km deep at the coldest point. By counting craters, the age of this region was determined to be around 0.1 Myrs (Herkenhoff 2000).

There is some evidence of small scale fluvial activity during the Amazonian (Plescia 2003), including in craters as recent as 2 to 140 Myrs (Berman & Hartmann 2002). The other major environmental factor is aeolian processes which produces dunes across the Martian surface. However, the rocks themselves have retained their primary textures and wind has played a minimal role in larger rocks, mainly affecting fragment materials.

Valley networks are also very rare, with uncertainty over whether the youngest may actually be Hesperian (Fassett & Head 2008a). It seems likely however that the Alba Patera valleys are indeed Amazonian (Costard et al. 2002). Small gullies of the order of a few meters wide are more common, usually on steep slopes on the polar face of craters (Balme et al. 2006) although the origin is uncertain. One of the most likely sources is temporary liquid water from melting ice sources (Head et al. 2003).

#### 1.4.3 Gale Crater

A key location on the Martian surface for work covered in later Chapter 3 is Gale crater. This crater, 154km in diameter, has a 5km high central peak called Aeolis Mons, also known as Mount Sharp. The crater has previously been proposed as a possible mission landing site for MER rovers (Grant et al. 2004), Mars Science Laboratory and the ExoMars missions, due to the spectral data indicating the presence of clay minerals, phyllosilicates and sulphates, as well as the likely past presence of water (Wray 2013). Located near the boundary of the two types of terrain that dominate the Martian northern and southern hemispheres, Gale provides an interesting geological comparison of the two materials.

#### 1.4.4 Mars as a Candidate for Supporting Life

Mars ranks as one of the most likely candidates in the search for evidence of past or present life. As such, the planet has been the focus of much planetary exploration interest over the last 40 years, from many different space agencies, with the common aim of detecting life or investigating the past and present habitability of the environment.

The lack of a strong magnetic field and thick ozone layer means the surface of Mars is constantly bombarded with radiation (Bisikalo et al. 2017; Hassler et al. 2014). However, some studies have shown that at a depth of 2m beneath the surface rock, the radiation shielding of the regolith would be sufficient to absorb much of that radiation, allowing for subterranean life to survive (Vago et al. 2013). The depletion of the atmosphere is largely due to the lack of a strong planetary magnetic field and magnetosphere to prevent solar wind from stripping away the atmospheric particles (Kass & Yung 1995).

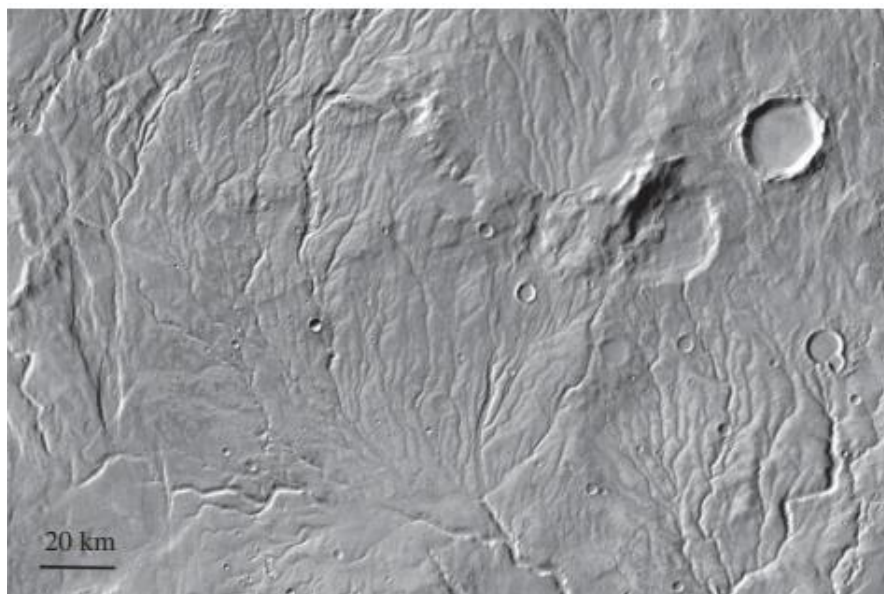


*Figure 1.12 Warrego Vallis, Mars, The drainage shows evidence of fluvial activity from rainfall and surface runoff.  
Image Credit NASA/JPL (Carr 2012)*

All life on Earth requires water (Cavicchioli et al. 2011) and, whilst Mars is mostly very dry, there is some recent evidence that there may be some form of briny seasonal flowing water on Mars (McEwen et al. 2011; Ojha et al. 2015). In its ancient past there is evidence that Mars would have been much wetter, see Figure 1.12. The salty

environment of Mars may not be ideal for life now, but there is evidence that it was much more habitable in its ancient past.

Simulations of the Late Heavy Bombardment indicate that a substantial amount of material is likely to have transited between Earth and Mars and vice versa (Gladman et al. 1996; Worth et al. 2013). This impact-driven interplanetary transfer could allow for exchange of biological material from Earth to Mars (or other planetary bodies) or vice versa, this is known as panspermia. However, any life from one planet would face substantial challenges adapting to the alien environment of another world. Overall, ancient Mars would likely have been a habitable environment for life (Vasavada et al. 2016).

However, Mars is not the only promising candidate location in the solar system for the search for astro-biological life and other potential locations are discussed in the following Sections.

## 1.5 Europa

Another possible location for astrobiological life is Jupiter's icy moon, Europa.

### 1.5.1 History of Europa Exploration

Despite its many promising features Europa has been the subject of much less study than Mars. This is primarily due to its location and difficulties associated with achieving an appropriate orbit within the Jovian system. A number of pioneer missions and the Voyager space craft have performed fly-bys of Jupiter, which gave the opportunity to examine Europa. However, the only mission to spend considerable time investigating the moon has been the Galileo orbiter (Moore 2001b; Greeley et al. 1998), which spent 8 years at Jupiter and performed many close fly-bys of the moon over the course of its mission. Galileo magnetometer data revealed evidence of a subsurface ocean under the outer ice (Kivelson et al. 2000), whilst imaging showed an icy surface marked with impact craters and tectonic deformation (Kargel 2000; Greeley et al. 1998).

NASA's planetary decadal survey identified Europa as a primary target for future missions (Clark et al. 2009). The JUICE mission (Jupiter Icy Moon Explorer) will conduct

multiple flybys (Dougherty et al. 2012; Dougherty et al. 2011), but will be mainly focused on the moon Ganymede.

The planned Europa Clipper mission will seek to carry on the work of Galileo investigating the geology and composition of Europa (Phillips & Pappalardo 2014). Future work constraining the exact structure of Europa, determining the thickness of the ice layers, the nature of water including its acidity, salinity and chemistry will lead to a better understanding of the chances of life under Europa's ice (Marion et al. 2003).

Due to the thick nature of the ice sheet covering the whole surface, any planned mission designed to examine the sea-floor will be extremely challenging. Some mission concepts propose drilling through the ice and then using a submersible craft (Weiss et al. 2011). This factor, coupled with the initial landing and transmission delay for operational instructions, would result in a highly complex mission (beyond those attempted previously).

### 1.5.2 The European Environment

Orbiting the gas giant Jupiter, Europa (Figure 1.13) is an icy moon heated mostly by tidal forces due to Jupiter's immense gravity (this compensates for its vast distance from the sun) (Sotin et al. 2002). Europa is slightly smaller than Earth's moon at 3120km in diameter (Anderson et al. 1998). It has a bright colouration due to its icy surface (Johnson et al. 1983).

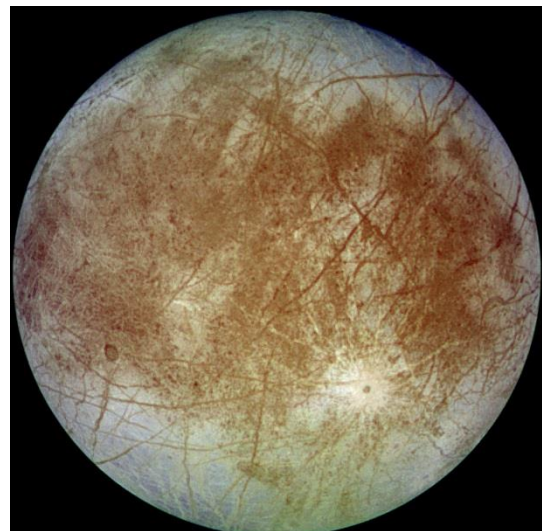


*Figure 1.13 Jupiter's Icy moon Europa. Image Credit: NASA/JPL/DLR taken by the solid state imaging television camera on board the Galileo spacecraft*

There is a great deal of evidence that there is a large subsurface ocean deep beneath the ice (Pappalardo et al. 1998; Carr et al. 1998; Khurana et al. 1998; Kivelson et al. 2000; Chyba 2000). The ice covering Europa is one of the smoothest planetary surfaces in the solar system, implying it is very young, perhaps only 10s of millions years old (Lissauer & Pater 2013).

Observation of Europa have detected plumes of liquid or vapour that emit from the surface, sending water vapour up to 26 km above Europa (Quick et al. 2013; Hand 2015; Sotin et al. 2002; Roth et al. 2014). An orbital mission may be able to sample these plumes without the need for a landing. The plumes were successfully imaged by the Hubble space telescope (Hand 2015).

The surface temperature varies between lows of 50K and highs of 125K with an average of 102K. The radiation level is intense, due to the close proximity to Jupiter, within the radiation belts (Chyba 2000).

### 1.5.3 Europa as a Candidate Supporting for Life

Given that on Earth, life can survive in similar conditions beneath arctic ice or near thermal vents at the bottom of oceans, it is possible, that some form of life could survive the conditions present there. The Mariana trench is a useful terrestrial analogue when discussing the possibility of life surviving on Europa (Marion et al. 2003). Generally wherever water is on Earth, there is life, so if there is indeed a subsurface liquid water ocean present, it would likely be habitable.

There is even some evidence of volcanism and this additional heat could be vital for life (Chyba & Phillips 2002). The ocean's salinity, if any, will be a major factor in constraining any model for what European life would be like (Marion et al. 2003). The European ocean is thought to be deeper (100km) than any terrestrial equivalent causing pressures of around 1,200 bars (Kargel 2000), greater than the largest pressures on Earth ~1,100 bars. Since the most habitable environment on Europa would likely be around any thermal vents on the ocean floor, life would need to be extremely well adapted to this pressure environment (Marion et al. 2003).

There are however some major problems with Europa as a life candidate, the most significant of which is radiation (McKay 2002), but whilst radiation on the surface, coupled with the freezing temperatures, may have a sterilising affect, deeper down it may actually be a vital source of energy for life processes (Chyba 2000).

## 1.6 Venus

### 1.6.1 History of Venus Exploration

The first flyby of Venus was accomplished by the Soviet probe Venera 1 but provided little data. That mission was followed by NASA's Mariner 2 the following year (Basilevsky & Head 2003) and additional Mariner and Venera missions, which performed fly-bys throughout the 60s and 70s (Basilevsky & Head 2003).

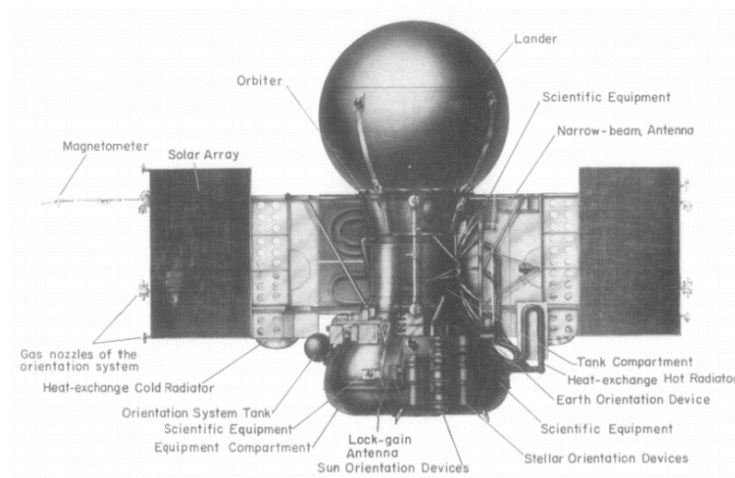


Figure 1.14 Design of Venera 9 and 10 Image Credit (Keldysh 1977)

Surface exploration of Venus has mainly been accomplished by the Venera missions which provided images of the surface and gamma ray spectroscopy of the surface (Keldysh 1977). See Table 1.2 for Venera mission instrumentation. Numerous missions have orbited Venus starting with Venera 9 (Figure 1.14), more recently NASA Magellan probe radar mapping the surface in the early 90s (Solomon et al. 1992; Basilevsky & Head 2003), The European Space Agency Venus Express for long term atmospheric analysis (Svedhem et al. 2007) and JAXA's Akatsuki which failed its initial orbit but later succeed in achieving an elliptical orbit for UV imaging (Kawakatsu et al. 2012).

Future missions are proposed that would involve a next generation lander with a suite of more advanced analytical instruments, potentially aiming to obtain samples from the surface or sub-surface via a drill in order to perform thorough analyses with an on-board instrument suite (Wilson et al. 2016; Smith et al. 2013; Wang, Wei, et al. 2015). Other mission proposals plan to conduct studies of the atmosphere in much greater detail, specifically looking for biomarkers of any life that may have adapted to such an environment. This characterisation of the atmosphere would also allow for much more accurate modelling of its past and a better understanding of Venus' potential early habitability. These missions could sample the atmosphere as they descended through

the atmosphere, fly low and take in samples, or utilise a balloon mechanism which would allow for longer term operation (Cockell 1999).

---

**Venera 13 and 14**

---

Accelerometer

Thermometer/Barometer

UV photometer

Gas Chromatography

Nephelometer

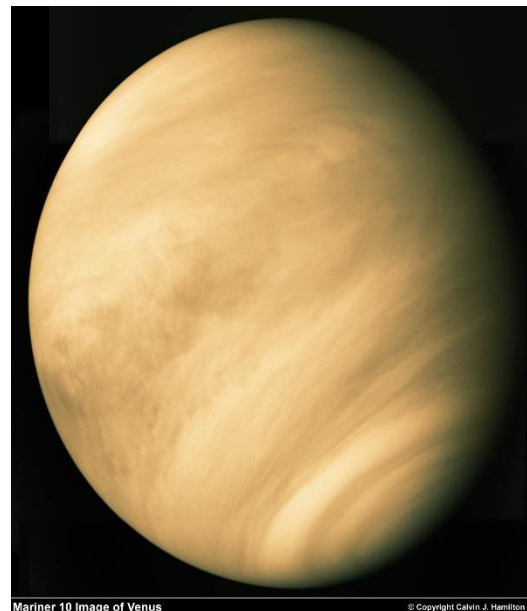
XRF

Soil drill

*Table 1.2 Scientific instruments used on the successful Soviet Venus landers*

### 1.6.2 The Venusian Environment

Like Mars, Venus shares many of its main key features with Earth, including its thick atmosphere and roughly equivalent size. However, it also has some marked differences which make it a much more hostile place with respect to supporting life. The atmospheric composition and thickness is the primary difference compared to Earth, with a much higher percentage of carbon dioxide compared to Earth, with Venus possessing an atmospheric composition of 96.5% carbon dioxide, 3.5% nitrogen, with trace amounts of sulphur dioxide, argon, water vapour, carbon monoxide, helium and neon (Schubert et al. 1980; Seiff et al. 1985), see Figure 1.15. The



*Mariner 10 Image of Venus*  
© Copyright Calvin J. Hamilton  
*Figure 1.15 Mariner 10 image of Venus. Image Credit NASA*

atmosphere is also considerably thicker than Earth's, with an average surface pressure of 93 bar (Schubert et al. 1980). The greenhouse effect causes extreme temperatures on Venus (Pollack et al. 1980), much greater than even those found on Mercury, despite its closer proximity to the sun. This atmospheric heating leads to a surface temperature of around 740K (Lewis 1968; Keldysh 1977; Gilmore et al. 2017).

The surface is rocky in nature and has been mapped comprehensively with radar altimetry (Solomon et al. 1992; Basilevsky & Head 2003), showing the elevation to be much more homogeneous than that of Earth (Martin et al. 2007). Images from the Soviet Venera probes showed a barren surface with eroded rocks, similar in composition to terrestrial basalts. Future missions will seek to sample and analyse these rocks in greater detail to determine their mineralogy.

The Magellan probe radar imagery showed many possible sources of volcanism across the surface. Many of the lowest parts of Venus are covered by volcanic deposits (Head et al. 1992) and there is evidence of active volcanism still occurring (Smrekar et al. 2010). In contrast to Mars, features on Venus indicate the presence of plate tectonics, including mountain ranges, which reflect terrestrial plate tectonic activity (Solomon et al. 1992; Anderson 1981).

Only impactors large enough to produce craters over 3km in diameter are able to make it through Venus' atmosphere. The number of craters indicate that the Venusian surface is much younger than that of Mars, but older than that of Earth (Schaber et al. 1987).

### 1.6.3 Venus as a Candidate for Supporting Life

These temperatures at the surface of Venus are far in excess of the limits that life can survive at on Earth (Schulze-Makuch & Irwin 2002). Whilst this does not eliminate the possibility of life surviving on Venus's surface, it does make it quite unlikely. One solution to the temperature problem would be for life to survive high up in a more favourable part of Venus' atmosphere (Cockell 1999; Schulze-Makuch & Irwin 2002).

However, the atmosphere is also known to be extremely acidic, pH 0 (Cockell 1999), so much so that missions to the surface only last hours before ceasing operation. On their

own, these acidic conditions would not necessarily prevent life: as discussed above, acidophiles can survive at levels as low as pH 0 (Edwards 2000). The thick atmosphere and H<sub>2</sub>SO<sub>4</sub> aerosols provide good protection against UV radiation from the Sun (Cockell 1999).

In the early solar system the greenhouse effect would also have not yet heated a young Venus to the same extent that is seen today, so conditions could have once have been much more favourable to life (Schulze-Makuch & Irwin 2002). There may have been a large quantity of water that has subsequently been lost over time (Kasting & Pollack 1983). During this time period, life could have developed on Venus, or been transported via meteorite from Earth or Mars (Melosh 2003). Unfortunately, Venus has undergone multiple melting and solidifying resurfacing events, leading to a very young surface, which would make it very hard to detect evidence of life from this time period (Grinspoon 1998), however it is possible some form of subsurface evidence could still exist.

## 1.7 Analytical Science Requirements

Various analytical science techniques can (and have) been used to interrogate these planetary environments. The following Section covers the key science questions analytical instrumentation seeks to answer.

When investigating an unknown sample, one of the features of primary importance is the sample's physical composition. For rocks, the major elements of interest are generally; silicon, iron, aluminium, magnesium, calcium, sodium, potassium and sulphur, with some additional minor elements also of interest such as titanium, phosphorus, zinc, copper and manganese (Deer et al. 1966). From an astrobiological perspective it is important to have the capability to detect the elements associated with life: carbon, hydrogen, nitrogen, oxygen, phosphorous and sulphur (Silva & Williams 2001). Various instruments are optimised for the qualitative and quantitative analysis of different selections of these elements; the specifics of these elemental and chemical instruments are discussed in further detail in Chapter 2. Due to historical reasons, geological

convention typically reports the rock forming elements in weight percent oxide form i.e. Si -> SiO<sub>2</sub> etc.

As well as determining the chemical composition it is also important to determine the molecular or mineralogical make-up of a target. This is useful to gain insight into the physical processes that an area would have undergone during its formation, as well as to determine the source region of a particular target. This can then be compared to that of other similar targets and the surrounding area. Different heating, cooling and pressure conditions lead to the formation of different minerals. Likewise, the base material undergoing these conditions can be predicted based on the grain, size, shape and type of mineral. Molecular information is also useful for investigating more complex structures such as biomarkers – molecules left behind by life processes - necessary for the detection of evidence for life. The techniques capable of providing this mineralogical data are detailed in Chapter 2, Sections 2.3, 2.5 and 2.6. Whilst it is possible to predict the mineralogical composition from the elemental data, as shown in the stoichiometry feldspar analysis presented in Chapter 3, it is much more straightforward (and reliable) to obtain mineralogical data.

Another feature of interest to be investigated with analytical techniques is whether the rocks and minerals located in an area are hydrated. This can either be directly detected or inferred by the presence of aqueous or anhydrous minerals and by examining the type of rocks present. Similarly, samples can be examined to determine whether they have been weathered or eroded or if they have undergone fluvial or Aeolian processes. In some cases, this can be accomplished visually from imaging both in orbit and in-situ.

The morphology of a sample is very useful for determining its structure: the textural identification, size, shape, spatial grain separation, the level of vesiculation a sample has undergone, clast dispersion, and physical properties, such as hardness or density of a rock, are all useful pieces of geological information (Yingst et al. 2013). On Earth, investigating these features would be very easy with the dexterity of a human geologist, but with the limitations of a robotic mission images and interactions with robotic arms must be used to predict these properties.

The age of a rock; i.e. how long it has been since it was formed, or was last geologically active, is vital when determining the timeline for geological changes at a target site or for determining its origin – a sample with the same geological age as the solar system formation is likely not from a geologically active planetary body, but in fact a meteorite from the asteroid belt (Anders 1968).

Magnetic and radiation environments are both important to map, particularly from an orbital mission, to establish the electromagnetic environment around a planetary body, as this will have an impact on the designs of future missions. Knowledge of the magnetosphere of a planet also informs astrobiological questions regarding solar radiation. Likewise, when planning a rover mission, the potential landing site and its wider geological context must be thoroughly investigated. This can use visual and spectral imaging to ensure that not only is it safe to land a mission there, but also that there are features of scientific interest, either inside the landing ellipse or within driving distance. Finally the landing site must be compared to the capabilities of the selected instruments to ensure that they will provide useful data in that environment (Golombek et al. 2012).

If one is present, then measuring the consistency and content of an atmosphere is one of the key tasks for a planetary mission, whilst this can be accomplished to some extent from orbit, analysis of atmospheric samples with an on-board laboratory will allow for more detailed data. Sub-surface investigations, either through the utilisation of radar sensors or with a physical drill, are useful to help examine the internal structure of a planet. The acquisition of drill cores allows for different geological ages to be examined simultaneously and can provide a useful history of the changes that an area undergoes. However, no robotic drill can approach the depths achieved by terrestrial drill cores. The overarching goal of almost all robotic missions' analytical instrumentation is to recreate both a geologist engaging in field work, and an analytical laboratory for the analysis of samples in-situ and remotely on another planetary body.

Chapter 2 details various types of scientific instrument which can accomplish these tasks and highlights examples of their use on planetary missions with particular focus on NASA's current MSL mission and ESA's future ExoMars mission.

## Chapter 2: Analytical Science techniques

### 2.1 Introduction

Chapter 2 describes some of the key types of analytical instrument routinely utilised by scientific laboratories to interrogate and characterise minerals and soil samples that have been recovered from field site locations. Furthermore, comments are provided on the appropriateness and suitability of each technique for use in planetary exploration applications, with particular focus placed on the instrument suites that have been developed for the Mars Science Laboratory Curiosity rover and the ExoMars missions. The advantages and disadvantages of each instrument type are outlined and the benefits of combining specific types of analytical instrument in order to comprehensively address the scientific goals of a particular mission are highlighted. Table 2.1 shows a comparison of the techniques and instruments that are discussed in the Chapter. Detailed information on the definitions of the relative Technology Readiness Level (TRL) with which the maturity of particular instrument concepts is usually assessed by space agencies is provided in Appendix 1.

Technique	Example	Chemical / Molecular	Sample prep	TRL	Mass (kg)	Depth	Target size	Range	Sample time
LIBS	ChemCam <sup>1</sup>	Chemical	No	9	10.6	>500µm	350 - 550µm	2 – 7m	Seconds
APXS	MSL APXS <sup>2</sup>	Chemical	No	9	1.5	N/A	17 mm	20 mm	10 minutes - hours
XRF	ExoMars XRF <sup>3*</sup>	Chemical	Generally	9	1.5	N/A	~200µm	N/A	6 hours
XRD	CheMin <sup>4</sup>	Molecular	Generally	9	10	N/A	50 µm	N/A	10 hours
Mössbauer	MIMOS II <sup>5</sup>	Molecular	No	9	0.55	50 µm - 200µm	2.8cm	Contact	1 – 12 hours
Neutron	DAN <sup>6</sup>	Chemical	No	9	4.5	2m	1m	2m	Seconds
Gamma ray	PhobosGrunt <sup>7</sup> **	Chemical	No	9	5.5	1-2m	4.5cm	1 – 2m	Minutes
Infra-Red	Micro Omega <sup>8</sup>	Molecular	Yes	9	2.4	N/A	Few mm	N/A	Seconds
Raman	RLS <sup>9</sup>	Molecular	No***	7	2.5	N/A	50 µm	N/A	Seconds
Raman Standoff	SHRS <sup>10</sup>	Molecular	No	4	-		20mm	12-19m	Seconds

Table 2.1 Comparison of different analytical science techniques with example instruments. \*Descoped, \*\* Lost, \*\*\* Sample prep not required but still has taken place due to other instrument requirements. 1. (Wiens et al. 2012), 2. (Gellert et al. 2009), 3. (Marinangeli et al. 2007), 4. (Bish et al. 2013), 5. (Klingelhöfer, Bernhardt, et al. 2003), 6. (Mitrofanov et al. 2012), 7. (Kozyrev et al. 2009), 8. (Leroi et al. 2009), 9. (Rull et al. 2011) 10. (Lamsal & Angel 2015)

### 2.1.1 Mars Science Laboratory



*Figure 2.1 Mosaic of MSL images from the MAHLI camera on the robotic arm to create a self-portrait of the rover on Sol 1126  
Image Credit: NASA/JPL*

NASA's most recently deployed rover mission, the Mars Science Laboratory, is the most advanced robotic platform deployed on another planet. The 900kg Curiosity rover landed at Gale crater in 2012 equipped with a comprehensive set of imaging cameras and analytical instruments;

- MastCam – main colour imaging camera system (Malin et al. 2005),
- MAHLI – close up camera on the robotic arm (Edgett et al. 2012),
- MARDI – descent imaging camera (Malin et al. 2005),
- ChemCam – Laser Induced Breakdown Spectroscopy (LIBS) and remote imaging system (Wiens et al. 2012),
- APXS – an Alpha Particle X-ray Spectrometer (Gellert et al. 2009),

- CheMin – an X-Ray Diffractometer (Blake et al. 2009),
- SAM – a Gas Chromatography Mass Spectrometer (Mahaffy et al. 2012),
- REMS – a suite of weather sensors (Gómez-Elvira et al. 2012),
- RAD – a radiation measurement system (Hassler et al. 2012),
- DAN, a neutron spectrometer (Mitrofanov et al. 2012).

Details of how these techniques have been implemented during the mission and a summary of key results obtained with the instruments are discussed below.

The Curiosity rover is powered by an RTG (Radioisotope Thermal Generator), a device capable of delivering 120 W of electrical power for at least 15 years (Lange & Carroll 2008) from an internal radioactive source. This technology avoids the need for solar panels as used on previous Mars missions, allowing Curiosity to operate during the night and Martian winter, which differs from the Mars Exploration Rovers (MER) rovers which could not operate without sunlight. This is particularly useful for analyses which require long acquisition times, such as X-Ray Diffractometer (XRD), because they can take place during the night, see CheMin (Blake et al. 2012).

In order to minimise the size of the mission's landing ellipse and therefore increase the number of potential landing sites that the rover could reach safely, a novel sky crane was developed by NASA. After its drogue parachute, which is designed to slow the falling craft down, and protective heat shield systems were released, the powered sky crane began to decelerate the craft to a height of 18.6m. As it approached the surface, the rover was lowered via cables and released safely onto the surface as the sky crane continued its trajectory and crashed a safe distance away (Prakash et al. 2008). This approach enables heavier rover payload masses to be deployed than have been achieved during any previous mission (at approximately 900kg, it is the largest mass of any of the Mars missions).

The mission's primary science goal is to determine the Mars environment's past habitability. A secondary goal is to characterise the chemical and geological make-up of the Gale Crater landing site. This site was chosen for the following reasons:

- Mineralogical diversity: there is a wide range of targets of scientific interest in the surrounding area with a variety of mineral types detected spectrographically (Vaz & Silvestro 2014),
- Geological context: the Gale crater environment is representative of a much wider area (Wray 2013),
- Habitability: orbital studies have found evidence for the presence of water in the past,
- Preservation: habitable features are likely to be preserved in a form that the rover can identify (Grotzinger et al. 2012; Golombek et al. 2012).

The rover has travelled over 17 km to the foothills of Mount Sharp and has begun its extended mission towards clay rich bedrock at higher elevations. Results obtained by Curiosity's instrument suite are detailed below in Sections 2.2.3, 2.4.5, 2.5.3 and 2.8. Further work from ChemCam and APXS is shown in Chapter 3.

NASA's 2020 rover will use a similar rover design to Curiosity but will rely on contact and remote instrumentation rather than on-board analyses such as those performed by CheMin or SAM.

### 2.1.2 ExoMars

In 2020, the European space agency will launch its first Mars rover (Figure 2.2). The portable laboratory will form the second phase of the ExoMars mission, following on from the successful deployment of the Trace Gas Orbiter and failed Entry and Decent Module (EDM) lander Schiaparelli in 2016. ExoMars' primary science goals include



*Figure 2.2 Artist's impression of the ExoMars rover Image Credit ESA*

attempting to detect evidence for past or present life (biomarkers), with a number of instruments designed specifically for this purpose (Barnes et al. 2006).

The spacecraft successfully achieved orbit and will begin science observations around a year after arrival (Korablev et al. 2017). However on October 19<sup>th</sup> 2016 the EDM lander platform failed to properly decelerate and ultimately impacted into the surface of Mars at around 150 m s<sup>-1</sup> (Banks 2016; Ferri et al. 2017). This failure was due to an altimeter reporting the craft was below the surface during descent whilst it was still at 3.7 km altitude (ESA 2016; Ferri et al. 2017). However, telemetry data were acquired during the descent and are being used to improve the landing system for the 2020 rover. During the descent, it was verified that each stage of the craft functioned correctly, although not for the required duration (ESA 2016).

The ExoMars rover will utilise solar panels to power a 6 wheel chassis. After initially landing via a powered descent platform, the rover will depart the platform down a ramp and deploy its panoramic camera (PanCam) to acquire stereo and 3D imagery the surrounding area in order to select initial science targets. The infrared spectrometer ISEM will aid PanCam in target selection (Vago et al. 2013).

The key difference between ExoMars and other Mars missions is the use of a 2m drill, for the extraction of sub-surface samples prior to delivery and analysis in the rover laboratory (the 'analytical drawer' or ALD). A ground penetrating radar (WISDOM) and neutron spectrometer (capable of measuring hydration) will be used to select a drilling site. During drilling the Infra-Red (IR) spectrometer (MA\_MISS) will characterise the sub-surface geological material. The close-up camera (CLUPI) will image the surface and the core samples acquired by the drill. After imaging, core samples will be passed into the rover, crushed and transported to the following analytical laboratory instruments:

- Micro-Omega, which provides IR and visual spectroscopy of the samples providing context for the other instruments (Leroi et al. 2009),
- RLS, a Raman spectrometer (Rull et al. 2017),
- MOMA, an organic molecule analyser which uses gas chromatograph-mass spectrometry and laser desorption-mass spectrometry to specifically target biomarkers (Brinckerhoff et al. 2013).

Several of these instruments and the analytical techniques involved are described in detail below. Further information on the operation of the RLS instrument is also provided in Chapters 4 and 5.

## 2.2 Laser Induced Breakdown Spectroscopy

LIBS is a laser based spectroscopy technique that is capable of remotely determining the elemental composition of a localised region on a target sample. The analytical technique has significant industrial heritage in a variety of commercial applications (Noll et al. 2001; Gondal & Hussain 2007). However, until the development of the ChemCam “Chemistry Camera” instrument on the Mars Science Laboratory in 2012, the technique had never been deployed for planetary exploration.

### 2.2.1 LIBS Method

Laser induced breakdown spectrometry involves the use of a high power pulsed laser to ablate material from a spot on the surface of a sample. See Figure 2.3 for an example instrument configuration. The first spectral analysis using LIBS was carried out in 1962 by Debras-Guédon and Liodec (Debras-Guédon & Liodec 1962). The ablation converts a small portion of the target (a few ng) to a plasma. This plasma emits photons with wavelengths corresponding to the atomic emission lines of the elements which make up the sample composition. This atomic emission spectrum emitted by the plasma can be obtained via the use of a spectrometer. The spectrometer disperses the light according to its wavelength, which is then imaged by a Charge Coupled Device (CCD) detector. The position of emission lines within the spectra are proportional to the emission line wavelength and vary in intensity with the chemical composition of the target, allowing for both qualitative and quantitative chemical analysis (Cremers & Radziemski 2013). However chemical matrix effects can complicate the quantitative elemental detections.

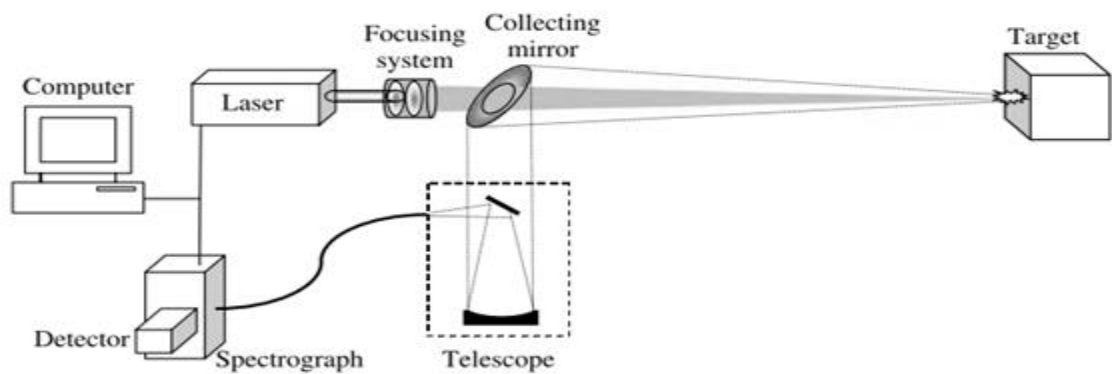


Figure 2.3 LIBS Experimental setup Image Credit: (Cremers & Radziemski 2013)

The intensity of photon emission from the LIBS plasma is pressure dependent. At low pressures (e.g. the lunar environment) plasma emission will be low intensity as the plasma will disperse with no exterior pressure reducing the signal detectable with the optics. Analysis becomes more straightforward above 130 Pa, with optimum plasma density and size occurring around 930 Pa (approximately Mars atmospheric pressure). At higher pressures such as on Earth and Venus the plasma formed is smaller as the additional atmospheric pressure is compressing the plasma preventing it from getting large enough to optimise the signal acquired (Cremers & Radziemski 2013). As a consequence of this, the LIBS technique is considered to be optimal for operation on Mars and whilst it would also work in other planetary environments, a pressurised sample containment system might be necessary. Lasers with wavelength 1064nm are typically used for LIBS as they have a breakdown threshold of  $8.2 \times 10^{10} \text{ W cm}^{-2}$  whereas shorter wavelengths require orders of magnitude more energy (Cremers & Radziemski 2013).

### 2.2.2 LIBS detection capability

LIBS is capable of distinguishing a numerous elements that are useful for geological analysis, particularly those that commonly form rocks. When reporting the elements detected, geological convention is to refer to them in oxide form and the main detectable rock forming elemental oxides are  $\text{SiO}_2$ ,  $\text{Al}_2\text{O}_3$ ,  $\text{FeO}$ ,  $\text{MgO}$ ,  $\text{CaO}$ ,  $\text{Na}_2\text{O}$ ,  $\text{K}_2\text{O}$  (Sallé et al. 2004). Other less common oxides, such as  $\text{TiO}_2$  and  $\text{MnO}$  (Cousin et al. 2011)

can also be quantified, along with additional detections of various trace elements such as Li, Ba, Sr, and Rb (Ollila et al. 2014). (Wiens et al. 2013) discusses the detection limits for the different major and minor elements by the MSL ChemCam LIBS instrument. Some of the key minor element detection limits are; H – 500ppm, Li – 5ppm, K – 20ppm, Cr – 360ppm, Mn – 270ppm, Cu – 425ppm and Pb – 300ppm (Wiens et al. 2013). Titanium can be useful as a wavelength calibration target due to its large number of peaks dispersed over a wide range of wavelengths. Stoichiometry can be used to estimate the likely mineralogical make up of target samples and this process is detailed in Chapter 3, Section 3.4.2. LIBS requires no sample preparation prior to the firing of the laser at a sample and only an extremely small mass of material (of the order of nanograms) is removed and so it is generally considered to be a nearly non-destructive process. LIBS only takes nanoseconds to produce and record the plasma emission, allowing for multiple data points per second, up to 30Hz for ChemCam (Maurice et al. 2012). Having been recently used on a planetary mission, the LIBS technology has a TRL of 9.

### 2.2.3 ChemCam on MSL

As of 2017, only one LIBS system has ever been operational on a planetary mission, the ChemCam LIBS instrument on the Curiosity rover (See Figure 2.4). The instrument was designed to increase Curiosity's range for chemical analysis, in line with the mission's science goal of geologically characterising the Gale crater area



Figure 2.4 The ChemCam Mast Unit Image Credit: NASA/JPL

(Maurice et al. 2012). The ChemCam instrument comprises a LIBS system paired with a Remote Micro-Imager (Le Mouélic et al. 2015) which function with the use of a telescopic lens within the Curiosity rovers' mast unit. ChemCam also uses three wavelength specific spectrometers housed within the rover body unit that are connected to the Mast via fibre optics (Maurice et al. 2012). The laser utilised by ChemCam has a NIR wavelength of 1067 nm (Wiens et al. 2012; Maurice & Cousin 2012).

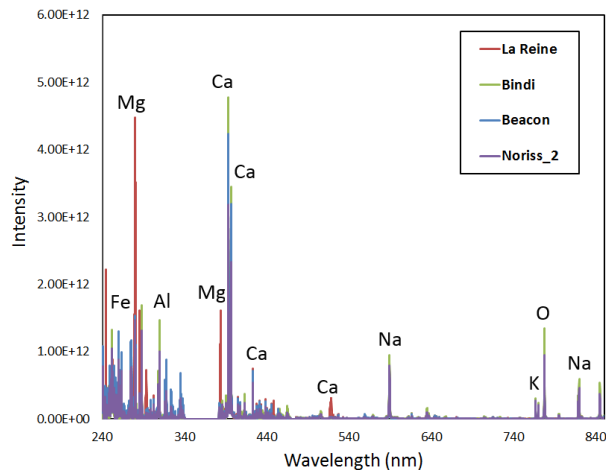


Figure 2.5 The unnormalised LIBS spectra from single shot at an observation point from each of four ChemCam targets. For comparison each of the spectra shown is shot number 10 of the first observation point for each target. Elemental peaks are identified and marked (Edwards et al. 2017)

ChemCam has a target stand-off range capability of up to 7m, although most target distances are typically around 4m (Mezzacappa et al. 2016; Wiens et al. 2012). Each LIBS spectrum is recorded using three individual CCDs. Each of them focused on a specific range of wavelengths: one is dedicated to sampling ultra-violet (UV) light in the 240 to 340 nm range, another samples spectra in the 380-470 nm

(blue-violet - VIO) range, and the final includes the visible and near infrared wavelengths (VNIR) spanning a spectral range of 470-900 nm. This design approach ensures the resolution necessary to adequately distinguish between the bands of interest; particularly those that are close together at the lower wavelength end of the LIBS spectra. The scientific goals of the instrument require a full-width at half maximum (FWHM) of < 0.2 nm at UV wavelengths and 0.65 nm in the VNIR wavelength range (Wiens and Maurice 2012). Figure 2.5 shows typical LIBS spectra acquired from four ChemCam targets with data from all three spectrometers combined to obtain a single spectrum (Edwards et al. 2017).

Typically, 30-50 spectra (one spectrum is produced with each individual laser pulse) are recorded from each single point on the Martian surface. Several points are observed per target in a raster pattern (e.g. 3 x 3 points) or linear formations (e.g. 5 x 1 points) across a single target. The individual footprint for each point varies slightly depending on the distance of the target, but will be approximately 350-550  $\mu\text{m}$  (Maurice & Cousin 2012; Maurice et al. 2007; Maurice et al. 2012). Therefore, ChemCam is used as a microprobe (Wiens & Maurice 2015), with the small laser spot size capable of reporting compositions from individual mineral grains (Gasda et al. 2016). However if a mineral grain is smaller than this spot size no pure measurements can be obtained as surrounding material will always be present, this is potentially the case in Chapter 3 with olivine grains.

Once the laser has completed these pulses, a dark frame is obtained which is then subtracted from the other collected spectra to remove background light levels. The data is also pre-processed so as to remove the Bremsstrahlung continuum and normalise the whole emission of the spectrum (Maurice et al. 2012). The spectra from the three spectrometers is wavelength calibrated via a titanium calibration samples (Maurice et al. 2012; Wiens et al. 2012; Maurice et al. 2016). Datasets are also corrected for the differences between the instrument response of the flight model on Mars and those lab spectrometers used for obtaining the calibration sets. Further detailed descriptions of these calibration methods and the sample suite used are given in (Wiens et al. 2013; Vaniman et al. 2012; Clegg et al. 2016).



*Figure 2.6 RMI images before and after LIBS 5 x 1 Raster of observation points Image Credit NASA/JPL*

The ChemCam telescope RMI (Remote Micro Imager) provides context imagery of the area surrounding each of the LIBS observation points. These greyscale images contain the highest spatial resolution of any of the remote cameras on board MSL; one RMI pixel corresponds to  $19.6 \mu\text{rad}$ . These images are useful to visually identify the mineral grains in the sample and provide textural context to all the spectra acquired by the ChemCam instrument. The RMI is used both before and after acquiring a set of LIBS spectra, enabling interpretation of the texture of the target area, as shown in Figure 2.6 (Le Mouélic et al. 2015).

#### 2.2.4 LIBS Planetary Science Results

Since ChemCam is the first LIBS instrument to be deployed on a planetary mission, much of the early work involved testing and calibrating the instrument in-situ (Wiens et al. 2013; Fabre et al. 2014), comparing its results to other instruments with heritage of use in planetary exploration, such as the robotic arm mounted APXS (See Section 2.4.1 APXS Method). Early studies of the data obtained reported evidence of an Fe-enrichment throughout the ChemCam data, potentially due to an iron rich cement (Blaney, Wiens, Maurice, Clegg, Anderson, Kah, et al. 2014). Another factor offsetting the data was early calibration issues. As such as the mission progressed, the training set of calibration samples used to generate the Partial Least Squared (PLS) and Independent Component Analysis (ICA) algorithms became more representative of the actual samples on Mars. This leads to a more accurate quantitative calibration when compared to the on board calibration targets and APXS results of homogeneous sites examined by both instruments (reducing elemental uncertainty in the ChemCam data) - see Clegg et al. (2014, 2016b).

ChemCam campaigns were common at the various sedimentary outcrops sampled by the Curiosity rover, including the area around Yellowknife bay (Mangold et al. 2015), Shaler (Anderson et al. 2015) and The Kimberley (Rice 2014; Blaney, Wiens, Maurice, Clegg, Anderson, Kahn, et al. 2014) and provide the most finely grained measurements available on Mars, smaller than the 3.8cm of the MER APXS (Maurice et al. 2016; Gellert et al. 2006). A diverse range of Igneous float rocks were also investigated, identifying heterogeneous compositions (Sautter et al. 2014; Sautter et al. 2015; Stolper et al. 2013; Schmidt & Campbell 2014; Edwards et al. 2017). Many of these compositions were more alkaline in composition than the samples analysed at the Spirit and Opportunity landing sites (Edwards et al. 2017). Chapter 3 considers some of the comparisons between these targets and others detected on Mars in greater detail. Some ChemCam observations partially covered feldspar grains giving a mixed composition (Gasda et al. 2016).

The composition of the dust covering the surface of each target was examined and a distinct elemental signature was identified. Almost all ChemCam target spots have detected the spectral signature of dust in approximately the first 5 shots (Lanza et al.

2015; Maurice et al. 2016). The lessons learned from the ChemCam operational campaign will be vital to the development of SuperCam as a successor instrument for NASA's Mars 2020 mission (Wiens et al. 2016).

## 2.3 Raman Spectroscopy

Raman Spectroscopy is a technique for determining the molecular structure of a target sample. First discovered in 1928 by Indian scientist C. V. Raman (Raman & Krishnan 1928). The technique responds to the vibrational modes in a sample to determine its molecular structure. Often used in the chemical industry (Lewis & Edwards 2001), pharmaceutical compositional studies (Vankeirsbilck et al. 2002), archaeological investigations (into origin and similarity of pigments in historical works), (Vandenabeele et al. 2007; Lewis & Edwards 2001) and art analysis (investigating the origin of materials used in production allowing for the detection of forgeries), (Edwards et al. 1998; Vandenabeele et al. 2000). The technique has often been proposed for space missions (Wang et al. 2003; Ellery & Wynn-Williams 2003). However, 2020 will see the first missions to feature the technique with both ESA's ExoMars Raman Laser Spectrometer (Rull et al. 2011) and NASA's MARS 2020 which included both the SuperCam and SHERLOC (Wiens et al. 2016; Beegle et al. 2014).

### 2.3.1 Raman Method

Raman scattering is generated by exciting a target sample with a monochromatic light source, usually a laser. The incident photons induce a dipole in the target molecules, exciting them into virtual states (see Figure 2.7). Almost instantaneously, the molecule relaxes, back to its original state, scattering the incident photon with no measureable energy loss. This is known as Rayleigh scattering, an elastic process. However, a small

proportion of the light (approximately 1 in  $10^6$  photons) will interact inelastically with the target molecules. In this case the molecules are excited to a vibrational state by the incident photons but ultimately relax to a different vibrational state

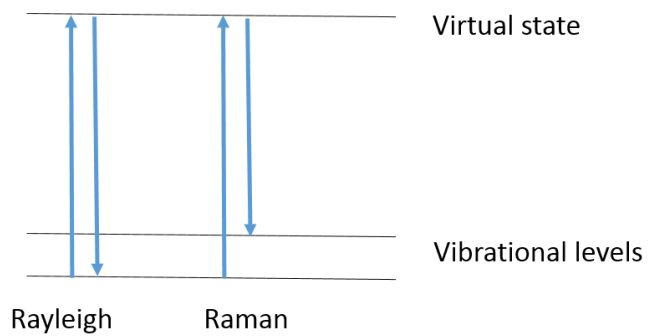


Figure 2.7 Energy level diagram of Rayleigh and Raman scattering

(compared to the original). The shift in wavelength of the resulting photon (compared to the incident wavelength) corresponds to the energy difference between the initial and resulting vibrational state of the molecule. The Raman scattered light provides a unique spectral “fingerprint” since it corresponds to the vibrational modes of the target molecules, and can therefore be used to identify the material in the target (Lewis & Edwards 2001).

In order to measure to the Raman scattered photons, the intense Rayleigh scattered light is removed using a notch filter or a holographic lens. This leaves only the Raman shifted light, which is split by wavelength using a spectrometer and measured with a detector. An example of such a spectrum is shown below in Figure 2.8.

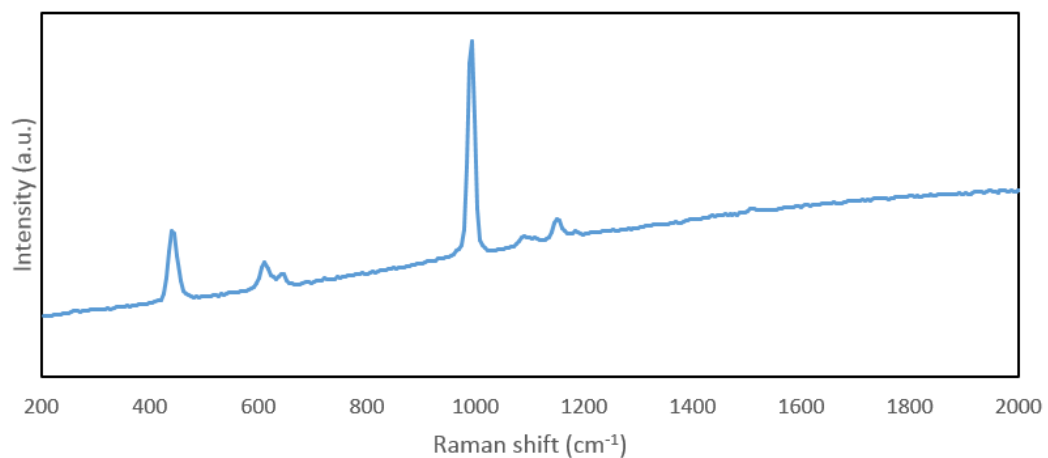


Figure 2.8 Raman spectra of a celestine sample obtained with the Raman Laser Spectrometer Engineering Qualification Module

The spectral bands created by the shift in vibrational state of the celestine molecules can be seen clearly in Figure 2.8, above the background emission caused by a separate physical process known as fluorescence. Fluorescence is a photon absorption process that occurs if the incident photon energy matches the energy gap between a molecule's original state and an excited electronic state. In this case, the photons excite electrons to a higher energy state, from which they subsequently relax through a range of lower states until reaching the ground electronic configuration, creating a continuous emission spectrum. Since the electronic states of a molecule are at a higher energy level compared to the vibrational states involved in Raman scattering, the fluorescence process can heavily obscure a Raman spectrum. However, a photon with energy corresponding to a Raman mode (vibrational state) within an excited electronic state can induce an enhanced scattering effect called resonance Raman scattering. The resonance Raman effect is  $10^6$  times more intense than non-resonance Raman scattering and can be exploited by selecting the frequency of the incident light source such that it coincides with the energy gap between lower vibration states and those in an excited electronic state.

Libraries of samples can be built up to compare to unknown spectra in order to facilitate rapid identification. Raman observations are relatively quick compared to other types of analytical instrumentation, typically between 0.1s and 60s (Rull et al. 2017). Numerous different laser wavelengths are used to produce Raman bands (L. V. Harris, Hutchinson, et al. 2015) including 532nm, 785nm and more rarely UV and IR lasers. There are advantages and disadvantages to each of these choices and their selection must be made in line with the instrument science goals. For example 532 nm Raman resonates with many biomarkers and shows hydration bands for relevant minerals, whereas 785nm Raman has less fluorescence obscuring the Raman signal and gives clearer spectra of some carbon based minerals, a choice of wavelength lower than 532nm risks damaging the sample (L. V. Harris, Hutchinson, et al. 2015). Work comparing data from a 785nm Handheld Raman with a 532nm representative prototype is discussed in Chapters 4 and 5. The many similarities in the instrumentation requirements makes Raman and LIBS very good candidate techniques for use as part of a combined

instrument; they both share the requirements for an excitation source, optical head, optics and a detector which records the spatially-dispersed light. This is elaborated on further in Section 2.9.1.

Raman measurements are relatively rapid compared to many other techniques, particularly when those techniques are working within the limitations of a space mission rather than a terrestrial lab. Raman typically requires between 0.1s and 60s for analysis with a usual integration time of 1s commonly used (Rull et al. 2017). In contrast some other techniques can take hours or even an entire an entire night in order to function effectively.

### 2.3.2 Raman Detection Capability

Raman spectroscopy is capable of identifying many minerals of geological interest (Sharma et al. 2003; Angel et al. 2012). Some key examples are members of the feldspar group (Freeman et al. 2008), carbonates (Edwards et al. 2005), pyroxenes (Wang et al. 2001), sulphates (Fleischer et al. 2008) and olivine (Kuebler et al. 2006). It is also useful for the detection of biomarkers, evidence left behind by life processes (Edwards et al. 2012). Some of the key organic and inorganic biomarkers detectable with Raman spectroscopy are detailed in Table 2.2 below (Edwards et al. 2014).

<b>Bioorganic molecules</b>	<b>Bioinorganic molecules</b>
scytonemin	whewellite
carotenoids	weddellite
carotanes	aragonite
chlorophyll	vaterite
trehalose	mellite
phycocyanins	
hopanoids	
oxalates	

*Table 2.2. Table of key biomarkers detectable with Raman Spectroscopy from Edwards et al. (2014).*

Raman does not require sample preparation before measurement and is effectively a non-destructive technique. Since a Raman spectrometer has not yet flown on a mission, but is in the advanced stages of development, it has a TRL of 7.

### 2.3.3 ExoMars Raman Laser Spectrometer

In 2020, when the second component of the ExoMars mission will launch, one of the instruments on board will be the Raman Laser Spectrometer (RLS), the design of which is shown in Figure 2.9 RLS is one of 3 instruments in the ExoMars on-board analytical laboratory (Rull et al. 2011). The RLS instrument is designed to fulfil scientific goals to identify organic compound and search for life and the mineral products that are associated with biological activity, the instrument will also characterise the geological, mineralogical and hydration of the geochemical environment (Rull et al. 2017).

The ExoMars drill will acquire samples from up to 2m beneath the Martian surface. This sample will be analysed with instruments within the drill before being powdered and delivered to the instruments within ExoMars, including an Infra-Red spectrometer Micro-Omega and RLS itself. It will cover a spectral range of  $\sim 150$  to  $3800\text{ cm}^{-1}$ . RLS is responsible for providing a mission assessment of organic content in a sample to determine whether it should be passed to the MOMA instrument.

Once the sample is crushed and placed beneath the laser, the sample will be precisely moved in order to perform raster scans of the surface. Each laser spot will be approximately  $50\text{ }\mu\text{m}$  on the target samples (Rull et al. 2011). Since the samples are crushed, it will not be possible to obtain spatial data and samples will be homogeneous in nature.

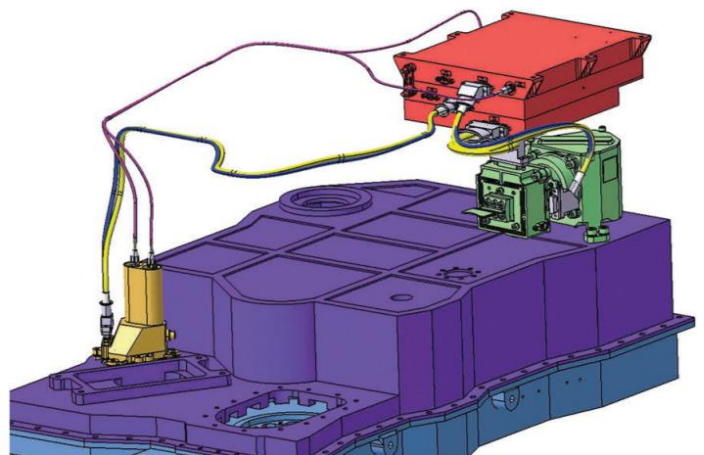


Figure 2.9 RLS instrument design. ICEU - Instrument Control and Excitation Unit (Red). SPU - Spectrometer unit (Green). IOH - Internal optical head (Yellow). Image Credit (Rull et al. 2017)

RLS will use a green 532nm laser, selected to allow for the detection of relevant minerals and the capability to determine the hydration of minerals. (Rull et al. 2011). To ensure the samples avoid damage, the irradiance of the laser will be limited to  $1.2 \text{ kW cm}^{-2}$  (Rull et al 2011). The instrument will be capable of performing up to 400 different measurement cycles over the course of the mission (Rull et al. 2011).

The initial RLS concept was a combined Raman and LIBS spectrometer. While different excitation energies and wavelengths are required, much of the instrument optics, focal plane and electronics were originally combined (Ahlers et al. 2008). Whilst this was eventually de-scoped to comply with a strict instrument mass budget, the design will be discussed further in the Raman/LIBS combined Section 2.9.1.1 and work with the ExoMars RLS prototype system, and more detail on the instrument design, will be discussed in Chapter 5.

#### 2.3.4 SHERLOC on MARS 2020

SHERLOC (Scanning Habitable Environments with Raman & Luminescence for Organics and Chemicals) is a planned and selected Raman spectrometer instrument for NASA's 2020 Mars rover (Beegle et al. 2014). Unlike RLS, SHERLOC will use a 248nm ultraviolet laser to obtain its Raman signatures (Eshelman 2016). This allows it to use Ultraviolet spectroscopy along with the mineralogical and bio signature benefits afforded by Raman spectroscopy. However, it should be noted that UV lasers are much higher in energy so there is an added risk of damaging the targets during measurement (L. V. Harris, Hutchinson, et al. 2015). SHERLOC will represent the first use of UV Raman on a planetary mission. Each image will analyse a 7mm by 7mm area, providing spatial information via rasters, this will also allow for borehole analysis to a depth of 25mm (Beegle et al. 2014). Like the ExoMars RLS, the SHERLOC spot size will be around  $50 \mu\text{m}$  in diameter. The instrument is non-contact, located on the arm of the rover (as seen in Figure 2. and should be capable of characterising the minerals and possible bio-signatures on the Martian surfaces (Beegle et al. 2015). SHERLOC is designed to be capable of detecting minerals with less than  $20 \mu\text{m}$  grain size (Beegle et al. 2015).

SHERLOC has additional science goals alongside that of the search for biosignatures, which are to investigate the past aqueous history of individual target samples and the wider Martian environment whilst also supporting investigations into sample return (Beegle et al. 2014) by providing mappings of organic molecules on samples analysed by other instrumentation (Beegle et al. 2015).

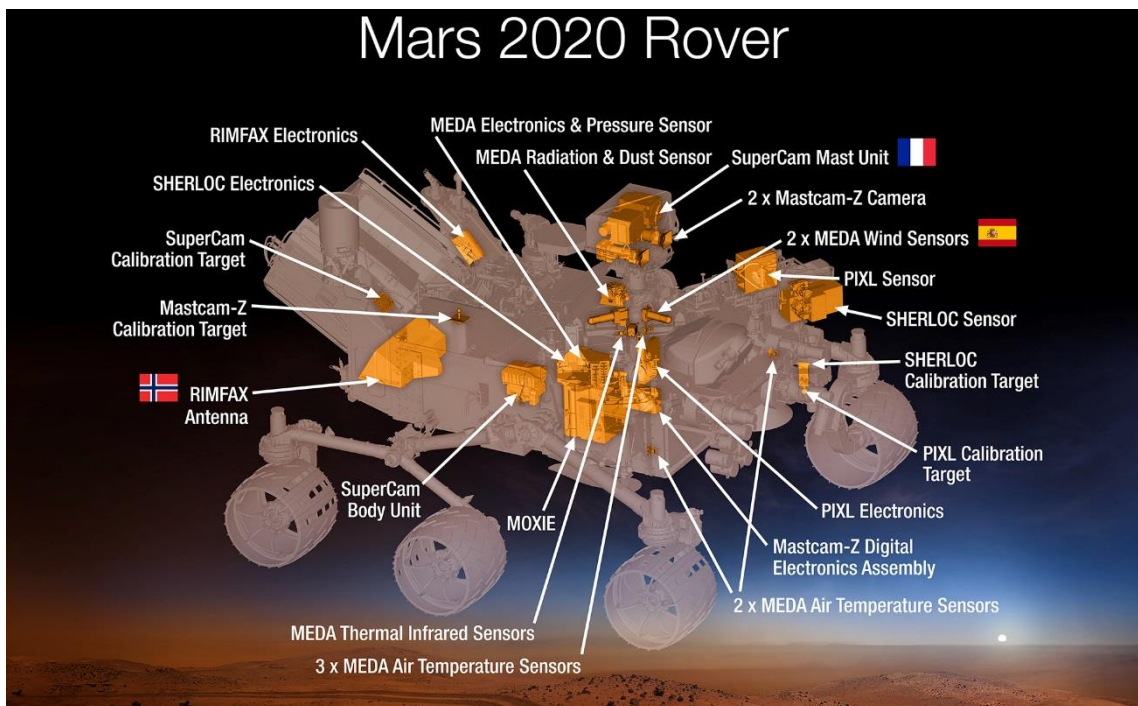


Figure 2.10 MARS 2020 instrument layout showing position of SHERLOC on the robotic arm Image Credit NASA

### 2.3.5 CIRS

CIRS (Compact Integrated Raman Spectrometer) is a proposed Raman instrument that would be applicable to a mission to Venus to study fine scale mineralogy, currently under development with a TRL of 6 (Wang, Wei, et al. 2015), CIRS utilises a 532nm laser and a design similar to the RLS instrument. with a spectral range spanning  $183\text{ cm}^{-1}$  to  $4432\text{ cm}^{-1}$ , allowing for hydration peaks to be detected (Wang et al. 2016). The spot size is slightly smaller than that of RLS and SHERLOC at  $35.7\text{ }\mu\text{m}$ . A prototype has been constructed and a range of performance verification tests have been performed (Wang et al. 2016).

Automatic line analysis of target points enables rapid characterisation of target material and detection of quartz, feldspars, carbonates, sulphates and carbonaceous materials in the field is possible (Wei et al. 2015).

Due to the nature of the Venusian environment, missions there will have an extremely limited window for acquiring data. Due to Raman's capability to identify molecules with integration times of the order of seconds rather than minutes or hours, it is ideally suited to the task. CIRS is capable of acquiring 100 separate spectra or spots in less than an hour (Wang, Wei, et al. 2015). The pressure of the environment would also have a significant effect on measurements and as such, testing in representative atmospheric environments, as well as with geological analogues is highly important (Wang et al. 2016).

#### 2.3.6 SuperCam on MARS 2020

The successor to ChemCam, SuperCam, will combine LIBS and Raman spectroscopy for remote measurements on MARS2020. This instrument is described in the combined instrumentation Section, 2.9.1.2 SuperCam.

### 2.4 X-Ray Fluorescence and Alpha Particle X-Ray Spectroscopy

X-Ray Fluorescence (XRF) and Alpha Particle X-Ray Spectroscopy (APXS) are two X-ray techniques which have been adopted for planetary exploration applications (note: for the Pathfinder rover the P in APXS refers to Proton, in all other instruments it refers to Particle (Bridges et al. 2001)). Both techniques utilise X-rays to obtain elemental information regarding the composition of the sample. In the case of APXS, the target area is of the order of a few cm (compared to LIBS instruments which typically sample regions with mm scale size) so is very useful for obtaining a more representative view of the bulk composition of a target. APXS has a long heritage of use on numerous space missions including all of NASA's Mars Rovers from Pathfinder (Bridges et al. 2001), through MER (Gellert et al. 2006) to the most recent Curiosity rover (Gellert et al. 2009). Many other missions such as Rosetta, Phobos Grunt and Mars 96 also used the APXS

technique, adding to its substantial heritage. XRF has been used for many years in a wide range of industrial applications, with portable instruments widely available (Beckhoff 2006). The technique was adopted for the NASA Mars Viking missions (Clark et al. 1977) and the Soviet Venus Venera missions (Blake 1999) but was descope from the Mars Science Laboratory CheMin XRD instrument (Bish et al. 2007). It was also originally included as part of the ESA ExoMars instrumentation package before being descope in 2010 due to budget limitations (Motamedi & Davies 2010).

#### 2.4.1 APXS Method

During APXS experiments, alpha particles that are emitted from a radioactive source are directed towards atoms on the surface of a sample, which then generate characteristic X-rays associated with the elements present in the target. This causes the back-scattered of alpha particles (also known as Rutherford backscattering), which can be detected and the counts at various energies are used generate a histogram of different energy bands so that elemental peaks can be identified. This technique is non-destructive to the samples. In the laboratory, APXS instruments typically use an MeV Helium ion accelerator whereas the MER APXS instrument uses a Curium-244 source to produce the alpha particles (Gellert et al. 2006). Generally contact or near contact is required for APXS to function effectively (Gellert et al. 2016).

#### 2.4.2 XRF Method

X-Ray fluorescence is a very similar analytical technique to APXS. The first X-ray fluorescence spectrometer was built by Friedman and Birk in 1948 (Friedman & Birks 1948). X-rays are directed towards a target sample and if they are of sufficiently high energy, they result in the removal of an electron from a low energy state. As a result of this process, a higher energy electron takes its place and a characteristic X-ray is emitted from the material. Measurement of the energy and intensity of these X-rays enables the elements present in the samples to be quantified. The heavier the element the higher the energy of the x-ray. The quantities of each energy detected by the detector are plotted to obtain the spectrum, there will be alpha and beta peaks for most elements

detectable (Beckhoff 2006). Some handheld devices do not require sample preparation however to get the highest signal it is often desirable to powder the samples (Young et al. 2016).

#### 2.4.3 APXS Detection Capability

APXS is typically capable of detecting the Major elements – Si, Ti, Al, Fe, Mg, Mn, Ca, K, Na, P, S, Cl as well as some lighter elements. The main detectable elements are typically from atomic mass 23 – 80 (This covers Sodium to Bromide) (Gellert et al. 2009). The MSL APXS, the most advanced APXS system used on a planetary mission can detect 100ppm for Ni and around 20ppm for Br over 3 hours of measurements, 0.5% abundance of major elements can be detected over a much shorter measurements time (around 10 minutes) (Schmidt et al. 2013).

#### 2.4.4 XRF Detection Capability

XRF can also analyse elemental data, depending on the x-ray source samples with a higher Z number than 11 (Sodium) can be detected (Beckhoff 2006) providing the main rock forming elements quantitatively with Silicon, Calcium, Titanium and Potassium giving the clearest results (Young et al. 2016). These elements can sometimes be detected down to a few ppm. A synchrotron source can be used to increase sensitivity. Depending on the x-ray source chosen different spectral resolution will be possible.

#### 2.4.5 Viking and Venera missions XRF

Multiple early lander missions to both Mars and Venus from the United States and the Soviet Union had XRF capability.

In 1975 the Viking landers arrived at Mars, their instrumentation suite was primarily focused on astrobiological experiments but they also has a geological aspects partly using XRF (Clark et al. 1977). The instrument was planned to analyse around 20 samples (Clark et al. 1977). XRF was added later in the mission developmental process and so had to be adapted to pre-existing sample collection mechanics for other instruments

rather than specifically informing their design (Clark et al. 1977; Baird et al. 1977). Despite this the XRF instrument succeeded with its science goals analysing the chemical composition of the Martian soils at both Viking landing sites. The Viking landers used two sources Iron 55 and Cd 109 (Blake 1999).

The Soviet Venera Venus missions in the 70s had multiple soft landings on the Venusian surface. Of these landers Venera 11 to 14 contained XRF instruments. Around 2 hours of data was returned from the surface before contact was lost with the longest lived mission (Surkov et al. 2008). The samples were accessed with a drill which brought the material inside the instrument. These missions had to adapt to the extreme environment of Venus. These Soviet landers used iron 55 and Pu 238 X-ray sources to produce the fluorescence.

#### 2.4.6 MER and MSL APXS

On both the MER and MSL rovers the APXS instrument is located on the rover's robotic arm turret (see Figure 2.11). It irradiates a target sample with its  $^{244}\text{Cm}$  source with both alpha particles and X-rays (Gellert et al. 2009; Schmidt et al. 2013; Gellert et al. 2006) and then measures the resulting X-rays and the scattered alpha particles. The detection of the major elements are

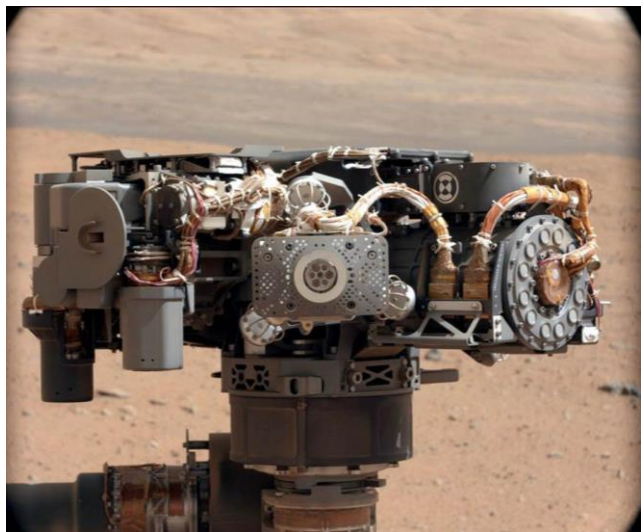


Figure 2.11 MastCam image of the MSL APXS instrument on the robotic arm. Image Credit NASA/JPL

typically normalised to 100%. Several improvements were implemented for the MSL APXS over instrument designs used on previous missions to give improved levels of sensitivity and accuracy (Campbell et al. 2012). Over 1000 different samples have been analysed by MER APXS from Spirit Opportunity, and MSL (Gellert et al. 2016), generating a significant dataset to characterise the Martian environment and compare to other

instruments. Studies using data from the Spirit and MSL APXS instruments, particularly in comparison to other Mars Science Laboratory instruments such as Curiosity and terrestrial samples, is detailed in Chapter 3 alongside ChemCam analysis.

#### 2.4.7 PIXL on MARS 2020

PIXL (Planetary Instrument for X-ray Lithography) is an X-ray instrument which will be located on the robotic arm of MARS 2020, functioning as a replacement for APXS. It functions via scanning a 0.12mm x-ray beam over a 25 x 25mm area to generate

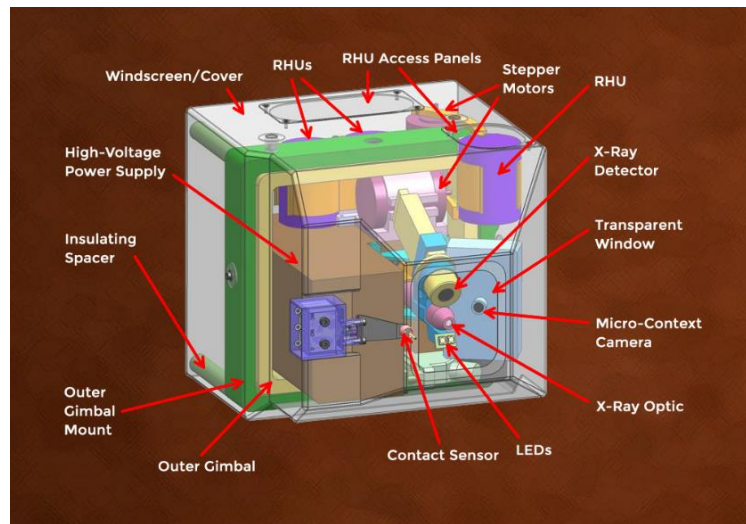


Figure 2.12 PIXL instrument design Image Credit NASA/JPL

a spectral map, this map can then be compared to visual imaging to connect textural and chemical features (Allwood et al. 2016).

PIXL (Figure 2.12) will aim to determine the bulk composition of targets with relative abundances of elements, investigate spatial differences, constrain mineralogy via stoichiometry and investigate formation times through cross cutting. The data can be compared to that of SHERLOC and SuperCam (Allwood et al. 2016).

#### 2.4.8 Planetary Science Results from APXS and XRF

Since multiple missions have used these techniques, there is a long heritage of results from these various planetary landers and rovers which can provide a useful comparison.

Viking XRF data corresponds well with that seen later by MSL APXS (Schmidt et al. 2013). Both the Viking landing sites had broadly similar chemistry implying a broadly homogeneous surface (Clark et al. 1977). Results indicated a mafic (Mg and Fe rich) composition with much higher sulphur content than Earth (Yen et al. 2005). Definitions of some of the geological terms referred to can be found in Appendix 2

Pathfinder APXS was a proof of concept of the technique on a rover mission analysing 16 samples around the landing site with 11 measurements of sufficient quality to achieve elemental compositions, finding that dust covered much of the rocks and soils were consistent with Viking data (Bridges et al. 2001). Since Pathfinder was a mobile science platform it had the ability to access rocky targets as opposed to just the surrounding soil as with the stationary Viking landers. Its APXS had lower detection limits than that of the Viking XRF (Yen et al. 2005). Martian rocks were found to be typically much richer in iron content than their terrestrial counterparts (McSween et al. 1999).

MER APXS analysed many igneous and sedimentary rocks at each landing site (Gellert et al. 2016) , Spirit at Gusev crater (Gellert et al. 2006) and Opportunity landing at the hematite rich Meridiani Planum (Soderblom et al. 2004; S W Squyres et al. 2004; Yen et al. 2005). samples from Gusev crater (Gellert et al. 2006) are of particular interest when compared to MSL at Gale see Chapter 3, work comparing these is discussed in Chapter 3. The use of identical instrumentation at two different landing sites allowed for useful comparisons (Yen et al. 2005).

The MSL APXS has sampled over 300 different targets (Gellert et al. 2016). Of particular note is Jake\_M a possible Martian mugearite (Stolper et al. 2013). Data can be compared with ChemCam data of the same targets. Numerous Igneous and Sedimentary rocks were encountered over the course of the mission, many of these fell into classifications analogous to those from the MER missions (Gellert et al. 2015).

## 2.5 X-Ray Diffraction

X-Ray Diffraction (XRD) is a molecular and mineralogical X-ray technique. This technique has a long heritage of terrestrial laboratory, geological and industrial usage and is well trusted in the field. However some of the components can be quite large and heavy, as such the usage on planetary missions have been limited to the CheMin instrument, although an instrument was developed for the ExoMars rover (Marinangeli et al. 2007) which would have been combined with XRF, however this instrument was descope before the 2020 launch date.

### 2.5.1 XRD method

The X-ray diffraction technique involves focusing x-rays onto a target material. This will usually be a powdered or crystalline sample. The scattering of these x-rays produces a diffraction pattern (called a diffractogram) that can be measured by moving a detector through different angles around the sample. This will detect peaks produced according to Bragg's law. The location and space between these peaks can be used to determine the internal structure and lattice size (Ashcroft & Mermin 1976). XRD measurements of Martian analogues are recorded in Chapter 4.

### 2.5.2 XRD detection capability

XRD detects minerals and examines crystalline structures. Many different types of minerals are detectable with XRD including; Iron rich (Schulze 1981), Feldspar, Pyroxene and Olivine (Bish et al. 2013). The lattice structure of samples can be calculated and well characterised based of the diffractograms produced by the XRD system. XRD functions with Bragg reflections within a reciprocal space. Once the mineralogy is determined it can be possible to estimate the elemental composition of a target but this cannot be measured directly without the use of XRF techniques.

### 2.5.3 CheMin on MSL

CheMin is one of the largest instruments on board Curiosity with a mass of 10 kg partially due to the large and heavy sample acquisition and preparation system. It uses a Co anode X-ray tube to produce X-rays for the XRD process and uses the powder diffraction method (Figure 2.13). CheMin examines samples collected either by drill or scoop that has been crushed powdered and delivered to

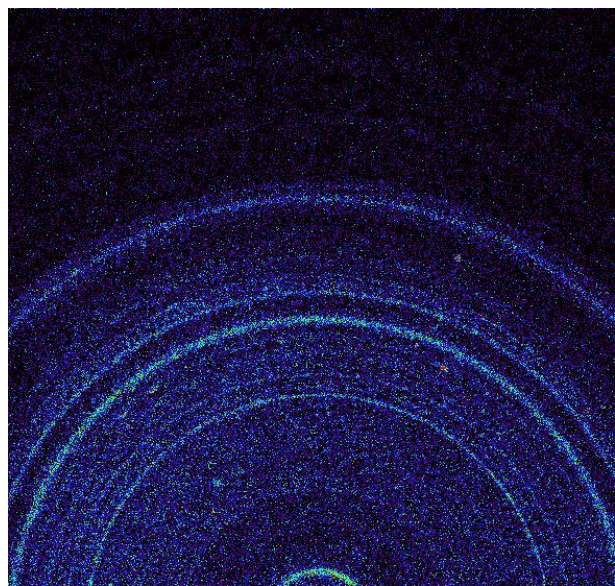


Figure 2.13 XRD diffractogram for MSL at Rocknest showing evidence for olivine Image Credit NASA/JPL

CheMin by the rover's sample handling system (Bish et al. 2007) this allows it to sample subsurface homogeneous samples from the various drill holes produced at points of interest. The instrument was initially planned to be a combined XRF/XRD instrument, hence the name CHEmistry MINeralogy (Blake et al 1999).

Over the course of the mission the instrument should be able to analyse 27 pristine samples and can be reused to give a total of 74 analyses (Blake et al. 2012).

#### 2.5.4 Planetary Science Results from X-ray Diffraction

To date CheMin has conducted measurements of 17 samples, 15 of which are drills (see Figure 2.14) samples and 2 are scoops (Dehouck et al. 2017). It has provided insight into the mineralogy of Gale crater. Mudstone like samples with the presence of calcium sulphates, iron oxides and sulphides, amorphous material, as well as smectites, were detected at Yellowknife Bay from the Cumberland and John Klein drill holes (Vaniman et al. 2014), analysis of analogue samples based off this data can be found in Chapter 4.

Later drill holes at the Confidence Hills site detected large quantities of hematite, phyllosilicates, feldspars and mafic silicates, consistent with orbital measurements (Cavanagh et al. 2015).

CheMin provides a useful opportunity to test the same (or at least similar) samples with multiple instruments. ChemCam observations of the drill holes allow for comparison between the mineralogical XRD and elemental LIBS for nearly the same sample. Measurements of the drill tailings can also be valuable for comparison.



*Figure 2.14 MAHLI image of John Klein drillhole on sol 270 ChemCam laserspots are visible next to a light vein. Image Credit NASA/JPL*

## 2.6 Infra-Red Imaging Spectroscopy

Infra-red spectroscopy is another mineralogical technique focusing on the infra-red end of the spectrum. There is some overlap between the molecular structures which can be identified by Raman and IR. However there are some minerals which each specific technique has advantages at detection, as a result to the techniques are useful to pair up together, see Section 2.9.3 for more information. IR has flown before on the Philae lander including on the Rosetta mission and is planned to be included as one of the instruments on ExoMars, Micro-Omega.

### 2.6.1 Infra-Red spectroscopy method

An infra-red source, either generated passively such as solar reflectance, or actively with an IR light source, is directed at the target sample. From this the absorption intensities

at various different wavelength can be measured. Vibrations within the material characterise the absorption at these wavelengths in the target. These spectra are typically composed of narrow line widths and are detailed (Pasquini 2003). It is often necessary to prepare the samples before applying IR spectroscopy (Leroi et al. 2009). IR spectroscopy typically requires a more complex calibration technique than Raman spectroscopy (Colthup et al. 1975). Typically a reference spectra from a database will be compared to the sample to assess its composition. Measurements generally take around 10 minutes to obtain useful data (Leroi et al. 2009).

### 2.6.2 Micro Omega on ExoMars

The ExoMars instrument suite will include Micro Omega, a miniaturised IR spectrometer. It is an enhanced version of the IR spectrometer instrument, ROSETTA/CIVA-M/I, on Philae, with adaptations for the specific temperature variation and environment of Mars (Leroi et al. 2009; Bibring et al. 2007). The instrument will be used to analyse the samples acquired from the drill system before they are delivered to other instruments (Leroi et al. 2009). Algorithms will be used to select grains of particular size and consistency (Pilorget & Bibring 2014). Micro-Omega will launch on ExoMars in 2020 but the technique already flew on Rosetta and as such has a TRL of 8 as the technique has been used before but in different configuration to Micro-Omega.

## 2.7 Mössbauer Spectroscopy

Mössbauer Spectroscopy specialises in iron rich mineral detection. The technique functions via the use of a beam of gamma rays which are focused on to a solid sample. The transmission and reflection of this beam will then be measured. This technique investigates the nuclear energy level transitions (Gütlich et al. 2011). The nucleus' chemical environment has an effect on the nuclear transition energies which changes the Mössbauer lines in the spectrum. Different gamma ray sources are optimised for different targets with  $^{57}\text{Fe}$  for iron rich minerals. Due to the backscatter geometry

employed by Mössbauer Spectroscopy no sample preparation is needed before data can be obtained. However prior information about the sample is necessary for the data to be able to be interpreted correctly. The MER rovers both carried the Mössbauer Spectroscopy instrument MIMOS II which allowed for the detection of olivine, pyroxene, hematite, magnetite and other minerals (Klingelhöfer, Bernhardt, et al. 2003; Klingelhöfer, Morris, et al. 2003). Since it has been used multiple times over different missions the technology readiness level of Mössbauer Spectroscopy is 9.

## 2.8 Gas Chromatography Mass Spectroscopy

Gas Chromatography Mass Spectroscopy (GCMS) is a technique that is well established in terrestrial laboratory environments and is used for determining the constituent components in a sample, including trace elements. The technique is used for industrial applications, law enforcement, food analysis and for anti-doping procedures in sports. Gas Chromatography is used to determine the composition and abundances of various atmospheric gases whilst also being useful for analysing complex organics (Bellar & Lichtenberg 1974) and chirality (Sicoli et al. 2009). The technique can typically determine concentrations in the order of parts per billion. The Sample Analysis at Mars (SAM) instrument also contains a mass spectrometry component which determines both the mass and charge of atomic particles (Mahaffy et al. 2009). SAM utilises a QMS (Quadrupole mass spectrometer) which uses ion traps for mass discrimination (Webster & Mahaffy 2011). This method is necessary for the detection of noble gases (Mahaffy et al. 2012) but can suffer from interference from stable isotopes, water, methane and ammonia. Having been used on multiple surface missions, GCMS has a TRL of 9. The ExoMars rover will incorporate the MOMA instrument, a mass spectrometer designed to search for organics and provide chemical analysis of the drill samples delivered to the Pasteur instrument suite by the ExoMars drill sample handling system (Brinckerhoff et al. 2013; Vago et al. 2013)

## 2.9 Combined instrumentation

On a space mission the desire for as many different techniques as possible, to provide the most comprehensive analysis of samples and the environment, must be balanced against the mass and energy requirements of the mission design due to the costs of launch. One way of getting more scientific information per kg is to use combined instrumentation techniques. These are various techniques which share similar component parts such as optical lenses, fibre optics, CCDs or laser and radiation excitation sources. Techniques with similar sampling or integration times also make useful combinations as little time will be wasted waiting for one or the other technique to complete. Often neither technique will be as optimised as it would be if all the components were designed specifically for purpose, however the savings on both mass and space on a mission can be considerable. The table below shows some of the most useful or commonly suggested combinations. Most of these are discussed in further detail in the Sections below.

Technique	Example Instrument	Chemical or Molecular	Sample prep required	TRL	Mass	Depth	Target size	Range	Sample time
Raman/LIBS	RLS/LIBS (de-scoped) <sup>1</sup>	Chemical / Molecular	No*	5	1.6kg	~500µm	20 - 100µm	N/A	Seconds
Raman/LIBS standoff	SuperCam <sup>2</sup>	Chemical / Molecular	No	4	~10kg	~500µm	~250 - 550µm	7m (LIBS) /12m (Raman)	Seconds
XRF/XRD	CheMin (de-scoped) <sup>3</sup>	Chemical / Molecular	Yes	6	10kg	N/A	50 µm	N/A	10 hours
Raman/IR	ExoMars <sup>4</sup>	Molecular	Yes	7	5kg	N/A	Few mm/ 50 µm	N/A	Seconds
LIBS/XRD		Chemical / Molecular	Yes	3	~15kg	N/A		N/A	Seconds/hours
Raman/XRF		Chemical / Molecular	Usually	3	~3.6kg	N/A		N/A	Seconds/hours

Table 2.2 Combined instrumentation techniques and their uses for planetary science.

1. (Bazalgette Courrèges-Lacoste et al. 2007), 2. (Wiens et al. 2016), 3. (Bish et al. 2007) 4. (Vago et al. 2013)

### 2.9.1 Raman/LIBS

As discussed above both Raman Spectroscopy and Laser Induced Breakdown Spectroscopy use very similar components for the design of their systems. The main differences between these two techniques being the laser wavelength (LIBS typically uses higher wavelengths, such as 1064 nm to increase the energy of pulses, whilst Raman usually benefits from lower wavelengths which generate Raman scattering without damaging the samples, such as 532 or 785 nm) and power used (LIBS seeks to ablate the sample whilst Raman only causes Raman scattering) and finally the application of a notch filter or other wavelength blocking techniques for Raman spectroscopy to prevent the laser light wavelengths coming back to allow detection of the Raman shifted light (Bazalgette Courrèges-Lacoste et al. 2007; Ahlers et al. 2008). A mode switching laser, capable of operating at different powers and wavelengths, could solve these issues or instead separate lasers could use the same optical system. Given they also provide very complimentary data, they are amongst the techniques most often considered for combination in a single instruments for planetary exploration missions. Whilst no combined Raman LIBS instrument has yet been included on a completed mission there are a number of planned or proposed instruments some of which will be included on upcoming missions in 2020 for both ESA's ExoMars and NASA's MARS 2020.

#### 2.9.1.1 RLS Raman/LIBS

The original design for the ExoMars Raman Laser Spectrometer had both a Raman and LIBS capability (Figure 2.15). Separate lasers would be used for the two techniques with different orders (area on the CCD with the useful spectra) projected from spectrometers onto the same CCD to save on detection equipment. The prototype was developed in the Netherlands and tested in simulated Martian atmosphere (Ahlers et al.

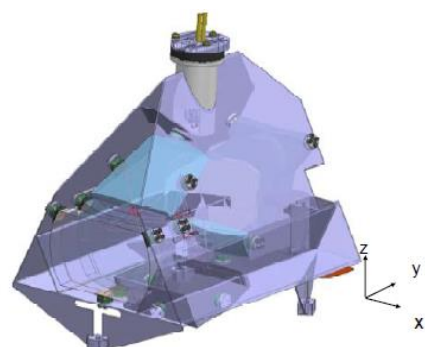


Figure 2.15 Combined Raman LIBS RLS instrument design

2008). The CCD would have covered the wavelength range 240nm to 840nm, this

provides coverage of most key LIBS peaks with the Raman focused between 650 to 840 nm (Ahlers et al. 2008; Bazalgette Courrèges-Lacoste et al. 2007) . The 1064nm LIBS illumination optics are separate from the 660nm lower power Raman illumination and both optical heads, this is to allow for a different angle for the high energy LIBS pulses whilst also preventing damage to the optics. Plans were changed to use a green 532nm Raman rather than the red 660nm, this was carried forward after the LIBS section was descoped (Rull et al. 2011).

Work on Martian analogue samples with the RLS Raman LIBS combined prototype from The Netherlands will be detailed in Chapter 5 and compared to the current RLS prototype system.

### *2.9.1.2 SuperCam*

Building on the successful instrument campaign of ChemCam, SuperCam (See Figure 2.16) is designed to add stand-off Raman capability to the pre-existing LIBS setup for ChemCam. On MARS 2020 SuperCam should be able to remotely determine elemental and mineralogical makeup of many targets throughout the new rover's mission. Lessons

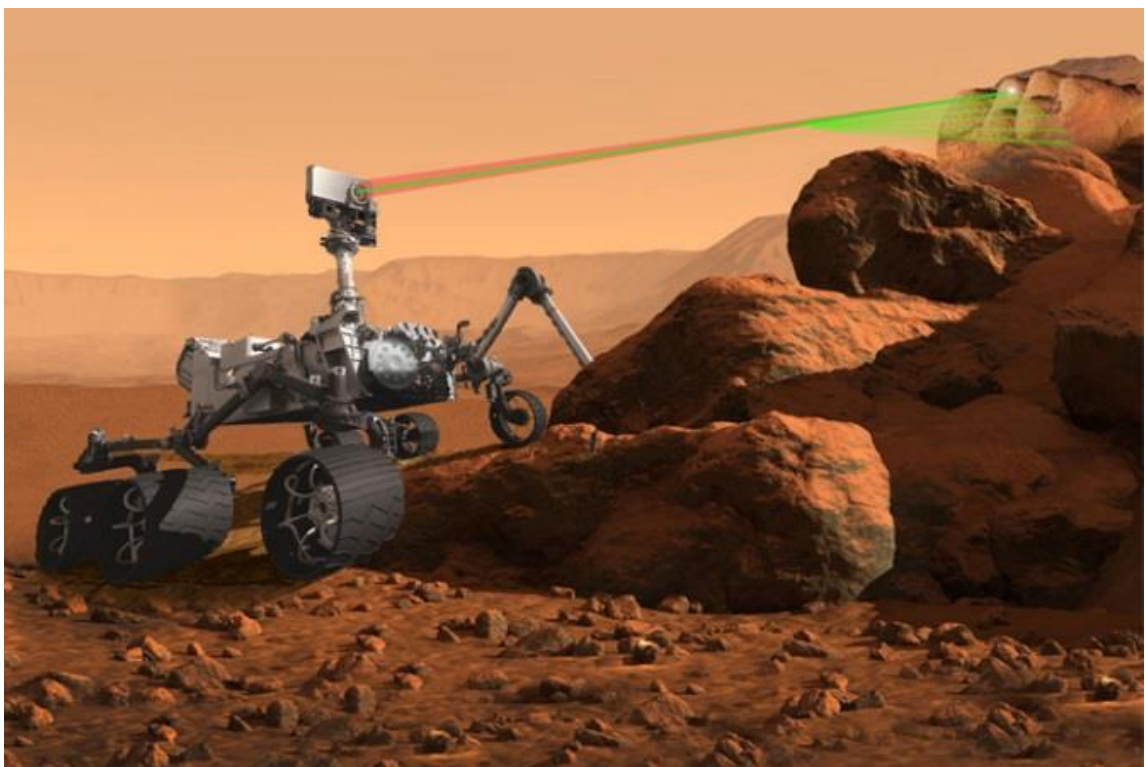


*Figure 2.16 Artist's impression of SuperCam in action with the green 532nm Raman laser and the 1064nm LIBS laser  
Image Credit NASA/JPL*

learned from ChemCam on MSL will be used to refine the LIBS design that will be paired with Raman (Wiens et al. 2016). Like RLS the Raman component will use a 532nm laser, the LIBS will use a 1064nm laser similar to ChemCam's wavelength of 1067nm.

Both will have a standoff remote sensing capability with LIBS equalling ChemCam up to 7m and the Raman spectra to be acquired up to 12m (Wiens et al. 2016).

SuperCam will also contain a remote micro imager (RMI) similar to the one on ChemCam but capable of producing full colour images of both targets for analytical science and long range observations.

The two techniques will complement each other mechanically, with the LIBS laser first being used to remove the initial layer of Martian dust that covers the sampling area allowing the Raman to then detect the surface level of the actual sample of interest without interference from the iron oxide dust. Even though the Raman and LIBS spot sizes are not identical, the shockwave from the plasma formation will clear away dust from the surrounding area.

Lessons learned from ChemCam can be applied directly to SuperCam with a refinement of the LIBS system and many more calibration targets planned to be used. Software designed for automatic target selection AEGIS (Autonomous Exploration for Gathering Increased Science) has been recently deployed for ChemCam which can then be applied directly to SuperCam (Francis et al. 2015). This allows for many more targets to be hit by removing some of the communication time with Earth.

Testing for SuperCam is ongoing at Los Alamos National Laboratory in the United States. (Wiens et al. 2016)

### 2.9.2 XRF/XRD

Both XRF and XRD share much of the same instrumentation requiring an x-ray source and the ability to manipulate or powder a sample. As with Raman and LIBS the combination of mineralogical and elemental data is a useful tool for characterising the makeup of a sample (Blake 1999) with the more widely used XRF capable of confirming the results of XRD and vice versa, providing an additional level of confidence in the data

(Loubser & Verryin 2008). Many terrestrial lab instruments have the capability for both but size and weight requirements make adapting it for a planetary science mission a challenging prospect.

CheMin was initially planned to be a combined XRF/XRD instrument. Ultimately the XRF features were descope due to constraints and only XRD can be used (Bish et al. 2007; Blake et al. 2012).

The descope ExoMars XRF/XRD instrument also possessed these combined techniques in a compact package with the aim to analyse clays, silicates, carbonates, and evaporates. The instrument would have been low mass at 1.3kg (Marinangeli et al. 2007).

### 2.9.3 Raman/IR

Given the relatively complementary nature of Raman and Infra-red data they are considered two techniques useful to pair. Whilst they don't share much of the same instrumentation, the mechanism for manipulating the samples can be shared between the two instruments as will be the case on ExoMars. Unfortunately some of the sample preparation for IR can cause the loss of spatial data from Raman. ExoMars will analyse sample produced by the drill with both the IR Micro-Omega and RLS focusing on the same targets in sequence (Richter et al. 2015). These instruments form the Pasteur instrumentation suit alongside the MOMA Mars organic molecule analyser heading to Mars on the 2020 ExoMars rover. Each sample will cycle through the different instruments in the analytical suite.

### 2.9.4 LIBS/XRD

The Mars Science Laboratory rover possess both the mineralogical XRD analysis and chemical LIBS. The two techniques are very different with CheMin; internal sample analysis, multiple hours measurement time, full MSL drill scoop sample size (Blake et al. 2009). Whilst ChemCam; external target acquisition, multiple measurements per second, 400µm sample size (Wiens et al. 2012). Despite these differences it is still possible to use the instruments to analyse the same samples. ChemCam can be used to

target the interior wall of drill core samples, acquisitions can also be taken of the drill tailings. Joint analysis took place of samples from the John Klein and Cumberland drill holes. The combined data quantifies sulphate veins to 19% in the John Klein and 8 % in the Cumberland sample (Jackson et al. 2014). Additional studies compared the ChemCam data to the derived chemical compositions from the XRD mineralogy finding the majority of XRD data within the ChemCam compositional cloud (Dehouck et al. 2017).

## 2.10 Future missions

Major Space agencies have roadmaps of their plans for future space exploration of the types of missions and destinations they are likely to investigate. For the past few decades Mars has been a major target for these agencies and will continue to be a target for a number of upcoming missions.

The key targets for these future missions are generally; Mars, Jupiter's icy moon Europa, asteroids, possibly redirected into Earth's orbit, returning to the moon, and in some cases Venus. They include additional landers and rovers which generally seek to pave the way for human missions to return to the moon and eventually reach Mars. A key future mission would see samples returned from Mars or another planet which can then be analysed in a lab with state of the art equipment without the miniaturisation requirements of a mission. NASA's MARS 2020 rover contains multiple experiments with the goal to prepare for future sample return possibilities. Such a mission would have to deal with planetary protection issues for any lab on Earth (McKay 2002).

# Chapter 3: ChemCam analysis at Mars

## 3.1 Introduction

Over the course of the NASA Mars Science Laboratory mission to Gale Crater, the Curiosity rover utilised its ChemCam, Laser Induced Breakdown Spectrometer to characterise numerous sedimentary outcrops, soils, igneous float rocks and conglomerate targets along the route towards the foothills of Mount Sharp. From landing on Mars, August 6th 2012, the first 1000 sols of operation saw Curiosity travel 10.6 km across the Martian surface. This period of operation saw nearly 200 targets analysed with the APXS instrument and over 750 ChemCam targets analysed, with over 230000 LIBS spectra acquired. The majority of the igneous rocks encountered are of a fluvial origin with some possibly displaced by impact mechanics after the formation of Gale crater, sometime in the early Hesperian period (Milliken et al., 2010). Throughout this Chapter, data from the ChemCam instrument is used; for further details on the ChemCam instrument, its operating modes and data processing techniques, see Chapter 2, Section 2.2.3. For information on how Laser induced Breakdown Spectroscopy can be used to determine the chemical composition of materials, see Chapter 2 Section 2.2.1.

The ChemCam data is used to determine the elemental composition of targets by performing numerous grain-scale elemental investigations across the surface of the sample. These compositions are compared to: data from other instruments on board Curiosity, other rover missions to Mars (with similar instrumentation), the Shergottite Martian meteorites and terrestrial analogues in order to provide new insights into the processes which govern Martian magmatism. ChemCam analyses of individual targets or outcrop locations have been undertaken by others in detail (Sautter et al. 2014; Sautter et al. 2015; Anderson et al. 2015; Jackson et al. 2016). However, the large quantity of ChemCam data allows for an estimate of the bulk composition based on the average composition of numerous observation points. This chapter uses a “bulk-data” approach looking at the broader trends throughout the ChemCam data from the first 1000 sols. Definitions of some of the geological terms referred to can be found in Appendix 2.

## 3.2 ChemCam data acquisition

ChemCam is a Laser Induced Breakdown Spectrometer instrument (see Chapter 2 Section 2.2.3 for details). ChemCam obtains LIBS measurements which are obtained by collecting light emitted from a plasma generated by ablating a target surface with a laser. This light is collected by an optics assembly in the Mast Unit, which is transmitted by fibre optic cables to a spectrometer within the body unit. This spectrometer disperses the light to form a spectrum at the focal plane assembly covering three separate detectors (CCDs), over wavelength ranges from 240nm – 900nm (Wiens et al. 2012). The light incident on the CCDs is constrained into pixels which are then binned to produce a 1D spectrum of signal intensity versus wavelength. A dark frame is taken to remove background light not produced as a consequence of the LIBS plasma and the spectra is normalised, which allows for comparison between the relative peak heights in the LIBS spectra (Maurice et al. 2012; Wiens et al. 2013).

This raw spectrum can be analysed in a variety of ways, perhaps the most simple of which is univariate analysis. This approach involves the measurement of a number of known calibration targets with well-established chemical compositions and abundances, to produce a calibration curve of peak heights of the relevant elemental peaks. An unknown sample can then be compared to these known peaks and compositions to determine its own chemical make-up. However, this technique suffers from chemical matrix effects when peaks of different elements overlap one another inflating the peak height and giving incorrect compositions (Fabre et al. 2014).

Another technique that has been used by the MSL team is the Partial Least Squares (PLS1) algorithm (Wiens et al. 2013). The PLS1 multivariate analysis method uses replicas of the full ChemCam instrument in laboratories on Earth (in Los Alamos and Toulouse). These replicas can be used to characterise training sets of known analogue samples analysed with other techniques, which can be used to compare the unknown samples on the surface of Mars (Wiens et al. 2013). One advantage of this system is that the training set can constantly be enlarged and updated. As this set expands to become more analogous in composition to the Martian samples, the accuracy of the algorithm

output increases. If the training set samples are not similar enough in composition and elemental abundance to the targets, then inaccurate results can be produced. ChemCam data calibration algorithm reports compositions in weight percent of the major rock forming oxides. These inaccuracies can include the sum of reported weight percent oxides exceeding 100% or being well under at around 80%. However, this can also be due to the presence of large weight percent quantities of elements such as sulphur which are not reported by the main algorithm, although work is in progress to detect these elements (Clegg et al. 2017). Newer calibrations use a combination of both PLS1 and Independent Component Analysis (ICA) to achieve the smallest error in calibration, which independently characterise each of the major rock forming oxides; SiO<sub>2</sub>, TiO<sub>2</sub>, Al<sub>2</sub>O<sub>3</sub>, FeO, MgO, CaO, Na<sub>2</sub>O and K<sub>2</sub>O. This most recent calibration uses a training set comprised of 408, well characterised samples, to provide the most accurate calibration (Clegg et al. 2016). This calibration can then be applied to spectra returned by the rover in order to obtain the weight percent oxide values of the target observation point's composition. ChemCam targets (Figure 1.1) are selected from the MastCam images of the surrounding area.

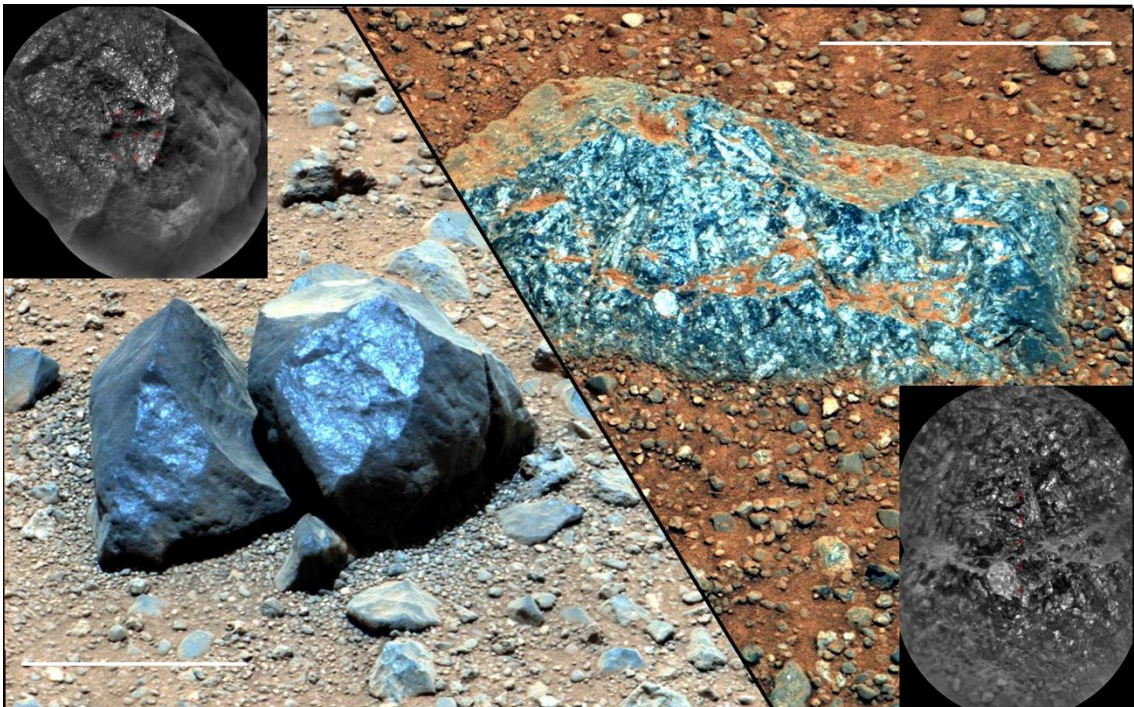


Figure 3. 1 Representative MSL ChemCam igneous targets Ashuanipi sol 337 (Left) and Robin Hood Sol 365 (Right) Images used Ashuanipi, RMI based on CRO\_427406326PRC\_F0080234CCAM03337L1, Mastcam 0337MR0013640000301066E01 Robin Hood, RMI based on CRO\_429891264PRC\_F0120560CCAM02365L1, Mastcam 0365MR0014840010301460E01 The RMI mosaics were produced by the ChemCam team (Olivier Gasnault and William Rapin) (Edwards et al. 2017)

### 3.3 Geology

The following section describes a number of key geological features encountered by the Curiosity rover.

#### 3.3.1 Basalt

Basalts are a common igneous rock, both terrestrially and throughout the solar system rocky planets. These rocks are formed from rapid cooling of lava, generally between 45 – 55 weight percent silica, though they often possess relatively diverse chemical compositions (Stolper & Walke 1980). Basalts are usually composed of clinopyroxene and plagioclase, whilst they also can contain the minerals: olivine, nepheline, melilite, hypersthene, or quartz, and additional minor phases (Yoder & Tilley 1962).

#### 3.3.2 Trachybasalts

Trachybasalts are a type of effusive igneous volcanic rock on the compositional trend between basalt and trachyte (Bowes 1989), i.e. they are relatively fractionated compared to basaltic compositions and mineralogy. They commonly have high alkali content, as can be seen from a TAS (Total Alkali Silica) plot (Figure 3.2) where their compositions lie between 45 and 51% wt% SiO<sub>2</sub> with between 5 and 7 wt% alkali (Le Bas et al. 1986). Trachybasalts often incorporate alkali feldspar, plagioclase, augite and olivine.

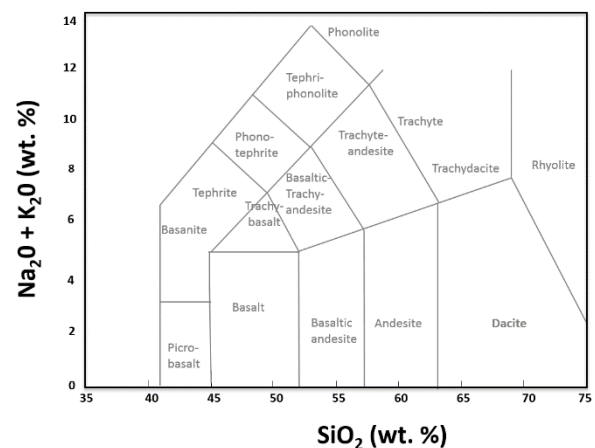


Figure 3. 2 TAS (Total Alkali Silica) plot. Different rock types fall into the separate compositional areas based on the silica and alkali content

On Earth, trachybasalts are found within both alkaline and tholeiitic environments. Figure 3.3 shows a sample of trachybasalt sourced from an alkaline province in Mt. Dore, Auvergne, France. This particular sample is an extrusive rock, with visible light coloured plagioclase grains. In contrast to the Gale trachybasalts, this particular sample contains amphibole and biotite.



*Figure 3.3 Representative specimen of trachybasalt from Mt. Dore, Auvergne, France. University of Leicester Geology department collection.*

### 3.3.3 Alkali and sub alkaline basalts

When silica-saturated and rich in alkali, basalts can be described as alkali or mildly alkaline (McSween & Ruff 2006; Nekvasil et al. 2007). The use of the alkaline/ sub alkaline divide from Irvine and Baragar (1971) can produce some uncertainty in characterisation as tholeiitic rocks fall within the alkali/silica field as shown by Delong and Hoffman (1975). For clarity, alkaline basalts are described here as those with silica under-saturated, feldspathoid normative compositions. Whilst hypersthene normative and silica saturated are within the sub-alkaline group.

### 3.3.4 Feldspar

Feldspars are a mineral group formed by the crystallisation of magma within igneous rocks (though they can also be found in metamorphic rocks or as detrital grains in sedimentary rocks). They are found between three different endmember compositions: potassium orthoclase endmember feldspar  $\text{KAlSi}_3\text{O}_8$ , sodium endmember albite  $\text{NaAlSi}_3\text{O}_8$  and the calcium endmember anorthite  $\text{CaAl}_2\text{Si}_2\text{O}_8$ . Samples containing feldspar measured by ChemCam will typically have higher  $\text{SiO}_2$ ,  $\text{Al}_2\text{O}_3$  content with lower FeO and MgO. Comparisons between different feldspar can be viewed with a ternary plot wherein the ratios of the Ca, Na and K content of the feldspar determine its location on a triangular plot with each endmember placed at the vertices (Elkins & Grove 1990). An example of such a plot is provided in Figure 3.4. These plots provide valuable insight into the feldspars parental melt and fractionation processes. Many of the Martian meteorites contain a large quantity of feldspar (Freeman et al. 2008) and as such, the Shergottite feldspar are plotted on the ternary in Section 3.4.2 for comparison to felsic ChemCam data.

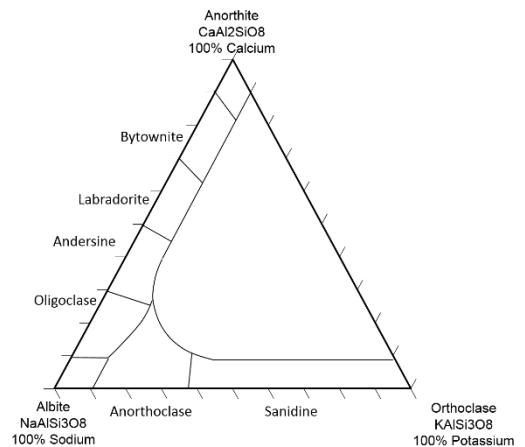


Figure 3. 4 Example of a feldspar ternary plot with terrestrial feldspar locations marked

### 3.3.5 Normative compositions

The CIPW Norm composition algorithm (named after the geologists: Cross, Iddings, Pirsson and Washington, who developed the algorithm) is a tool used by geologists to determine the sorts of minerals likely to be within an anhydrous target based on the bulk mineral composition. Whilst this method will not give a definite comparison, it will give an idealised mineralogy based on certain assumed conditions about the samples. An individual CCAM target area is too small to form the basis of a CIPW norm. However, we can use the wider selection of data over the different observation points in order to estimate the bulk average chemistry.

### 3.3.6 Martian Geology

Prior to the landing of the Mars Science Laboratory mission, our understanding of the igneous rocks on the Martian surface was mostly derived from the study of the Martian meteorites (McSween & Treiman 1998) known as SNC meteorites- Shergottites, Nakhilites and Chassignites. This has been developed with in-situ science from lander and rover missions. In particular, the APXS (Alpha Particle X-ray Spectroscopy) instruments on the Pathfinder, Spirit and Opportunity rover missions (see Chapter 2 Section 2.4.5) (Gellert et al. 2006). These studies are supplemented with spectral mineralogy data from measurements of surface mineralogy by the multiple orbiting instruments on various spacecraft (Poulet et al. 2009). From these sources, there is evidence of a Martian crust which is dominated by basalt, both compositionally and from a mineralogical standpoint (Bandfield et al. 2000; Dunn et al. 2007; Koeppen & Hamilton 2008; Poulet et al. 2009; Taylor et al. 2010; Rogers & Hamilton 2015), with evolved rocks localised in nature (Bandfield 2004; Carter & Poulet 2013; Wray et al. 2013; Sautter et al. 2015). Likewise, the analysis of the Shergottite meteorites showed they were also basaltic (Bridges & Warren 2006; McSween et al. 2009; Gross et al. 2011) with some evidence for more evolved magma compositions within melt inclusions and clasts (Ikeda et al. 2003; Nekvasil et al. 2007; Santos et al. 2015; Humayun et al. 2013).

#### 3.3.6.1 *Shergottites*

The Shergottites are the most common form of Martian meteorites with 75% of all SNC meteorites in terrestrial collections classified as Shergottites. Hence they are one of the most studied sources of information about the Martian surface that is accessible for detailed analysis. Studies of these Shergottites show a restricted range of chemistry that is rich in iron but poor in alkali, composed of undifferentiated basaltic rocks. Mineralogically, the meteorites are dominated by pyroxene, plagioclase with a varying quantity of olivine. Overall Shergottites are a mixture of cumulates and melts (Bridges & Warren 2006; Treiman & Filiberto 2015; Filiberto et al. 2012; Filiberto & Dasgupta 2012; Gross et al. 2011; Burgess et al. 2006; Stolper & McSween 1979; McSween et al.

2015; McSween et al. 2009), with some samples exhibiting the composition of nearly primary magmas or partially evolved magmas (Gross et al. 2011; Filiberto et al. 2012; Filiberto & Dasgupta 2012; Musselwhite et al. 2005; McSween et al. 2015; Shearer et al. 2008; Papike et al. 2013). Compared to the mantle source for terrestrial basalts, the Shergottite source region is iron and relatively alkali-rich but with much less aluminium (Stolper & McSween 1979; Dreibus & Wänke 1985; Taylor 2013).

### *3.3.6.2 MER missions*

In contrast to the Shergottites, the MER missions Spirit and Opportunity, landing at Gusev Crater and Meridiani Planum respectively, found that the local igneous rocks analysed by the APXS instruments (on board both rovers), possessed a wider chemical compositional range. Whilst the targets shared the Fe-rich basaltic compositions, some possessed much more alkaline-rich magmatic composition (Ming et al. 2008; Usui et al. 2008; McSween & Ruff 2006; McSween et al. 2009; Zipfel et al. 2011). Whilst Opportunity (at Meridiani Planum) only analysed a single relatively unaltered basaltic rock, known as “Bounce Rock”, which is similar in mineralogy to the Martian meteorites, Elephant Moraine (EET) 79001 lithology B and Queen Alexandra Range (QUE) 94201 (Zipfel et al. 2011), Spirit analysed a number basaltic targets (McSween & Ruff 2006; McSween et al. 2008). These analyses produce constraints for the source region of these basalts and Gusev Crater’s magmatic and crustal evolution (McCubbin et al. 2008; Schmidt & McCoy 2010; Filiberto & Dasgupta 2015; Filiberto & Dasgupta 2011; Schmidt et al. 2013). The Spirit rover landed on a possible basaltic lava flow area, but it was not until it had travelled to the Columbia Hills region where the instruments detected ultramafic cumulates and silica saturated, alkali-rich (Ming et al. 2008; Usui et al. 2008; McSween & Ruff 2006; McSween et al. 2009; Squyres et al. 2007). One of the subdivisions of the Spirit Gusev Crater basaltic data is the Wishstone class, which are moderately alkaline but not silica under saturated with pyroclastic rock and intrusive samples (McSween & Ruff 2006). The likely source of these is fractional crystallisation of a primitive, basaltic magma which is similar in composition to the olivine-rich basalts

seen elsewhere in Gusev Crater. These olivine rich-basalts are known as the Adirondack Class (Hamilton & Ruff 2012) and are key to the interpretation of the Gale igneous data.

### *3.3.6.3 MSL*

The Curiosity rover mission has shed new light on Martian geology (Grotzinger 2013). Some of the rocks analysed earliest in the MSL mission have proved to be rich in alkalis of unknown source, possibly igneous or sedimentary in origin. In particular, the possible igneous float rock, Jake\_M (Stolper et al. 2013), has been analysed with the MSL APXS instrument with the results showing a combined alkali content of  $\text{Na}_2\text{O} + \text{K}_2\text{O} = 9 \text{ wt}\%$  with an alkaline nature, with >15% nepheline normative composition which is similar compositionally to the terrestrial mugearites (Stolper et al. 2013). A study from Schmidt et al. (2014) used the APXS instrument to draw attention to the occurrence of alkali, particularly potassium, in some of the basaltic Gale sediments indicating an alkali-rich source region. In particular, the Kimberley sedimentary region has high quantities of  $\text{K}_2\text{O}$  (Le Deit et al. 2016). The CheMin XRD instrument detected alkali feldspar as the likely source of this enrichment (Treiman et al. 2016). Treiman and Filberto (2015) likened the Gale K- enrichment to the parental magmas which would have formed the Nakhlite meteorites.

The ChemCam compositional analysis coupled with RMI imaging has been used by Sautter et al. (2014, 2015) to classify the different igneous rocks encountered in the early part of the mission. The imager has been used to examine the felsic, extrusive igneous rocks and the darker basaltic rocks within the float samples and Hottah conglomerate clasts (Williams et al 2013). Sautter et al. identified the extrusive nature of the felsic lithologies suggesting they may be an ancient crust analogue to the lunar highlands transported from the crater rim, forming coarse gravel or conglomerates.

The ChemCam data, coupled with an improved calibration, (Clegg et al. 2016) gives us a new and valuable tool to examine the igneous rocks at Gale, within their wider Martian context. This is compared with studies of terrestrial basaltic differentiation and other related rocks. Possible controls on crystal fractionation for Gale's differentiated igneous

samples are examined along with the nature of the magmatic differentiation series and the relationship of the igneous compositions throughout Gale to the Shergottites and MER basalts. This work uses a statistical method, using a bulk composition of the many targets rather than individual sample analysis, to give context to igneous samples and how they relate to other observations.

### 3.4 ChemCam results from the first 1000 sols at Gale Crater

#### 3.4.1 Igneous rock classification

The composite mosaic of HIRISE (High Resolution Imaging Science Experiment) images from Mars Reconnaissance orbiter shown below in Figure 3. 5, highlights the route travelled by the rover over the first 1000 Martian sols of rover mission operations. Over the course of this period, more than 700 targets were selected for ChemCam analysis, producing over 200,000 individual LIBS spectra. From this group of targets, we have used the MastCam, MAHLI and RMI to select twenty-five igneous float rocks from the first 533 sols. An analysis of many of these igneous targets can be found in (Sautter et al. 2014).

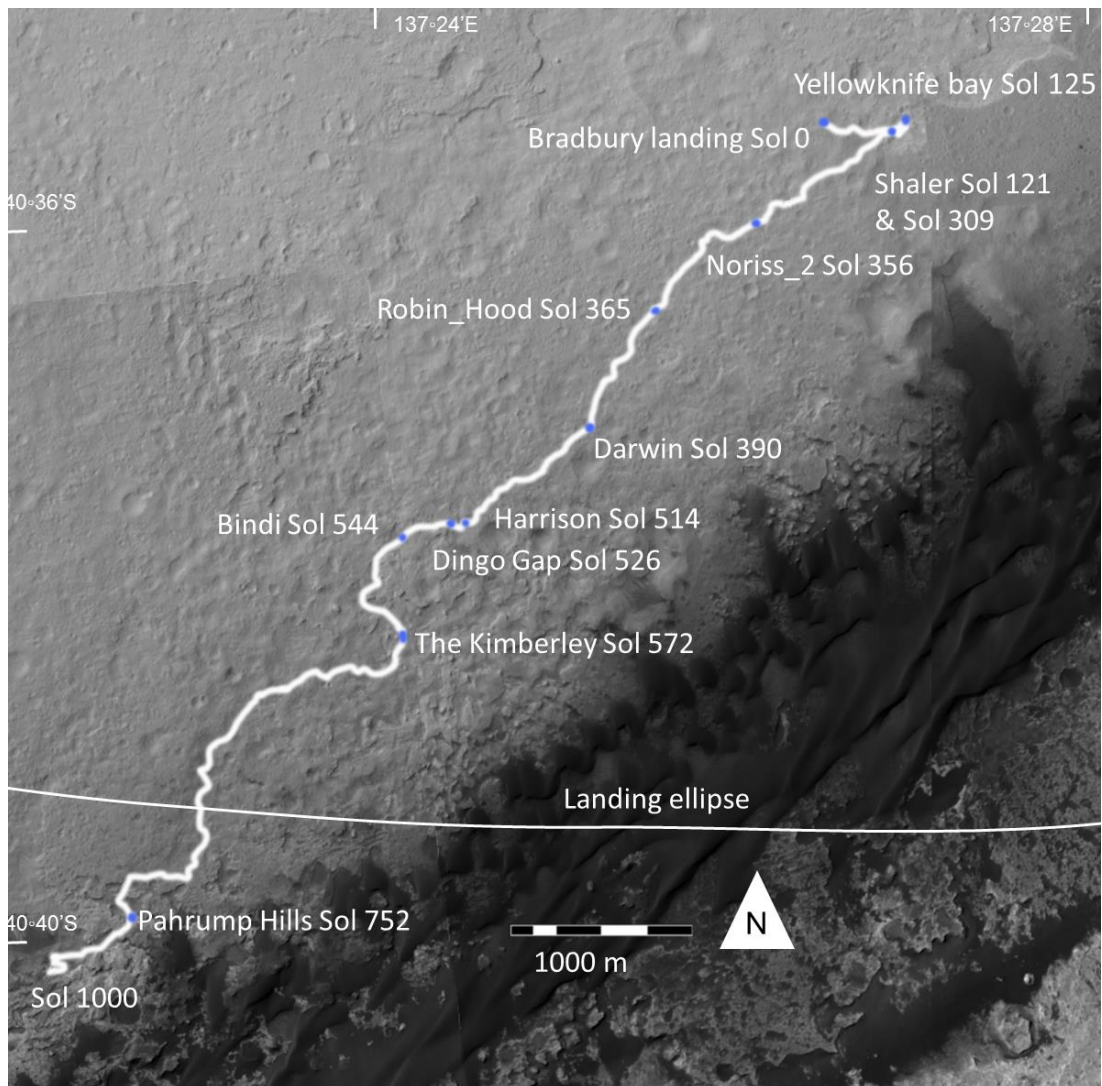


Figure 3. 5 Mosaic of HIRISE images marking the first 1000 sols of MSL Curiosity rover's progress since landing with some of the various targets or target sites of interest marked – sedimentary units and some key igneous locations. The image was produced with the HIRISE images; ESP\_027834\_1755\_RED, ESP\_035917\_1755\_RED, and ESP\_028401\_1755\_RED (Edwards et al 2017)

These rocks were broadly characterised into two compositional endmember groupings based on composition and grain size (Edwards et al. 2017). One group (Basalt group) has a basaltic composition, and is dark in colour, smooth, fine grained, volcanic mainly aphanitic samples such as Ashuanipi. The other grouping (Trachybasalt group) has a trachybasaltic composition and is much more coarse-grained (>500  $\mu\text{m}$  median grain size; Sautter et al. 2015). Trachybasalt group samples are rich in feldspars (see Robin Hood and Harrison conglomerate clasts on sol 365 and sol 514). These feldspars are identified compositionally from the LIBS data (Gasda et al. 2016) and supported by the presence of pale colouration and tabular crystalline forms (Williams et al. 2013; Sautter et al. 2015). The feldspar are discussed further in Section 3.4.2. Example MastCam

images of the two igneous end member groups are shown below in Figure 3.6, the top six targets are in the Basaltic group and the bottom six in the Trachybasaltic group.

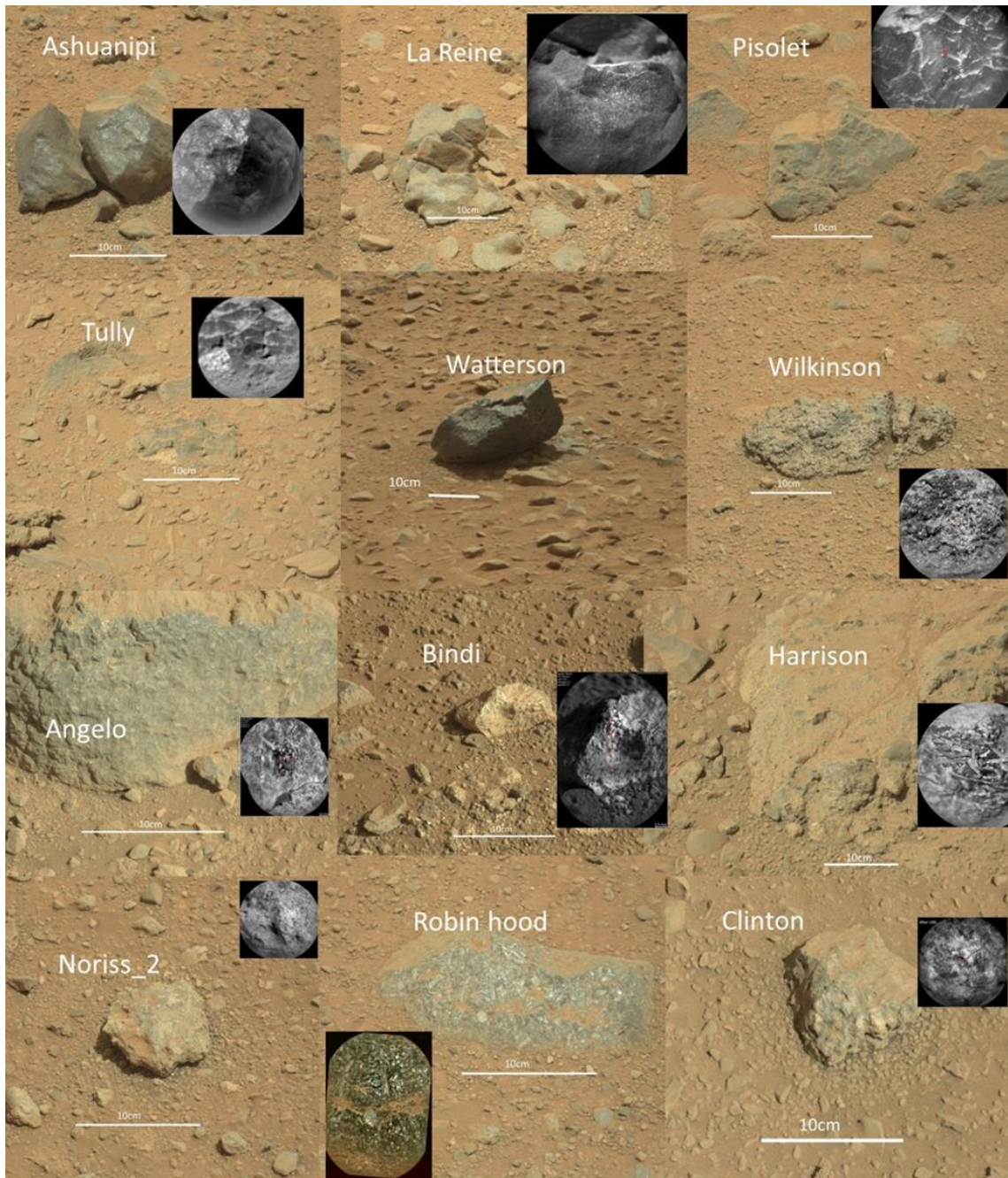


Figure 3. 6 Collage of example end-member trachybasalt and basalt igneous samples. Each image shows a Mastcam and RMI image. Samples Ashuanipi, La Reine, Pisolet, Tully, Watterson and Wilkinson are part of the Basaltic group whilst Angelo Bindi, Harrison, Noriss\_2, Robin Hood and Clinton are members of Trachybasaltic group.

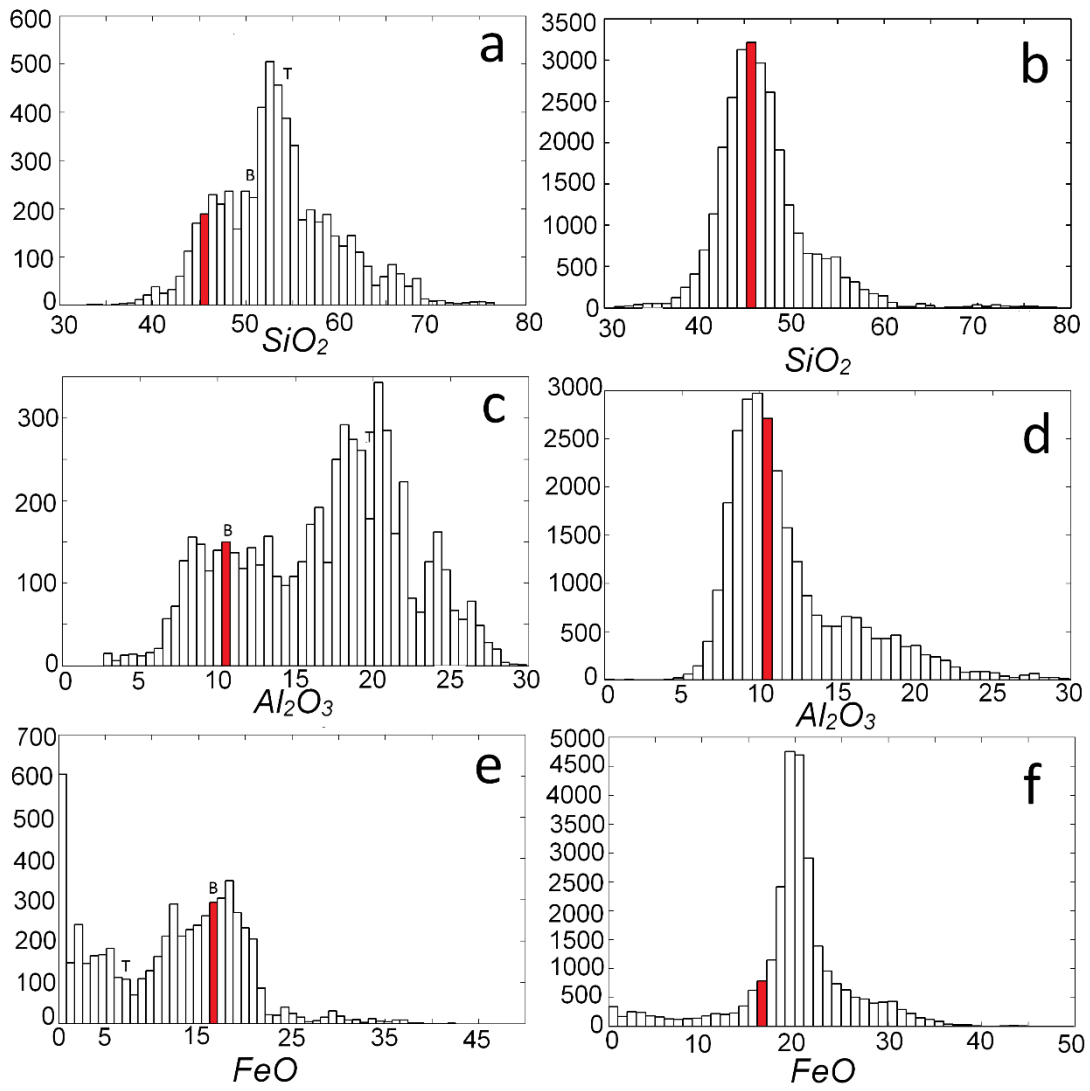
The LIBS spectra for these targets were selected and the ChemCam PLS algorithm was applied allowing for analysis of the data in weight percent oxide form. For the following plots the dataset was optimised to remove values which did not appear to be an accurate composition (total weight percent higher than 105% or lower than 95%), additionally the first 5 shots for each observation point were removed to prevent the iron oxide content of the surface dust from offsetting the measurements compositions. This provided a broad dataset of compositions to complement the more sample specific analysis the ChemCam team had already undertaken.

#### *3.4.1.1 Histograms*

The following histograms (see Figure 3.7) were produced from the elemental data from selected igneous and sedimentary CCAM targets. Each plot shows the distribution in elemental compositions for each subdivision of the dataset, for all the rock forming oxides. The igneous endmember average composition have been marked: the Basaltic (B) and Trachybasaltic (T). Both datasets show a comparison to the MER Spirit APXS data from Gusev Crater (marked with a red bar).

### Igneous

### Sedimentary



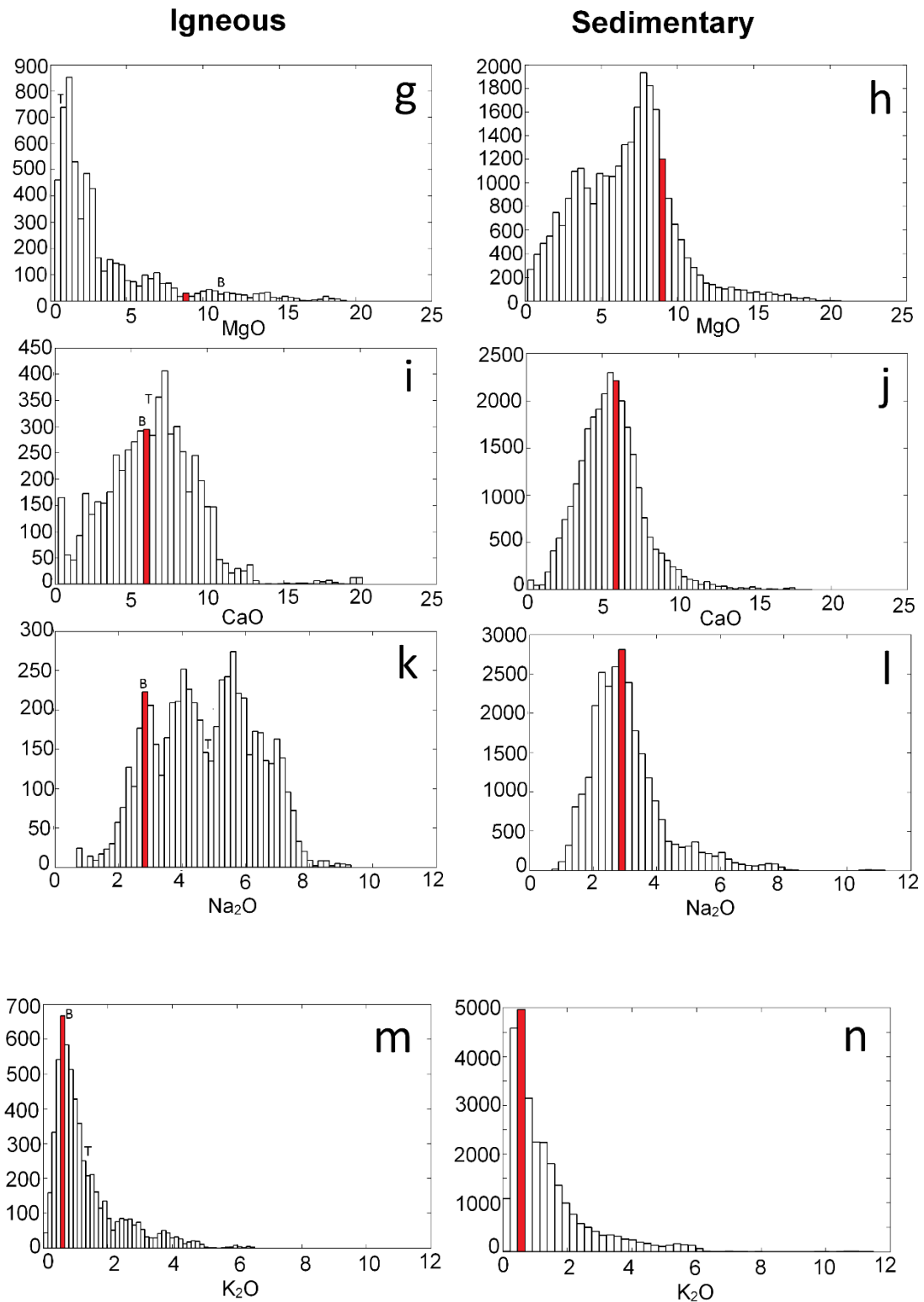


Figure 3. 7 Histograms showing the compositional distribution of both Igneous and Sedimentary ChemCam targets. *B* represents the composition of the basaltic group targets and *T* the trachybasalts in the igneous data. The red bar represents the mean MER composition. These histograms are produced using the single shot ChemCam data with weight percent totals between 95 – 105 weight percent oxides.

Strata from the various sedimentary units along the rover's route were analysed to produce a sedimentary dataset which is then compared to the igneous data. The sedimentary units are detailed in (Grotzinger 2013; Anderson et al. 2015; Rice 2014; Le Deit et al. 2016; Mangold et al. 2016). The bulk of these sediments are fluvio-lacustrine mudstones and also coarse sediments possessing a source region near Gale Crater (Grotzinger, Crisp, et al. 2015). The LIBS data from these outcrops are considerably more homogeneous than those of the igneous data for all except the MgO plots (g and h), for which the igneous is uniformly low in MgO and the sedimentary has a wider distribution. The focal point of the sedimentary silica distribution lies at 45 wt% similar to that of the basaltic igneous endmember. Likewise it can be seen from the sedimentary histogram a well-defined peak in Al<sub>2</sub>O<sub>3</sub> compositions at 10 wt%, much more homogeneous than the wide 6 - 25 wt% distribution of the igneous samples. The iron content is at around 19 wt% for the sedimentary, which is higher than the igneous, but aligns well with the MER data. The CaO content is broadly similar between the two types of rock, with the sedimentary outcrops exhibiting slightly less, at 5.5 wt%, compared to igneous at 6.4 wt%. Both the igneous and sedimentary support a classification of the Gale material as Al poor, Fe-rich moderately alkali basaltic composition from the highlands, differing in composition from the source region of the Shergottites. Further comparison with the shergottites is shown below in Figure 3.8.

#### 3.4.1.2 Contour Harker plots

Harker plots are comparisons between two oxides (one is usually  $\text{SiO}_2$ ) and are used in order to examine the distribution of the chemical data. The TAS plot in Figure 3.9 is a specific Harker plot which compares silica and alkali and is often used to compare samples to known compositions of igneous rocks.

Due to the large quantity of grain scale data, it is useful to use density contour plots. A scatter plot of ChemCam data would be difficult to interpret due to the large volume of data. Instead, these plots show the density of the data at different points. This shows the key points of interest; the homogeneity or heterogeneity of a dataset, the focal point of the data, or the distribution that the compositions form. Each contour for a dataset contains an equivalent quantity of data, with additional contours indicating denser data. These plots show both the data sub divided into sedimentary and igneous rocks for comparison. The two endmember groups lie at either end of the igneous data. Single shot LIBS data were used with the major oxide totals between 95 and 105%. The initial five spectra at each LIBS observation point are discarded due to them mostly composing of a high percentage of Martian dust giving an unrepresentative iron-rich view of the main target composition. The olivine subtraction model (discussed below in Section 3.4.3) is marked with each yellow point on the black line representing 10% olivine extractions, moving from low to higher silica

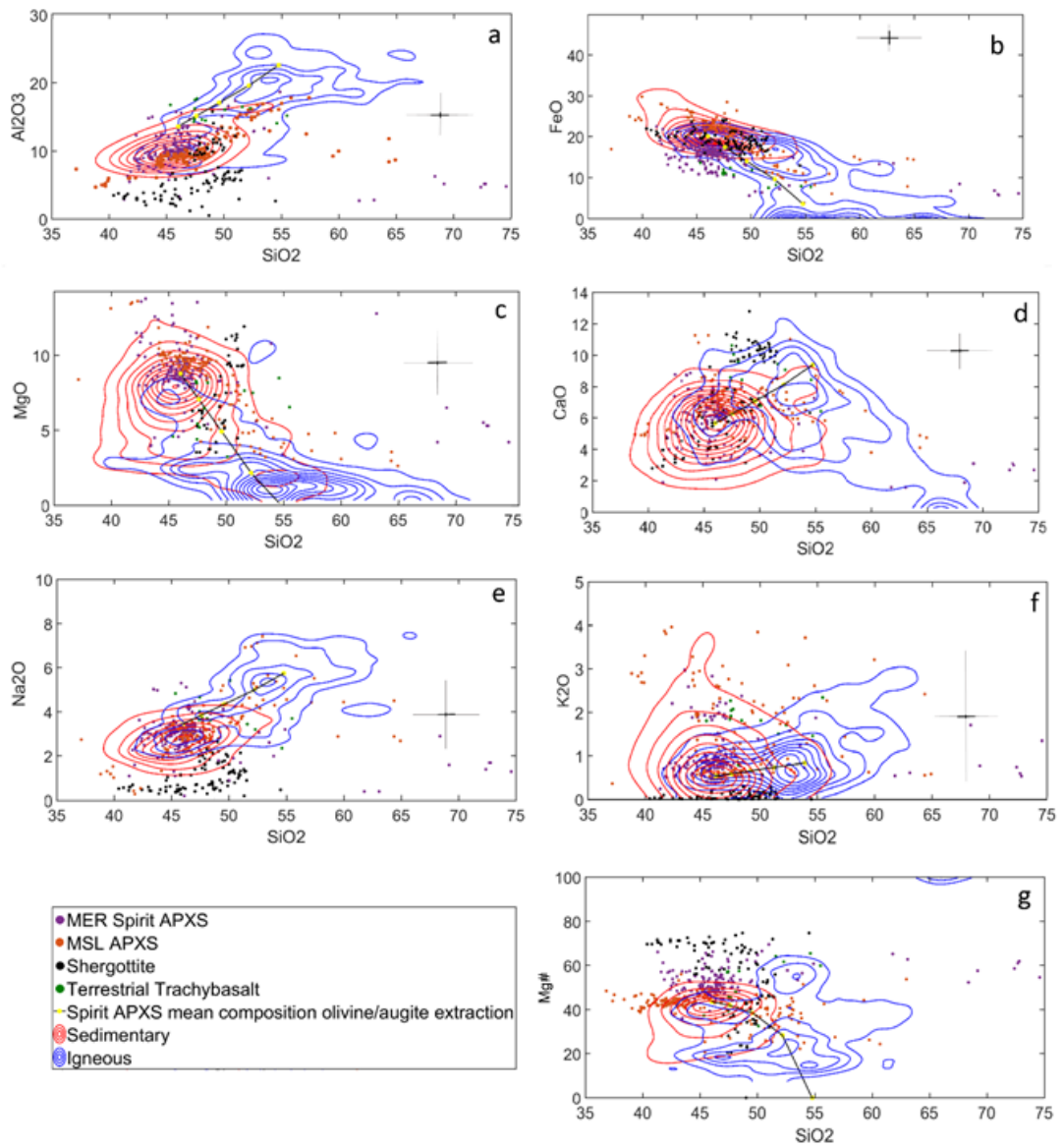


Figure 3. 8 Harker contour plots showing the distribution of ChemCam data over different combinations of oxides. Contour plots a – f show the distribution of the major rock forming oxides. Each of the contour levels contains an equal fraction of the LIBS igneous and sedimentary datasets. Terrestrial trachybasalts are included from the literature (Baker 1969). Light crosses on each plot show the RMSE error (accuracy) for each ChemCam oxide darker crosses show precision. Mars Exploration Rover APXS data from the Spirit rover during its campaign at Gusev crater.

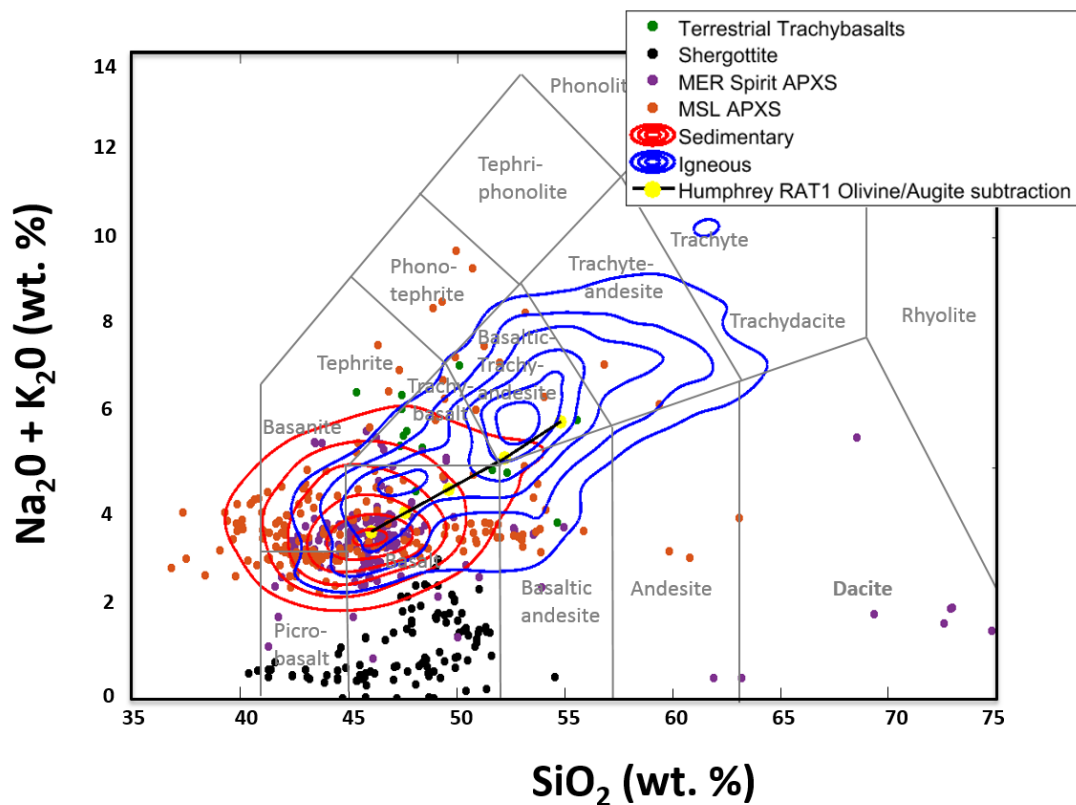


Figure 3.9 TAS plot of the sedimentary and igneous samples from the first 1000 sols of MSL mission. Contour plots show density of data. The model of the igneous trend based on olivine subtraction from a basaltic base is shown with a black line and yellow data points. The model is further discussed below.

In Figure 3.8 and Figure 3.9, the locations of the igneous and sedimentary compositions are in line with that expected from the observed mineralogy; Basaltic group samples are lower in  $\text{SiO}_2$  and high in FeO, whilst the feldspar-rich Trachybasalt group is much higher in  $\text{SiO}_2$ ,  $\text{Al}_2\text{O}_3$  and alkalis (particularly  $\text{Na}_2\text{O}$ ) with lower quantities of FeO and MgO. The trend focuses at a local maxima with basaltic compositions at around 47-51 wt%  $\text{SiO}_2$  and trachybasaltic to the higher  $\sim 55$  wt%, ( $53 \text{ wt}\% \pm 5 \text{ wt}\%$ )  $\text{SiO}_2$ . These groups were used as a starting point to calculate the composition of end members for the trend. A bulk average of the much more homogeneous sedimentary data was also obtained for comparison (see Table 3). As with the histograms in Figure 3.7, the basaltic end member of the igneous trend and the sedimentary data are shown to have very similar compositions. Throughout the data, there is a compositional trend in the igneous compositions, the source of this trend is discussed in Section 3.4.3. The trend towards

extreme calcium enrichment (Figure 3.8d) reflects the existence of Ca-sulphate veins likely due to diagenetic origin (Schwenzer et al. 2016; Nachon et al. 2014) and is unrelated to bulk changes in the other trends in the data. MSL APXS data (see Chapter 2 Section 2.4.5) shows broad agreement with the ChemCam sedimentary data, with silica foci at 45 wt%. The Shergottites are generally lower in  $\text{Al}_2\text{O}_3$  compared to the Gale endmembers which have local maxima at 11 wt% and 22 wt% (Smith et al. 1984). The Shergottite silica distribution is also quite different with a much smaller range and focused at a lower content than the MSL targets. The combined alkali content is much lower for the meteorites compared to the Gale  $\text{Na}_2\text{O} + \text{K}_2\text{O}$  of 4-6 wt%. In contrast, the Shergottites are much more magnesium-rich with a  $\text{Mg}\# = 59$  ( $\text{Mg}\#$  is the ratio magnesium to iron within the sample) similar to the basaltic end member at  $\text{Mg}\# = 54$  but much higher than the Trachybasaltic  $\text{Mg}\# = 27$ , the Basaltic and Shergottites are similar in this aspect to the MER Spirit APXS data from Gusev crater which has a  $\text{Mg}\# = 52$ .

The Trachybasalt group compositions are similar to those found for terrestrial trachybasalts although the Martian trachybasalts group samples are richer in FeO and poorer in MgO, as would be expected from terrestrial-Martian comparisons (McSween 2002). Compositional similarities were found with both oceanic island basalts and mid ocean ridge basalts, which are found alongside trachybasalts in a variety of environments (Humphreys & Niu 2009; Gale et al. 2013; Baker 1969). In particular, oceanic island basalts show a similar alkali content to those of the Gale basalts. It is possible that the two foci of igneous data visible are the result of two different igneous sub-components (Sautter et al. 2014; Sautter et al. 2015). Below, we treat them as compositional end members in the context of their relationship with other Martian basaltic rock formations.

### 3.4.1.3 Tetrahedral plots

Another method of comparing the large quantity of data over numerous elements simultaneously is to display the data using a tetrahedral plot, with different vertices representing different oxides or combinations of oxides. The use of a tetrahedral plot allows for 4 dimensions of data to be displayed in 3 dimensional space. This comparison, uses more of the elemental data to draw links. Comparison between different outcrops shows changes in homogeneity and alkali with a trend between feldspar and pyroxene. Figure 3.10 below shows a comparison between the different sedimentary outcrops, and a comparison between the sedimentary and igneous data.

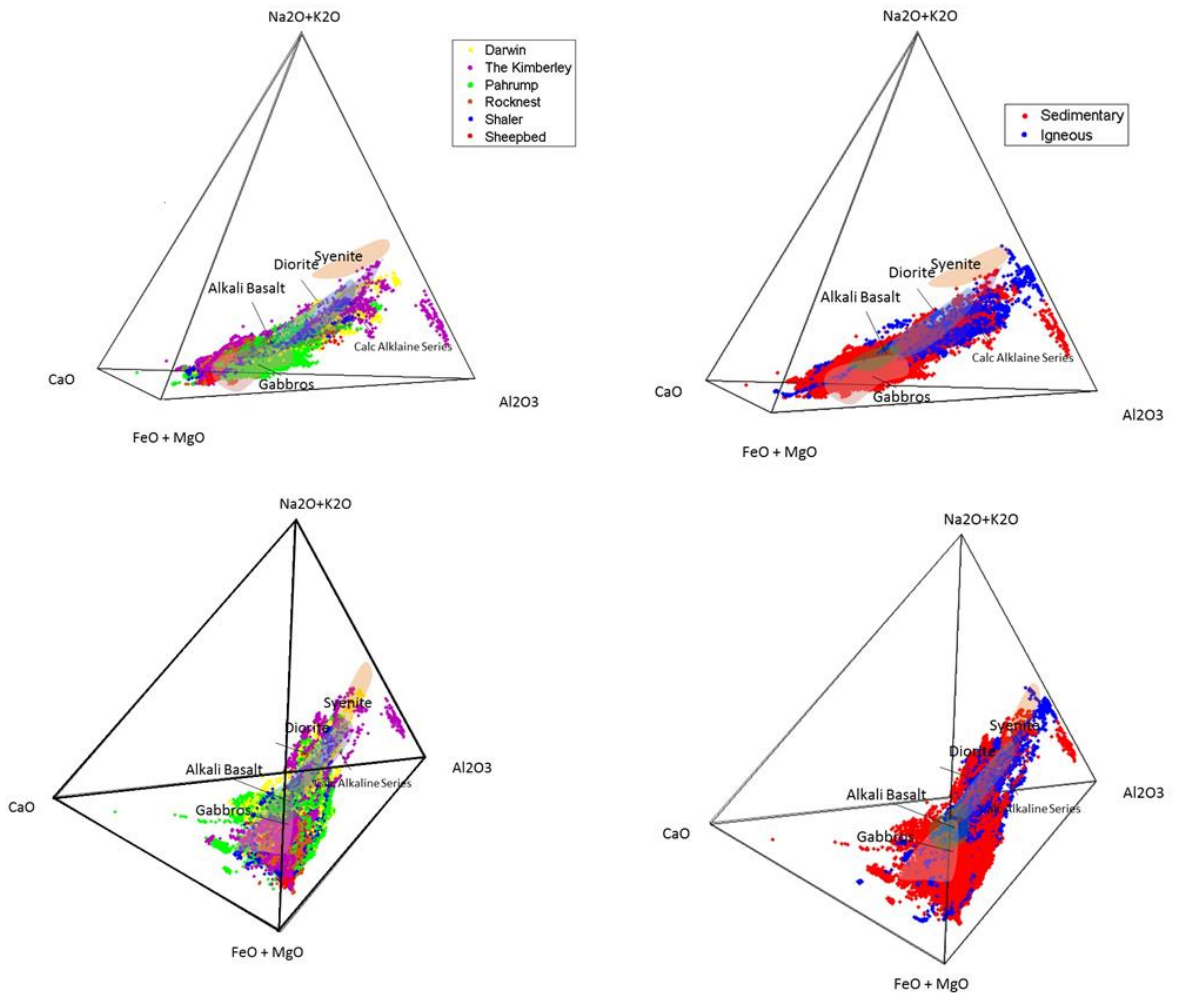


Figure 3. 10 Tetrahedral plots of ChemCam single shot data for (a) Sedimentary outcrops and (b) Sedimentary compared to Igneous.

These tetrahedral plots show a compositional mixing trend from the iron and magnesium-rich pyroxenes towards the high silica, high aluminium, and low iron feldspar compositions. The sedimentary units encountered over the first 1000 sols such as Sheepbed, Shaler, Darwin, the Kimberley and Pahrump Hills (Grotzinger, Crisp, et al. 2015) are generally similar in chemical composition to the olivine-rich basalts encountered by the Spirit rover and analysed with the APXS instrument at Gusev Crater. However there are differences within this sedimentary ChemCam dataset from the various different units.

The distribution of the outcrops and other ChemCam data along this trend demonstrate their compositional differences; the Kimberley and Darwin are much more alkaline than the earlier Rocknest and Sheepbed outcrops encountered earlier in the mission (see Figure 3.5 for a map detailing Curiosity's route to the different outcrops). We can see Darwin has a much higher  $\text{Na}_2\text{O} + \text{K}_2\text{O}$  composition indicating that the conglomerates there came from an alkali source region (Mangold et al 2016). Alkali enrichment was also seen within subsections of Shaler formation and the Kimberley units as they both possess high quantities of potassium and with the CheMin XRD instrument, which also detected sanidine at The Kimberley (Anderson et al. 2015; Treiman et al. 2016; Thompson et al. 2014). Also, the float rock Jake\_M, analysed with the APXS instrument on sols 46 and 47, indicates an enrichment of sodium that is either silica under saturated nepheline normative, alkali igneous rock (Stolper et al. 2013) or a sedimentary float rock with sampling of alkali igneous minerals from the surrounding environment. Silica undersaturated, alkali-rich rocks most likely come from the Peace Vallis area (Treiman et al. 2016) and are not the dominant Gale igneous rocks.

### 3.4.2 Possible feldspar mineral detections

Stoichiometric analysis is the process of using the known atomic formula to determine the elemental composition of minerals and mineral groups. This can be used to estimate the mineralogy of ChemCam samples from their elemental composition. The ratio of the relevant weight percent oxides can be compared to determine the mineralogy from the elemental composition.

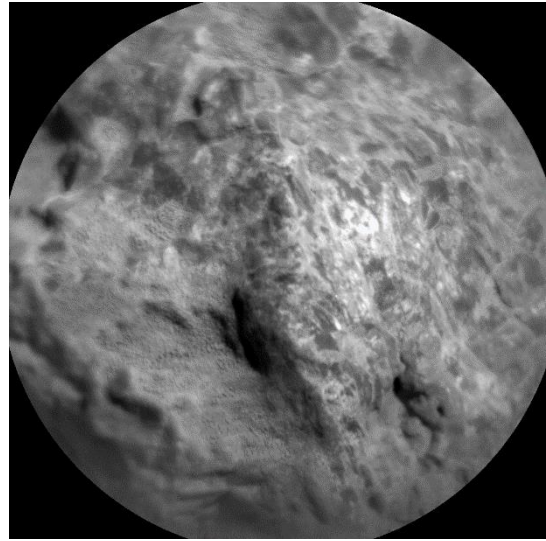


*Figure 3. 11 RMI image of Noriss\_2 target (Trachybasalt group), showing white felsic mineral grains*

RMI images of multiple ChemCam targets

show evidence of multiple felsic mineral grains (see Figure 3.11). This can then be cross-referenced with a stoichiometric analysis of the ChemCam data to detect the presence of feldspars in the Gale ChemCam targets group (Cousin et al. 2017).

To detect feldspar this stoichiometric technique was used with an Al/Si ratio of 0.33 as this would be expected for alkali feldspars due to their compositions for orthoclase  $\text{KAlSi}_3\text{O}_8$  and albite  $\text{NaAlSi}_3\text{O}_8$ . For these feldspar, the ratio of  $\text{Al/Si} = 0.33$ , eliminating false positives from jadeite, leucite, or analcime (Gasda et al. 2016). Any data with weight percent totalling above 105% and below 95% was removed as the derived composition cannot be certain to be accurate. Samples with  $\text{SiO}_2$  content below 60% were eliminated as were all samples with greater than 5 weight percent FeO. Only those samples with a felsic chemical composition were left and these are plotted on the ternary below (see Figure 3.12).

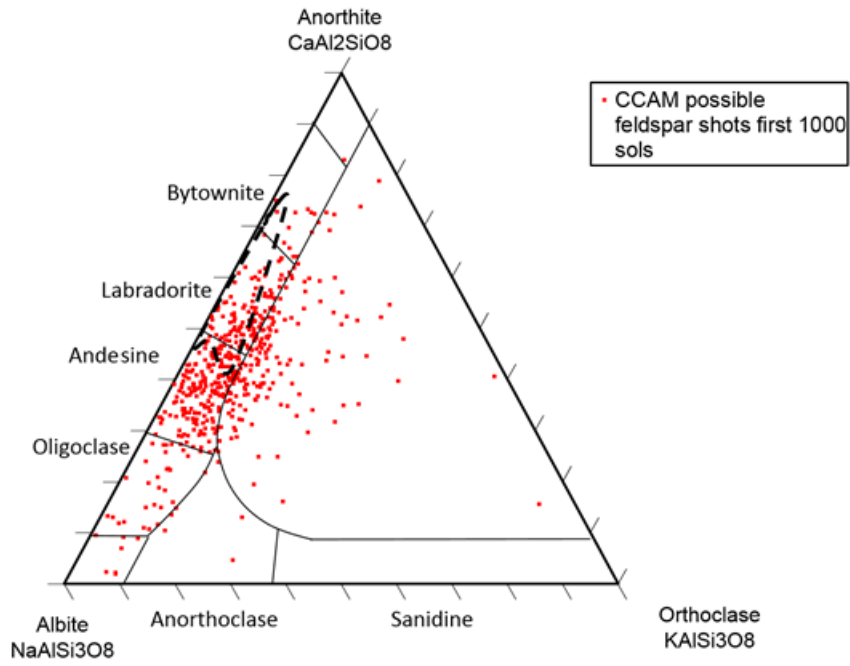


Figure 3. 12 Ternary plot of detected possible feldspars, dashed line indicates Shergottite felsic compositions terrestrial feldspar compositions from (Gasda et al. 2016)

Table 3.3 Feldspar classifications of possible detected feldspars in order of quantity

Feldspar	Count
Andesine	187
Mixture	176
Labradorite	74
Oligoclase	35
Bytownite	12
Anorthoclase	10
Albite	7
<b>Total</b>	<b>501</b>

Table 3.1 shows that andesine was the most common compositional grouping of the 501 possible feldspar compositions identified from the ChemCam data, which had been detected over the first 1000 sols from a set of 5724 target spots through that period. This correlates with work by Gasda et al. (2016) finding feldspar-rich in sodium. The possible stoichiometric feldspars were most common in the Trachybasalt group of the igneous samples which correlates with the expectation from visible coarse grains in the RMI images of the selected target samples. In contrast, felsic data were uncommon in the basaltic rocks which were richer in iron (Gasda et al. 2016). Table 3.2 shows representative ChemCam compositions of the possible feldspars.

Target	Sol	Shot Number	Spot number	Distance (m)	SiO <sub>2</sub>	TiO <sub>2</sub>	Al <sub>2</sub> O <sub>3</sub>	FeO <sup>T</sup>	MgO	CaO	Na <sub>2</sub> O	K <sub>2</sub> O	Total	Al/Si	Ca	K	Na
Bird_River	358	30	5	3.6	60.6	0.6	26.9	1.0	0.6	1.3	7.1	2.6	100.7	0.35	29.7	29.1	40.3
Gowganda	370	23	9	3.3	60.0	0.7	25.8	0.2	0.4	5.5	7.4	1.1	101.1	0.35	27.8	8.2	55.9
Kinsman	663	20	2	2.6	61.4	0.6	21.6	2.2	0.5	0.7	8.6	4.3	99.9	0.30	63.5	7.4	49.4
Rock_Stream	469	16	8	4.1	60.8	0.6	24.3	3.7	2.5	4.7	6.1	0.3	103.0	0.34	2.2	8.1	46.8
Wilkinson	365	6	3	4.1	63.8	0.8	22.2	3.3	0.9	2.5	9.2	2.4	105.0	0.30	59.8	4.0	42.4
Antelope_Valley	744	26	5	3.8	60.4	0.7	22.0	1.8	1.9	6.0	5.8	0.2	98.7	0.32	46.5	12.1	41.9
Ross	379	29	5	4.1	63.5	0.7	24.5	0.1	1.1	5.5	6.5	0.9	102.8	0.33	83.0	9.0	47.3
Sledgers	381	13	1	2.5	66.0	0.3	24.4	0.0	0.5	0.3	8.3	3.2	103.0	0.32	72.7	8.2	41.6
Beacon	376	106	2	2.7	60.5	0.7	21.7	2.0	0.9	5.9	5.7	1.7	99.1	0.31	72.8	5.3	58.6
Chakonipau	338	25	4	2.3	67.0	0.3	24.2	0.0	0.4	0.2	7.9	4.7	104.6	0.31	33.5	6.8	43.8
Clinton	512	16	4	2.4	60.2	0.7	21.7	0.8	1.2	6.3	6.2	1.4	98.4	0.31	46.1	4.7	46.0
Exeter	646	12	4	3.1	60.4	0.7	21.5	0.2	1.5	6.8	6.9	3.3	101.3	0.31	10.8	9.8	54.1
Kenwood_River	358	21	2	3.3	60.8	0.7	21.1	1.8	1.0	6.0	6.8	1.3	99.4	0.30	7.0	6.8	47.5
Noriss_2	356	11	8	2.4	60.1	0.7	22.2	0.5	0.7	4.1	7.5	1.4	97.2	0.32	37.1	10.1	54.2
Ruker_RP_ccam	387	17	8	2.5	60.8	0.7	22.5	2.6	0.7	1.4	8.5	2.0	99.2	0.32	9.3	6.0	45.4
Togo	520	15	1	3.5	62.2	0.2	25.0	0.1	0.3	5.2	6.6	3.9	103.6	0.34	72.3	12.6	42.4
Kanyuak	123	20	3	5.2	63.2	0.6	26.1	0.9	0.5	0.3	7.6	5.3	104.5	0.34	75.0	0.7	49.6
King_Leopold	574	25	7	2.8	61.3	0.7	21.6	0.4	0.8	6.8	6.6	2.0	100.1	0.31	40.7	57.3	30.0
Roebuck	584	12	5	5.4	60.4	0.7	23.2	0.8	0.9	4.8	7.6	4.4	103.0	0.33	19.8	5.3	46.9

Table 3.2 Table of representative feldspar compositions from the selection described above

### 3.4.3 Igneous trend modelling

To evaluate the crystal fractionation process that could produce a trend such as those seen in the igneous data (see Figure 3.8 and 3.9), a simple model was used to simulate the effects on composition of crystal fractionation. The model subtracted olivine and pyroxene from the Spirit MER APXS data of the Humphrey sample, which is broadly representative of the Adirondack class – a



Figure 3. 13 MER image of Humphrey a Spirit APXS target, image credit: NASA/ JPL/ Cornell/ USGS. This is part of the Adirondack class of basalt (McSween & Ruff 2006; Hamilton & Ruff 2012) this samples composition is related to the trachybasalts found in Gale Crater

Martian basalt, rich in olivine (See Figure 3.13). The Humphrey sample composition (Gellert et al. 2006) was normalised to 100% totals, from which a 10% augite composition was removed and the result renormalized. Following this, a sequence of olivine subtraction in 10% intervals between 0 and 40% were removed with the results also being renormalized to 100%. For this olivine subtraction a composition of  $\text{SiO}_2 = 32$  wt%,  $\text{FeO} = 44$  wt% and  $\text{MgO} = 24$  wt% was used as this is representative of the FeO rich MgO poor surroundings. This olivine composition has an  $\text{Mg\#} = 50$  which is within the range of MER Mossbauer spectroscopy measurements (Morris et al. 2006; Filiberto et al. 2008) (Chapter 2 Section 2.9) for the Adirondack class basalts at Gusev  $\text{Mg\#} = 60 \pm 10$ . For the augite the composition  $\text{SiO}_2 = 42$  wt%,  $\text{FeO} = 19$  wt%,  $\text{MgO} = 14$  wt% and  $\text{CaO} = 24$  wt% was used due to a similar  $\text{Mg\#}$  to the Humphrey target.

As shown in Figure 3.8 and Figure 3.9, this model matches well with the igneous compositional trends across major elemental comparisons and  $\text{Mg\#}$  of 54-27 from the

basaltic samples similar to the sedimentary and Gusev samples to the trachybasalt high silica alkali endmember, which suggests a trend of fractionation of olivine. However, no olivine has been detected by ChemCam measurements, likely due to the grain size of olivine being sub 350  $\mu\text{m}$  in size and, as such, smaller than the spot size for ChemCam measurements. The XRD instrument, CheMin (see Chapter 2 Section 2.5.3) has identified variable quantities of olivine in several of the sediments it has analysed (Vaniman et al. 2014).

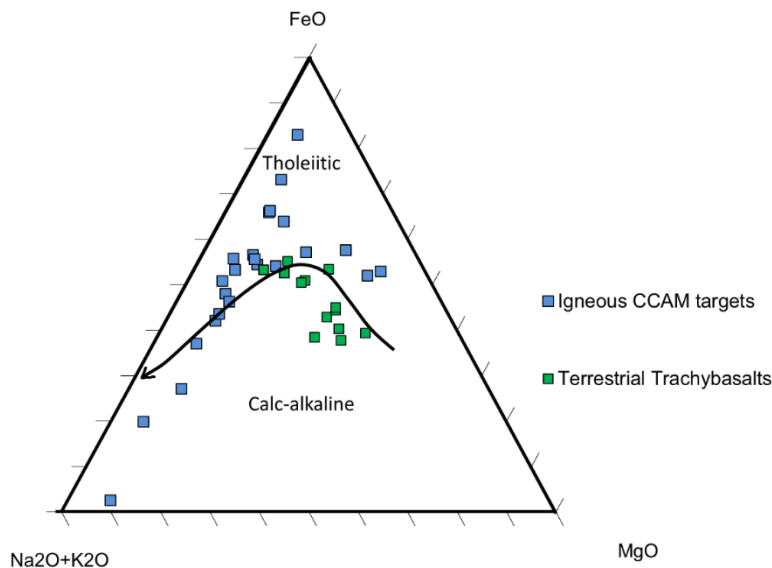
Table 3.3 below shows the CIPW weight norm values (see Section 3.3.5) from the basaltic and trachybasaltic igneous endmember compositions with a mean taken of the representative sample single shot data. CIPW normative compositions are usually used to approximate the mineralogical makeup of anhydrous igneous rocks such as the ones at Gale.

### 3.4.4 CIPW Normative and AFM compositions

	Basalt	Trachybasalt	Sedimentary
Mean			
SiO <sub>2</sub>	51.4	55.2	49.6
TiO <sub>2</sub>	1.2	0.8	1
Al <sub>2</sub> O <sub>3</sub>	10.7	19.8	14.3
FeO	17.7	7.7	18.7
MgO	11.8	1.6	5.8
CaO	5.6	6.4	5.3
Na <sub>2</sub> O	3	5.4	3.3
K <sub>2</sub> O	0.6	1.2	1.3
Total	101.9	98	99.2
Mg#	54.3	27	35.6
One standard deviation			
SiO <sub>2</sub>	2.6	3.5	4.4
TiO <sub>2</sub>	0.9	0.2	0.3
Al <sub>2</sub> O <sub>3</sub>	4	2.5	3.6
FeO	2.4	5.6	5.4
MgO	4.1	1	2.9
CaO	1.4	2.4	2.2
Na <sub>2</sub> O	0.9	1.3	1.1
K <sub>2</sub> O	0.5	0.9	1.1
Total	2.8	1.9	2.6
Fe3+/(Total Iron)	0.1	0.2	0.1
Plagioclase	39.3	39.3	71.9
Orthoclase	3.7	3.7	6.9
Diopside	11.1	11	4.5
Hypersthene	24.7	28.4	11
Olivine	18.3	11.9	1
Ilmenite	2.3	2.3	1.5
Magnetite	2.9	5.7	1.3
Total	102.1	102.3	98.1

Table 3.3 Mean basalt and trachybasalt end member alongside Sedimentary compositions showing the CIPW norms for the Basalt and Trachybasalt groups. Separate Fe3+/Total Iron values are shown for the Basalt group.

The AFM plot in Figure 3.14 is a ternary (similar to those used for feldspar), showing alkali - iron - magnesium abundances for both the igneous rocks and reference terrestrial trachybasalts. These types of plot are useful for the identification of tholeiitic trends in sample sets. For this plot, each individual igneous ChemCam target used a mean composition from all the CCAM observation points on that target. The first 5 shots



at any particular point were not used, as they would typically be composed of dust. The AFM plot shows a similar trend to terrestrial tholeiitic basalts (Zimmer et al. 2010).

Figure 3. 14 AFM plot showing a trend analogous to terrestrial tholeiites. Individual target data used with totals between 95 – 105%. Terrestrial tholeiitic trend marked with the black arrow is from the Shishaldin volcanics, Aleutians (Zimmer et al., 2010). Trachybasalts from Barker et al 1969 and Tanguy et al 1978

### 3.5 Discussion

The Martian surface is usually considered to be a basaltic world with a crust dominated by basalt compositions. This view is based on the historical analysis of Martian meteorites, spectral data from orbiter missions and in-situ data obtained with instruments on previous landers and rovers (Adams 1968; Bridges & Warren 2006; Bandfield et al. 2000; Bibring & Erard 2001.; McSween et al. 1999; Karunatillake et al. 2006). In contrast, Dreibus and Wänke (1985) proposed a Martian interior rich in alkali. This view has been supported by the MER Spirit detection of alkali-rich basalts (McSween & Ruff 2006), showing moderately alkali-rich basalt trachybasalts were present at Gusev crater. Also, the Adirondack type (another MER Gusev sample type), sub-alkaline and olivine-rich basalts, such as the Humphrey sample that was used in the

olivine subtraction model described above, demonstrate a complex record of planetary differentiation. The Chassignite Martian meteorites also provide further evidence of alkali-rich basalts, based on their mineralogy and their mineralogical chemistry (Nekvasil et al. 2007). As such, a connection between the Gusev basalts and the Chassignite meteors was proposed based on mineralogy and the results of studies of crystallisation trends (Filiberto et al. 2008; Nekvasil et al. 2009). Most of the 90 known Martian meteorites are sub-alkaline. However, the impact regolith breccia have an abundance of K-feldspar and contain alkali basalt clasts (Humayun et al. 2013; Santos et al. 2015) implying a parental magmatic crust to some of the clasts in the rock that was alkali-rich.

The tholeiitic affinity from the CIPW matches well with the trends on the AFM plot in Figure 3.14. Tholeiite rocks are formed from basaltic magmas by the process of crystal fractionation (Morris et al. 2016) showing first an iron enrichment due to crystallisation of Mg-rich phases such as those of olivine and clinopyroxene (Gast 1968). The magmas become saturated with Fe as the silicate increases during fractionation, which then crystallise into iron oxides (Nicholls & Ringwood 1972). This causes the residual magma to become progressively enriched with alkali as the melts evolve to become silica and alkali-rich compositions. The tholeiite fractionation process can result in a diverse range of igneous rock types including trachybasalt, trachyte and rhyolite, such as shown by the Shishaldin volcanoes in the Aleutian Islands (Spulber & Rutherford 1983; Whitaker et al. 2005; Zimmer et al. 2010; Cox et al. 1970). This olivine subtraction fractional crystallisation (shown in Figure 3.8 and 3.9) correlate with differentiation occurring. MSL recently detected tridymite, a high temperature silica polymorph (Morris et al 2016), which, even though is not diagnostic of a particular melt composition, would be expected with a more fractionated tholeiitic igneous environment at Gale.

In a terrestrial environment, the combination of alkali and tholeiitic lavas can be seen, often in Ocean Island environments (DeLong & Hoffman 1975; Floyd et al. 1991). At Gale it can be seen that the coarse grained sediments such as conglomerates and some sandstones are generally much richer in both silica and alkali and felsic in nature. The fine-grained targets including the Mudstones at Yellowknife Bay (Vaniman et al. 2014; Mangold et al. 2015) are much more mafic (Mangold et al. 2016) and closer in

composition to the Martian global average (McLennan and Tayler, 2009) suggesting that regions near Gale, which provided the source region for the coarse grained material, are more felsic whilst those further from Gale are mafic in nature.

The data from both the Mars Exploration Rovers and Mars Science Laboratory match regarding sedimentary and basalts, indicating the mantle source regions at Gale and Gusev are likely similar in composition and nature but quite different from the Shergottites. The Shergottites are usually considered to have sourced from depleted mantle melts underlying the northern lowlands and Tharsis from less than 600 million years ago (Nyquist et al. 2001; McSween et al. 2003). McSween et al. (2006) describe mantle partial melting controls leading to primitive picritic basalts (such as the Humphrey target) in Gusev Crater. The Gale rocks show a later, crustal stage of evolution.

### 3.5.1 Terrestrial and experimental analogues for Martian samples

It is generally accepted that Mars lacks the plate tectonic processes seen on Earth (Karlsson et al. 1992; Banerdt et al. 1982; Mezger et al. 2012). If this is the case then intraplate magmatism is the most relevant factor for the interpretation of the ChemCam data. On Earth, intraplate magmas are often included within large different groups of other magmas from basalt to rhyolite, alkali and tholeiitic trends (Whitaker et al. 2005). Spirit rover results from Gusev have indicated samples that bear similarity to these terrestrial basaltic rocks such as Oceanic Island Basalt (“OIB”). The Oceanic Island magma processes are connected with both alkaline and tholeiitic magmas (Wilson 2007) thus making a useful analogue to the igneous rocks encountered at Gale Crater. The main limitation on OIB as an analogue for Gale is the water content, given Gale’s anhydrous mineralogy and OIB H<sub>2</sub>O contents of 2000 – 8000 ppm (Johnson et al. 1994; Dixon and Clague 2001). On Earth terrestrial trachybasalts are found in a wide range of environments both alkaline and tholeiitic in nature. Experimental work has sought to characterise the fractionation conditions likely to have occurred to produce the Martian igneous environment. Nekvasil (2004); Nekvasil et al. (2007) and Whitaker et al. (2005)

performed tests on melt fractionation starting with hawaiite compositions which are associated with both Ocean Islands and continental hotspots.

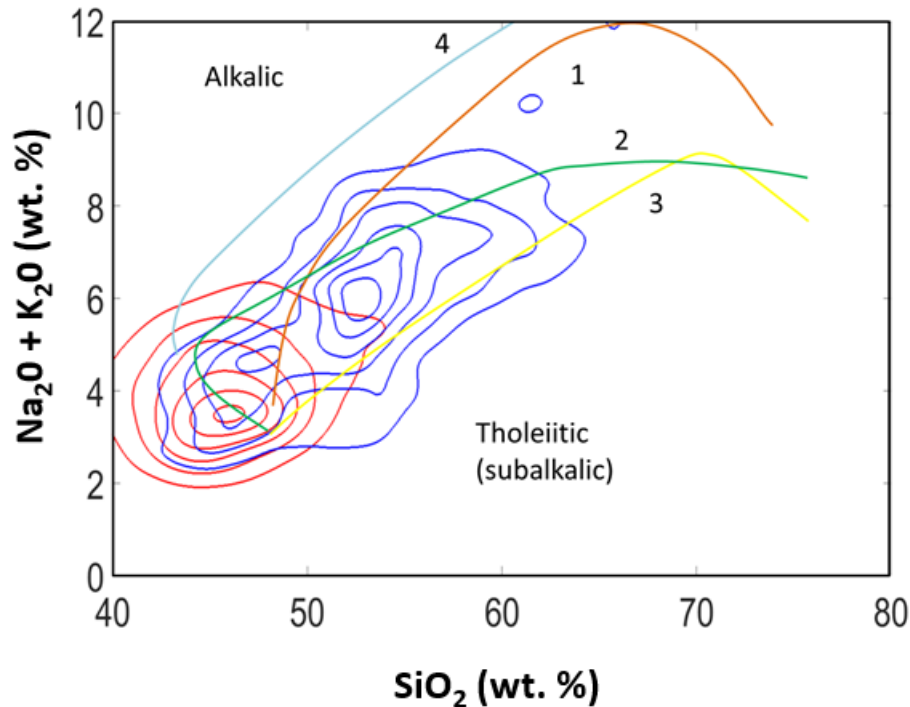


Figure 3.15 TAS Diagram showing the four major trends from (Whitaker et al. 2005) (1) The silica saturated sodic alkalic, (2) silica saturated potassic alkalic, (3) ocean island tholeiitic, and (4) silica undersaturated sodic alkalic trends (Nekvasil et al. 2007). The contours are ChemCam shots of igneous samples are shown in blue and the sedimentary samples contour plot are in red. Trend 3 corresponds most closely to the igneous trend in Gale.

These studies show four distinct major trends that compositions can follow; 1. silica-saturated, Na-rich; 2. silica-saturated K-rich; 3. ocean island tholeiitic and 4. silica undersaturated, Na-rich, as illustrated in Figure 3.15. When these trends are compared to the igneous trends within the ChemCam data, they can be used to constrain the nature of the melt source region and the conditions under which fractionation has occurred (Nekvasil et al. 2007; Whitaker et al. 2005). The igneous Gale data matches best to the Curve 3 trend of Whitaker et al. (2005), as shown in Figure 3.8 and Figure 3.9, which represents the Ocean Island tholeiitic trend. There is some similarity to the other curves but not the initial composition change. However, the igneous rocks analysed at Gale are richer in alkali than this experimental set. The Ocean Island tholeiitic trend was produced using a relatively low sub surface pressure of 4.5 kbar, with a low water environment of the order of 0.3 wt% water starting from a parental basaltic magma source. As such, it suggests that the igneous trend at Gale from basaltic to trachybasaltic is also associated

with the relatively low pressure, anhydrous environment of subalkaline tholeiitic magmas. Likewise, Nekvasil et al. (2004) showed that in shallow depth crustal conditions, the large quantity of early olivine produces a strong silica enrichment and sub alkaline, total alkali to silica ratio in the subsequent evolved basaltic rocks.

### 3.6 Conclusions

There are 3 main conclusions to draw from this work with relation to Martian geology and analogue studies.

First, the ChemCam observation campaign at Gale crater during the early parts of the MSL mission have, coupled with textural observations from MastCam images, allowed the identification of numerous igneous float rocks and conglomerate clasts distinct from the wider sedimentary environment. Some of these in turn have been identified as extrusive basalts or trachybasalts.

Second, the ChemCam chemical compositional dataset of igneous samples contains two foci composed of targets which are texturally as well as compositionally distinct. Those identified as part of the basaltic end member group have an average SiO<sub>2</sub> content between 47 and 51 wt% and Mg# = 54, whilst the trachybasalt SiO<sub>2</sub> average is higher, at around 55 wt% with its Mg# = 27. This distribution of igneous compositions is consistent with a system of crystal fractionation dominated by olivine from an initial subalkaline, Fe-rich basaltic source region similar in composition to the Adirondack class of basalts identified at Gusev Crater by the Spirit MER rover.

Finally, the melts present at Gale crater, which are associated with the basaltic to trachybasaltic compositional trend, were both silica-saturated, tholeiitic and with sub-alkaline composition. The olivine subtraction model shows that this makeup is consistent with a relatively low sub-surface formation pressure and anhydrous conditions. As such, rocks on the basalt – trachybasalt fractionation trend and feldspar-rich samples, particularly those rich in the feldspar such as andesine and labradorite, are

useful analogues for testing future missions' instrumentation. Work with Martian analogues is discussed further in Chapters 4, and 5.

## Chapter 4: MURFI field trials – Raman Spectroscopy

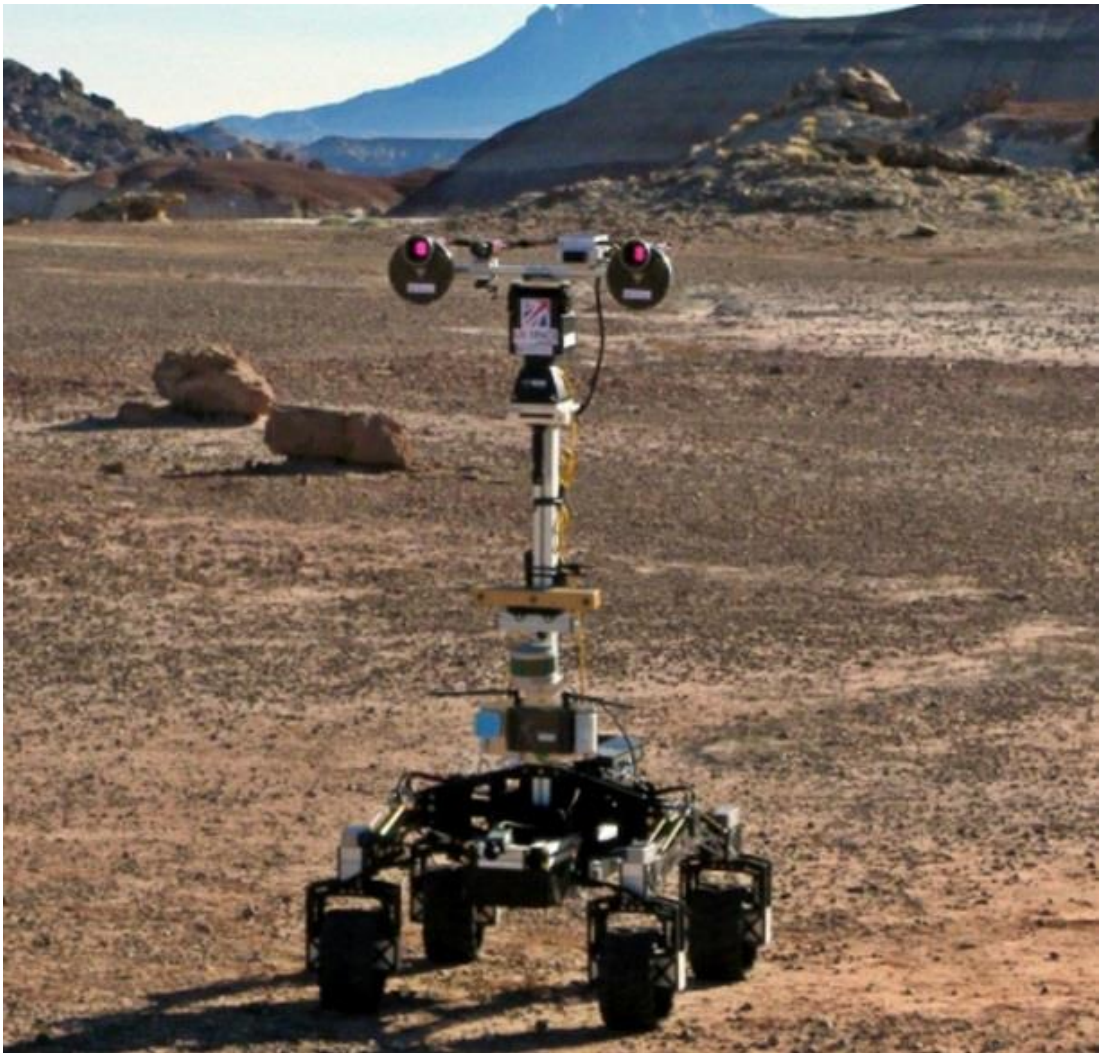


Figure 4.1 MURFI 2016 Rover Q14 Platform supplied by Oxford University Robotics Institute. (Balme et al 2017)

### 4.1 Introduction

Chapter 4 covers field work performed near Hanksville, Utah in the USA as part of the UKSA MURFI (Mars Utah Rover Field Investigation) field trials. Samples were acquired from a Mars analogue site and analysed in the field with instrumentation representative of a planetary rover mission (Edwards et al. In prep.). Samples were then further analysed at the University of Liege with microscope Raman spectroscopy and XRD.

## 4.2 Importance of analogue studies

Since planetary exploration missions to targets such as Mars are infrequent, there are very few opportunities to test newly developed analytical instruments in a representative environment. This can make testing new techniques and instrumentation challenging. As of 2017, there has not yet been a sample return mission from the Martian surface, although NASA's Mars 2020 rover will cache samples with the expectation that they will be eventually recovered by a future mission. Geological samples from Mars are consequently restricted to the Martian meteorites of which there are limited numbers. Consequently, it is necessary to locate similar terrestrial samples on Earth that, have undergone equivalent processes to those on Mars, are mineralogically and compositionally similar, and which come from a Martian-like environment. These Martian analogue sites, such as the Rio Tinto in Spain (Fleischer et al. 2008; Cockell et al. 2017), the Atacama desert (Navarro-González et al. 2003; Wei et al. 2015), and parts of the desert areas in the United States, including the Utah desert discussed below (Clarke & Stoker 2011), can provide a large selection of representative samples which can be used for the testing and optimisation of instruments before deployment on missions to Mars.

## 4.3 MURFI 2016

MURFI was the first UK Space Agency rover field trial, performed in preparation for the 2020 launch of the European Space Agency's ExoMars rover (Balme et al. 2017). The trials took place during the 3 weeks from October 22nd to November 13<sup>th</sup>, 2016 (followed by a week of joint operations with the Canadian Space Agency). The trials were performed in the southern Utah desert near to the town of Hanksville, UT. The mission operations team was based at the Mission Operations Centre at the Harwell Campus (MOC) in the UK.

#### 4.3.1 Mission Goals

The main science goal for ExoMars is “to search for signs of past and present life on Mars” (Vago et al. 2015). As such, the MURFI mission goals were chosen to be representative; i.e. “to locate suitable areas in the field site that have sedimentary geology indicative of an ancient habitable environment, then to drill into the surface to acquire a sample from those materials, and finally, to examine these samples with the analytical instruments available on-board the rover” (Balme et al. 2017).

As well as addressing the primary scientific goal, the field trial programme sought to ensure the development of rover operation skills within the UK planetary science community in preparation for ExoMars (by simulating the conditions necessary for planning an analogous mission).

#### 4.3.2 Rover platform

The rover platform, that was deployed to the Utah field site (see Figure 4.1), was a four wheeled Q14 Platform supplied by Oxford University Robotics Institute. This MURFI rover was equipped with:

- The Aberystwyth University PanCam Emulator (AUPE, (J. K. Harris et al. 2015)) to recreate the functionality of ExoMars’ PanCam instrument (Griffiths et al. 2006), as well as the High Resolution Camera (HRC) emulator,
- A CLUPI (The Close-UP Imager) emulator, a Digital SLR camera with macro lens, mounted to simulate its location on the ExoMars rover (Josset et al. 2012) with an equivalent range of motion and field of view,
- An ASD Inc. FieldSpec4 field reflectance spectrometer to simulate the use of the Infrared Spectrometer for Mars Instrument (ISEM, (Korablev et al. 2014)), and
- A Raman Spectrometer, the use of which on the final drill-samples acquired would signify “mission success”. The Raman instrument is similar to RLS in the ExoMars rover analytical laboratory drawer (Rull et al. 2011).

In addition, to replicate the ExoMars rover's ability to drill to depths of up to 2m and to obtain a core sample, the field team were equipped with a hand-held core drill and other necessary tools to extract an analogue of the ExoMars drill core from depths of ~1m.

The main ExoMars instruments that are not represented on the MURFI rover are: the Ground Penetrating RADAR, WISDOM (Dorizon et al. 2013), and the other instruments within the Analytical Laboratory Drawer, which include MOMA and Micro-Omega (IR spectroscopy) that will be used to analyse the drill samples (Barnes et al. 2006). Future UK rover trials will seek to replicate these instrument capabilities.

#### 4.3.3 Landing site

The field site was selected due to its Mars-like geology and collaborations with the CSA who have used the site for numerous previous field trials. The location was used by the CSA in 2015 for Mars Rover trials (E. A. Pilles et al. 2017), and in 2016 several different teams used the site, each with their own separate designated working areas (E A Pilles et al. 2017). The area is also host to the Mars Desert Research station, a facility designed for the testing of techniques necessary for a future Mars mission.

##### 4.3.3.1 Landing site geology

The Hanksville field trial location is part of the Canyonlands of the 337000 km<sup>2</sup> Colorado Plateau. The plateau is geologically stable and is composed of a crustal block of unreformed rocks with neighbouring deformed mountainous regions: Basin and Range Province, Uintas Mountains and the Rocky Mountains. South West of the plateau, the boundary is the Mogollen highlands, parting the plateau from the basin and ranges (Banham 2017). Deposits on the plateau, range in age from Precambrian to recent depositions. The very oldest samples are exposed in the Grand Canyon and Uintas Mountains.

The specific study area at Hanksville exhibits stratigraphy from Jurassic and Cretaceous era clastic sediments. It is part of the Morrison Formation which is divided into Tidwell – lakes and mud flats, Salt wash – coarse alluvial sediments deposited by river systems, and Brushy Basin Member – fine grained alluvial sediments. The Brushy Basin Member contains the study area. In this region, the member is a 100 m thick slope forming unit, characterised by weathered, interbedded red-brown and white soils layering in slopes up to 30° (shown in Figure 4.2). The colour and textural changes are variable over the area, with the red-brown soils covering roughly two thirds of the area. This colouration is representative of the geology of the area, rock weathering and accumulation close to the samples initial source region. The brown units are usually silt and finely grained sandstones which are well cemented and often have climbing ripple strata and horizontal lamination. In contrast, the white soils are well sorted, sub rounded, medium grained sandstones which are much less cemented than the red-brown material. These red-brown, fine grained parts of the succession are likely overbank deposits and wetlands where sediments form over a long period of time (Banham 2017). The white coloured textures of the formation are likely sediment depositions in channels or crevasses in which the sediment is quickly deposited from a waning flow during a flooding period (Edwards et al. In Prep.). The wider landing site can be seen in Figure 4.3.



Figure 4.2 Red brown / Light layering Image taken during MURFI mission

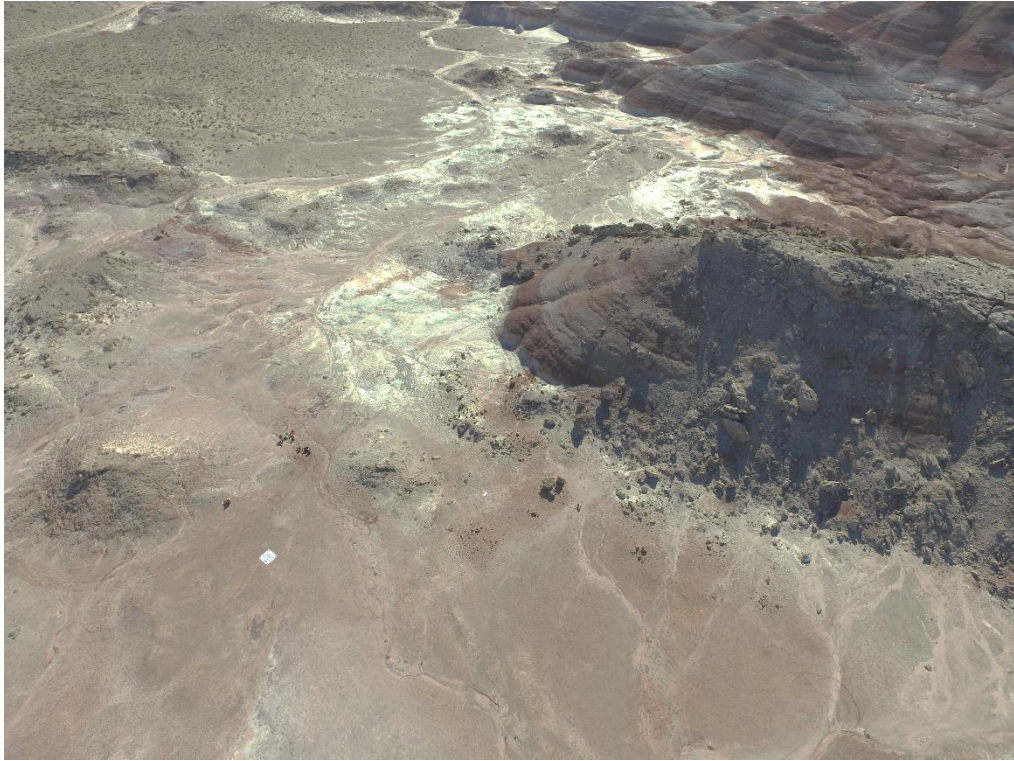


Figure 4.3 UAV image Mission operations area, Brown-red and white soil layers are visible, Image Credit Steve Kay

#### 4.3.3.2 Landing site as a Martian Analogue

Brushy Basin Member is part of a larger alluvial fan system, which drained off to the north east on the Mogollon Highlands (Owen et al. 2015); these alluvial fan features are seen on Mars (Tanaka et al. 1987). The area contains numerous inverted channels (Clarke & Stoker 2011) which have been identified in numerous satellite images of the Martian surface (Pain et al. 2007). Sulphate soils bedded with evaporates are present in the area around the landing site (Clarke & Stoker 2011) with similarity to the sulphates at Marwth Vallis (Wray et al. 2010).

#### 4.3.4 Mission operation

The first week of the mission was dedicated to initial setup of the landing site instrumentation, carrying the rover to its starting position and performing the initial “post landing” panoramic images and the mission operations centre at Harwell. Work included mapping of the rover landing site from remote sensing data. This was then followed by the main ExoMars simulation phase of the mission, which aimed to replicate the functionality of the rover and took place over the next 9 “sols”. The mission began with the placement of the rover platform at the landing site and the first of the PanCam panoramas was transmitted back to the UK via an FTP site. The team at Harwell then used ~3 hours in the UK morning to plan the day’s activities and send a tactical plan to the field team to execute the following morning (8 am Utah time). The plan incorporated specific rover traversals, camera operation schedules and instrument deployment plans thereby fully emulating the processes adopted in a typical mission.

In the earliest stage of the mission (i.e. up to around sol 5), characterisation of the local area and planning of the rover’s route and destination for further investigation were performed. The subsequent 3 sols were used to locate a suitable target site for the simulated drilling process. On sol 8 the drilling command was received from Harwell, with CLUPI and Raman analysis of the drill core samples performed on sol 9, which was the end of the main stage of the field trial. This campaign was followed by a week of joint operations with the Canadian Space Agency, as described below in Section 4.3.5.

##### 4.3.4.1 Raman operating modes

In order to simulate the ExoMars mission, the Raman Spectrometer was deployed on samples retrieved by the drill, following the selection of a suitable site at the end of the MURFI mission. A total of three drill pellets were retrieved from the core. Each of these pellets were analysed with the spectrometer, with a series of 10 spectra each (with an integration time of 1 second) obtained from 3 separate analysis points, resulting in 90 spectra in total from the drill cores. The acquisition of numerous frames for each sample observation point aids peak identification, through SNR improvement.

Alongside the drill cores, 50 analogue samples were selected from the surrounding area (i.e. near the rover trials mission site location). These samples were either analysed in-situ or taken back to the camp for subsequent characterisation. At least 10 spectra were obtained from each textural feature apparent on the surface of a sample in order to determine their composition. Further work was undertaken on some of the samples using another portable benchtop 532nm spectrometer in controlled conditions.

#### 4.3.5 CSA joint operations and AEGIS Tests

The joint rover operations campaign involved working with the Canadian Space Agency and Western University (aiming to emulate the capabilities of NASA's MARS2020 mission). The joint field trials did not include a rover platform, rather cameras were physically positioned to simulate the various on-board camera systems. From the images obtained with these cameras, targets were selected for XRF analysis (simulating the use of the PIXL instrument), LIBS (ChemCam) analysis, and both 785 nm and 532 nm Raman (SuperCam and SHERLOC) analysis. The targets were selected using the AEGIS (Automated Exploration for Gathering Increased Science) (Francis et al. 2015) software, which was designed for use on the ChemCam instrument to automatically select targets of different material types. This approach eliminated the delays normally associated with data transmission, allowing for additional data to be obtained during the restricted timeslot. The selected targets were then sampled with the SuperCam emulation instruments (Francis, Gaines, et al. 2017). The AEGIS software has since been deployed on Curiosity to select ChemCam targets (Francis, Estlin, et al. 2017).

Without the need for rover operations, it was possible to accelerate the data acquisition process, performing 3 sols of work per day. This enabled the simulation of a much longer mission than the length of the field trial would have fundamentally permitted (E A Pilles et al. 2017).

## 4.4 Analogue Samples

Over 50 separate samples were acquired from the MURFI landing site area and a sub selection were returned to the laboratory for further study.



Figure 4.4 Images of key samples, Scale bars indicate 1cm on each of the sample. A – 4cr, B – Barclay, C – Moon, D – Lyra, E – Cross, F – Watney, G – Stamford, H – Galliger, I – Justineau, J – Melanie, K – Milkybar

Eleven of the samples (shown in Figure 4.4), were retrieved from the field trial rover landing site, as well as the area immediately surrounding it, with sample J - Melanie selected further from the field site but still within the Utah desert area. The set of samples were selected to reflect the various diverse minerals amongst the geological materials rather than the specific local quantities of the materials.

#### 4.4.1 Sample Preparation

Raman spectroscopy does not typically require sample preparation in order to achieve high SNR spectra. As such, the field samples were either measured directly as they lay, or returned to the camp base for detailed investigation. Once the samples were returned to the laboratory, measurements were obtained with both the 785 nm Raman spectrometer and a 532 nm Raman spectrometer. The samples were then crushed



*Figure 4.5 The mortar and pestle used for crushing the samples*

with a mortar and pestle (Figure 4.5) to simulate the form that samples would be delivered to the analytical laboratory in, on the ExoMars rover. These samples were then re-measured following the crushing/powdering process in order to identify variations in the spectra obtained. For the XRD measurements, finer grained powdering was required; to fulfil this, a tungsten mortar and pestle was used to crush the harder silicate targets.

#### 4.4.2 Instrumentation

One spectrometer was used for fieldwork with another representative instrument used for further study at the University of Leicester. The samples were then well characterised at the University of Liege with two microscope Raman instruments and an X-ray diffractometer.

#### 4.4.2.1 Rockhound 785 nm

The Rockhound Deltanu spectrometer (Figure 4.6) (used in the field) is a 785 nm Raman handheld instrument designed for geological investigations. The instrument requires contact, or near contact, with a target sample. The laser is a 120mW, 785 nm IR laser with a spot size of around 50  $\mu\text{m}$ . The spectra obtained have a spectral range of 200 – 2000  $\text{cm}^{-1}$ , which covers the main peaks for most geological targets and a resolution of 8  $\text{cm}^{-1}$ .

The handheld spectrometer can operate from a battery for up to 5 hours and was taken into the field for the initial measurements as part of the MURFI mission. The compact nature of this instrument (and the associated compromises in design and performance) emulate the compact design adopted for the ExoMars RLS instrument, making it a useful and appropriate instrument analogue.



Figure 4.6 Rockhound Raman spectrometer

#### 4.4.2.2 Advantage 532 nm

The Advantage spectrometer (Figure 4.7) is a benchtop laboratory based instrument which uses a green (532 nm) laser. The instrument was used to provide additional information to extend the dataset collected with the 785 nm Rockhound instrument. Unlike the Rockhound, the laser is a (frequency doubled, Nd:YAG) 100mW, 532 nm laser. The spectrometer has a resolution of  $10\text{ cm}^{-1}$  and a spectral range spanning  $200 - 3400\text{ cm}^{-1}$ . Since that spectrometer utilises a green laser, the spectra obtained are reasonably representative of those that would be acquired by the ExoMars RLS instrument. This spectrometer also has a  $50\text{ }\mu\text{m}$  laser spot size.



Figure 4.7 Advantage 532 nm spectrometer

#### 4.4.2.3 Raman Microscopes

Laboratory Raman spectra were acquired with two Horiba Jobin-Yvon Labram 300 (Figure 4.8), confocal Raman spectrometers equipped with an Olympus LMPlanFL 50X (N.A. 0.50) microscope with a Peltier, air-cooled CCD detector operating at  $-69^{\circ}\text{C}$  (an Andor iDus 1024 X 128 BR-DD). Two spectrometers were used with different lasers: a Coherent doubled Nd-YAG DPSS laser (532 nm) and a Torsana Starbright 785 XM laser (785 nm). Data acquired with the 532 nm laser exhibit a spectral range of  $100 - 3300\text{ cm}^{-1}$  and data acquired with the 785 nm laser exhibit a spectral range of  $150 - 2000\text{ cm}^{-1}$ . It is possible to obtain spectra with the 785 nm spectrometer for spectral regions above  $2000\text{ cm}^{-1}$ . However, most of the relevant bands for mineralogy are in this sub  $2000\text{ cm}^{-1}$  region. The main features of interest in the higher spectral range are the hydration bands, which are not visible with the 785 instrument (L. V. Harris, Hutchinson, et al. 2015). The spot size for both instruments was approximately  $4\text{ }\mu\text{m}$  in diameter. A stage with high spatial resolution allowed for fine manipulation of the samples in order to select specific materials for study.

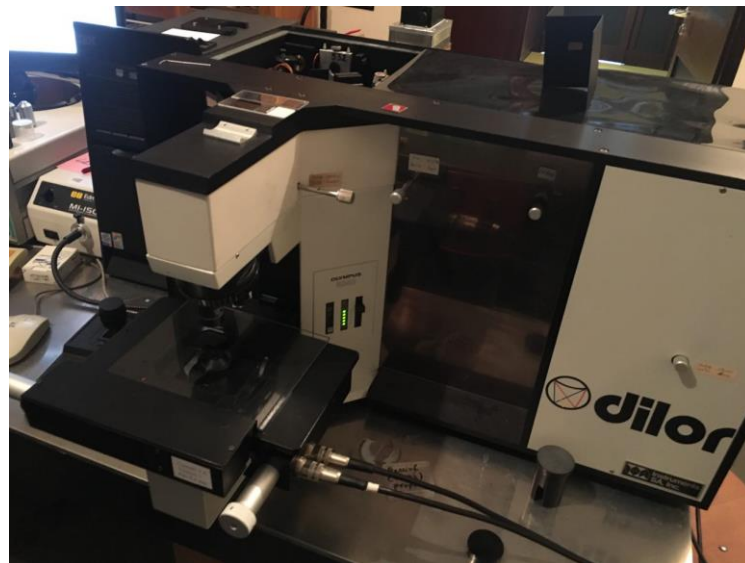


Figure 4.8 The 532 nm Labram Raman microscope used at the University of Liege

#### 4.4.2.4 XRD

XRD diffractograms were obtained using a parallel beam diffractometer (Bruker D8 Twin-Twin, with Cu K- $\alpha$  radiation). The diffractograms were measured in the 2 theta range between 5° and 60° with a step size of 0.04° and a step time of 16 seconds per step. The qualitative analysis of the crystalline phases in the diffractograms was performed with the DIFFRAC.EVA software (Bruker 2017) search and match tool, using the PDF4+ database from the International Centre for Diffraction Data.

### 4.5 Results

All of the samples were first analysed with the Rockhound, 785 nm spectrometer in the field and later in the laboratory with both the Rockhound spectrometer and an Advantage, 532 nm spectrometer. Following these measurements, a sub selection of samples selected for their geological diversity and relevance to possible ExoMars landing sites were selected for comprehensive analysis, with both the microscope based Raman spectrometers and the XRD facility.

#### 4.5.1 Silicate field studies

The large Raman band at 465  $\text{cm}^{-1}$ , which is apparent in both the 785 nm and 532 nm spectra, indicates the presence of quartz (Kobayashi et al. 2008) and was common to many of the investigated samples (see example spectra in Figure 4.9).

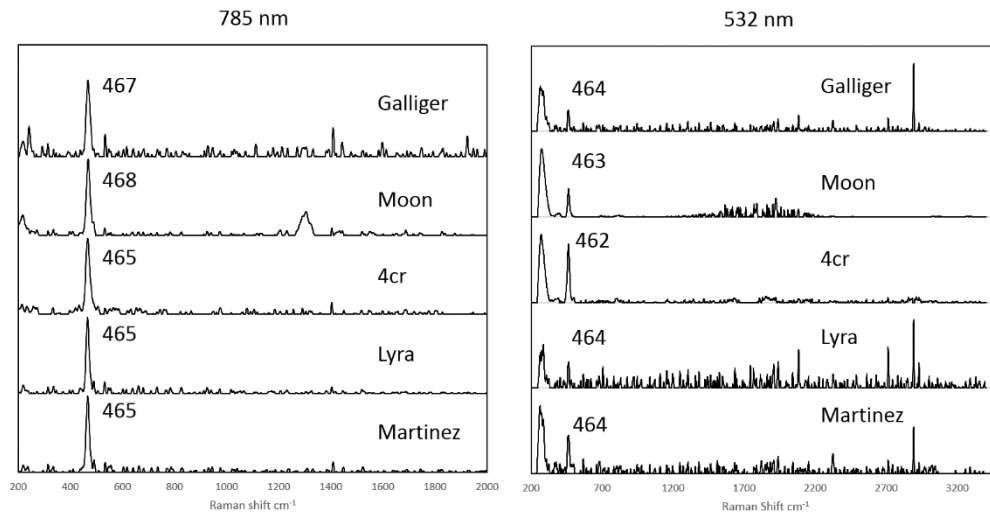


Figure 4.9 785 nm and 532 nm Raman spectra with Main Raman Bands at 465  $\text{cm}^{-1}$ . Spectra have had background and fluorescence subtraction with all negative values set to 0. The Gallagher sample only refers the red outer surface as shown in Figure 4.4 H.

The samples in this subset were similar in textural nature to one another although differing in colour. In general they were found to be smoother and harder than most of the other samples that were obtained that didn't have the main peak at 465  $\text{cm}^{-1}$ . The only exception of the Moon sample which exhibited a granulated appearance and was poorly cemented.

The Hanksville field site is a desert and as such is expected to incorporate many samples of silicates. All of the 785 nm spectra are within 4  $\text{cm}^{-1}$  of this main band location, with the 532 nm laser producing bands that are within 2  $\text{cm}^{-1}$ .

#### 4.5.2 Sulphate field studies

Some of the other samples shown below in Figure 4.10 exhibited a major band close to 1000  $\text{cm}^{-1}$  in their Raman spectra. This band is typically associated with sulphates.

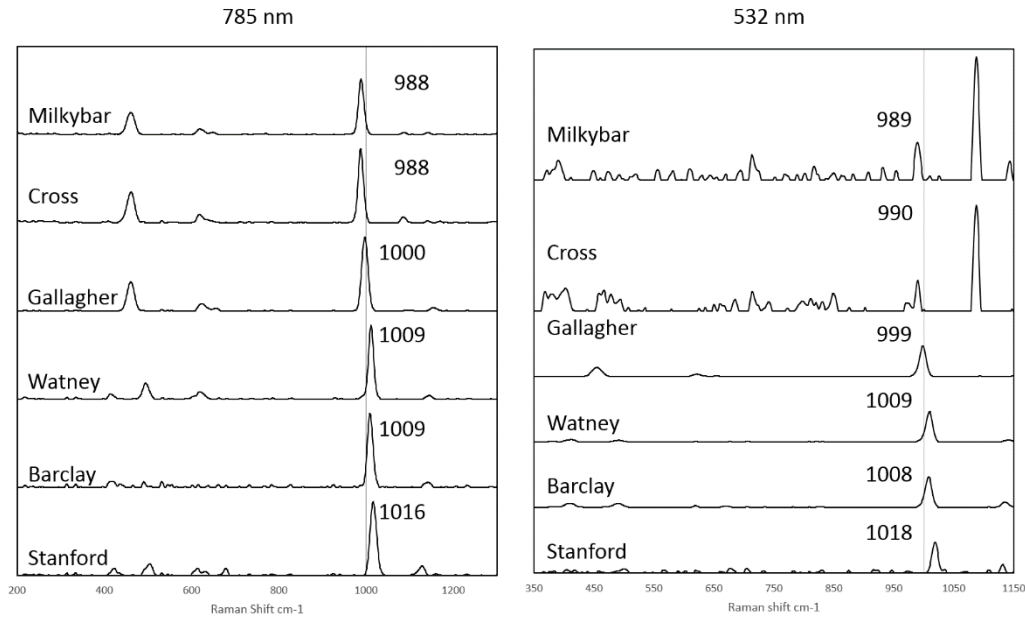


Figure 4.10 532 nm and 785 nm Spectra of possible Sulphates. Spectra have background and fluorescence subtraction with all negative values set to 0. The Cross sample refers only to the pink coloured parts whilst Gallagher only the white.

This subset of samples exhibits much more diverse textural, colour and hardness features within the groupings than those examined in Figure 4.9. The Watney and Barclay samples are both translucent and brittle (snapping easily), but the vein on Gallagher (see Figure 4.4 H) is smooth white. The Stanford sample incorporates a white vein within a dark substrate and the Cross and Milkybar samples consist of a pink coloured material within a mineralogically distinct cream coloured material.

The band close to  $1000\text{ cm}^{-1}$  is associated with sulphates. The exact Raman shift can be affected by multiple different factors including the particular compound of sulphate or the hydration state of the sample. Consequently, care must be taken to avoid misidentifying the spectra (see, for example, Wang et al. 2006). Some of the spectral bands obtained are associated with calcium sulphates, such as gypsum (i.e. band at  $1008\text{ cm}^{-1}$ ) or anhydrite (i.e. band located at  $1016\text{ cm}^{-1}$ ), (Sarma et al. 1998; L. V. Harris, McHugh, et al. 2015). This identification can be corroborated by the minor bands which are apparent at  $1140\text{ cm}^{-1}$ ,  $619\text{ cm}^{-1}$  and  $495\text{ cm}^{-1}$ .

The Watney sample has been identified as being composed of Gypsum, both from visual identification (due to its translucent brittle nature) and the major and minor bands

which match those of gypsum. The same is true for the larger sample (Barclay). The minor bands are clear in both wavelength datasets. The Stanford sample likewise matches closely with the anhydrous state of calcium sulphate (anhydrite) with the main band located at  $1018\text{ cm}^{-1}$  (Sarma et al. 1998).

Of the other sulphate samples, the Milkybar, Cross and Gallagher samples are more complex to identify. Since there is a certain amount of variation between the band locations in the 785 nm and 532 nm (of the order of 1 or 2 wavenumbers), it is desirable to obtain known mineralogical samples for comparison as each instrument will have a slightly different calibration.

The main bands observed for the red portion of the Milkybar and Cross samples are located at  $990\text{ cm}^{-1}$  (in 785 nm) and  $988\text{ cm}^{-1}$  (in 532 nm). The Milkybar sample shows the clearest minor bands at  $1142\text{ cm}^{-1}$ ,  $648\text{ cm}^{-1}$ ,  $618\text{ cm}^{-1}$  and  $460\text{ cm}^{-1}$ . This corresponds with Barite which exhibits bands at  $1145\text{ cm}^{-1}$ ,  $987\text{ cm}^{-1}$ ,  $647\text{ cm}^{-1}$ ,  $630\text{ cm}^{-1}$ ,  $616\text{ cm}^{-1}$ ,  $460\text{ cm}^{-1}$  and  $452\text{ cm}^{-1}$  see RRUFF database (Lafuente et al. 2015). Whilst some of these bands are a few wavenumbers different, this is likely to arise from calibration differences between different instruments (Lewis & Edwards 2001).

The white vein that is apparent on the Gallagher sample is also a sulphate and exhibits a band at  $1000\text{ cm}^{-1}$ . The white powdery substance also exhibits minor bands at  $1156\text{ cm}^{-1}$ ,  $653\text{ cm}^{-1}$ ,  $622\text{ cm}^{-1}$  and  $455\text{ cm}^{-1}$ . It is likely that the material is the strontium sulphate, celestine which produces bands at  $1158\text{ cm}^{-1}$ ,  $1000\text{ cm}^{-1}$ ,  $656\text{ cm}^{-1}$ ,  $638\text{ cm}^{-1}$ ,  $620\text{ cm}^{-1}$ ,  $460\text{ cm}^{-1}$  and  $453\text{ cm}^{-1}$  (Kloprogge et al. 2001).

#### 4.5.3 Feldspar field studies

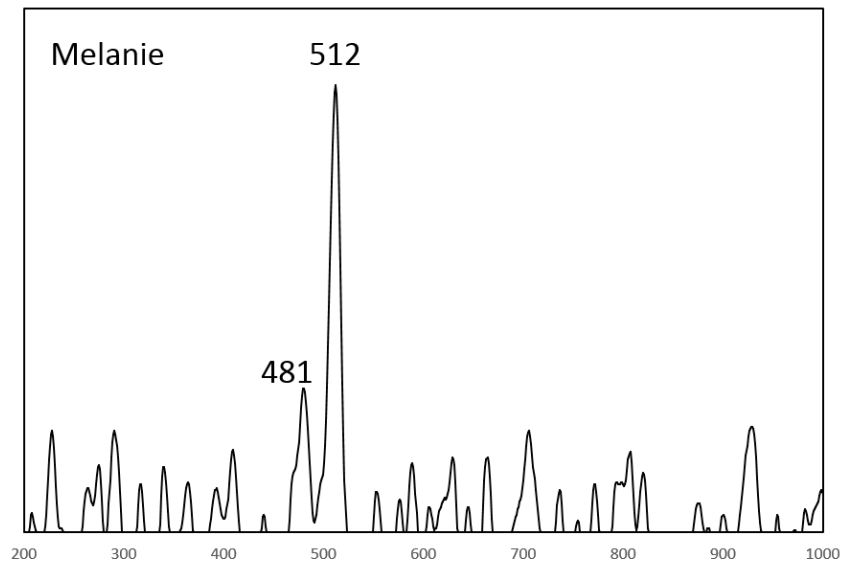


Figure 4.11 785 nm spectra of Melanie sample white crystal, background subtraction has taken place

The Melanie sample (see Figure 4.4 J) was acquired from a different, but nearby location to the field site area. It incorporates visible crystals that produce Raman spectra with clear bands at 481  $\text{cm}^{-1}$  (major) and 512  $\text{cm}^{-1}$  (minor). Feldspars typically exhibit two or three major bands between 450 and 515  $\text{cm}^{-1}$ , with the largest closer to 515  $\text{cm}^{-1}$  (Freeman et al. 2008). Without additional sub bands, it is not possible to specify which feldspar has produced the Raman bands in the spectra (it should be noted, that given the spot size, the spectra could result from multiple types of feldspar).

#### 4.5.4 Carbonate field studies

Another sub-group of samples (Figure 4.4 E and K), which includes those obtained from the MURFI drill cores, exhibit a large clear Raman band at 1086  $\text{cm}^{-1}$  (Figure 4.12), with some of these samples also showing minor bands at 712  $\text{cm}^{-1}$  and 281  $\text{cm}^{-1}$ . These bands are visible in the Cross and Milkybar samples as well as drill cores 2 and 3. The Drill core sample set also exhibit bands at around 465  $\text{cm}^{-1}$  (with slight variations in peak location observed between the samples).

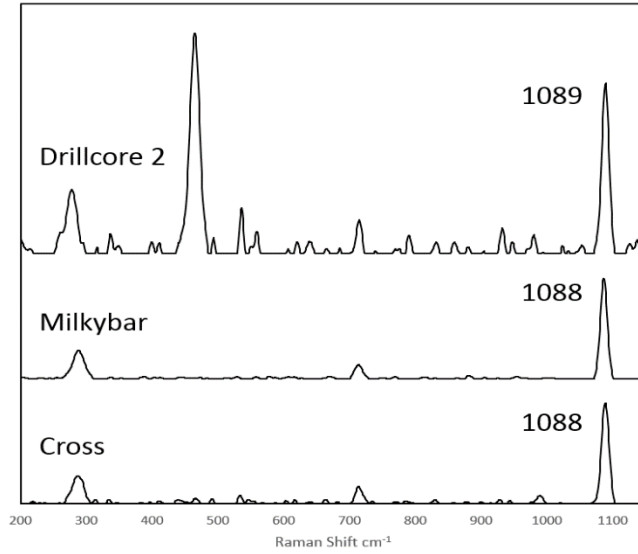


Figure 4.12 785 nm samples of possible Calcite. Spectra have background and fluorescence subtraction with all negative values set to 0. Cross and Milkybar refer only to the white parts are included. Milkybar in a similar class of sample to Cross

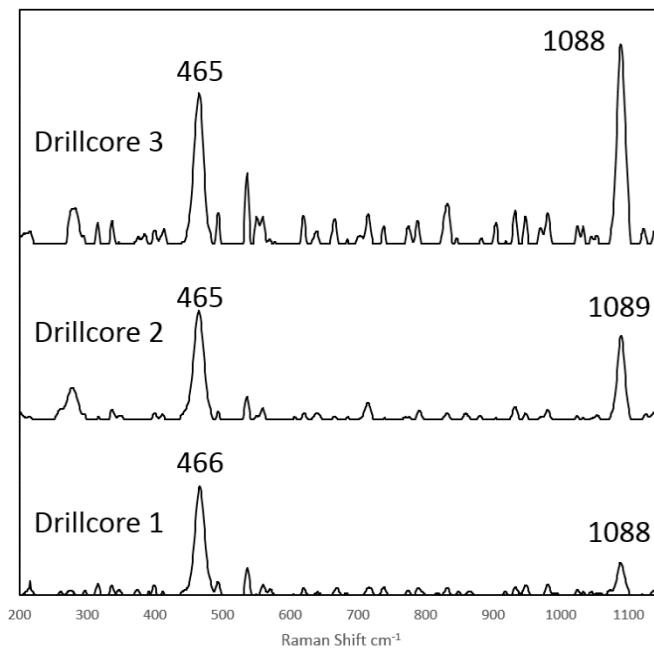


Figure 4.13 MURFI Drill core samples with multiple major peaks. Spectra have background and fluorescence subtraction with all negative values set to 0.

Two of the forms of calcium carbonate, calcite and aragonite, have a main Raman band at  $\sim 1086 \text{ cm}^{-1}$ . To distinguish between these two materials, the minor Raman bands also

need to be identified. Those for calcite are at  $711\text{ cm}^{-1}$  and  $281\text{ cm}^{-1}$ , while those for Aragonite are at  $702\text{ cm}^{-1}$  and  $209\text{ cm}^{-1}$  (Gillet et al. 1993). From the spectra shown in Figure 4.11, it is clear that the samples exhibit minor Raman bands at  $714\text{ cm}^{-1}$  and  $287\text{ cm}^{-1}$  indicating the presence of calcite rather than aragonite (Edwards et al. 2005). The slight wavenumber differences between the positions of the major bands within the spectra obtained with the two different spectrometers are expected to be associated with slight differences in the calibration of the two spectrometers.

During the MURFI mission, the operations team could only deploy the Raman instrument on drill core samples (in order to simulate the ExoMars activities). All samples show clear quartz bands and 2 of the 3 samples measured also showed strong calcite bands with minor bands present at  $715\text{ cm}^{-1}$  and  $279\text{ cm}^{-1}$ . Some of the drill cores, particularly drill core 3, exhibit high levels of noise, which could be due to many different factors, including the challenging sampling conditions in the field site (leading to non-constant light levels between the dark frame and the spectral acquisition). The feature visible at around  $1400\text{ cm}^{-1}$  (see Figure 4.13) is a hot pixel in the  $785\text{ nm}$  spectrometer's detector. These non-Raman features and other challenges for spectral identification are discussed in further detail below in Section 4.6.3.

#### 4.5.5 Raman Microscope and XRD sample mineralogical identification

The following samples were chosen for further analysis in order to represent the specific mineralogical diversity of the analogue environment. In particular, a selection of sulphates were chosen as they represent an interesting identification challenge (as the main peak is often very close to  $1000\text{ cm}^{-1}$ ) hence distinguishing between the close spectral locations a useful test for the RLS data. Sulphates are thought to be present at Mawrth Vallis, one of two selected landing site candidates for ExoMars (Poulet et al. 2014) and have been detected by MSL at Gale Crater, so are particularly relevant to future exploration plans (Rampe et al. 2017; Achilles et al. 2017; Rapin et al. 2016). The Justineau sample was selected for its heterogeneity, the presence of multiple different minerals including quartz, hematite and sulphates make it a challenging sample for Raman spectroscopy. The Melanie sample shows visible evidence of feldspar. As highlighted in Chapter 3, felsic minerals have been a common finding at the Gale Crater

landing site. The Moon sample was selected as it provided a clear example of the ubiquitous quartz which made up much of the landing site area.

#### 4.5.5.1 *Cross and Milkybar*

The Cross and Milkybar samples are both creamy white with a pink/red material within the white. Figure 4.14 shows that the Milkybar sample is predominantly the white material whereas the Cross sample is evenly composed of the two. Both samples were sourced from locations near to the MURFI landing site area. The samples are both thin (of the order of a few mm) and brittle, with the Cross sample slightly larger than the Milkybar sample.



Figure 4.14 Samples Milkybar (Left) and Cross (Right) scale bar indicates 1 cm

The two types of material exhibit distinct Raman spectra. However, both samples appear to be from a similar source. The data in this chapter taken with the handheld and 532nm lab instruments have a spot size of 50  $\mu\text{m}$ , which generally overlaps both the red and white areas to a certain extent (as shown in Figure 4.14). In addition, the samples could

not be as finely positioned with the handheld instrument, complicating the analysis of a single particular material. However, the microscope based Raman spectrometer was able to distinguish individual grains, producing very clear spectra of both distinct types of material. Microscope analyses with the 785nm laser indicated the presence of thin quartz grains. This analysis confirmed the white area to be calcite and the red, a sulphate material, with characteristic bands close to  $1000\text{cm}^{-1}$ . In Section 4.5.2 this sulphate is identified as barite.

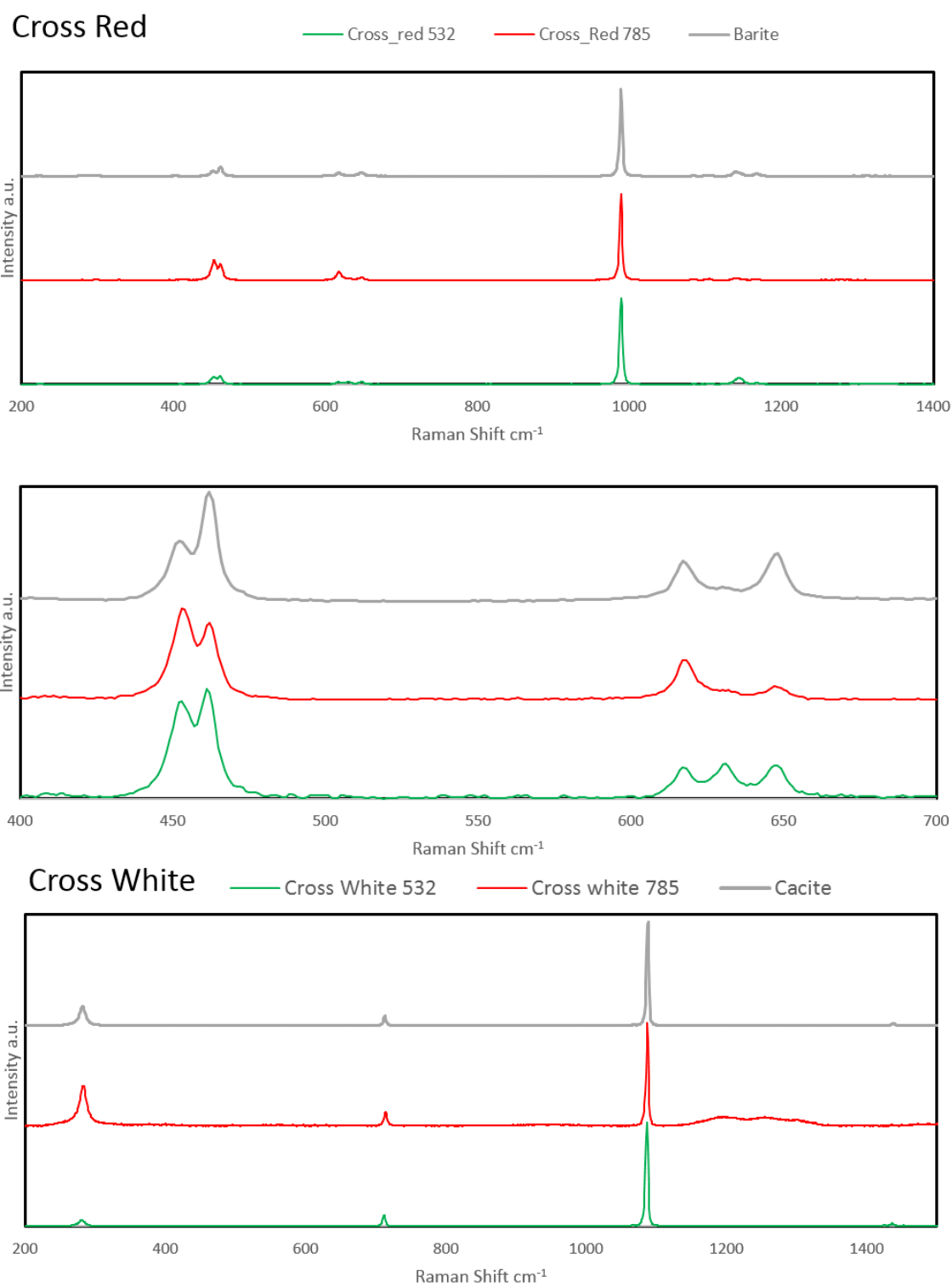


Figure 4.15 Spectra of both materials in the Cross samples. 785nm, 532nm and Barite and Calcite reference samples from the University of Liege are shown. Spectra are background subtracted

The Table 4.1 below shows the Raman band locations from Figure 4.15 for the two materials within the cross sample, alongside reference samples of barite and calcite for comparison. Reference samples were sourced from Department of Chemistry at University of Liege (Malherbe 2017)].

Cross_Red 532nm (cm <sup>-1</sup> )	Cross_Red 785nm (cm <sup>-1</sup> )	Barite (cm <sup>-1</sup> )	Cross_White 532 (cm <sup>-1</sup> )	Cross_White 785 (cm <sup>-1</sup> )	Calcite (cm <sup>-1</sup> )
-	-	-	155	157	156
-	-	-	281	282	282
453	453	452	-	-	-
461	462	462	-	-	-
617	618	617	-	-	-
648	647	648	-	-	-
-	-	-	712	714	713
989	989	989	-	-	-
-	-	-	1086	1087	1088
1145	1138	1140	-	-	-
1169	-	1168	-	-	-

*Table 4.1 Table showing Cross sample peak locations alongside barite and calcite reference samples*

Almost all of the bands from barite and calcite are found in the relevant Cross samples. This identification of the minerals as calcite and barite is supported by the XRD data (Figure 4.16) obtained from the powdered sample which was a homogenised mixture of both of the materials.

(Coupled TwoTheta/Theta)

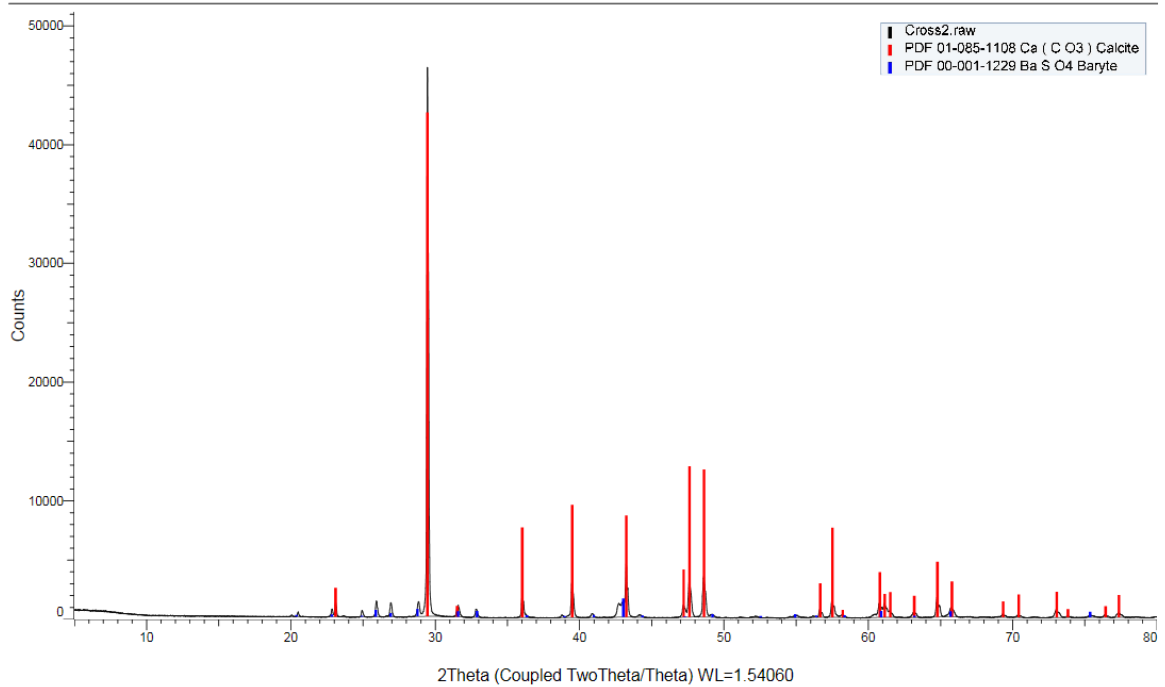


Figure 4.16 XRD diffractogram with calcite and barite peaks fitted

With the 532nm Raman instrument, there was a detection of carotene (Figure 4.17), a biomarker pigment (Edwards et al. 2014). However, since the samples were not stored in a sterile environment throughout the mission and journey back to the UK, it is not possible to confirm the biomarker's source as being the desert analogue site where the MURFI missions took place. It should be noted that these detections were relatively low in intensity, it is anticipated sensitivity levels would need to be very high if the presence of such a pigment was to be detectable on Mars.

### Cross Carotene

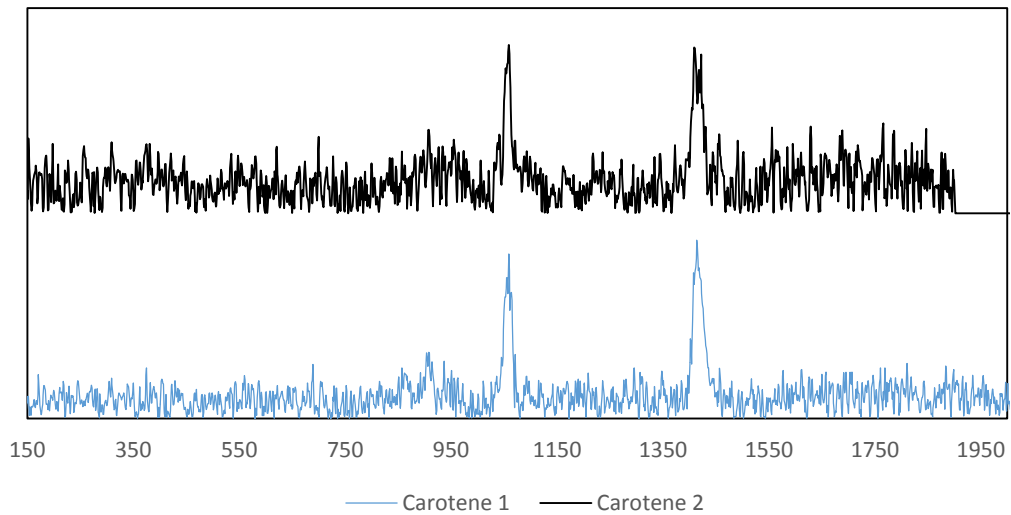


Figure 4.17 Carotene spectra detected on the surface on the Cross sample. Background continuum has been subtracted

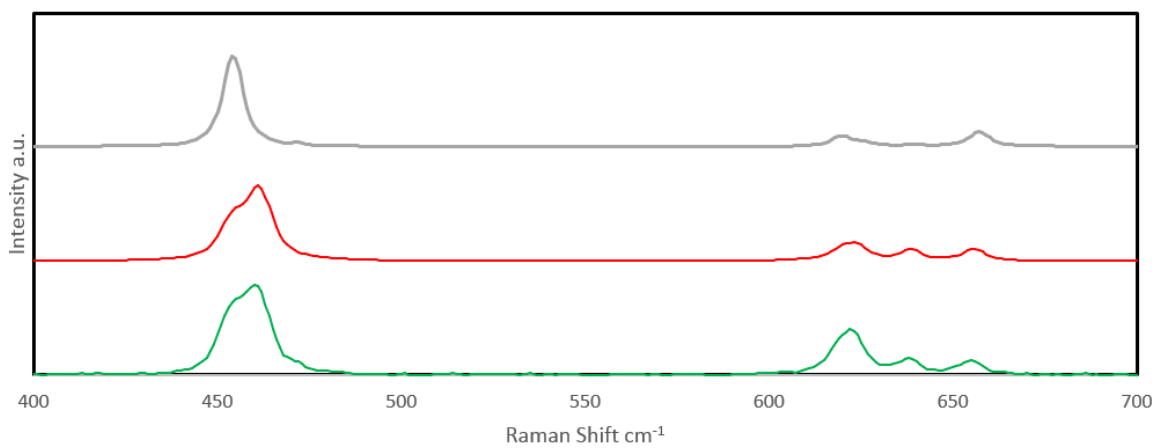
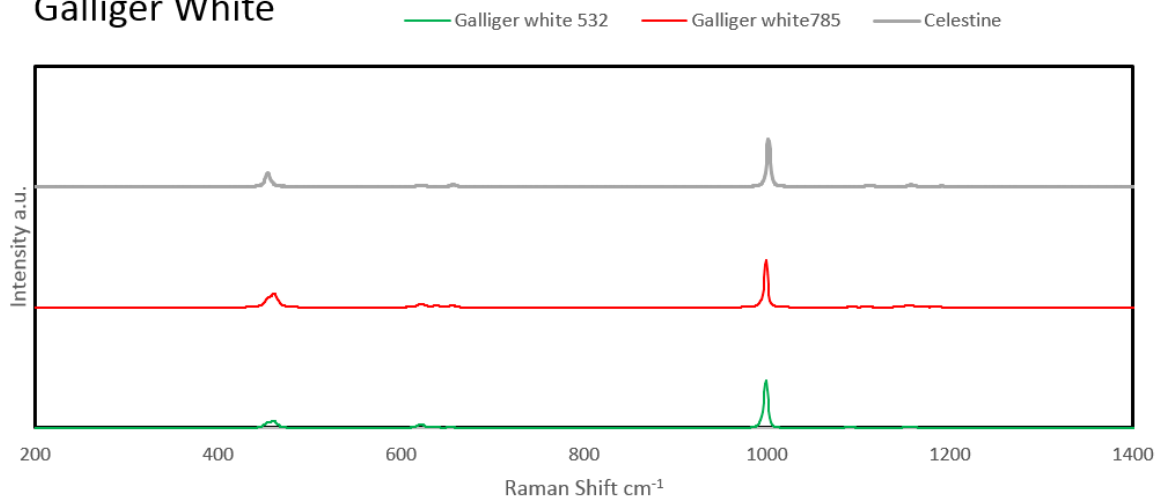
#### 4.5.5.2 Galliger

The Galliger (Figure 4.18) sample is a rock with Red materials embedded in its outer surface and a clear white vein visible through the middle of one side of the sample which exhibits a sulphate spectra. The bulk of the sample is composed of red, hard silicate grains with the vein composed of a white powdery material. In Sections 4.5.1 and 4.5.2 these were identified as quartz and celestine respectively.



Figure 4.18 Galliger sample with two clear different types of material, scale bar represents 1 cm

## Galliger White



## Galliger Red

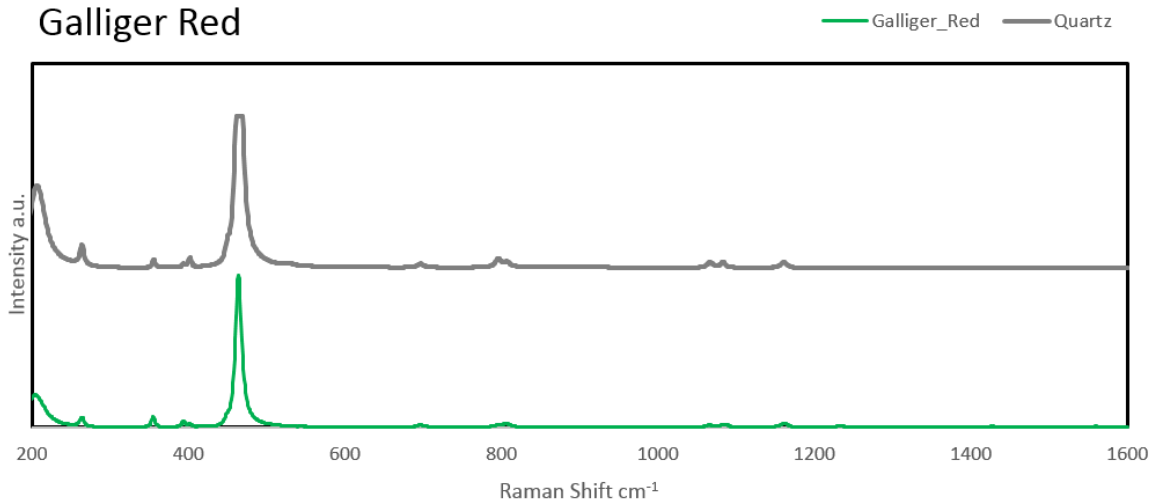


Figure 4.19 Galliger Raman spectra showing comparison to Celestine and Quartz Raman spectra

The table below shows Raman bands from both the Figure 4.19 types of material in the Galliger sample alongside reference samples of celestine and quartz from the Department of Chemistry at University of Liege (Malherbe 2017).

Galliger White 532 (cm <sup>-1</sup> )	Galliger White 785 (cm <sup>-1</sup> )	Celestine (cm <sup>-1</sup> )	Galliger Red (cm <sup>-1</sup> )	Quartz (cm <sup>-1</sup> )
-	-	-	-	-
-	-	-	128	128
-	-	-	205	206
-	-	-	264	264
-	-	-	355	355
-	-	-	394	-
460	461	454	401	402
-	-	-	464	464
622	623	620	-	-
638	639	639	-	-
655	656	657	-	-
-	-	-	796	796
-	-	-	806	806
999	999	1001	-	-
-	-	-	-	1066
-	-	-	1086	1083
1091	-	-	-	-
1107	-	1112	-	-
1155	1155	1157	-	-
-	-	-	1162	1161

Table 4.2 Table showing Galliger sample peak locations alongside celestine and quartz reference samples

These spectra correlate with the handheld data although many more minor bands are apparent in the microprobe data for the quartz samples with most of the sub 400 cm<sup>-1</sup> sub bands merging to a single band in the data in Section 4.5.1. Almost every minor band was visible in the Galliger samples in comparison to the reference sample (with at most 4 wavenumbers difference between corresponding bands). XRD data (Figure 4.20) for both the white and red material were obtained independently, with the white confirming the celestine identification and the red quartz.

(Coupled TwoTheta/Theta)

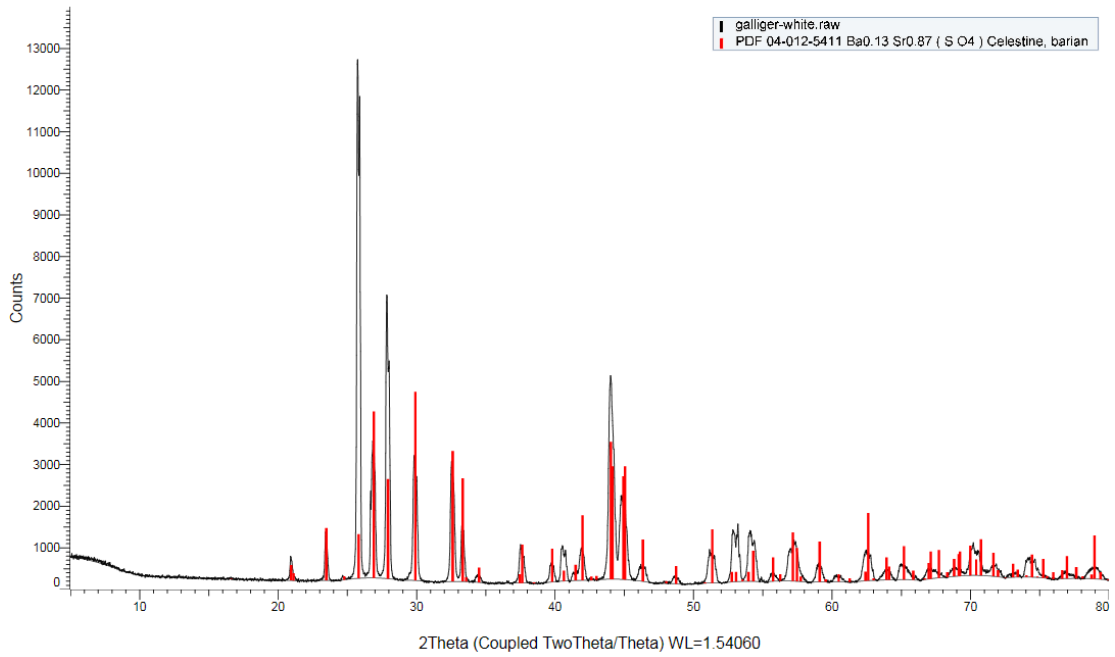


Figure 4.20 XRD Diffractogram of Galliger White material with Celestine Reference peaks

#### 4.5.5.3 Barclay

The Barclay (Figure 4.21) sample was a large brittle semi-translucent sample which was generally homogenous in texture and composition.

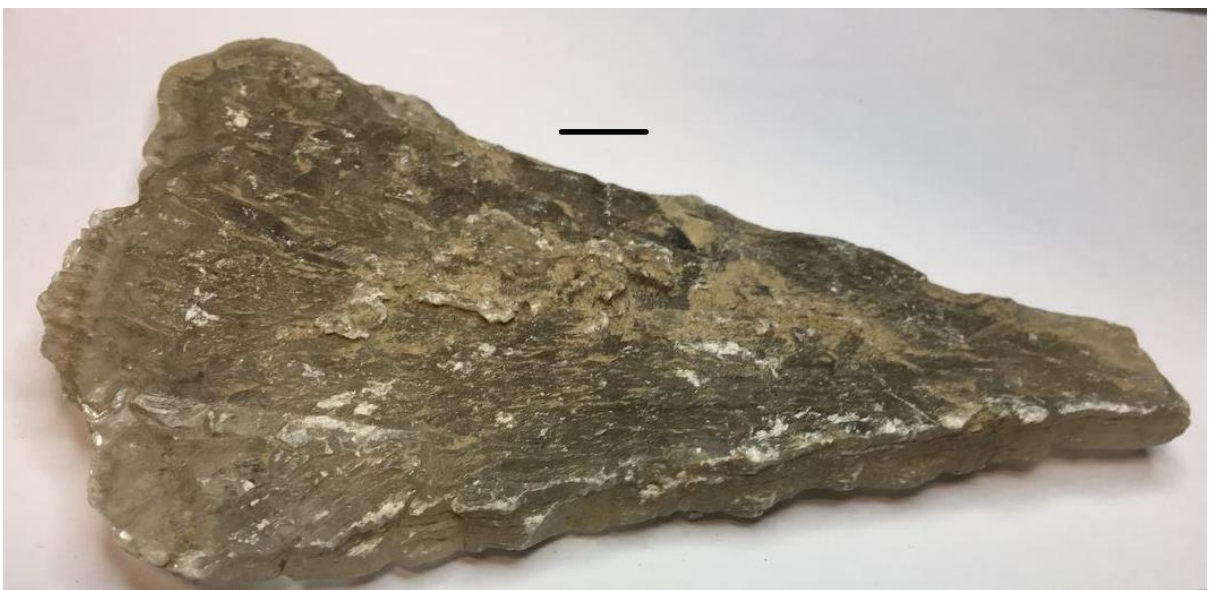


Figure 4.21 Barclay sample, black line indicates 1 cm

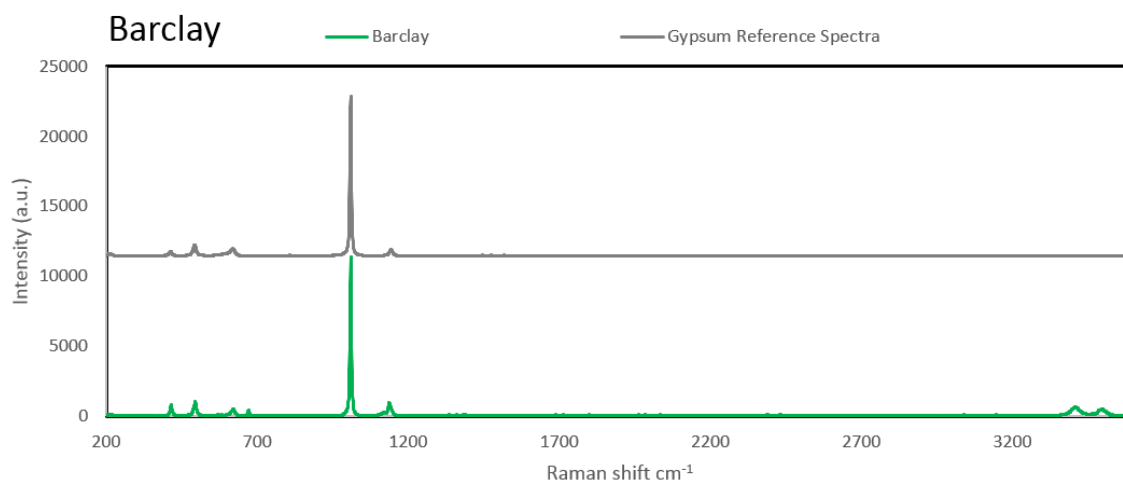


Figure 4.22 Raman Spectra of Barclay sample showing the gypsum hydration bands. Spectra has background subtraction. Gypsum reference sample sourced from RRUFF R040029 (Lafuente et al. 2015)

The Barclay sample exhibits a clear gypsum spectrum with evidence for all the major bands. In the 532nm data, (shown below in Table 4.3), the hydration bands are also visible at  $>3200\text{ cm}^{-1}$ . It should be noted that the gypsum reference spectra only had a spectral range of  $160 - 1600\text{ cm}^{-1}$ , hence the lack of hydration bands in that spectra in Figure 4.22.

Barclay ( $\text{cm}^{-1}$ )	Gypsum Reference Spectra ( $\text{cm}^{-1}$ )
182	-
415	413
494	-
620	619
671	-
1009	1009
1120	-
1137	1143
3408	-
3495	-

Table 4.3 Table showing Barclay sample peak locations alongside a gypsum reference spectra from RRUFF

#### 4.5.5.4 Stanford

The Stanford (Figure 4.23) sample is a hard dark grey sample with white veins across the surface. The dark grey material mostly fluoresces but the white material exhibits a clear anhydrite spectrum with low background noise.



Figure 4.23 Stanford sample, the black scale line indicates 1 cm

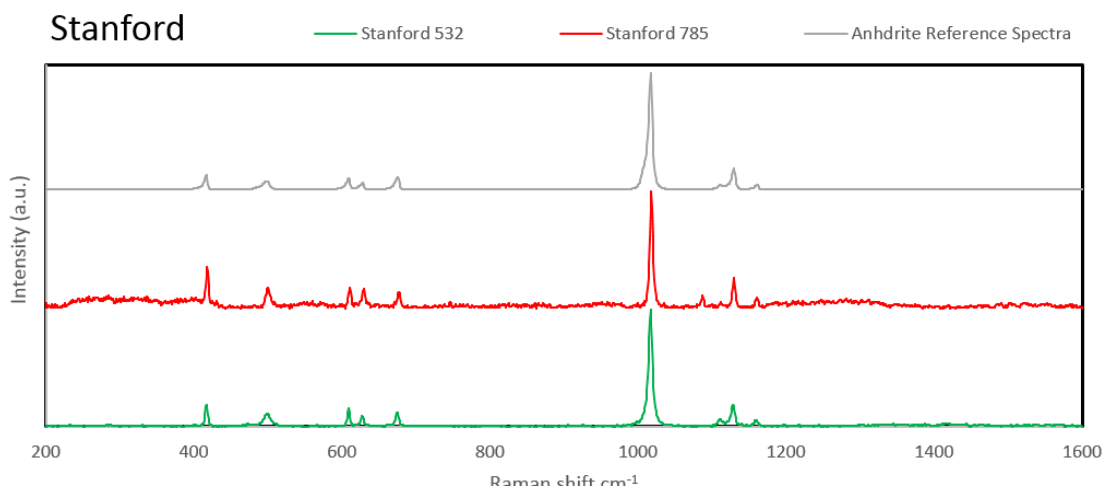


Figure 4.24 Anhydrite spectra from Stanford sample, 532nm and 785nm. Anhydrite reference spectrum from RRUFF R040012 (Lafuente et al. 2015)

Stanford 532 (cm <sup>-1</sup> )	Stanford 785 (cm <sup>-1</sup> )	Anhydrite Reference Spectra (cm <sup>-1</sup> )
-	397	-
-	402	-
417	418	417
499	500	498
609	611	609
627	630	628
675	677	676
1017	1018	1017
-	1087	-
1110	-	1111
1128	1129	1129
1159	-	1161

*Table 4.4 Table of band locations in Stanford sample alongside an anhydrite reference spectra*

The Stanford sample spectra confirm the presence of anhydrite. This can be distinguished from gypsum as it lacks the hydration peaks at  $>3000\text{ cm}^{-1}$  (Figure 4.24 only shows the spectral range of  $200 - 1600\text{ cm}^{-1}$  as there are no spectral features above this range). The main band is 10 wavenumbers away from that of gypsum located at  $1017\text{ cm}^{-1}$  (Table 4.4) (L. V. Harris, McHugh, et al. 2015)

The band in the 785nm spectra at  $1087\text{ cm}^{-1}$  is normally associated with calcite although the quartz reference sample exhibits a small band at  $1083\text{ cm}^{-1}$ . A calcite identification is also verified in the XRD data (Figure 4.25) with a small number of calcite bands. There also appears to be a quartz component in the diffractogram.

(Coupled TwoTheta/Theta)

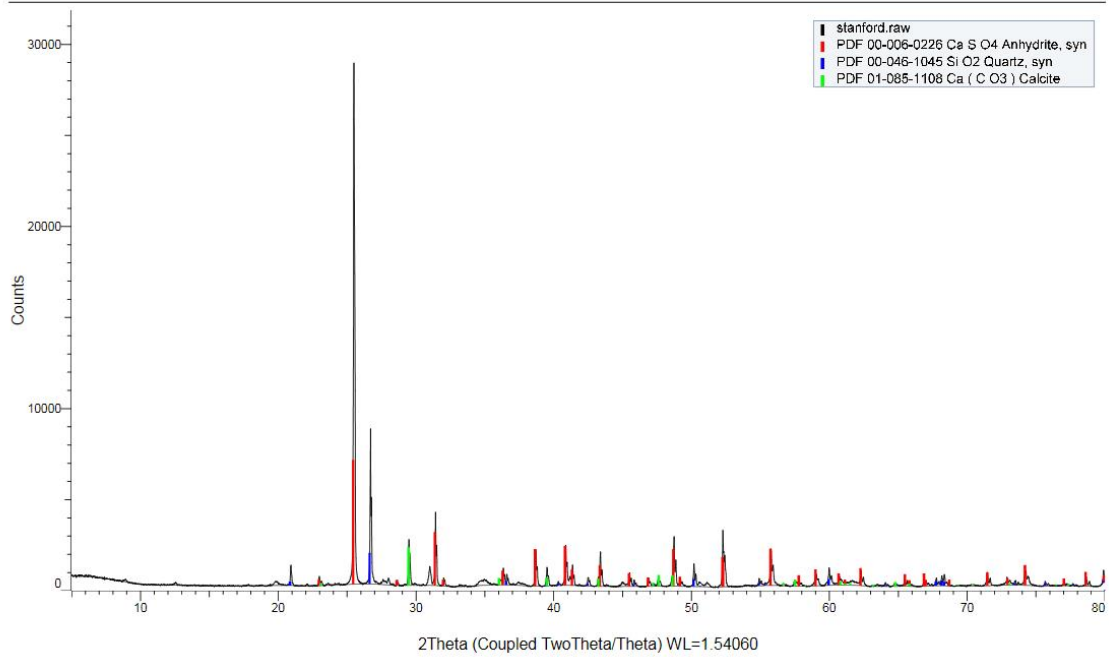


Figure 4.25 XRD Diffractogram of Stanford sample showing Anhydrite, Quartz and Calcite

#### 4.5.5.5 Justineau

Justineau (Figure 4.26) is a yellow sample with some darker orange and brown colouration. The sample crumbles easily and exhibits numerous distinct spectral components.



*Figure 4.26 Image of the Justineau sample with the scale bar is equivalent to 1cm*

The Justineau sample is one of the most mineralogically diverse. As well as the quartz, which was common to many of the samples in the desert region, grain scale analyses showed the presence of both barite and hematite from separate grains. These spectra were clear in the data obtained from both of the spectrometers.

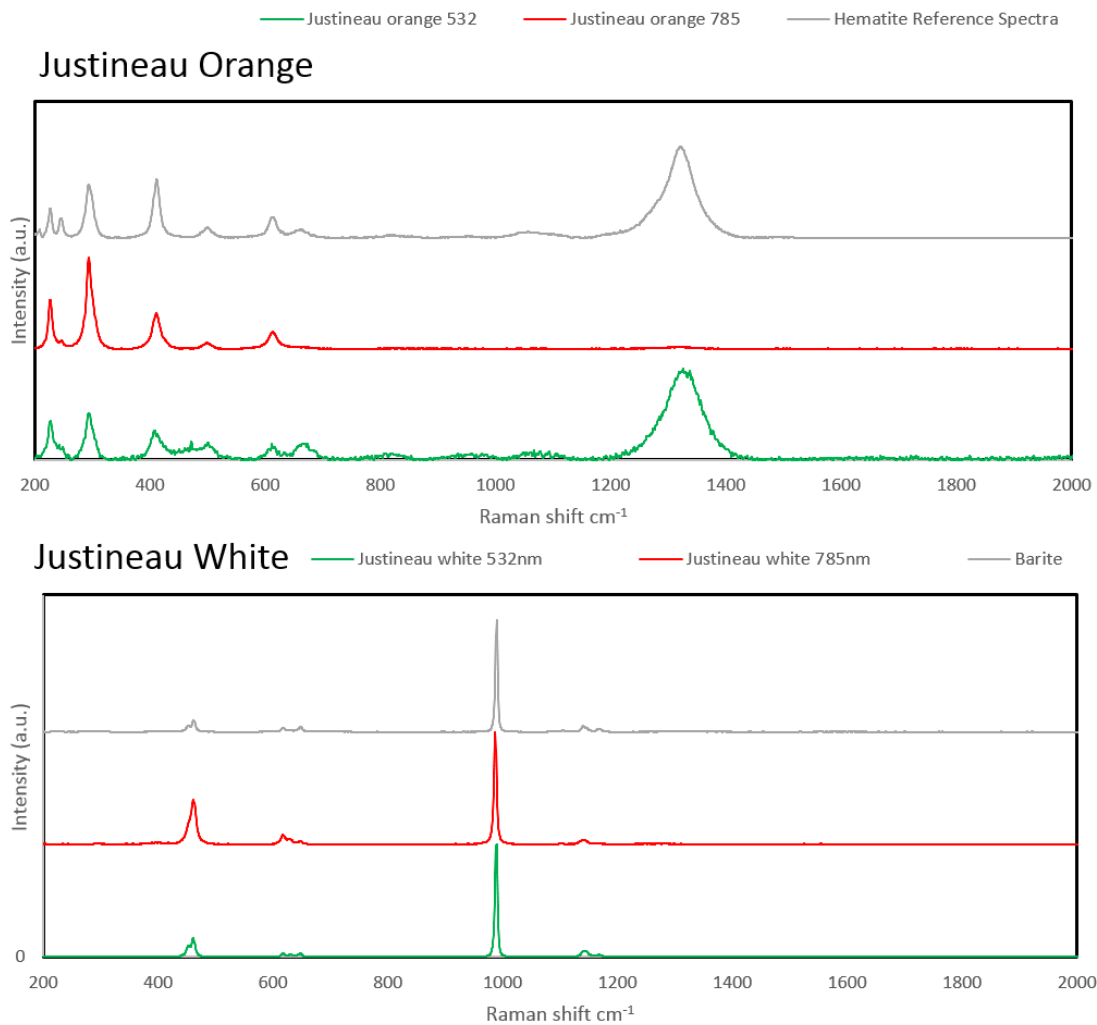


Figure 4.27 Two types of material detected within the Justineau sample Barite reference samples from the University of Liege, Hematite reference spectra from RRUFF R050300 (Lafuente et al. 2015)

Justineau orange 532 (cm <sup>-1</sup> )	Justineau orange 785 (cm <sup>-1</sup> )	Hematite Reference Spectra (cm <sup>-1</sup> )	Justineau white 532nm (cm <sup>-1</sup> )	Justineau white 785nm (cm <sup>-1</sup> )	Barite Reference Sample (cm <sup>-1</sup> )
227	226	227	190	-	-
242	246	245	-	-	-
293	293	293	-	-	-
408	411	411	-	-	-
-	-	-	453	-	452
-	-	-	461	461	462
472	-	-	-	-	-
-	498	-	-	-	-
500	-	-	-	-	-
612	613	612	-	-	-
-	-	-	617	617	617
-	-	-	630	630	630
-	-	-	647	647	648
667	-	-	-	-	-
-	-	-	989	987	989
1325	-	1321	-	-	-
-	-	-	-	-	1105
-	-	-	1142	1139	1140
-	-	-	1168	-	1168

Table 4.5 Table of Justineau sample band locations alongside hematite reference spectra and barite reference sample

The White crystalline part of the sample matches well with the barite referenced in Table 4.5 from Figure 4.27 above, with all but the 1105 cm<sup>-1</sup> sub band of the reference sample appearing in one or both of the spectrometers. In contrast, the orange material exhibits a hematite spectrum with all sub bands from the reference samples in the 532nm whilst the 785nm data does not show the wide 1321 cm<sup>-1</sup> band. However, the Justineau XRD only shows quartz detection and did not show hematite or barite.

#### 4.5.5.6 Melanie

The Melanie sample (shown in Figure 4.28) was obtained from a region near to the landing site area. The sample is composed of a hard blue grey bulk material with white crystals engrained within the sample. Section 4.5.3 shows the detection of feldspar within Melanie.



Figure 4.28 Image of Melanie sample. Scale bar marks 1cm

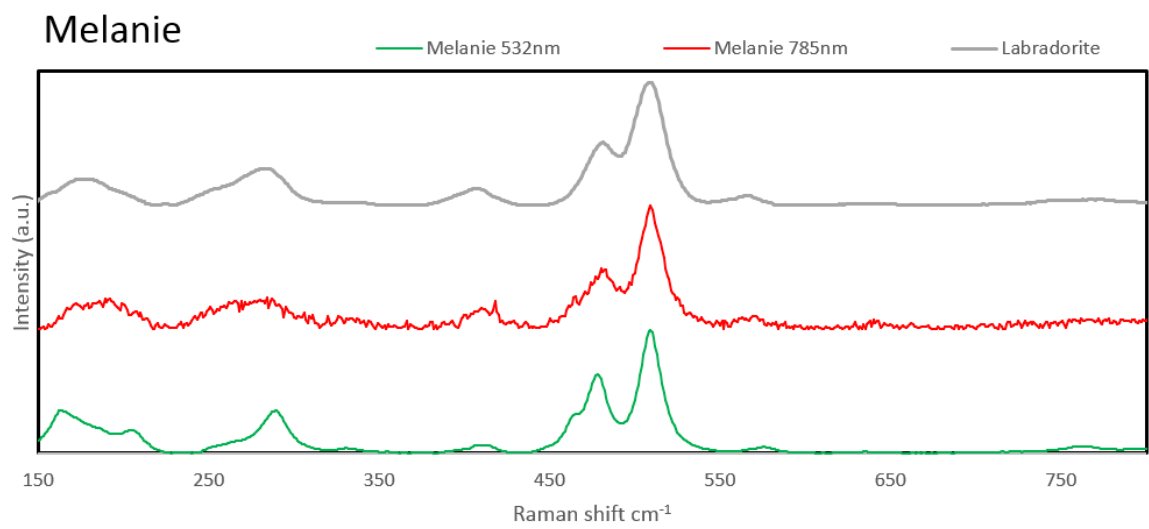


Figure 4.29 Feldspar spectra from the Melanie sample compared to a labradorite reference spectra from RRUFF R050104 (Lafuente et al. 2015)

Melanie 532nm (cm <sup>-1</sup> )	Melanie 785nm (cm <sup>-1</sup> )	Labradorite (cm <sup>-1</sup> )
163	-	-
-	179	180
204	199	-
290	284	284
410	410	407
478	480	481
509	509	509
576	570	566
762	-	758

*Table 4. 6 Melanie sample band locations alongside Labradorite spectra from RRUFF*

These feldspar spectra (Figure 4.29) match well with that of Labradorite – one of the most common feldspars detected at Gale (see Chapter 3, Section 3.4.2). All of the sub bands were detected in one or both of the data obtained with the spectrometers. However, the feldspar, oligoclase, exhibits a very similar spectrum and it is likely that the sample contains multiple different types of feldspar. All these possible feldspar detections are sodium – calcium type feldspars (not rich in potassium), similar to those investigated by MSL (see Figure 3.6). Additional observation points on the Melanie sample (with both spectrometers), reveal a clear quartz band at 465 cm<sup>-1</sup> (Table 4.6). This band overlaps one of the two feldspar bands, complicating identification. The XRD data also indicates the presence of albite with quartz detections apparent too (Figure 4.30).

(Coupled TwoTheta/Theta)

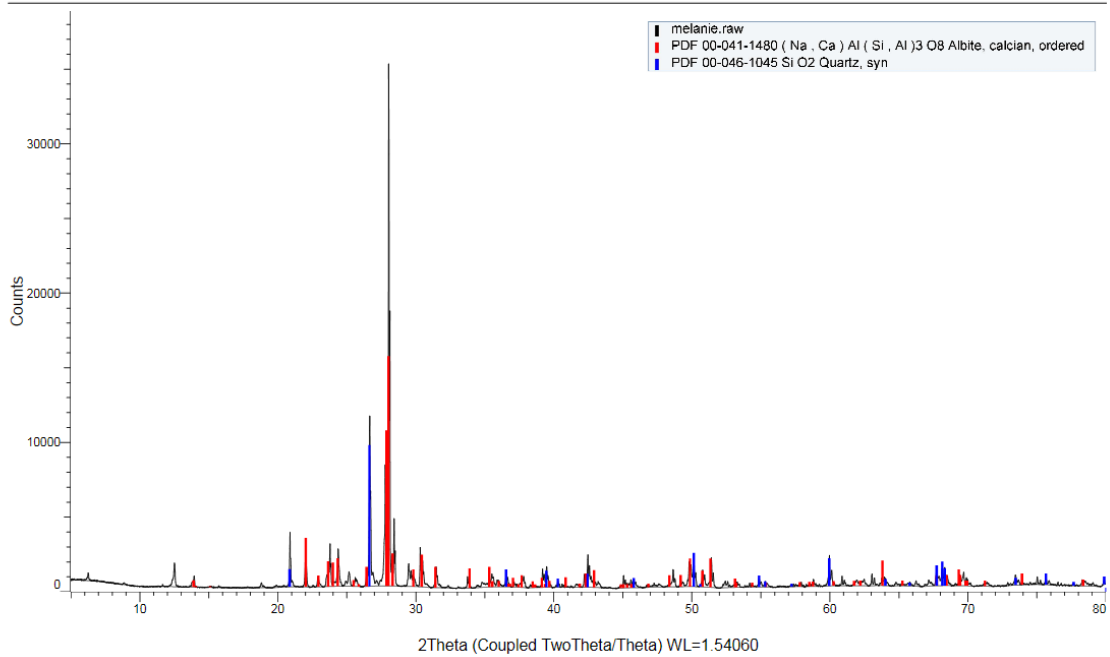


Figure 4.30 XRD diffractogram of Melanie sample showing evidence of Albite and Quartz

#### 4.5.5.7 Moon

The Moon sample (shown in Figure 4.31) is a small spherical nodule made up of aggregated grains that crumble easily under force. Numerous samples of the same type were located in quantity near Moon.



Figure 4.31 Moon sample. Scale bar shows 1cm

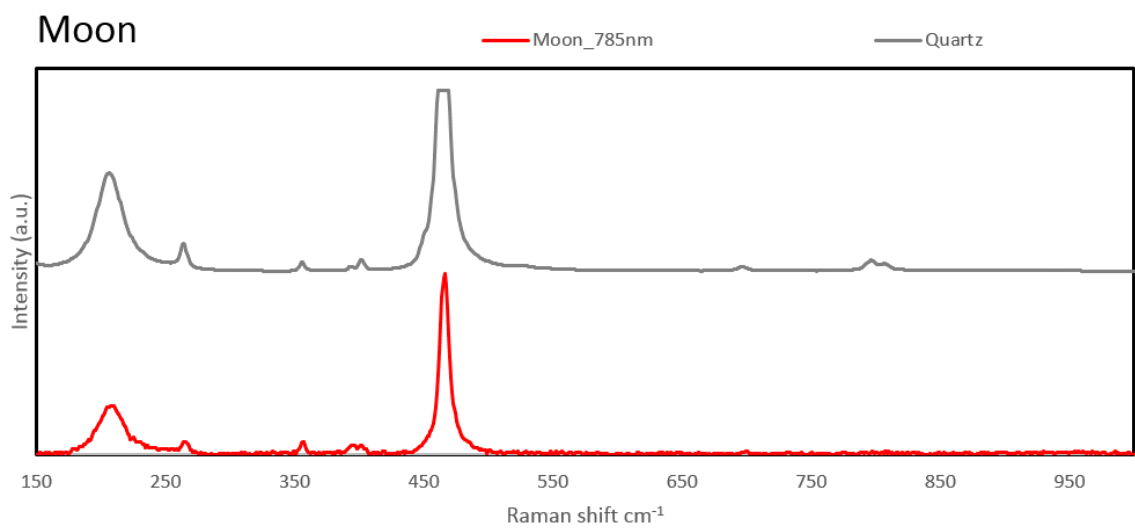


Figure 4.32 Moon 785nm spectra compared to reference Quartz spectra from the University of Liege

Moon_785nm (cm <sup>-1</sup> )	Quartz (cm <sup>-1</sup> )
-	128
208	206
250	-
265	264
356	355
395	-
401	402
466	466
500	-
-	796
1263	-

Table 4.7 Table of Moon sample band locations compared to a reference sample

Moon sample shows a clear quartz spectra. The reference sample in Figure 4.32 reached saturation and so the peak location was determined via fitting a Gaussian curve to the peak width. Almost all the sub bands were detected with an exception of those at  $796\text{ cm}^{-1}$  (Table 4.7).

#### 4.5.6 Phyllosilicate samples

Phyllosilicates are hydrated sheet silicates with silicon and oxygen in a 2:5 atomic ratio which vary in both structure and chemical composition (Wang, Freeman, et al. 2015).

Of the remaining landing site options, both show evidence of the presence of phyllosilicates with Oxia Planum exhibiting iron-magnesium phyllosilicates (Quantin et al. 2016) and Mawrth Vallis exhibiting aluminium phyllosilicates (Bibring et al. 2006). Due to these compositions of minerals in the vicinity of the landing site, it is important to obtain spectra of various types of phyllosilicate with representative instruments in order to predict and optimise instrument performance. Phyllosilicates tend to exhibit hydration bands in the  $3500\text{-}800\text{ cm}^{-1}$  range (outside of the spectral range). In the lower wavenumber range there are 3 or 4 main bands which make it possible to distinguish between Mg, Al and Fe phyllosilicates, Fe rich having a band at  $550\text{ cm}^{-1}$ , Mg rich identified from the peak at  $350\text{ cm}^{-1}$  and Al rich at near to  $430\text{ cm}^{-1}$ . These peak connections are based on observation of reference samples by Wang et al. 2015. However, due to the complex structure of phyllosilicates, there can also be other features present which obscure those bands. Due to this it is important to pre-determine the location of likely Raman bands when analysing a sample to aid in the band detection process. Data from the grain scale microscope Raman provides a baseline identification which can later be compared to representative spectra in order to detect phyllosilicates when in the field.

##### 4.5.6.1 Talc

A sample of Talc was acquired from the Department of Chemistry at University of Liege (Malherbe 2017) for phyllosilicate testing. Talc is a hydrated magnesium silicate and is therefore representative of the Oxia Planum landing site.

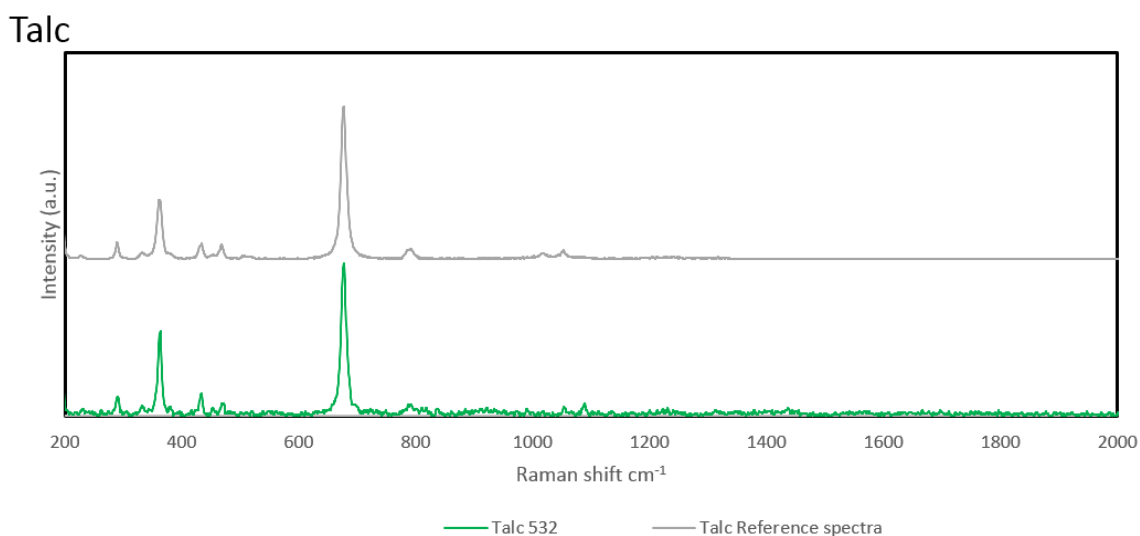


Figure 4.33 Talc sample 532nm spectra compared with RUFF reference spectra R050087 (Lafuente et al. 2015)

Talc 532 ( $\text{cm}^{-1}$ )	Talc Reference spectra ( $\text{cm}^{-1}$ )
111	109
194	193
290	289
331	-
363	362
379	-
433	434
469	467
677	677
697	-
790	793
-	1052
1089	-

Table 4.8 Table of talc band positions alongside the RRUFF talc reference spectra

The sample matches well with the reference spectra (Figure 4.33). Since Talc ( $\text{H}_2\text{Mg}_3(\text{SiO}_3)_4$ ) is an Mg – phyllosilicate, with the largest band is observed in the sub 600  $\text{cm}^{-1}$  region is close to 350  $\text{cm}^{-1}$  (Table 4.8) suggested in Wang et al. 2015, at 363  $\text{cm}^{-1}$ .

#### 4.5.6.2 Montmorillonite

Montmorillonite (Figure 4.34),  $((\text{Na,Ca})_{0.33}(\text{Al,Mg})_2(\text{Si}_4\text{O}_{10})(\text{OH})_2 \cdot n\text{H}_2\text{O})$ , is a member of the smectite group. Clays present a particular challenge for Raman spectroscopy due to extremely small grain sizes (less than  $2\ \mu\text{m}$ ). These grains cause significant levels of scattering, reducing the Raman SNR. The low crystalline nature of clays also contributes to this effect (Wang, Freeman, et al. 2015), and as such, care must be taken to distinguish bands from the background noise. Montmorillonite contains aluminium and a large, wide band, with a peak at  $446\ \text{cm}^{-1}$  (Table 4.9) close to the  $430\ \text{cm}^{-1}$  band associated with Al-phyllsilicates (See Wang et al. 2015).

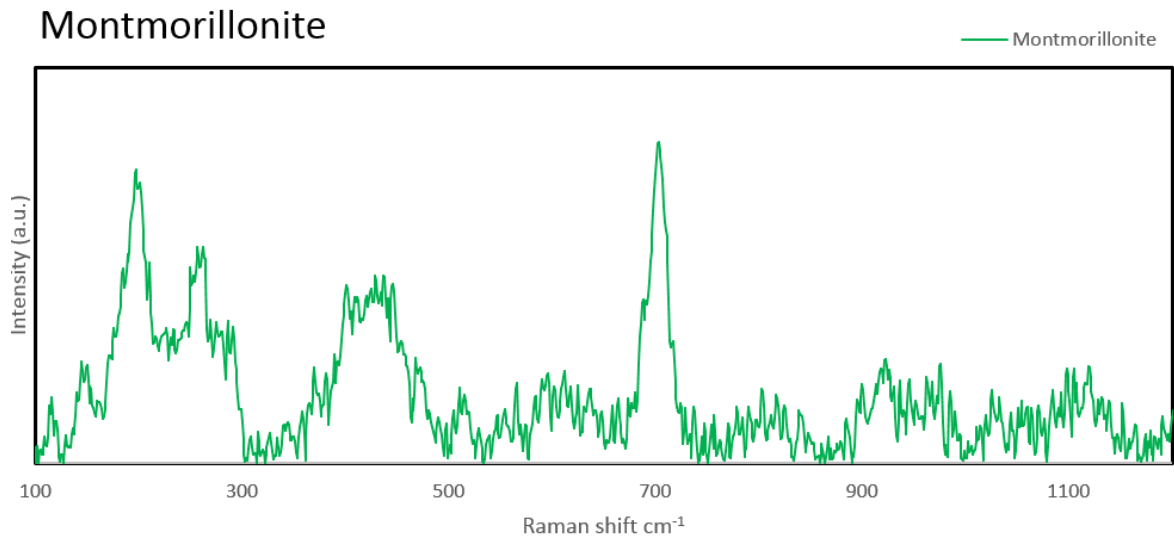


Figure 4.34 Montmorillonite sample spectra, large fluorescence background subtracted

Montmorillonite ( $\text{cm}^{-1}$ )	Montmorillonite (Wang et al 2015) ( $\text{cm}^{-1}$ )
150	-
197	205
227	-
257	-
291	290
401	-
446	440
468	-
515	-
703	705

Table 4.9 Table of Montmorillonite band locations alongside locations from Wang et al (2015)

#### 4.5.6.3 Biotite

Biotite,  $(\text{K}(\text{Mg},\text{Fe})_3\text{AlSi}_3\text{O}_{10}(\text{F},\text{OH})_2)$ , is a phyllosilicate in the mica group and contains a mixture of iron and magnesium. It exhibits bands at  $560\text{ cm}^{-1}$  near the  $550\text{ cm}^{-1}$  iron phyllosilicate peak and  $342\text{ cm}^{-1}$  (Table 4.10) near the  $350\text{ cm}^{-1}$  magnesium phyllosilicate band from Wang et al. 2015 (Figure 4.35).

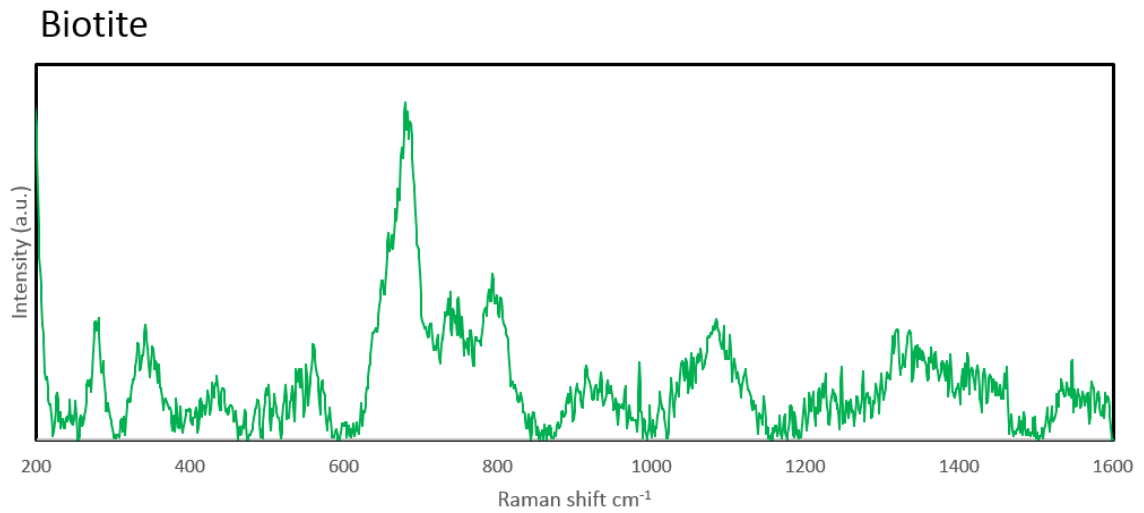


Figure 4.35 Biotite 532nm spectra large background fluorescence removed

<u>Biotite</u> <u>(cm<sup>-1</sup>)</u>
148
198
281
342
560
680
738
793

Table 4.10 Table of Biotite band locations

## 4.6 Discussion

### 4.6.1 Comparison between mission representative spectrometers and lab instrumentation

This study comprehensively characterises the mineralogy of the samples selected from the Utah field site as well as those chosen to represent the phyllosilicates located at the two possible ExoMars landing sites. Throughout this study, the benefits of micro-grain analyses of the samples are clearly evident, allowing for straightforward spectral confirmation of the different minerals present within each rock sample. These spectra are typically lower in fluorescence and have a higher signal to noise ratio than those obtained with the handheld instrument studies described earlier in this chapter. Characterisation of the selected samples was also performed with XRD measurements. These measurements provide a comparison between both the grain scale Raman and other Raman spectra obtained from the field.

The Raman spectra obtained with the microscope were typically clearer and exhibited higher SNR levels, with many more minor bands visible than those obtained with the handheld and lab 532nm Advantage spectrometers. However, the actual minerals detected by each are roughly the same (although the handheld measurement of hematite is very ambiguous and the feldspar spectra obtained in the field would not be sufficient to identify a specific feldspar). These representative instruments demonstrate the capability of flight equivalent instruments to identify a wide variety of different relevant minerals with a success rate comparable to that of the much more refined laboratory techniques presented in this chapter. Chapter 5 details further testing of a sub selection of these samples using the RLS Engineering Qualification Model. This gives the most representative view of the capability of RLS to analyse such samples analogous to these within the Martian environment.

The gypsum hydration peaks were not visible in the 785 nm data, neither within the microscope data nor the handheld spectrometer data (though the handheld spectrometer lacks the spectral range to detect anything above  $2000\text{ cm}^{-1}$ ). Whilst the laboratory 532nm instrument used in this chapter does not detect them, RLS will possess

the required spectral range and sensitivity to obtain hydration OH and CH bands of the sampled material from regions beneath the Martian surface (Rull et al. 2017).

The microscopic Raman analyses of the Justineau sample only confirmed the presence of barite and haematite (not quartz). This demonstrates a case where the larger spot size of the handheld instrument was able to detect mineralogy missed by the microscope. A longer microscope sampling campaign, with many more acquisition points, would have been required to detect quartz. A campaign of many more measurement locations could have quantified the different mineralogies present within the samples by measuring a large number of random points and measuring the ratio of counts of each spectra type. The handheld instrument used in the field detected both barite and quartz but only exhibited one very weak possible hematite detection. The sulphate crystals were visible within the powdered sample without the use of a microscope and spectra typically obtained include both barite and quartz when the laser spot covered one such crystal within the laser footprint.

The feldspar analysis is complex as many feldspar have very similar Raman spectra. Additionally some of the felsic samples that were analysed contained both quartz and feldspar which both exhibit a large band at around  $465\text{ cm}^{-1}$ . The larger quartz band can dominate one of the two main feldspar Raman bands. This could lead to a misidentification of a band location produced from a combination of the quartz and feldspar peak. This combined band could be several wavenumbers from the actual feldspar band leading to misidentification of the specific feldspar. In this case, it would assist the mineralogical identification to obtain chemical data such as XRF or LIBS analysis in order to determine (from the chemistry), which types of feldspar to consider during specific identification.

The classification of these analogues will allow for further tests with the ExoMars RLS EQM (Engineering Qualification Model, see Chapter 5). From the work detailed above, the composition of the samples is well known. Tests with the EQM will determine how the RLS Martian analysis will compare with dedicated laboratory instrumentation.

## 4.6.2 XRD analyses

The XRD data broadly agreed with the Raman analyses. Only one of the XRD measurements contradicted the Raman band measurements (see Justineau, Section 4.5.5.5) whilst in all other cases giving very consistent results and verifying the presence of most of the same minerals as detected by the microprobe and handheld Raman. The Justineau XRD diffractogram only indicated the presence of quartz within the samples. This could be because the relatively low concentrations of haematite and barite within the sample.

## 4.6.3 Challenges for Raman identification

### 4.6.3.1 Fluorescence

A major component of many Raman spectra is the fluorescence background, which is caused by the excitation of the electrons within a sample when it is exposed to a high intensity laser such as that used to generate Raman scattering. The large signal levels associated with fluorescence can complicate/compromise band identification, both in a lab environment and on planetary science missions. Fluorescence features (as shown in Figure 4.36) could lead to misidentification of minerals due to confusion with possible Raman bands. In addition, large background fluorescence levels can obscure the mineralogical Raman peaks resulting in reductions in sensitivity compared to the background noise. Typically, before band identification is performed, the background fluorescence signal has to be subtracted. However, since the fluorescence signal is not always consistent in size or spectral shape, a polynomial must be fitted on a spectrum by spectrum basis in order to adequately correct for it. This process can occasionally result in spectral artefacts so care must be taken not to misidentify candidate Raman bands. Fluorescence can often be caused by organics within the samples and it has been suggested that fluorescence levels will be very low in the Martian environment (Rull et al. 2017; Chou & Wang 2017). However, it will still be necessary to eliminate fluorescence from non-organic sources, and as such, RLS will seek to reduce

fluorescence by keeping the samples illuminated for a longer period of time. Raman spectra from an illuminated sample will be periodically checked to verify the levels of fluorescence reduction and when the algorithm detects a lowering in fluorescence, it will then acquire the spectra that will be transmitted to Earth (Rull et al. 2017).

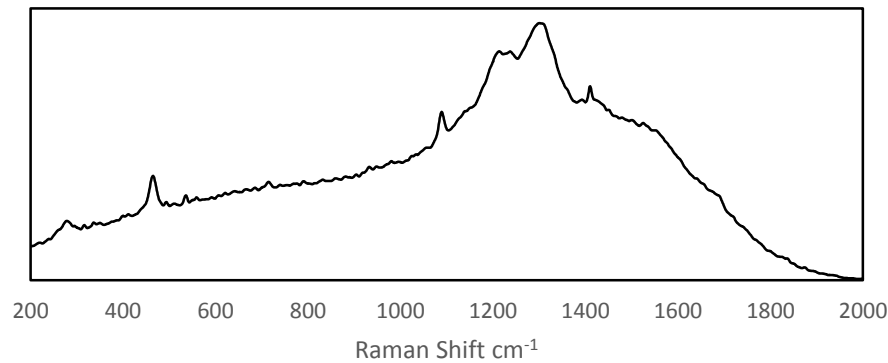


Figure 4.36 Background fluorescence shown, features above  $1200\text{cm}^{-1}$  are from the fluorescence effect and not due to Raman scattering. The peak at  $1408\text{ cm}^{-1}$  is a hot pixel as discussed below.

#### 4.6.3.2 Hot pixels and Cosmic Rays

Detector “hot pixels” can result in spectral artefacts which can be falsely identified as Raman bands. In actuality they are caused by cascading defects within a single pixel and lead to significantly higher levels of dark current for that specific pixel (Hopkinson 1993). Possible causes for this can be defects or damage inside the detector (CCD), potentially caused by radiation damage (in space applications). The feature seen at  $1408\text{ cm}^{-1}$  on the 785 nm handheld Raman spectrometer is a hot pixel. One way these features are different from genuine Raman bands is that the spikes generally appear as isolated pixels rather than the several contiguous pixels usually observed for Gaussian shaped bands. The intense radiation environment encountered by a rover mission en-route to and during operation on Mars will increase the likelihood of the development of hot pixels and so it is important to ensure that steps are taken to eliminate these features from the data before analysis, particularly if automated detection algorithms are being utilised (Rull et al. 2017).

Cosmic rays have a similar effect to hot pixels, generating spurious spectral features that are not associated with Raman bands. The specific characteristics of the Martian environment mean that the impact of cosmic rays on a spectrometer's operations are more significant than usually experienced with laboratory based instruments. To address this issue, the ExoMars RLS spectrometer will implement a data processing algorithm to detect and remove the features associated with cosmic ray signals before the spectral identification process is completed (Rull et al. 2017).

#### *4.6.3.3 Chemical and mineralogical Matrix effects*

Rocks often contain a number of different types of mineral. As such, a Raman laser spot can sample multiple molecular structures, producing simultaneous Raman scatter from each separate feature. This leads to the superposition of each set of Raman bands, with the potential for some minor bands to become confused, thereby complicating the compositional analysis of the samples. This can be mitigated by using multiple observation points transecting the sample surface, identifying which bands vary in intensity, enabling them to be grouped together and separated out. Multiple sampling points can be used to investigate variations in composition across the surface of the sample (which can then be compared to contextual images of the samples to obtain complementary data in order to correlate the visual and textural changes with spectral differences). The SHERLOC (UV Raman) instrument on the NASA MARS 2020 mission will make use of this technique (Beegle et al. 2014). However, during the ExoMars mission, each sample will be acquired by the drill and then crushed before being delivered to the analytical laboratory (Rull et al. 2017). Due to this the material will be homogenised by the powdering system. This process will compromise the Raman spectrometer's ability to detect mineral variations within the sample but will enable a bulk composition of the average mineralogy to be obtained. Figure 4.37 shows an example of this chemical matrix effects.

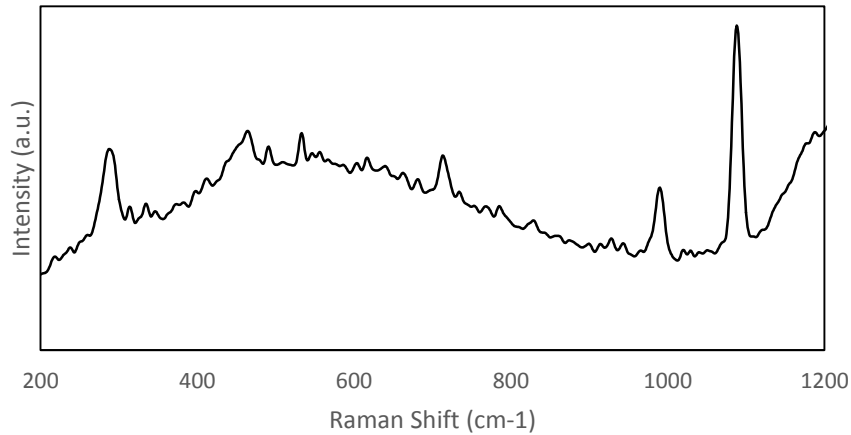


*Figure 4.37 Sample Cross measured with 785 nm Raman with a laser spot covering the colour change within the sample, demonstrating the mineralogical matrix effects from two mineralogically distinct materials*

#### 4.6.3.4 Sample preparation

In a planetary exploration mission, the sample handling system must be completely autonomous. However, for this type of system to function correctly, each sample must be spatially identical. Consequently, the ExoMars samples will be crushed and homogenised and this process obviously results in the loss of spatial information. Whilst as a technique, Raman Spectroscopy does not require any sample preparation (Jorge et al. 2005), other techniques used by the mission do. By homogenising the sample it can be ensured that each instrument analyses the same material, allowing for straightforward, complementary data analysis. Powdering of the sample can lead to a reduction in the total signal intensity as light can be scattered away from the reception cone. The mixing of samples can also cause a reduction in signal intensity as the concentration of the material in the beam reduces, and this is demonstrated in Figure 4.38. Increased background can result of the additional scattering from the crushed samples.

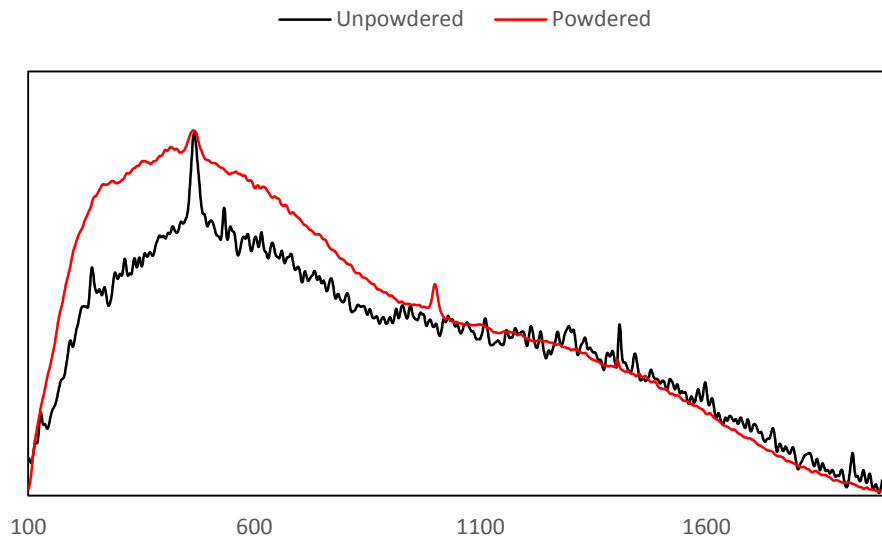


Figure 4.38 785 nm Comparison of both the powdered and unpowdered versions of the Galliger sample, unpowdered sample refers to the Red material on the surface of the sample.

#### 4.6.3.5 Spectrometer wavelength

One of the major factors to consider when selecting an appropriate Raman spectrometer for a planetary exploration mission is the laser wavelength. In order to determine which wavelength is best, it is particularly important to consider the prioritisation of the various different scientific mission goals. For example, 532 nm Raman (as selected for both the ExoMars RLS instrument and the Mars2020 SuperCam instrument) is superior at detecting organic compounds in particular as it benefits from a resonant effect with the carotene molecule (Jorge et al. 2005). In contrast, at 785 nm, a good balance between inorganic and organic sample sensitivity is achieved with good sensitivity to reduced carbon in particular (L. V. Harris, Hutchinson, et al. 2015). Figure 4.39 shows additional fluorescence in the 532 nm spectra compared to the 785nm.

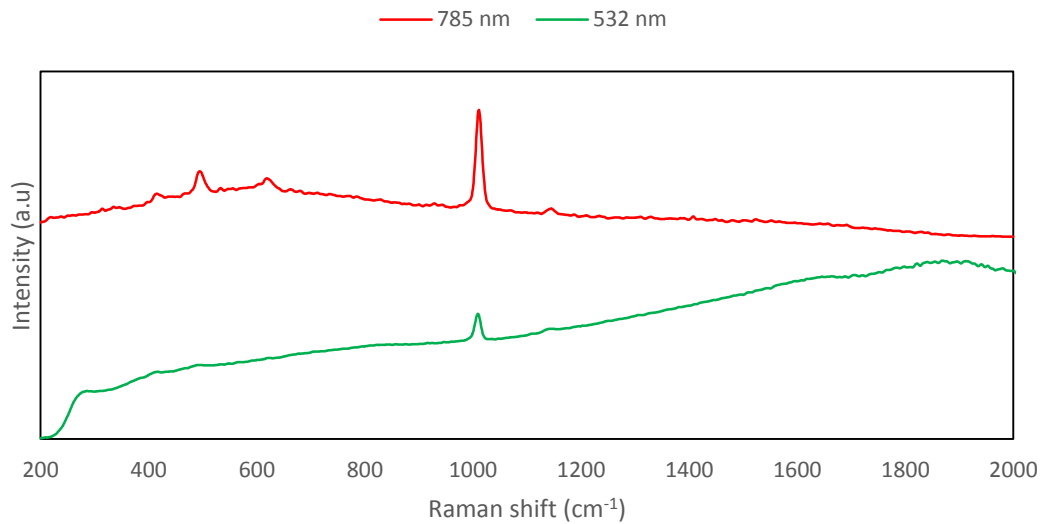


Figure 4.39 Comparison between 532 nm and 785 nm wavelengths spectra have been normalised with no fluorescence subtraction.

## 4.7 Conclusion

To prepare for the ESA 2020 ExoMars rover mission, UKSA rover trials were performed near Hanksville, Utah in the USA. To simulate the functionality of the RLS instrument, a handheld Raman spectrometer was deployed in the field. Drill core samples were obtained and analysed with the Raman spectrometer. In addition, a diverse collection of samples were collected in order to investigate the mineralogical diversity of the area. The mineralogical classification of these samples highlights the value of Raman Spectroscopy as a useful tool for planetary exploration and geological classification. Both 785 nm (used for field work and laboratory studies) and 532 nm (used for laboratory studies) excitation wavelengths were used to obtain the results, allowing comparison between the 785nm and 532nm. Raman analysis complications associated with fluorescence, hot pixels, cosmic rays and matrix effects were accounted for and will be important factor on Mars missions.

A selection of samples, primarily from a Mars analogue site in the Utah desert, were examined with grain scale Raman spectroscopy and analysed with an X-Ray Diffractometer. Data obtained with the Raman spectrometer and the XRD agreed well for all but one of the samples, providing clear compositional information for all of the analogues. The microscale Raman correlated well with the handheld and benchtop instrumentation used in the field with a maximum of 3-4 wavenumbers difference for the common bands in the majority of samples. However, many of the sub peaks were not visible in the flight representative instrumentation.

With these samples now mineralogically characterised, a sub selection of samples will be selected to represent the most useful analogues for the ExoMars landing sites, primarily sulphates and phyllosilicates. These are analysed in Chapter 5 with the RLS Engineering Qualification Model (EQM) to determine the capability of the RLS instrument to detect and identify the samples analysed in this chapter. Chapter 5 will examine the relative analytical capability of the RLS EQM will be compared to the lab instrumentation from this chapter in order to make recommendations for RLS testing and operating modes in preparation for launch.

Future work will involve the study of a broader range of analogues in order to fully investigate the limits of Raman analysis. In particular, a much wider selection of phyllosilicates will be necessary for landing site preparation.

Future rover trials will be performed to investigate the performance of other analytical techniques, such as IR spectroscopy, included in the ExoMars ALD alongside Raman spectroscopy. Particular focus will be on sample preparation and acquisition which should carefully and adequately replicate crushing handling system utilised by ExoMars. In summary, it is clear that testing with a carefully selected appropriate analogue samples is crucial for preparing adequately for the operation and optimisation of the RLS instrument on the ExoMars rover.

# Chapter 5: Raman Laser Spectrometer Engineering Qualification Model tests

## 5.1 Introduction

The work presented in Chapter 4, described the selection and characterisation of Martian analogues recovered from a field site in Utah during the MURFI field trial. These samples were analysed with instruments representative of those used on previous rover missions before being fully characterised (mineralogically) using both a laboratory XRD system and a microscope based, grain scale Raman spectrometer. Whilst the miniaturised instruments provide insight into the quality of data that a rover based system could obtain, it is clearly important to gain a detailed and accurate view of likely instrument performance by analysing samples with fully representative prototypes. Consequently this chapter presents sample analysis work conducted using two RLS (Raman Laser Spectrometer) prototype instruments, the Engineering Qualification Model of the RLS instrument which has been constructed at INTA (Instituto Nacional de Técnica Aeroespacial), in Spain (see Section 5.2.3) and the UKBB (UK Breadboard Instrument) (see Section 5.2.4) which has been developed at the University of Leicester to test the UK camera system.

## 5.2 Raman Laser Spectrometer

As discussed previously in Chapter 2, Section 2.3.3 the RLS is one of the analytical instruments included on ESA's 2020 ExoMars rover (Vago et al. 2015). It will be the first such instrument to be used on a planetary rover mission.

The RLS instrument was designed to fulfil five major scientific goals (Rull et al. 2017)

- identify organic compounds and search for life,
- identify mineral products and indicators of biological activity,
- characterise mineral phases produced by water related processes,

- characterise igneous minerals and their alteration products,
- characterise the water/geochemical environment as a function of depth in the shallow subsurface.

The spectrometer is expected to be used on at least 6 different drill sites, with 2 samples acquired at each (Richter et al. 2015). One analysis will be performed on material found at the surface and another will be performed on material recovered from the measurement depth. Along with these samples, 2 further sets of depth profiling measurements will be performed, in which 5 different samples are selected over various depths. The RLS instrument will obtain spectra from multiple observation points over the surface of the samples, with a series of 20 frames acquired at each point. Observation point locations can be ordered rasters of points across the sample or a randomised selection of points. Both approaches provide a representative view of the sample by quantifying materials statistically (Lopez-Reyes et al. 2012). Points can also be selected in coordination with the data obtained by other instruments included in the Pasteur instrument suite which will analyse the samples first (Rull et al. 2017).

To maximise the quality of the spectra, software algorithms will be implemented that adjust the instrument's integration time and other operating modes automatically. This will prevent the acquired signal from saturating the detector (i.e. when the full well capacity of a CCD (Charged Coupled Device) pixel is reached). Specific operating modes will also be implemented to minimise the background fluorescence of the analysed samples. For example, fluorescence can be reduced by exciting the sample with a laser spot for an extended period of time. The rate of change in fluorescence will be measured and when it has been reduced as far as possible, the RLS spectral acquisition process will be initiated (Rull et al. 2017). It is known that cosmic rays can degrade the spectra obtained (i.e. are a source of background signal), particularly if automatic spectral identification processes are used as the rays may be misidentified as spectral signal. The instrument itself is shielded (by other parts of the rover) but some cosmic rays are still expected to interact with the detector. Consequently, a cosmic ray removal algorithm will be utilised to remove as many of these as possible from the data stream automatically. The Signal to Noise Ratio (SNR) of the camera system will be continuously monitored and used to threshold the data acquired so that only useful spectral

information is returned to Earth (Quintana et al. 2016). This process saves on the bandwidth requirements for the instrument (López Reyes 2015), although occasional full frame CCD images will also be returned to check instrument alignment and therefore the reliability of the data.

### 5.2.1 Instrument design

The RLS instrument is composed of three major sub-systems: the ICEU (Instrument Control and Excitation Unit), the SPU (Spectrometer Unit) and the iOH (internal Optical Head) (Rull et al. 2017).

The SPU was developed by the Spanish and UK teams. The system incorporates a holographic grating and a TEC (Thermo Electric Cooler) cooled CCD (typically operating in the 263K to 233K range) which detect the spectral signature of the Raman scattered light. The total mass of the SPU is 0.85kg. The iOH (also the responsibility of the Spanish team) is an optical system that generates a focused 50  $\mu\text{m}$  (diameter) laser spot on the surface of the prepared samples delivered by the rover's sample handling system (del Rosario Canchal et al. 2017). The iOH automatically focuses the spot onto the target sample and collects the light that is scattered. The iOH is the only part of the instrument that is in near contact with the samples for cleanliness reasons (Melzer et al. 2015). An optical fibre is used to direct the collected signal towards the spectrometer unit so that a spectrum can be acquired. Finally, the ICEU system (developed by the French and UK teams) contains the instrument control and data processing electronics and the laser. The system uses the rover's 28V primary power supply and is controlled via the rover's data communication (CAN bus) interface. The instrument processor manages the data from the CCD and formats it for transmission back to Earth, as well as ensuring the laser retains the correct wavelength, power and temperature levels throughout operation (Rull et al. 2017).

During the development of the RLS instrument, one major design choice was the selection of the excitation wavelength. Spectra obtained from the commonly used 532 nm excitation source often exhibit increased levels of fluorescence which can obscure the Raman bands (compared to longer wavelengths in the IR range, such as 1064 nm).

However, Raman scattering is much more efficient at the shorter 532nm wavelength. This excitation source has the ability to detect OH and CH hydration bands at higher spectral ranges (see Chapter 4, Section 4.5.5.3) which are necessary for meeting the scientific objectives of the ExoMars instrument. The use of a 532 nm laser is also beneficial because it is possible to take advantage of resonance effects with certain, relevant biomarkers (Marshall et al. 2007) resulting in clear, high intensity Raman bands. Detector efficiency is also greater in the visible range and as such, a green Nd:YAG 532nm laser was selected for the RLS instrument (Rull et al. 2017).

One of the most important components of the instrument is the calibration target, which will be critical for confirming functional performance of the instrument and its spectral response throughout the duration of the mission. A 1mm PET (Polyethylene terephthalate) target will be used for these purposes (due to the number and spread of spectral bands that the material produces) and will have to be sterilised to reduce the risk of contamination during astrobiological studies (and to comply with planetary protection requirements).

### 5.2.2 RLS Engineering Qualification Model

The EQM (Engineering Qualification Model) is a flight like prototype which will be integrated into the rover EQM in Italy. The instrument is designed to be a duplicate of the flight model. The EQM was developed at INTA and will be delivered to TAS-I in Italy for integration into the test rover. Tests on the EQM instrument using the samples described in Chapter 4, provide a fully representative view of how the RLS instrument is likely to perform during the mission. It is necessary to operate the EQM in a clean room during all tests due to planetary protection requirements. The detector can be cooled using a TEC, but for the measurements described here, the instrument was operated in ambient conditions (the temperature was 295K). During operation of the EQM detector,

integration times of 0.1s, 0.3s, 0.5s, 0.7s, 1s and 10s were used. Once the EQM is delivered for integration into the ALD, a replica of the EQM (EQM2) will be used to perform tests on sample sets such as these all the way through to deployment of the RLS instrument on the surface of Mars. The system will also be used with appropriate analogue samples to help understand the data returned by the ExoMars instrument when it is operational.

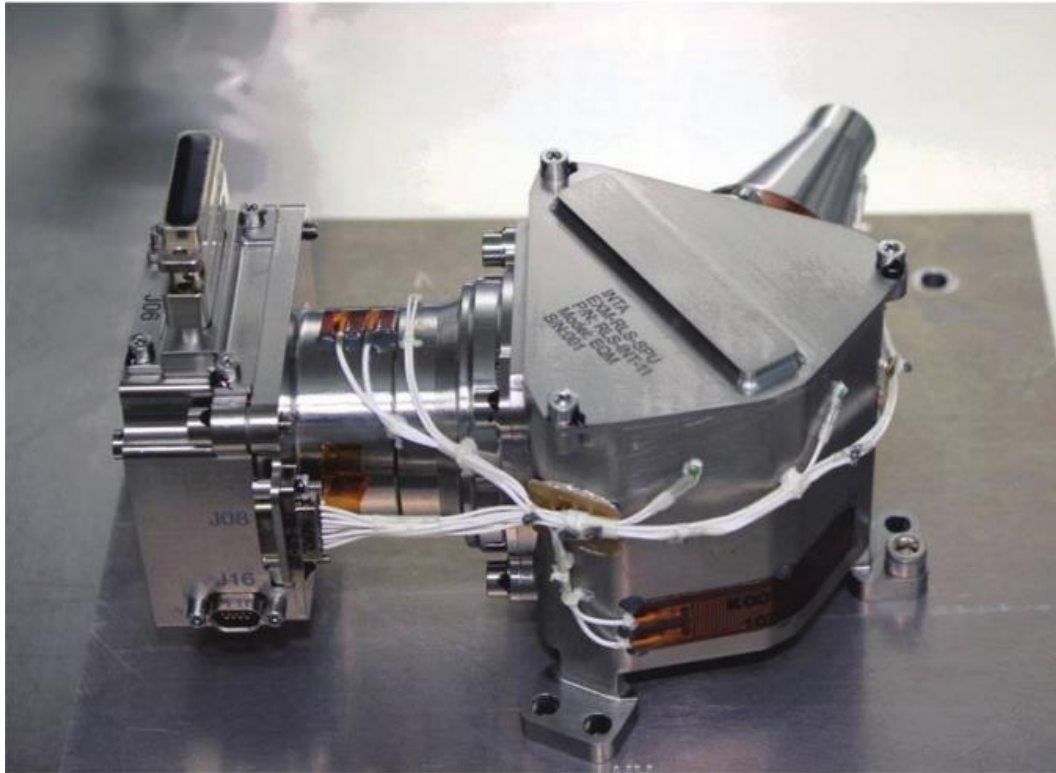


Figure 5.1 EQM SPU component Image Credit (Rull et al. 2017)

### 5.2.3 RLS UK Breadboard Instrument

A representative prototype system has also been developed at the University of Leicester, the UKBB, which was specifically built to replicate the CCD electronics interface and optical performance of the RLS spectrometer system. Using an analogous 532 nm laser (Edwards et al. 2012) with a variable spot size (between 50 – 100  $\mu\text{m}$ ), the functionality of the iOH is replicated by a RamanRXN ME probe head (with a 25-mm objective) manufactured by Kaiser Optical Systems Inc, the SPU by a Holospec f/1.8 spectrograph also produced by Kaiser Optical Systems Inc. and a transmission and return

optical fibre connecting the sub systems together. The instrument has a spectral range of  $175\text{ cm}^{-1}$  to  $4400\text{ cm}^{-1}$  from the  $532\text{ nm}$  laser line, spanning the full spectral range of the RLS instrument (Edwards et al. 2012). The spectral range is split over two orders on the surface of the CCD. The prototype system was designed so that it can use a variety of different CCDs. The CCD used for these studies is a Starlight Xpress CCD camera. A TEC is used to cool the detector to  $263\text{K}$ .

Although the prototype is a laboratory based set-up, the instrument was assembled in the Utah desert during the MURFI field trials and spectra were obtained. For the studies detailed in this chapter, a spectral range of  $370\text{ cm}^{-1}$  to  $1300\text{ cm}^{-1}$  was used as that covered the range of bands of interest for the relevant samples. The resolution of the UKBB is greater than that of the EQM, so in order to ensure the data were representative, the resolution was reduced to  $4\text{ cm}^{-1}$  per pixel by summing the contents of each group of 6 pixels.

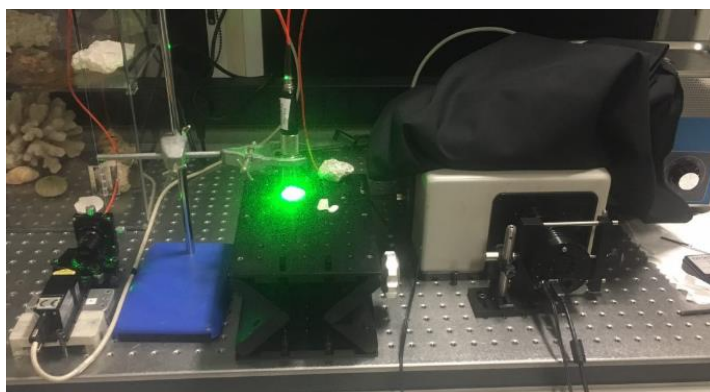


*Figure 5.2 The RLS UKBB setup, laser is on the left, spectrometer on the right and optical head and sample stage in the centre*

#### 5.2.4 Spectral acquisition and processing

The optics within the spectrometer form a diffraction order on the surface of the CCD, which is subsequently integrated onto the detector for an (optimal) period of time. The resulting image is converted to a list of pixel intensities from a  $1392 \times 1040$  CCD frame. In the case of the EQM instrument, the data product contained the pixel intensities from a smaller fraction of the CCD image which contain data from the spectral order. The reduced window is  $20 \times 2048$  in size compared to the full  $2048 \times 512$  pixel frame. The spectrum is extracted from the image by vertically summing pixel intensities and plotting the variation across the order.

Only pixels containing relevant data are summed, minimising the number of off order pixels which ultimately add additional noise (i.e. from the dark current and electronics

noise associated with every pixel that does not contain useful data). The resulting spectrum is uncalibrated and therefore needs to be corrected.

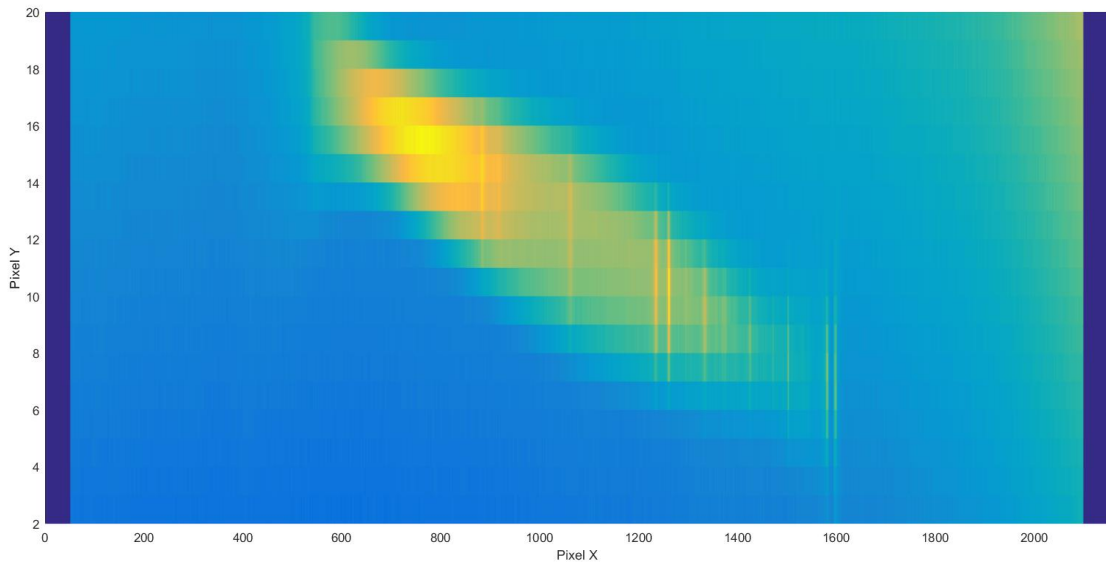


Figure 5.3 CCD Image showing the order of the Raman spectra from an EQM measurement. A window has been used to select the relevant order so as to minimise dark current noise. Yellow indicates greater ADU whilst blue is weaker.

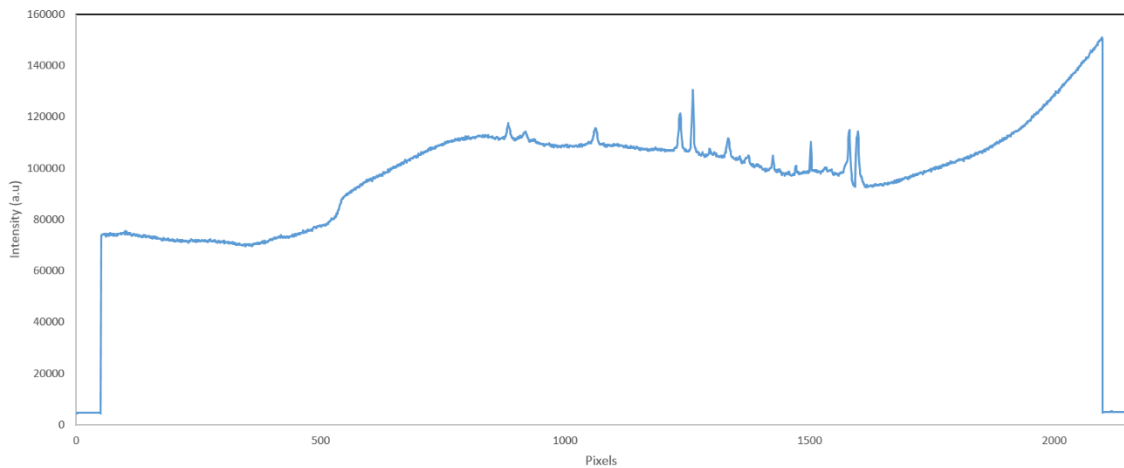


Figure 5.4 Uncalibrated PET spectra from RLS EQM

Figure 5.4 above shows the uncalibrated spectra of the PET calibration target from the binned CCD image. The significant drop in signal at either end of the spectrum arises from the underscan and overscan regions on the CCD detector, where there is no signal

present. The high intensity lines that are apparent on the CCD image (Figure 5.3) are seen to correspond to the peaks that are present in the uncalibrated spectrum (Figure 5.4). These data are compared to a PET reference spectrum, with known Raman band locations. A plot of CCD pixel number versus wavenumber is then used to derive a wavenumber/pixel correlation factor for the system.

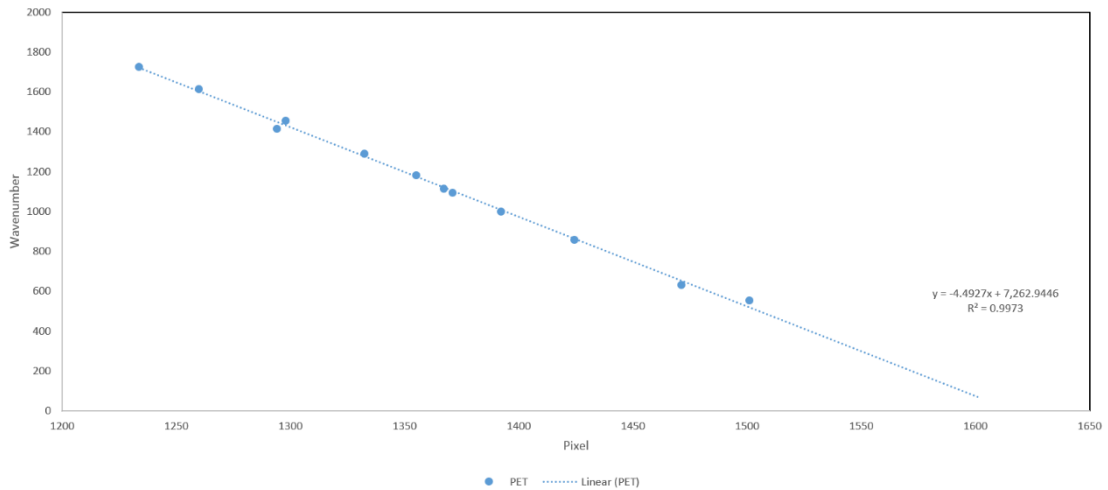


Figure 5.5 Calibration conversion from the PET CCD image for the RLS EQM

The correlation factor is derived from Figure 5.5 is then used to convert all of the spectra extracted from the CCD images to wavelength calibrated datasets.

Care must be taken to correctly identify the peaks, since as an incorrect calibration can lead to misidentification of sample components. The PET spectra can sometimes exhibit relatively low SNR bands for sub 800  $\text{cm}^{-1}$  spectral regions and so it is desirable to obtain clear bands in this region for band identification. A similar correlation factor can be created with the addition of the known peaks from the highest SNR bands in the samples using the peak locations derived in Chapter 4. This process shows the precise trend of wavenumber-pixel relationship over these lower wavenumber ranges. In the Martian environment, once a sample has been identified, a similar system can be used to validate the initial PET calibration.

A separate calibration is used for the high spectral range (above 3000  $\text{cm}^{-1}$ ) as there are few Raman bands between 1600  $\text{cm}^{-1}$  and 3000  $\text{cm}^{-1}$  so the independent calibrations can be more accurate for the specific samples.

When analysing data in the detector frames, it is desirable to remove external sources of light which can obscure the Raman signal. A dark frame (a CCD frame acquired without inducing a Raman signal) can be obtained, for the same acquisition time in order to correct for this source of background.

### 5.3 Samples



Figure 5.6 The samples selected for EQM in Spain analysis prepared in the University of Liege.

Figure 5.6 shows the selection of samples used in this study. These samples were selected from the larger collection described and analysed in Chapters 4. They were chosen to provide a representative view of the mineralogy encountered in the analogue field site, whilst also preparing for the possible ExoMars landing sites.

- Sulphate samples (1. Galliger White, 2. Cross, 3. Barclay, 4. Stanford and 5. Justineau), which demonstrate the capability of the RLS instrument to distinguish between closely neighbouring bands in Martian analogues that

are representative of materials like to be found in the area around Mawrth Vallis (Wray et al. 2010),

- Feldspar sample (6. Melanie) analogous to some of the feldspar found by MSL at Gale (Gasda et al. 2016),
- Silicate samples (7. Galliger Red, 8. Moon) rich in quartz, which was very common at the MURFI analogue site and its surrounding area,
- Phyllosilicate sample (9. Talc) relevant to potential ExoMars landing sites (Quantin et al. 2016),

### 5.3.1 Preparation

The samples prepared for the XRD tests described in Chapter 4 were reused. Crushing of the samples with the tungsten mortar and pestle ensured that the material was evenly distributed and incorporated reasonably consistent grain sizes. The grain size distribution obtained was confirmed to be representative of that expected from the sample handling system used on ExoMars, the samples were then smoothed to best represent ExoMars samples (Richter et al. 2015).

## 5.4 Results

### 5.4.1 Sulphates

The EQM was used to analyse the five samples which contained sulphates. In each case, 5 frames were acquired and stacked in order to optimise the SNR. The spectra for Samples 1, 3, 4 and 5 were obtained with 1 second acquisition times. In each case, multiple bands with a high SNR were found. For each sample, a dark frame was subtracted and the background fluorescence was removed using the RRUFF algorithm (Lafuente et al. 2015). Spectra were acquired from  $100\text{ cm}^{-1}$  to  $4000\text{ cm}^{-1}$  although only the  $200\text{ cm}^{-1}$  to  $1600\text{ cm}^{-1}$  range is shown in Figure 5.7 below, as that is the range which is relevant for the key mineral bands.

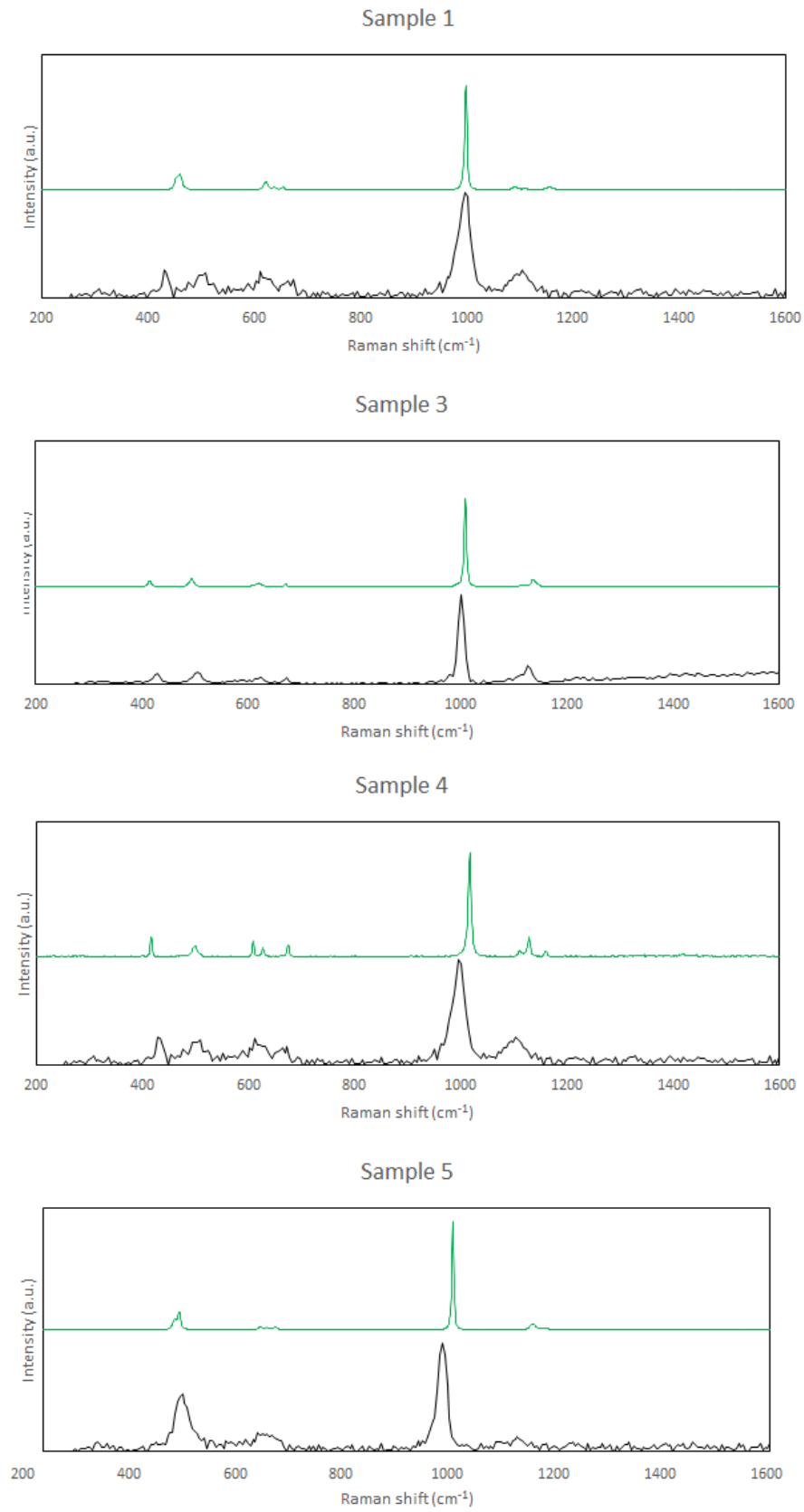
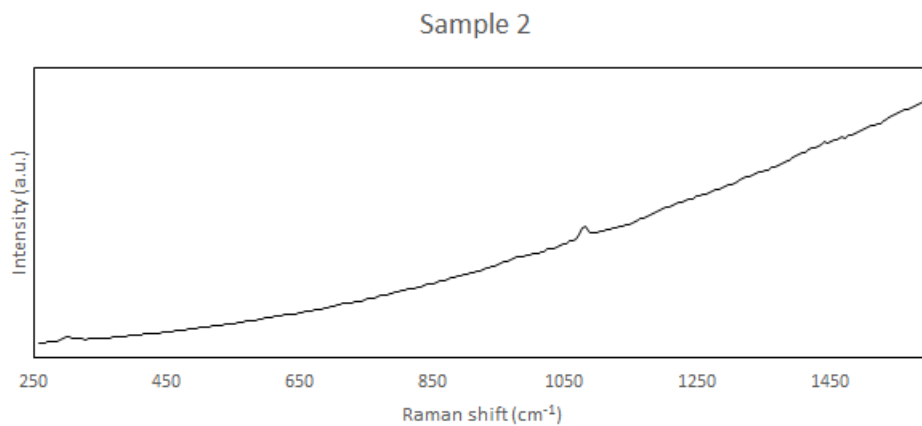


Figure 5.7 Sulphate sample Raman spectra acquired with the RLS EQM. Spectra have been optimised using dark frame subtraction and background removal. Green spectra are Raman Microscope measurements of the relevant samples.

The analysis of the Sample 2 spectra proved more challenging. At first inspection, the spectra appeared saturated, so the acquisition time was reduced to 0.5s and then again to 0.1s before good quality spectra could be obtained. This was due to a large fluorescence component, which obscures most of the Raman bands. At the first sampling point, no bands could be distinguished from the background but at a second point, small bands with low SNR were visible (See Figure 5.8). Sample 2 is the Cross sample which incorporated two main types of material; white calcite and red barite (see Chapter 4, Section 4.5.5.1). In the EQM spectra of the crushed homogenised sample, only the calcite peaks were visible. Although there is a very small band where the sulphate peak would be expected, alone it is insufficient for an identification.



*Figure 5.8 Sample 2 Raman spectra acquired with the RLS EQM. Spectra has a dark frame subtracted but has not had fluorescence removed*

Additional analyses of the cross sample using the UKBB system (Figure 5.9) were undertaken. Numerous acquisitions showed similar Raman bands to the EQM but some longer exposure measurements detected bands from both materials within the sample. Four of the ten sampling locations produced bands corresponding to both materials.

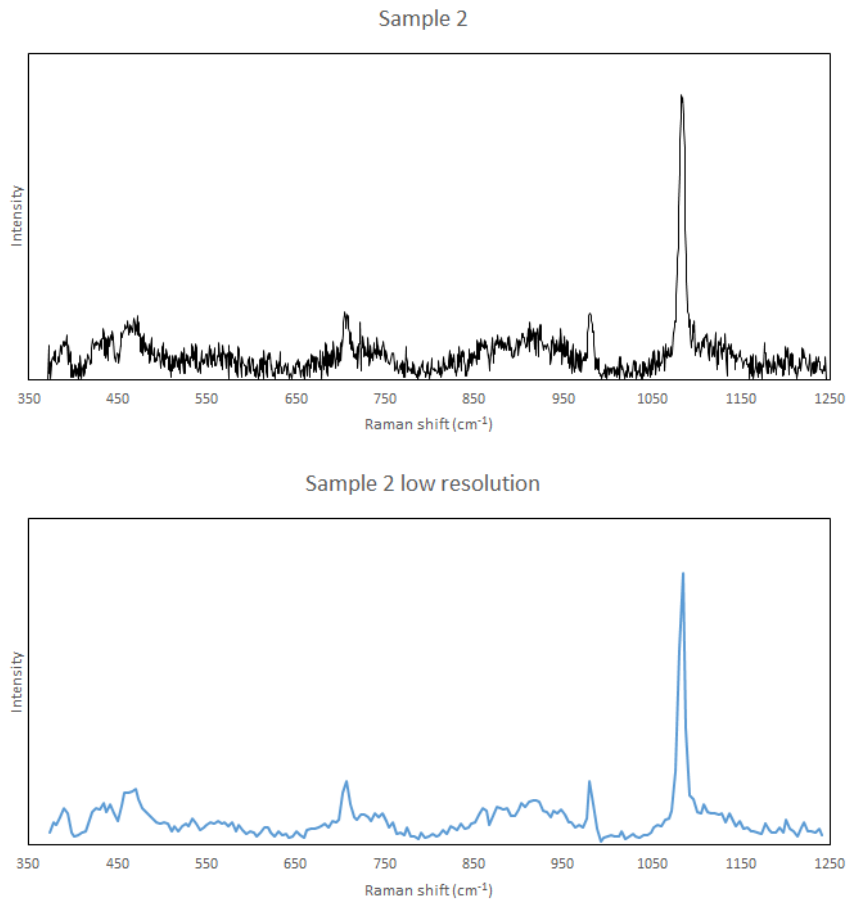


Figure 5.9 Sample 2 Raman spectra acquired with the RLS UKBB. Spectra have back fluorescence subtracted and cosmic rays removed. Since the UKBB has a higher resolution than the EQM groups of 6 pixels were summed to produce a resolution of 4  $\text{cm}^{-1}$  per pixel.

#### 5.4.2 Feldspar

Sample 6 (Melanie) contained feldspar and some measurements also indicated the presence of quartz. For Sample 6, a 1 second acquisition time was used, the initial sampling location did not show clear Raman bands. The second sampling point appears to show weak feldspar bands at  $476 \text{ cm}^{-1}$  and  $523 \text{ cm}^{-1}$  with a larger quartz peak at  $467 \text{ cm}^{-1}$  confusing the peak (Figure 5.10).

### Sample 6

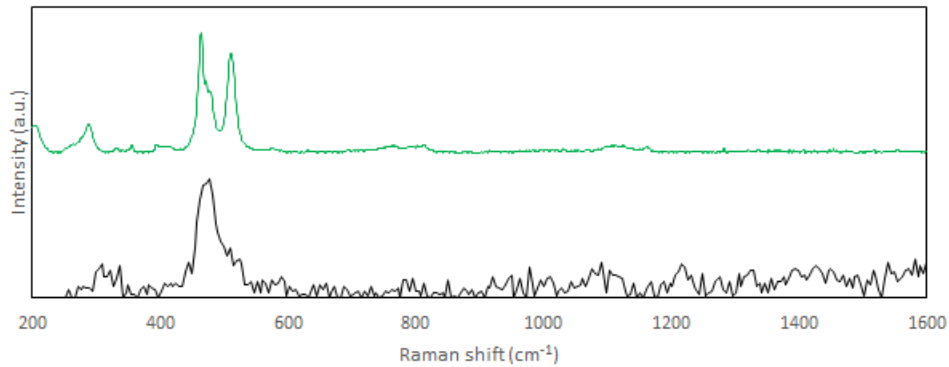
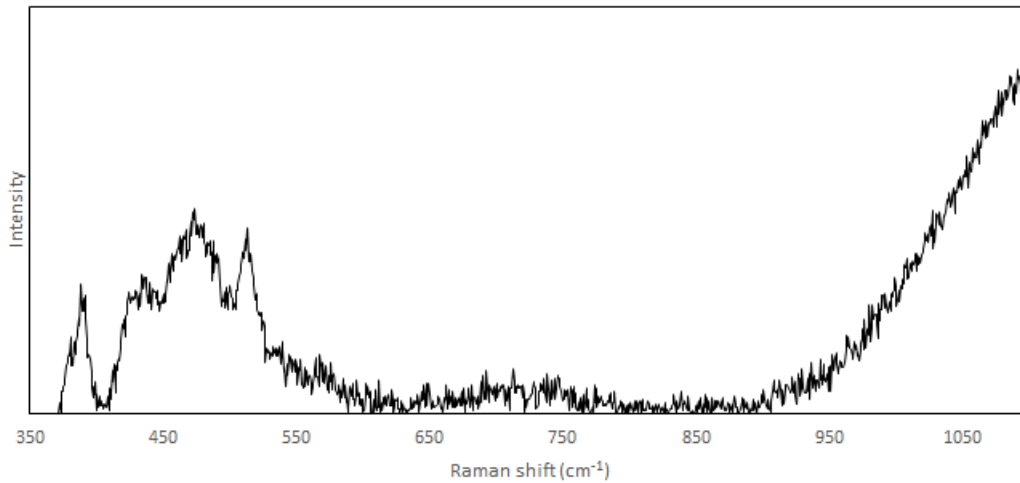


Figure 5.10 Raman spectra acquired with the RLS EQM for feldspar sample. Spectra have had dark frame subtraction and background removal. Green spectra are Raman Microscope measurements of the same sample.

UKBB studies (See Figure 5.11) with more observation points were able to detect to distinct peaks with locations in agreement with the data obtained from the microscope based spectrometer, at  $471\text{ cm}^{-1}$  and  $511\text{ cm}^{-1}$ , although there is an unknown band at  $437\text{ cm}^{-1}$  close to the feldspar bands. Once the UKBB data had been reduced in resolution to that corresponding to the EQM, the bands were still clearly distinguishable. Numerous observation points were required to detect these bands, with only 2 spectra from 30 points detecting both feldspar bands. This is likely due to the nature of the sample material containing additional minerals rather than pure feldspar, causing clear Raman band detection to be relatively rare.

Sample 6



Sample 6 low resolution

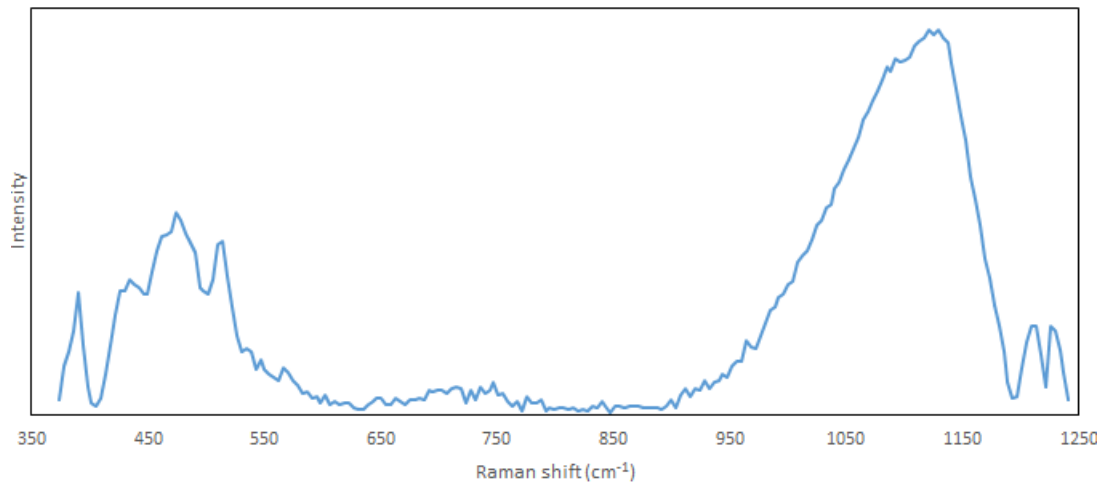


Figure 5.11 Spectra of Sample 6 with the RLS UKBB. Spectra have back fluorescence subtracted and cosmic rays removed. Since the UKBB has a higher resolution than the EQM groups of 6 pixels were summed to produce a resolution of 4 cm<sup>-1</sup> per pixel.

#### 5.4.3 Silicates

Two samples containing silicates were analysed: the red portion of the Galliger sample (Sample 7) and the Moon sample (Sample 8). Both of these samples were analysed using a 1 second acquisition time. Figure 5.12 shows Sample 7 has a clear peak located at 1075 cm<sup>-1</sup> which is not apparent in other measurements of the sample in Chapter 4. The quartz peak obtained from Sample 8 appears at a wavenumber of 490 cm<sup>-1</sup>. This quartz band is usually observed at a wavenumber of 467 cm<sup>-1</sup>. It is possible that the apparent

shift is due to the presence of additional material within the sample with a band close by as the peak is wide and appear to have a shoulder to the left at  $476\text{cm}^{-1}$  much closer to the expected location.

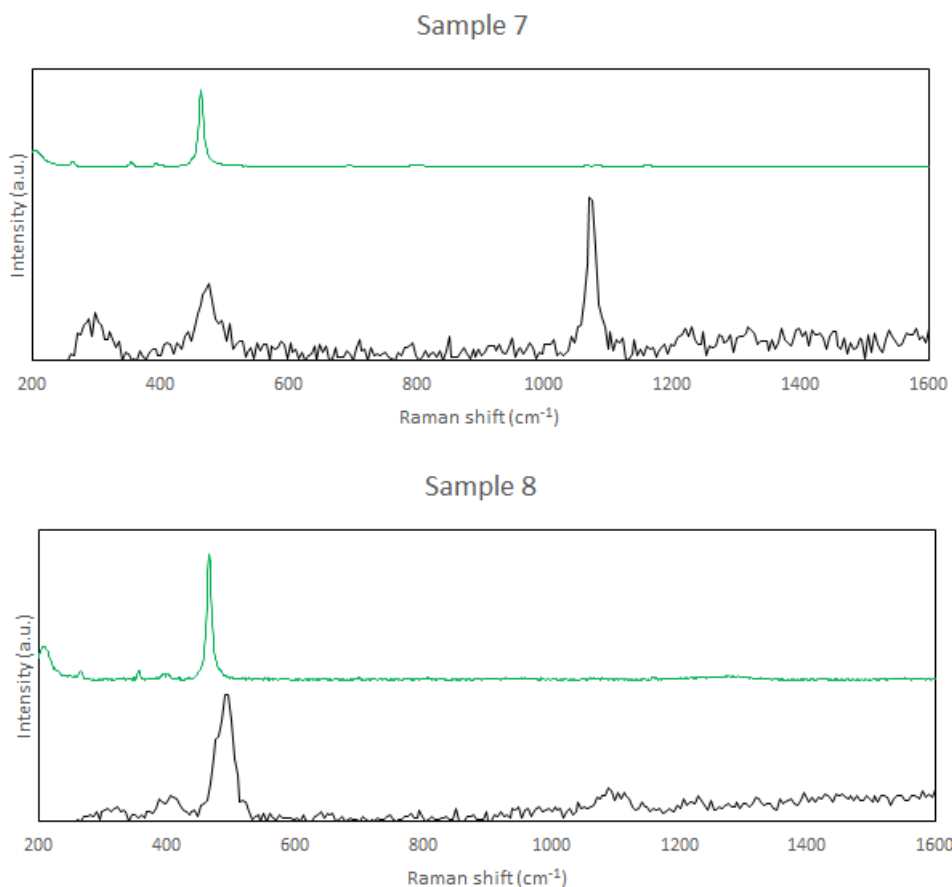


Figure 5.12 Silicate samples Raman spectra acquired with the RLS EQM. Spectra have had dark frame subtraction and background removal. Green spectra are Raman Microscope measurements of the relevant samples.

Additional UKBB measurements of Sample 8 showed the band located at  $465\text{cm}^{-1}$  in agreement with the data from Chapter 4. The lower resolution data only shows a shift to  $466\text{cm}^{-1}$ .

#### 5.4.4 Phyllosilicate

The Talc (Sample 9) exhibits relatively clear Raman bands, including a hydration peak at  $3640\text{cm}^{-1}$ . This sample was measured with a 1 second acquisition time over 5 frames which were then stacked (coadded) together. A first level background subtraction was

performed using the RRUFF algorithm (Lafuente et al. 2015), followed by a polynomial subtraction (see Figure 5.13).

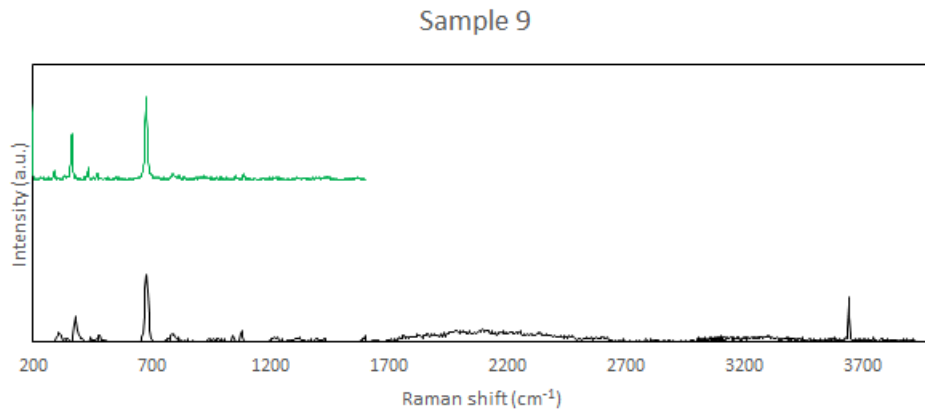


Figure 5.13 Raman spectra acquired with the RLS EQM for Talc sample. Spectra have had dark frame subtraction and background removal. Green spectrum are Raman Microscope measurements of the same sample.

## 5.5 Discussion

### 5.5.1 Spectra comparison

The EQM data are compared to comprehensive mineralogical classification performed with data acquired from a microscope based Raman instrument and an XRD instrument at the University of Liege (Malherbe 2017) in order to assess the detection capability of RLS. Many of the minor bands necessary for detailed mineralogical investigations were confirmed to be present throughout the EQM dataset, with the exception of Sample 2 (a mixture of two materials) and Sample 6, a mixture of multiple types of feldspar samples, as detailed below. Other than these two samples, the aims for identification of the various different spectra were fulfilled. Although this identification was only possible once a calibration over the full spectral range had been completed.

### 5.5.1.1 Sulphates

Samples 1, 3, 4 and 5 all possess clear Raman bands and many of the sub bands associated with the relevant sulphates. Each of the sub bands in the microscope based spectrometer data are present in the EQM spectra, although they exhibit additional noise. Due to the resolution of the RLS instrument (1 pixel is approximately  $4\text{ cm}^{-1}$ ) many of the neighbouring bands are difficult to distinguish, particularly the gypsum and anhydrite samples (Sample 3 and Sample 4). Additionally, many of the neighbouring sub bands merge to a single peak, as can be seen in Sample 5. The main sulphate bands are also much broader in the EQM data, further complicating specific sulphate identification. Figure 5.14 shows the relative locations of the bands. As expected, barite in Sample 5 exhibits the lowest band at  $988\text{ cm}^{-1}$  followed by celestine (Sample 1) at  $1003\text{ cm}^{-1}$ . Normally, these would be followed by the gypsum band (Sample 3) and then the anhydrite band (Sample 4), at  $1007\text{ cm}^{-1}$  and  $1013\text{ cm}^{-1}$  respectively. However, these bands are not readily distinguishable in the EQM data. It should be noted that given that the lower resolution of RLS allows for a much wider spectral range, the gypsum and anhydrite samples can be distinguished by the hydration bands seen in gypsum at around  $3400\text{ cm}^{-1}$ , (detection of the hydration band with the EQM is discussed in more detail in Section 5.5.1.5).

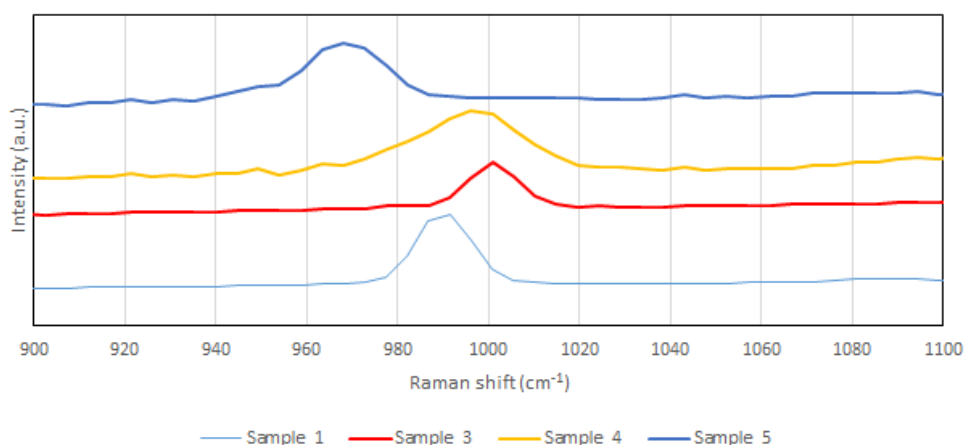


Figure 5.14 Comparison of the locations of the main sulphate bands in the EQM data

The very high fluorescence levels encountered with Sample 2, were also observed when using the benchtop advantage 532 nm spectrometer to perform studies of the

powdered sample. However, since the microscope based system could pick out the individual grains of a specific mineral, those datasets did not suffer from such difficulties. Analyses performed with the UKBB systems were able confirm the detection of bands from both materials in 40% of cases.

#### *5.5.1.2 Feldspar*

The feldspar bands detected by the EQM are very small in comparison to the quartz band, which occupies a very similar spectral location. Microscope data revealed the presence of some feldspar which did overlap with the quartz band and others that did not. Additional measurements would be necessary to clearly confirm the presence of a specific feldspar in the sample, distinguishing between the similar spectra. A possible minor feldspar band is visible at  $523\text{ cm}^{-1}$ .

Further testing of this sample with the UKBB showed bands at  $471\text{ cm}^{-1}$  and  $511\text{ cm}^{-1}$ , this matches with the peaks at  $478\text{ cm}^{-1}$  and  $509\text{ cm}^{-1}$  from Chapter 4, Section 4.5.5.6. A larger number of acquisitions (30) were required for 2 detections of this feldspar, hence the lack of clear peaks from 2 measurements with the EQM.

#### *5.5.1.3 Silicates*

The silicate samples both exhibit a large quartz band close to  $465\text{ cm}^{-1}$ . However, many of the smaller bands appear to merge together to create one large, wide band in both Sample 7 and Sample 8 (Figure 5.12). Both spectra incorporated high levels of fluorescence, which had to be removed before band analysis and identification was performed. Sample 8 exhibits a main band at  $495\text{ cm}^{-1}$ , rather than the expected  $467\text{ cm}^{-1}$  which was observed in the microscope measurements of the same sample and the UKBB system. This could be related to inaccurate calibration at lower wavenumbers or contamination of the sample with another material. Spectra obtained from Sample 8

also include a wide hydration band at  $3521\text{ cm}^{-1}$  and the implications of this are discussed further in Section 5.5.1.5. The large band observed at  $1075\text{ cm}^{-1}$  in spectra obtained from Sample 7 is close to the band normally associated with calcite. However, none of the minor calcite bands are present.

#### *5.5.1.4 Phyllosilicate*

Talc was selected to be representative of the phyllosilicates detected at the ExoMars landing sites (Quantin et al. 2016; Bishop et al. 2008). The major band and almost all of the sub bands are visible in the EQM talc spectra, including the hydration band. The bands are clear, although wider than those obtained with the microscope based system. There is a large amount of fluorescence produced by the sample and as such, saturation is a major issue for longer detector acquisition times.

Given the wider peaks in the EQM data, it is desirable to determine the representative spectra for distinguishing between similar phyllosilicates via testing numerous phyllosilicates with spectrometers with a similar spectral resolution to RLS.

#### *5.5.1.5 Hydration bands*

The wide spectral range of the RLS instrument was chosen in order to enable detection of the OH and CH bands. These bands were not detectable in any of the 785 nm spectra or in the Advantage 532 nm instrument but were in the 532 nm microscope spectra. The relevant hydration bands are shown below in Figure 5.15.

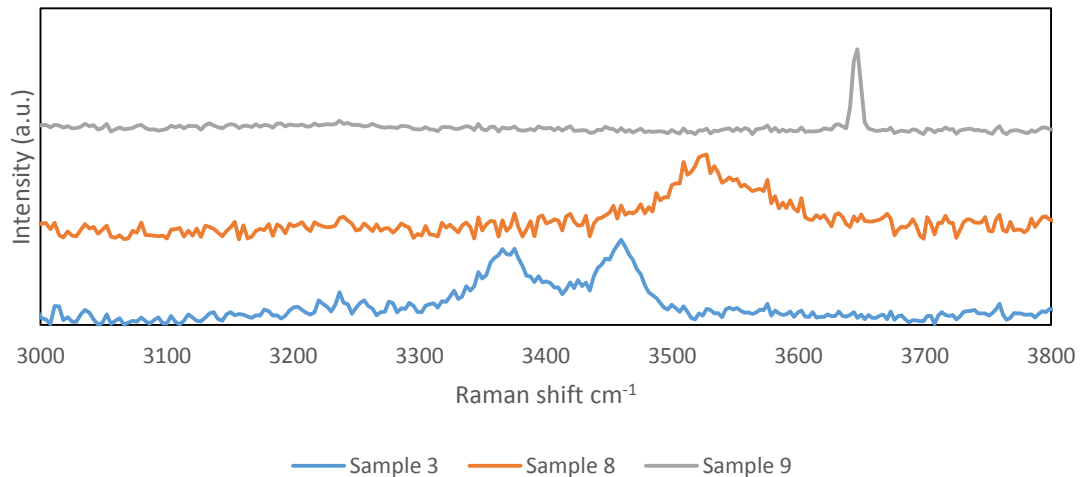


Figure 5.15 Hydration bands in the high spectral range from the EQM

The water band observed during analyses of Sample 8 is wide and has a low signal to noise, indicating the presence of liquid water rather than a component part of a mineral crystal structure. As such, it is likely the result of contamination of the sample and this could also explain the shift in the observed quartz band to  $490\text{ cm}^{-1}$ .

### 5.5.2 Recommendations for RLS

Samples with multiple materials, such as the barite, calcite mixture present in Sample 2 or the mixture of different feldspar materials in Sample 6, which are crushed into powder, will require multiple sampling points to identify heterogeneity in the samples. Since these samples may exhibit large amounts of fluorescence, increasing detector integration times will result in camera saturation, so numerous frames at the same spectral acquisition position will have to be stacked together to obtain spectra with sufficiently high SNR. The work with the UKBB emphasises the importance of large numbers of observation points to successfully detect the features of interest in samples such as these.

Further studies, using analogues appropriate for the proposed landing sites: Mawrth Vallis and Oxia Planum are necessary to ensure fully optimised instrument operation. Given the relatively low spectral resolution of the instrument (compared to instruments

proposed for many previous studies - see, for example, (Wang, Freeman, et al. 2015) bands and features which appear to be well separated in the literature, may merge together in the ExoMars data and therefore detailed characterisation/understanding of the spectral response of the instrument will significantly aid in the development of automatic identification algorithms and detailed spectral analysis (so that appropriate deconvolution algorithms can be implemented).

Further work to corroborate PET calibration for the lower wavelengths (specifically 200 – 800  $\text{cm}^{-1}$ ) is required to facilitate accurate placement of the minor bands for many minerals. The key PET bands are mostly in the 800 – 1700  $\text{cm}^{-1}$  range and so small variations can significantly affect the calibration of the lower wavenumbers significantly. Once a sample has been identified, the known peaks locations can be used to improve the calibration by comparing wavenumber and pixel position.

## 5.6 Conclusion

A set of nine samples from the MURFI field trial samples were selected for analysis with the RLS EQM instrument. This was to assess the capability of RLS to analyse similar samples. The results obtained were compared to those that could be acquired with representative portable instrumentation and laboratory based Raman microscopes. The EQM system was able to produce clear Raman bands for eight of the samples and faint ones for a ninth. Many of the minor bands detected with the microscopes were visible in the EQM data, although the bands were typically wider and therefore closely neighbouring bands occasionally merged together and became confused. This is due to the lower spectral resolution of the EQM instrument. The studies verified that gypsum, anhydrite, barite and talc could be readily and unambiguously detected with the main bands for quartz and calcite visible but with a lower SNR and one possible feldspar spectrum was also obtained. The EQM measurements also demonstrated successful detection of hydrated minerals, thereby satisfying one of the science goals of the RLS instrument: to characterise mineral phases produced by water related processes (Rull et al. 2017).

Additional measurements with the UKBB using more observation points were successful in detecting the mixture of materials present in Sample 2 and both of the feldspar bands in Sample 6. The bands were still distinct when the resolution was reduced to be comparable to that of the EQM instrument design.

This chapter describes recommendations for further RLS testing, specifically with regard to the analysis of a wide collection of phyllosilicates so as best to represent the planned landing site compositions. It was also noted that tests with the EQM 2 should be designed to best simulate Martian operations. When measuring samples that contain more than one component (as many drill cores are likely to), it is crucial that sufficient sampling points are included in order to obtain, clear, unambiguous Raman bands avoiding saturation of the detector caused by the sample fluorescing. Finally, tests with the PET calibration sample should ensure low wave numbers can be accurately calibrated to enable accurate band identification.

## Chapter 6: Conclusion

The overall aim of the work presented in this thesis was to prepare for the launch of ESA's 2020 ExoMars rover, specifically the operation of the Raman Laser Spectrometer (RLS), which will be the first Raman spectroscopy instrument to be used on a planetary mission. In order to fully optimise the operation of the RLS instrument, it is necessary to build a collection of analogue samples that can be used for testing prototype instrumentation, ensuring a useful scientific return for the mission. These analogues need to be representative of the samples that the ExoMars rover is likely to analyse, both molecularly and mineralogically. The studies described in this thesis aimed to assess the RLS' sensitivity limit to minerals in likely Martian combinations in order to determine whether they can be accurately distinguished during in-situ analysis.

NASA's Mars Science Laboratory rover has been conducting an analytical science campaign since landing in 2012. The rover's instruments have conducted chemical analyses with the ChemCam, Laser Induced Breakdown Spectrometer (LIBS) instrument and the Alpha Particle X-ray Spectrometer (APXS) and mineralogical analysis with the CheMin X-Ray Diffractometer XRD instrument. Using these instruments, the Curiosity rover has analysed a vast number of igneous float rocks and sedimentary outcrops. The data returned showed a basalt-trachybasalt igneous trend of compositions reflecting an olivine subtraction fractionation process. The trachybasalt samples which make up an endmember of this trend are rich in alkali feldspar. Work with the ChemCam instrument on MSL was described in Chapter 3 and in Edwards et al. (2017). Moreover, the analyses performed on these samples was used to inform the selection of analogues for RLS testing.

Sites geologically similar to Mars are a valuable source of relevant samples. These sites are found all over the world, including the Rio Tinto in Spain (Fleischer et al. 2008; Cockell et al. 2017), the Atacama desert in Chile (Navarro-González et al. 2003; Wei et al. 2015), and the Utah desert in the USA (Clarke & Stoker 2011). Studies with samples acquired in an analogous field environment will give a representative view of the operational ability of the RLS instrument on Martian samples. Notably, the field site in Utah was selected as the location for the UKSA MURFI (Mars Utah Rover Field

Investigation) rover trials, as detailed in this thesis. Samples were selected from the field site, representing the mineralogical diversity found there, including: quartz, gypsum, anhydrite, barite, celestine, hematite, feldspar and calcite. This work was described in Chapter 4.

A portable Raman spectrometer, representative of flight instrumentation, was deployed in the field during the rover trials. This spectrometer enable quick acquisition of spectra in-situ with a quality of data comparable to the RLS instrumentation. Fifty samples were analysed during the field trials in a manner consistent with a rover mission, with a sub selection returned for full characterisation. These field measurements demonstrated the ability of the representative instrumentation to determine the mineralogy of samples in the field. Though the SNR for some samples was low, it was generally possible to make an identification; if not of the exact mineral, then the group that it belongs to. Fluorescence from the samples was an issue for many of the spectra, but due to the lack of organic material on Mars, this will be less of a constraint (Rull et al. 2017; Chou & Wang 2017) when operating the ExoMars RLS instrument.

In order to comprehensively assess the performance of the RLS instrument, it is necessary to fully characterise the samples with high performance laboratory instruments (i.e. in order to determine to what extent the representative instrumentation was able to determine the actual mineralogical content of the samples). The samples were therefore all fully characterised using both 532 and 785 nm microscope based Raman spectrometer and an XRD facility.

The representative instrumentation spectra had, in general, a lower SNR than the microscope Raman. Using the grain scale analysis, it was possible to measure pure minerals, whereas the larger spot size of the portable spectrometer would sometimes sample multiple materials, leading to complex spectra incorporating bands from both materials. The minor Raman bands were much clearer in the microscope data, often merging into one much broader band in the portable instrument spectra. However, the identifications of the minerals from the field spectra was consistent with that from the laboratory techniques: i.e. the grain scale Raman and the XRD data. Feldspar detected with the representative spectrometer could not be specifically identified. However,

using the microscope data, it was possible to identify the material as labradorite, a feldspar commonly found in the ChemCam data.

Using these data, a sub selection of samples were chosen for analysis with the RLS Engineering Qualification Model (EQM) at INTA in Spain. The EQM replicates the full design of the RLS instrument, providing spectra as close as possible to those that the RLS instrument will obtain once on Mars. The samples were selected to be as representative as possible of those likely to be found at the possible ExoMars rover landing sites. They included five sulphates, representative of Mawrth Vallis (Wray et al. 2010), feldspars representative of those found during MSL studies and two silicate samples and a phyllosilicate sample, representative of materials found in the vicinity of both Mawrth Vallis and Oxia Planum (Quantin et al. 2016). This work was detailed in Chapter 5.

The RLS EQM spectra revealed clear Raman bands for 4 of the 5 sulphate samples, each sufficient for identification of the minerals. The silicates and phyllosilicate samples were also clearly distinguishable, but it was challenging to adequately calibrate the lower wavenumbers with the PET calibration sample. The sulphate sample that contained a mixture of barite and calcite was more challenging to analyse. The calcite bands were readily detectable but not the barite. For the feldspar sample, only one of the two characteristic feldspar bands were visible. Additional measurements performed with another prototype, the RLS UK Breadboard (UKBB). With an increased number of sampling locations, it was demonstrated that it was possible to detect both the barite and the feldspar bands with an RLS style instrument. This campaign demonstrated the ability of RLS to produce useful data from a wide variety of minerals extracted from a Martian analogue site.

Further testing with the replica of the EQM instrument (EQM2) should be continued prior to launch. Additional testing of phyllosilicates will be necessary to determine the capability of the instrument to distinguish between many similar mineralogical structures, given the lower spectral resolution of RLS compared to spectrometers typically used in laboratories. Whilst it is unlikely that biomarker pigments will be detected on Mars, it is possible that geological evidence of habitation could be detected (see, for example, Edwards et al. 2014). Sites with terrestrial extremophiles such as the Rio Tinto in Spain are an excellent source of this type of material.

As a result of this study, a number of recommendations for RLS operation are made. Comparison work on mixture samples between the EQM and UKBB highlighted the necessity for a large number of observation to be made at various locations across the surface of the powdered samples. This will be necessary to ensure that the different materials within the sample are all visible in at least some of the spectra. Further studies with the EQM2 should be performed with a cooled detector to best simulate operating modes. Additional work with calibration at the lower wavenumbers should ensure that the PET calibration target can produce an accurate calibration, particularly for wavenumbers below  $800\text{ cm}^{-1}$ .

Future missions using analytical technique should seek to combine systems, for example the MARS2020 SuperCam instrument, will includes both Raman and LIBS capabilities. This results in lower mass, volume and power budgets than would be possible with two independent instruments, offering the same overall scientific performance. The chemical information obtained with the LIBS component will significantly aid in Raman mineralogical identification. Both techniques have a similar measurement footprint and acquisition times, making them an ideal combination of complementary techniques.

In the future, it is likely that Raman spectroscopy instruments will be deployed on other planets, such as Venus. The short sampling times typically required for the technique make it an ideal candidate for maximising the scientific return of a short duration mission. Europa is also a key target for future astrobiology missions. Raman analysis of ice would provide some depth profiling capability to determine molecular makeup and search for biomarkers. Raman is a technique relevant to any mission to a rock body, and is a valuable tool for planetary exploration.

## References

- Achilles, C.N. et al., 2017. Mineralogy of an Active Eolian Sediment from the Namib Dune, Gale Crater, Mars. *Journal of Geophysical Research: Planets*. Available at: <http://doi.wiley.com/10.1002/2017JE005262> [Accessed July 27, 2017].
- Adams, J.B., 1968. Lunar and martian surfaces: petrologic significance of absorption bands in the near-infrared. *Science (New York, N.Y.)*, 159(3822), pp.1453–5. Available at: <http://science.sciencemag.org/content/159/3822/1453.abstract> [Accessed April 21, 2016].
- Ahlers, B., Hutchinson, I.B. & Inley, R., 2008. Combined Raman/LIBS spectrometer elegant breadboard-built and tested-and flight model spectrometer unit. ... *14-17 October 2008, 1023-1028*. Available at: <http://repository.tudelft.nl/view/tno/uuid:0884d07d-af88-4ac9-b604-eccc49a5e53c/> [Accessed December 14, 2015].
- Allwood, A.C., Wade, L.A. & Hurowitz, J.A., 2016. PIXL Investigation on the Mars 2020 Rover.
- Anders, E., 1968. Chemical processes in the early solar system, as inferred from meteorites. *Accounts of Chemical Research*, 1(10), pp.289–298. Available at: <http://pubs.acs.org/cgi-bin/doilookup/?10.1021/ar50010a001> [Accessed December 12, 2016].
- Anderson, D.L., 1981. Plate tectonics on Venus. *Geophysical Research Letters*, 8(4), pp.309–311. Available at: <http://doi.wiley.com/10.1029/GL008i004p00309> [Accessed December 15, 2016].
- Anderson, J.D. et al., 1998. Europa's Differentiated Internal Structure: Inferences from Four Galileo Encounters. *Science*, 281(5385).
- Anderson, R.C. et al., 2015. ChemCam results from the Shaler outcrop in Gale crater, Mars. *Icarus*, 249(First Year of MSL), pp.2–21. Available at: <https://pubs.er.usgs.gov/publication/70146541> [Accessed December 10, 2015].
- Angel, S.M. et al., 2012. Remote Raman spectroscopy for planetary exploration: a review. *Applied spectroscopy*, 66(2), pp.137–50. Available at: <http://www.ncbi.nlm.nih.gov/pubmed/22449277> [Accessed July 26, 2016].

- Ashcroft, N.W. & Mermin, N.D., 1976. *Solid state physics*, Holt, Rinehart and Winston.
- Baird, A.K. et al., 1977. The Viking X Ray Fluorescence Experiment: Sampling strategies and laboratory simulations. *Journal of Geophysical Research*, 82(28), pp.4595–4624. Available at: <http://doi.wiley.com/10.1029/JS082i028p04595> [Accessed July 11, 2016].
- Baker, I., 1969. Petrology of the Volcanic Rocks of Saint Helena Island, South Atlantic. *Geological Society of America Bulletin*, 80(7), p.1283. Available at: <http://gsabulletin.gsapubs.org/content/80/7/1283> [Accessed April 11, 2016].
- Balme, M.R. et al., 2006. Orientation and distribution of recent gullies in the southern hemisphere of Mars: Observations from High Resolution Stereo Camera/Mars Express (HRSC/MEX) and Mars Orbiter Camera/Mars Global Surveyor (MOC/MGS) data. *Journal of Geophysical Research*, 111(E5), p.E05001. Available at: <http://doi.wiley.com/10.1029/2005JE002607> [Accessed February 27, 2017].
- Balme, M.R. et al., 2017. UK Space Agency “Mars Utah Rover Field Investigation 2016” (MURFI 2016): Overview of Mission, Aims, and Progress. *48th Lunar and Planetary Science Conference, held 20-24 March 2017, at The Woodlands, Texas. LPI Contribution No. 1964, id.1837, 48.* Available at: <http://adsabs.harvard.edu/abs/2017LPI....48.1837B> [Accessed August 9, 2017].
- Bandfield, J.L., 2004. Identification of quartzofeldspathic materials on Mars. *Journal of Geophysical Research*, 109(E10), p.E10009. Available at: <http://doi.wiley.com/10.1029/2004JE002290> [Accessed May 5, 2016].
- Bandfield, J.L., Hamilton, V. & Christensen, P.R., 2000. A Global View of Martian Surface Compositions from MGS-TES. *Science*, 287(5458), pp.1626–1630. Available at: <http://science.sciencemag.org/content/287/5458/1626.abstract> [Accessed April 21, 2016].
- Banerdt, W. & Smrekar, S., 2013. InSight: A Discovery mission to explore the interior of Mars. *Lunar and Planetary ...* Available at: <http://adsabs.harvard.edu/abs/2013LPICo1719.1915B> [Accessed December 18, 2015].
- Banerdt, W.B. et al., 1982. Thick shell tectonics on one-plate planets: Applications to Mars. *Journal of Geophysical Research*, 87(B12), p.9723. Available at: <http://doi.wiley.com/10.1029/JB087iB12p09723> [Accessed April 28, 2016].

- Banham, S., 2017. Personal communications.
- Banks, M., 2016. European–Russian Mars lander feared lost. *Physics World*, 29(11), pp.8–8. Available at: <http://stacks.iop.org/2058-7058/29/i=11/a=13?key=crossref.8358c8ecf869edc72cd402763f24f999> [Accessed May 30, 2017].
- Barlow, N., 2008. Mars: An Introduction to its Interior, Surface and Atmosphere | Planetary Science | Cambridge University Press. *Cambridge Planetary Science*. Available at: <http://www.cambridge.org/gb/academic/subjects/astronomy/planetary-science/mars-introduction-its-interior-surface-and-atmosphere?format=HB&isbn=9780521852265>.
- Barnes, D. et al., 2006. The ExoMars rover and Pasteur payload Phase A study: an approach to experimental astrobiology. *International Journal of Astrobiology*, 5(3), p.221. Available at: [http://www.journals.cambridge.org/abstract\\_S1473550406003090](http://www.journals.cambridge.org/abstract_S1473550406003090) [Accessed January 3, 2017].
- Baross, J.A. & Hoffman, S.E., 1985. Submarine hydrothermal vents and associated gradient environments as sites for the origin and evolution of life. *Origins of Life and Evolution of the Biosphere*, 15(4), pp.327–345. Available at: <http://link.springer.com/10.1007/BF01808177> [Accessed December 14, 2016].
- Le Bas, M.J. et al., 1986. A Chemical Classification of Volcanic Rocks Based on the Total Alkali-Silica Diagram. *Journal of Petrology*, 27(3), pp.745–750.
- Basilevsky, A.T. & Head, J.W., 2003. The surface of Venus. *Reports on Progress in Physics*, 66(10), pp.1699–1734. Available at: <http://stacks.iop.org/0034-4885/66/i=10/a=R04?key=crossref.315eb5a139ca509ffceef73b6091bce9> [Accessed May 24, 2016].
- Bazalgette Courrèges-Lacoste, G. et al., 2007. Combined Raman spectrometer/laser-induced breakdown spectrometer for the next ESA mission to Mars. *Spectrochimica acta. Part A, Molecular and biomolecular spectroscopy*, 68(4), pp.1023–1028. Available at: <http://www.ncbi.nlm.nih.gov/pubmed/17466575> [Accessed December 10, 2015].
- Beckhoff, B., 2006. *Handbook of practical X-ray fluorescence analysis*, Springer.

- Beegle, L.W. et al., 2014. SHERLOC: Scanning Habitable Environments With Raman & Luminescence for Organics & Chemicals, an Investigation for 2020. *American Geophysical Union, Fall Meeting 2014, abstract #P24A-06.*
- Beegle, L.W. et al., 2015. SHERLOC: Scanning habitable environments with Raman & luminescence for organics & chemicals. In *2015 IEEE Aerospace Conference*. IEEE, pp. 1–11. Available at: <http://ieeexplore.ieee.org/lpdocs/epic03/wrapper.htm?arnumber=7119105> [Accessed July 26, 2016].
- Bellar, T.A. & Lichtenberg, J.J., 1974. Determining Volatile Organics at Microgram-per-Litre Levels by Gas Chromatographs (PDF). *Journal - American Water Works Association*, 66(12), pp.739–744.
- Berman, D. & Hartmann, W.K., 2002. Recent Fluvial, Volcanic, and Tectonic Activity on the Cerberus Plains of Mars. *Icarus*, 159(1), pp.1–17. Available at: <http://linkinghub.elsevier.com/retrieve/pii/S0019103502969204> [Accessed February 27, 2017].
- Bibring, J.-P. et al., 2007. CIVIA. *Space Science Reviews*, 128(1–4), pp.397–412. Available at: <http://link.springer.com/10.1007/s11214-006-9135-5> [Accessed December 29, 2016].
- Bibring, J.-P. et al., 2006. Global Mineralogical and Aqueous Mars History Derived from OMEGA/Mars Express Data. *Science*, 312(5772).
- Bibring, J.-P. & Erard, S., 2001. The Martian Surface Composition. *Space Science Reviews*, 96(1–4), pp.293–316. Available at: <http://link.springer.com/article/10.1023/A%3A1011909708806> [Accessed April 21, 2016].
- Biesbroek, R. & Janin, G., 2000. Ways to the Moon? , 103.
- Bish, D.L. et al., 2007. Field XRD/XRF Mineral Analysis by the MSL CheMin Instrument. *38th Lunar and Planetary Science Conference, (Lunar and Planetary Science XXXVIII), held March 12-16, 2007 in League City, Texas. LPI Contribution No. 1338, p.1163*, 38, p.1163.
- Bish, D.L. et al., 2013. X-ray diffraction results from Mars Science Laboratory: mineralogy of Rocknest at Gale crater. *Science (New York, N.Y.)*, 341(6153), p.1238932. Available at: <http://www.ncbi.nlm.nih.gov/pubmed/24072925> [Accessed July 27,

- 2016].
- Bishop, J.L. et al., 2008. Phyllosilicate Diversity and Past Aqueous Activity Revealed at Mawrth Vallis, Mars. *Science*, 321(5890). Available at: <http://science.sciencemag.org/content/321/5890/830> [Accessed September 1, 2017].
- Bisikalo, D.V. et al., 2017. Influence of the crustal magnetic field on the Mars aurora electron flux and UV brightness. *Icarus*, 282, pp.127–135.
- Blake, D.F. et al., 2012. Characterization and Calibration of the CheMin Mineralogical Instrument on Mars Science Laboratory. *Space Science Reviews*, 170(1–4), pp.341–399. Available at: <http://link.springer.com/10.1007/s11214-012-9905-1> [Accessed November 19, 2013].
- Blake, D.F., 1999. REMOTE X-RAY DIFFRACTION AND X-RAY FLUORESCENCE ANALYSIS ON PLANETARY SURFACES.
- Blake, F. et al., 2009. The CheMin Mineralogical Instrument on the Mars Science Laboratory. *Lunar and Planetary Science Conference.*, 40.
- Blaney, D.L., Wiens, R.C., Maurice, S., Clegg, S.M., Anderson, R.B., Kah, L.C., et al., 2014. *Chemistry and texture of the rocks at Rocknest, Gale Crater: Evidence for sedimentary origin and diagenetic alteration*, American Geophysical Union. Available at: [http://authors.library.caltech.edu/50548/20/jgre20297-sup-0005-FigureS3\\_part3\\_Blaneyetal.tiff](http://authors.library.caltech.edu/50548/20/jgre20297-sup-0005-FigureS3_part3_Blaneyetal.tiff) [Accessed December 10, 2015].
- Blaney, D.L., Wiens, R.C., Maurice, S., Clegg, S.M., Anderson, R.B., Kahn, L.C., et al., 2014. Rocknest, Bradbury Plateau, and Kimberly: Iron Cemented Sediments Observed in Gale Crater with ChemCam. *Eighth International Conference on Mars, held July 14–18, 2014 in Pasadena, California. LPI Contribution No. 1791*, p.1258, 1791, p.1258.
- Blatt, H., Tracy, R. & Brent, O., 2006. *PETROLOGY: IGNEOUS, SEDIMENTARY AND METAMORPHIC.*, W.H. Freeman.
- Bowes, D.R., 1989. Trachyandesite, trachybasalt. In *Petrology*. Dordrecht: Kluwer Academic Publishers, pp. 570–571. Available at: [http://www.springerlink.com/index/10.1007/0-387-30845-8\\_243](http://www.springerlink.com/index/10.1007/0-387-30845-8_243) [Accessed August 19, 2017].
- Brack, A., 1993. Liquid water and the origin of life. *Origins of Life and Evolution of the Biosphere*, 23(1), pp.3–10. Available at:

- <http://link.springer.com/10.1007/BF01581985> [Accessed May 16, 2016].
- Braun, R.D. & Manning, R.M., 2006. Mars Exploration Entry, Descent and Landing Challenges. In *2006 IEEE Aerospace Conference*. IEEE, pp. 1–18. Available at: <http://ieeexplore.ieee.org/document/1655790/> [Accessed December 14, 2016].
- Breuer, D., Spohn, T. & Wüllner, U., 1993. Mantle differentiation and the crustal dichotomy of Mars. *Planetary and Space Science*, 41(4), pp.269–283.
- Bridges, J.C. & Warren, P., 2006. The SNC meteorites: basaltic igneous processes on Mars. *Journal of the Geological Society*. Available at: [http://oro.open.ac.uk/71/1/Bridges-Warren-revised.\\_Jour\\_of\\_geo\\_soc\\_spec\\_iss.pdf](http://oro.open.ac.uk/71/1/Bridges-Warren-revised._Jour_of_geo_soc_spec_iss.pdf) [Accessed December 10, 2015].
- Bridges, N.T., Crisp, J.A. & Bell, J.F., 2001. Characteristics of the Pathfinder APXS sites: Implications for the composition of Martian rocks and soils. *Journal of Geophysical Research: Planets*, 106(E7), pp.14621–14665. Available at: <http://doi.wiley.com/10.1029/2000JE001393> [Accessed December 26, 2016].
- Brinckerhoff, W.B. et al., 2013. Mars Organic Molecule Analyzer (MOMA) mass spectrometer for ExoMars 2018 and beyond. In *2013 IEEE Aerospace Conference*. IEEE, pp. 1–8. Available at: <http://ieeexplore.ieee.org/lpdocs/epic03/wrapper.htm?arnumber=6496942> [Accessed August 11, 2016].
- Bruker, 2017. DIFFRAC.EVA. <https://www.bruker.com/products/x-ray-diffraction-and-elemental-analysis/x-ray-diffraction/xrd-software/eva/overview.html>.
- Burgess, K. D., Musselwhite, D. S. & Treiman, A. H., 2006. Experimental Petrology of Olivine-Phyric Shergottite NWA 1068: Toward Defining a Parental Melt. *37th Annual Lunar and Planetary Science Conference*. Available at: <http://adsabs.harvard.edu/abs/2006LPI....37.1972B> [Accessed April 26, 2016].
- Campbell, J.L. et al., 2012. Calibration of the Mars Science Laboratory Alpha Particle X-ray Spectrometer. *Space Science Reviews*, 170(1–4), pp.319–340. Available at: <http://link.springer.com/10.1007/s11214-012-9873-5> [Accessed November 19, 2013].
- Carr, M.H. et al., 1998. Evidence for a subsurface ocean on Europa. *Nature*, 391(6665), pp.363–5. Available at: <http://www.nature.com/doi/10.1038/34857> [Accessed April 14, 2016].

- Carr, M.H., 1999. Retention of an atmosphere on early Mars. *Journal of Geophysical Research: Planets*, 104(E9), pp.21897–21909. Available at: <http://doi.wiley.com/10.1029/1999JE001048> [Accessed May 20, 2016].
- Carr, M.H., 2012. The fluvial history of Mars. *Phil. Trans. R. Soc. A*. Available at: <http://rsta.royalsocietypublishing.org/content/370/1966/2193.short> [Accessed May 25, 2017].
- Carr, M.H. & Head, J.W., 2010. *Geologic history of Mars*,
- Carter, J. & Poulet, F., 2013. Ancient plutonic processes on Mars inferred from the detection of possible anorthositic terrains. *Nature Geoscience*, 6(12), pp.1008–1012. Available at: <http://dx.doi.org/10.1038/ngeo1995> [Accessed March 14, 2016].
- Cavanagh, P.D.D. et al., 2015. Confidence Hills mineralogy and CheMin results from base of Mt. Sharp, Pahrump Hills, Gale Crater, Mars. Available at: <https://ntrs.nasa.gov/search.jsp?R=20150002841> [Accessed December 27, 2016].
- Cavicchioli, R. et al., 2011. Life and applications of extremophiles. *Environmental Microbiology*, 13(8), pp.1903–1907. Available at: <http://doi.wiley.com/10.1111/j.1462-2920.2011.02512.x> [Accessed December 14, 2016].
- Chapman, C.R., Pollack, J.B. & Sagan, C., 1969. An Analysis of the Mariner-4 Cratering Statistics. *The Astronomical Journal*, 74, p.1039. Available at: [http://adsabs.harvard.edu/cgi-bin/bib\\_query?1969AJ.....74.1039C](http://adsabs.harvard.edu/cgi-bin/bib_query?1969AJ.....74.1039C) [Accessed December 14, 2016].
- Chassefiere, E., 1997. Loss of Water on the Young Venus: The Effect of a Strong Primitive Solar Wind☆. *Icarus*, 126(1), pp.229–232. Available at: <http://www.sciencedirect.com/science/article/pii/S0019103597956773> [Accessed May 16, 2016].
- Chou, I. & Wang, A., 2017. Application of laser Raman micro-analyses to Earth and planetary materials. *Journal of Asian Earth Sciences*, 145, pp.309–333. Available at: <http://www.sciencedirect.com/science/article/pii/S1367912017303425#b0890> [Accessed September 22, 2017].
- Chyba, C.F., 2000. Energy for microbial life on Europa. *Nature*, 403(6768), pp.381–2. Available at: <http://dx.doi.org/10.1038/35000281> [Accessed April 14, 2016].

- Chyba, C.F. & Phillips, C.B., 2002. Europa as an Abode of Life. *Origins of life and evolution of the biosphere*, 32(1), pp.47–67. Available at: <http://link.springer.com/article/10.1023/A%3A1013958519734> [Accessed April 14, 2016].
- Clark, B. et al., 1977. The Viking X Ray Fluorescence Experiment: Analytical methods and early results. *Journal of Geophysical Research*, 82(28), pp.4577–4594. Available at: <http://doi.wiley.com/10.1029/JS082i028p04577> [Accessed July 11, 2016].
- Clark, K., Stankov, A. & Pappalardo, R., 2009. The Europa Jupiter System mission. *EGU General*. Available at: <http://adsabs.harvard.edu/abs/2009EGUGA..1113998C> [Accessed September 4, 2017].
- Clarke, J.D.A. & Stoker, C.R., 2011. Concretions in exhumed and inverted channels near Hanksville Utah: implications for Mars. *International Journal of Astrobiology*, 10(3), pp.161–175. Available at: [http://www.journals.cambridge.org/abstract\\_S1473550411000048](http://www.journals.cambridge.org/abstract_S1473550411000048) [Accessed March 1, 2017].
- Clarke, J.T. et al., 1998. Hubble Space Telescope imaging of Jupiter’s UV aurora during the Galileo orbiter mission. *Journal of Geophysical Research: Planets*, 103(E9), pp.20217–20236. Available at: <http://doi.wiley.com/10.1029/98JE01130> [Accessed December 7, 2016].
- Clegg, S.M. et al., 2014. Expansion of the ChemCam Calibration Database. *45th Lunar and Planetary Science Conference, held 17-21 March, 2014 at The Woodlands, Texas. LPI Contribution No. 1777, p.2378, 45, p.2378.*
- Clegg, S.M. et al., 2016. Recalibration of the Mars Science Laboratory ChemCam Instrument with an Expanded Geochemical Database. *Spectrochimica Acta Part B: Atomic Spectroscopy*, In Press, pp.64–85. Available at: <http://linkinghub.elsevier.com/retrieve/pii/S0584854716303913> [Accessed January 3, 2017].
- Clegg, S.M. et al., 2017. Sulfur Chemical Analysis and Interpretation with ChemCam on the Curiosity Rover. *48th Lunar and Planetary Science Conference, held 20-24 March 2017, at The Woodlands, Texas. LPI Contribution No. 1964, id.2439, 48.* Available at: <http://adsabs.harvard.edu/abs/2017LPI....48.2439C> [Accessed July 25, 2017].

- Clifford, S.M., 2001. The Evolution of the Martian Hydrosphere: Implications for the Fate of a Primordial Ocean and the Current State of the Northern Plains. *Icarus*, 154(1), pp.40–79. Available at: <http://linkinghub.elsevier.com/retrieve/doi/10.1006/icar.2001.6671> [Accessed February 27, 2017].
- Cockell, C.S. et al., 2017. Anaerobic microorganisms in astrobiological analogue environments: from field site to culture collection. *International Journal of Astrobiology*, pp.1–15. Available at: [https://www.cambridge.org/core/product/identifier/S1473550417000246/type/journal\\_article](https://www.cambridge.org/core/product/identifier/S1473550417000246/type/journal_article) [Accessed August 13, 2017].
- Cockell, C.S., 1999. Life on Venus. *Planetary and Space Science*, 47(12), pp.1487–1501. Available at: <http://www.sciencedirect.com/science/article/pii/S0032063399000367> [Accessed May 24, 2016].
- Colthup, N.B., Daly, L.H. & Wiberley, S.E., 1975. *Introduction to infrared and Raman spectroscopy*, Academic Press.
- Connerney, J. et al., 2001. The global magnetic field of Mars and implications for crustal evolution. *Geophysical Research Letters*, 28(21), pp.4015–4018. Available at: <http://doi.wiley.com/10.1029/2001GL013619> [Accessed December 16, 2016].
- Costard, F. et al., 2002. Formation of Recent Martian Debris Flows by Melting of Near-Surface Ground Ice at High Obliquity. *Science*, 295(5552).
- Cousin, A. et al., 2017. Classification of igneous rocks analyzed by ChemCam at Gale crater, Mars. *Icarus*, 288, pp.265–283. Available at: <http://linkinghub.elsevier.com/retrieve/pii/S0019103516304572> [Accessed June 14, 2017].
- Cousin, A. et al., 2011. Laser induced breakdown spectroscopy library for the Martian environment. *Spectrochimica Acta Part B: Atomic Spectroscopy*, 66(11), pp.805–814.
- Cox, K.G., Bell, J.D. & Pankhurst, R.J., 1979. *The Interpretation of Igneous Rocks*, Dordrecht: Springer Netherlands. Available at: <http://link.springer.com/10.1007/978-94-017-3373-1> [Accessed December 14, 2016].

- Cox, K.G., Gass, I.G. & Mallick, D.I.J., 1970. The Peralkaline Volcanic Suite of Aden and Little Aden, South Arabia. *Journal of Petrology*, 11(3), pp.433–462. Available at: <http://petrology.oxfordjournals.org/content/11/3/433.short> [Accessed April 28, 2016].
- Craddock, R.A. & Howard, A.D., 2002. The case for rainfall on a warm, wet early Mars. *Journal of Geophysical Research: Planets*, 107(E11), pp.21-1-21–36. Available at: <http://doi.wiley.com/10.1029/2001JE001505> [Accessed May 20, 2016].
- Cremers, D.A. & Radziemski, L.J., 2013. Handbook of Laser-Induced Breakdown Spectroscopy. , p.432. Available at: [http://bib.convdocs.org/docs/18/17920/conv\\_1/file1.pdf](http://bib.convdocs.org/docs/18/17920/conv_1/file1.pdf) [Accessed December 10, 2015].
- Debras-Guédon, J. & Liodec, N., 1962. De l'utilisation du faisceau d'un amplificateur a ondes lumineuses par emission induite de rayonnement (laser a rubis), comme source energetique pour l'excitation des spectres d'emission des elements. *C.R. Acad. Sci.*, 257, pp.3336–3339.
- Deer, W.A., Howie, R.A. & Zussman, J., 1966. *An introduction to the rock-forming minerals*, Longmans.
- Dehant, V. et al., 2007. Planetary Magnetic Dynamo Effect on Atmospheric Protection of Early Earth and Mars. In Springer New York, pp. 279–300. Available at: [http://link.springer.com/10.1007/978-0-387-74288-5\\_10](http://link.springer.com/10.1007/978-0-387-74288-5_10) [Accessed December 14, 2016].
- Dehouck, E. et al., 2017. Probing Crystalline and Amorphous Phases at Yellowknife Bay, Gale Crater, Mars: Comparison of ChemCam LIBS Data with CheMin XRD Results. *48th Lunar and Planetary Science Conference, held 20-24 March 2017, at The Woodlands, Texas. LPI Contribution No. 1964, id.2268*, 48. Available at: <http://adsabs.harvard.edu/abs/2017LPI....48.2268D> [Accessed September 23, 2017].
- Le Deit, L. et al., 2016. The potassic sedimentary rocks in Gale Crater, Mars, as seen by ChemCam on board Curiosity. *Journal of Geophysical Research: Planets*. Available at: <http://doi.wiley.com/10.1002/2015JE004987> [Accessed May 27, 2016].
- Delong, S.E. & Hoffman, M.A., 1975. Alkali/Silica Distinction between Hawaiian Tholeiites and Alkali Basalts. *Geological Society of America Bulletin*, 86(8), pp.1101–

1108. Available at:  
[https://www.researchgate.net/publication/249524829\\_AlkaliSilica\\_Distinction\\_between\\_Hawaiian\\_Tholeiites\\_and\\_Alkali\\_Basalts](https://www.researchgate.net/publication/249524829_AlkaliSilica_Distinction_between_Hawaiian_Tholeiites_and_Alkali_Basalts) [Accessed December 10, 2015].
- Dorizon, S. et al., 2013. WISDOM GPR aboard the ExoMars rover : a powerful instrument to investigate the state and distribution of water in the Martian shallow subsurface. *American Geophysical Union, Fall Meeting 2013, abstract #P43D-07*. Available at: <http://adsabs.harvard.edu/abs/2013AGUFM.P43D..07D> [Accessed May 18, 2017].
- Dougherty, M.K. et al., 2011. JUICE (JUperiter ICy moon Explorer): a European-led mission to the Jupiter system. *EPSC-DPS Joint Meeting 2011, held 2-7 October 2011 in Nantes, France*. <http://meetings.copernicus.org/epsc-dps2011>, p.1343, p.1343. Available at: <http://adsabs.harvard.edu/abs/2011epsc.conf.1343D> [Accessed May 26, 2017].
- Dougherty, M.K. et al., 2012. JUperiter ICy moons Explorer (juice): AN ESA L-Class Mission Candidate to the Jupiter System. *EGU General Assembly 2012*. Available at: <http://adsabs.harvard.edu/abs/2012EGUGA..14.2260D> [Accessed April 14, 2016].
- Dreibus, G. & Wänke, H., 1985. Mars, a volatile-rich planet. *Meteoritics (ISSN 0026-1114)*, 20, pp.367–381. Available at: <http://adsabs.harvard.edu/abs/1985Metic..20..367D> [Accessed May 5, 2016].
- Dunn, T.L., McSween, H.Y. & Christensen, P.R., 2007. Thermal emission spectra of terrestrial alkaline volcanic rocks: Applications to Martian remote sensing. *Journal of Geophysical Research*, 112(E5), p.E05001. Available at: <http://doi.wiley.com/10.1029/2006JE002766> [Accessed May 6, 2016].
- Edgett, K.S. et al., 2012. Curiosity’s Mars Hand Lens Imager (MAHLI) Investigation. *Space Science Reviews*, 170(1–4), pp.259–317. Available at: <http://link.springer.com/10.1007/s11214-012-9910-4> [Accessed November 19, 2013].
- Edwards, H.G.M. et al., 2014. Biomarkers and their Raman spectroscopic signatures: a spectral challenge for analytical astrobiology. *Philosophical transactions. Series A, Mathematical, physical, and engineering sciences*, 372(2030), p.20140193. Available at: <http://www.ncbi.nlm.nih.gov/pubmed/25368349> [Accessed September 20, 2017].
- Edwards, H.G.M. et al., 2005. FT–Raman spectroscopic study of calcium-rich and

- magnesium-rich carbonate minerals. *Spectrochimica Acta Part A: Molecular and Biomolecular Spectroscopy*, 61(10), pp.2273–2280. Available at: <http://linkinghub.elsevier.com/retrieve/pii/S1386142505000752> [Accessed July 26, 2016].
- Edwards, H.G.M. et al., 2000. Vibrational Raman spectroscopic study of scytonemin, the UV-protective cyanobacterial pigment. *Spectrochimica Acta Part A: Molecular and Biomolecular Spectroscopy*, 56(1), pp.193–200. Available at: <http://www.sciencedirect.com/science/article/pii/S1386142599002188> [Accessed May 26, 2017].
- Edwards, H.G.M., Drummond, L. & Russ, J., 1998. Fourier-transform Raman spectroscopic study of pigments in native American Indian rock art: Seminole Canyon. *Spectrochimica Acta Part A: Molecular and Biomolecular Spectroscopy*, 54(12), pp.1849–1856.
- Edwards, H.G.M., Hutchinson, I.B. & Ingley, R., 2012. The ExoMars Raman spectrometer and the identification of biogeological spectroscopic signatures using a flight-like prototype. *Analytical and Bioanalytical Chemistry*, 404(6–7), pp.1723–31. Available at: <http://www.ncbi.nlm.nih.gov/pubmed/22865011> [Accessed December 13, 2013].
- Edwards, K.J., 2000. An Archaeal Iron-Oxidizing Extreme Acidophile Important in Acid Mine Drainage. *Science*, 287(5459), pp.1796–1799. Available at: <http://science.sciencemag.org/content/287/5459/1796.abstract> [Accessed March 18, 2016].
- Edwards, P.H. et al., 2017. Basalt-Trachybasalt Samples from Gale Crater, Mars. *Meteoritics & Planetary Science*.
- Edwards, P.H. et al., Raman Spectroscopy on the MURFI UKSA rover trials.
- Elkins, L. & Grove, T.L., 1990. Ternary feldspar experiments and thermodynamic models. *American Mineralogist*. Available at: <http://asu.pure.elsevier.com/en/publications/ternary-feldspar-experiments-and-thermodynamic-models> [Accessed August 22, 2017].
- Ellery, A. & Wynn-Williams, D., 2003. Why Raman Spectroscopy on Mars?—A Case of the Right Tool for the Right Job. *Astrobiology*, 3(3), pp.565–579. Available at: <http://www.liebertonline.com/doi/abs/10.1089/153110703322610654> [Accessed

- January 5, 2017].
- ESA, 2016. Schiaparelli landing investigation makes progress / ExoMars / Space Science / Our Activities / ESA. Available at: [http://www.esa.int/Our\\_Activities/Space\\_Science/ExoMars/Schiaparelli\\_landing\\_investigation\\_makes\\_progress](http://www.esa.int/Our_Activities/Space_Science/ExoMars/Schiaparelli_landing_investigation_makes_progress) [Accessed January 3, 2017].
- Eshelman, E.J., 2016. Stand-Off Detection of Organic Compounds on Mars Using Ultraviolet Raman Spectroscopy and Time-Resolved Laser-Induced Fluorescence.
- Fabre, C. et al., 2014. In situ calibration using univariate analyses based on the onboard ChemCam targets: first prediction of Martian rock and soil compositions. *Spectrochimica Acta Part B: Atomic Spectroscopy*, 99, pp.34–51. Available at: <http://www.sciencedirect.com/science/article/pii/S0584854714000901> [Accessed February 18, 2014].
- Farmer, J.D., Davies, D.W. & Laporte, D.D., 1976. Mars: Northern Summer Ice Cap—Water Vapor Observations from Viking 2. *Science*, 194(4271).
- Fassett, C. & Head, J.W., 2008a. The timing of martian valley network activity: Constraints from buffered crater counting. *Icarus*, 195(1), pp.61–89.
- Fassett, C. & Head, J.W., 2008b. Valley network-fed, open-basin lakes on Mars: Distribution and implications for Noachian surface and subsurface hydrology. *Icarus*, 198(1), pp.37–56.
- Fassett, C. & Head, J.W., 2006. Valleys on Hecates Tholus, Mars: origin by basal melting of summit snowpack. *Planetary and Space Science*, 54(4), pp.370–378.
- Ferri, F. et al., 2017. Atmospheric Mars Entry and Landing Investigations & Analysis (AMELIA) by ExoMars 2016 Schiaparelli Entry Descent Module. Available at: [http://oro.open.ac.uk/48861/1/Ferri\\_MAMOGGranada2017.pdf](http://oro.open.ac.uk/48861/1/Ferri_MAMOGGranada2017.pdf) [Accessed May 30, 2017].
- Filiberto, J. et al., 2012. Geochemistry of intermediate olivine-phyric shergottite Northwest Africa 6234, with similarities to basaltic shergottite Northwest Africa 480 and olivine-phyric shergottite Northwest Africa 2990. *Meteoritics & Planetary Science*, 47(8), pp.1256–1273. Available at: <http://doi.wiley.com/10.1111/j.1945-5100.2012.01382.x> [Accessed April 26, 2016].
- Filiberto, J. & Dasgupta, R., 2012. Constraints on the Depths and Thermal Vigor of Basalt Formation in the Martian Mantle. *The Mantle of Mars: Insights from Theory*.

- Available at: <http://adsabs.harvard.edu/abs/2012LPICo1684...11F> [Accessed May 26, 2016].
- Filiberto, J. & Dasgupta, R., 2015. Constraints on the depth and thermal vigor of melting in the Martian mantle. *Journal of Geophysical Research: Planets*, 120(1), pp.109–122. Available at: <http://doi.wiley.com/10.1002/2014JE004745> [Accessed May 5, 2016].
- Filiberto, J. & Dasgupta, R., 2011. Fe<sup>2+</sup>–Mg partitioning between olivine and basaltic melts: Applications to genesis of olivine-phyric shergottites and conditions of melting in the Martian interior. *Earth and Planetary Science Letters*, 304(3–4), pp.527–537. Available at: <http://www.sciencedirect.com/science/article/pii/S0012821X11001002> [Accessed May 5, 2016].
- Filiberto, J., Treiman, A.H. & Le, L., 2008. Crystallization experiments on a Gusev Adirondack basalt composition. *Meteoritics & Planetary Science*, 43(7), pp.1137–1146. Available at: <http://doi.wiley.com/10.1111/j.1945-5100.2008.tb01118.x> [Accessed May 5, 2016].
- Fleischer, I., Klingelhofer, G. & Rull, F., 2008. Sulfate minerals from two Mars analogue sites Rio Tinto and Jaroso Ravine, Spain, investigated by Mossbauer and Raman spectroscopy. *Eur. Planet. Sci.* Available at: <http://meetings.copernicus.org/epsc2008/crawl/abstracts/EPSC2008/00530/EPSC2008-A-00530-1.pdf> [Accessed August 8, 2017].
- Floyd, P.A., Castillo, P.R. & Pringle, M., 1991. Tholeiitic and alkalic basalts of the oldest Pacific Ocean crust. *Terra Nova*, 3(3), pp.257–265. Available at: <http://doi.wiley.com/10.1111/j.1365-3121.1991.tb00143.x> [Accessed May 23, 2016].
- Francis, R., Estlin, T., et al., 2017. AEGIS autonomous targeting for ChemCam on Mars Science Laboratory: Deployment and results of initial science team use. *Science Robotics*, 2(7). Available at: <http://robotics.sciencemag.org/content/2/7/eaan4582> [Accessed September 9, 2017].
- Francis, R. et al., 2015. AEGIS autonomous targeting for the Curiosity rover's ChemCam instrument. In *2015 IEEE Applied Imagery Pattern Recognition Workshop (AIPR)*. IEEE, pp. 1–5. Available at: <http://ieeexplore.ieee.org/document/7444544/>

[Accessed December 30, 2016].

- Francis, R., Gaines, D. & Osinski, G.R., 2017. Advanced Rover Science Autonomy Experiments in Preparation for The Mars 2020 Mission: Results from the 2016 CanMars Analogue Mission. *Lunar and Planetary Science*, XLVIII, p.2402. Available at: <https://www.hou.usra.edu/meetings/lpsc2017/pdf/2402.pdf> [Accessed August 25, 2017].
- Freeman, J.J. et al., 2008. Characterization Of Natural Feldspars By Raman Spectroscopy For Future Planetary Exploration. *The Canadian Mineralogist*, 46(6), pp.1477–1500. Available at: <http://www.canmin.org/cgi/doi/10.3749/canmin.46.6.1477> [Accessed July 26, 2016].
- Friedman, H. & Birks, L.S., 1948. A Geiger Counter Spectrometer for X-Ray Fluorescence Analysis. *Review of Scientific Instruments*, 19(5), pp.323–330. Available at: <http://aip.scitation.org/doi/10.1063/1.1741258> [Accessed May 30, 2017].
- Gabani, P. & Singh, O. V., 2013. Radiation-resistant extremophiles and their potential in biotechnology and therapeutics. *Applied Microbiology and Biotechnology*, 97(3), pp.993–1004. Available at: <http://link.springer.com/10.1007/s00253-012-4642-7> [Accessed September 20, 2017].
- Gale, A. et al., 2013. The mean composition of ocean ridge basalts. *Geochemistry, Geophysics, Geosystems*, 14(3), pp.489–518. Available at: <http://doi.wiley.com/10.1029/2012GC004334> [Accessed April 4, 2016].
- Gardner, J.P. et al., 2006. The James Webb Space Telescope. *Space Science Reviews*, 123(4), pp.485–606. Available at: <http://link.springer.com/10.1007/s11214-006-8315-7> [Accessed December 7, 2016].
- Gasda, P.J. et al., 2016. Identification of Fresh Feldspars in Gale Crater Using ChemCam. *47th Lunar and Planetary Science Conference*, 47, p.1604. Available at: <http://www.hou.usra.edu/meetings/lpsc2016/pdf/1604.pdf> [Accessed April 4, 2016].
- Gast, P.W., 1968. Trace element fractionation and the origin of tholeiitic and alkaline magma types. *Geochimica et Cosmochimica Acta*, 32(10), pp.1057–1086. Available at: <http://www.sciencedirect.com/science/article/pii/0016703768901087> [Accessed April 28, 2016].
- Gehrels, N. et al., 2004. The Swift Gamma-Ray Burst Mission. *The Astrophysical Journal*,

- 611(2), pp.1005–1020. Available at: <http://stacks.iop.org/0004-637X/611/i=2/a=1005> [Accessed December 7, 2016].
- Gellert, R. et al., 2006. Alpha Particle X-Ray Spectrometer (APXS): Results from Gusev crater and calibration report. *Journal of Geophysical Research: Planets*, 111(E2), p.n/a-n/a. Available at: <http://doi.wiley.com/10.1029/2005JE002555> [Accessed July 27, 2016].
- Gellert, R. et al., 2015. Distinct Igneous APXS Rock Compositions on Mars from Pathfinder, MER and MSL.
- Gellert, R. et al., 2016. Igneous and Sedimentary Compositions from Four Landing Sites on Mars from the Alpha Particle X-Ray Spectrometer (APXS).
- Gellert, R., Campbell, J.L. & King, P.L., 2009. The Alpha-Particle-X-Ray Spectrometer (APXS) for the Mars Science Laboratory (MSL) rover mission. *Lunar Planet. Sci. XL*. Available at: <http://www.lpi.usra.edu/meetings/lpsc2009/pdf/2364.pdf> [Accessed December 10, 2015].
- Gillet, P. et al., 1993. Raman spectroscopic studies of carbonates part I: High-pressure and high-temperature behaviour of calcite, magnesite, dolomite and aragonite. *Physics and Chemistry of Minerals*, 20(1), pp.1–18. Available at: <http://link.springer.com/10.1007/BF00202245> [Accessed August 1, 2017].
- Gilmore, M. et al., 2017. Venus Surface Composition Constrained by Observation and Experiment. *Space Science Reviews*, pp.1–30. Available at: <http://link.springer.com/10.1007/s11214-017-0370-8> [Accessed September 4, 2017].
- Gladman, B.J. et al., 1996. The Exchange of Impact Ejecta Between Terrestrial Planets. *Science*, 271(5254).
- Gold, T., 1992. The deep, hot biosphere. *Proceedings of the National Academy of Sciences*, 89(13), pp.6045–6049. Available at: <http://www.pnas.org/cgi/doi/10.1073/pnas.89.13.6045> [Accessed December 14, 2016].
- Goldstein, J.J. et al., 1991. Absolute wind velocities in the lower thermosphere of Venus using infrared heterodyne spectroscopy. *Icarus*, 94(1), pp.45–63.
- Golombek, M. et al., 2006. Erosion rates at the Mars Exploration Rover landing sites and long-term climate change on Mars. *Journal of Geophysical Research: Planets*,

- 111(E12), p.n/a-n/a. Available at: <http://doi.wiley.com/10.1029/2006JE002754> [Accessed February 21, 2017].
- Golombek, M. et al., 2012. Selection of the Mars Science Laboratory Landing Site. *Space Science Reviews*, 170(1–4), pp.641–737. Available at: <http://link.springer.com/10.1007/s11214-012-9916-y> [Accessed December 12, 2016].
- Golombek, M., 1997. The Mars Pathfinder Mission. *Journal of Geophysical Research: Planets*, 102(E2), pp.3953–3965. Available at: <http://doi.wiley.com/10.1029/96JE02805> [Accessed December 15, 2016].
- Gómez-Elvira, J. et al., 2012. REMS: The Environmental Sensor Suite for the Mars Science Laboratory Rover. *Space Science Reviews*, 170(1–4), pp.583–640. Available at: <http://link.springer.com/10.1007/s11214-012-9921-1> [Accessed November 19, 2013].
- Gondal, M.A. & Hussain, T., 2007. Determination of poisonous metals in wastewater collected from paint manufacturing plant using laser-induced breakdown spectroscopy. *Talanta*, 71(1), pp.73–80.
- Grant, J. et al., 2004. Selecting landing sites for the 2003 Mars Exploration Rovers. *Planetary and Space Science*, 52(1), pp.11–21. Available at: <http://www.sciencedirect.com/science/article/pii/S0032063303001715> [Accessed June 5, 2017].
- Greeley, R. et al., 1998. Europa: Initial Galileo Geological Observations. *Icarus*, 135(1), pp.4–24.
- Greeley, R. et al., 2005. Fluid lava flows in Gusev crater, Mars. *Journal of Geophysical Research*, 110(E5), p.E05008. Available at: <http://doi.wiley.com/10.1029/2005JE002401> [Accessed February 27, 2017].
- Greeley, R. & R., 1985. Dust storms on Mars: Mechanisms for dust-raising. *Workshop on Dust on Mars. A Lunar and Planetary Institute Workshop held at Tempe, Arizona, 4-5 Feb. 1985. Edited by Steven Lee. LPI Technical Report 85-02, published by Lunar and Planetary Institute, 3303 NASA Road 1, Houston, TX 77058, 1985, p.3, p.3.*
- Greeley, R. & Schneid, B.D., 1991. Magma Generation on Mars: Amounts, Rates, and Comparisons with Earth, Moon, and Venus. *Science*, 254(5034), pp.996–998. Available at: <http://www.sciencemag.org/cgi/doi/10.1126/science.254.5034.996>

- [Accessed February 27, 2017].
- Griffiths, A.D. et al., 2006. Context for the ESA ExoMars rover: the Panoramic Camera (PanCam) instrument. *International Journal of Astrobiology*, 5(3), p.269. Available at: [http://www.journals.cambridge.org/abstract\\_S1473550406003387](http://www.journals.cambridge.org/abstract_S1473550406003387) [Accessed May 18, 2017].
- Grinspoon, D., 1998. *The Planet Venus*, Yale University Press. Available at: <https://books.google.com/books?hl=en&lr=&id=1EhmsgN9V94C&pgis=1> [Accessed May 24, 2016].
- Gross, J. et al., 2011. Primitive olivine-phyric shergottite NWA 5789: Petrography, mineral chemistry, and cooling history imply a magma similar to Yamato-980459. *Meteoritics & Planetary Science*, p.no-no. Available at: <http://doi.wiley.com/10.1111/j.1945-5100.2010.01152.x> [Accessed April 26, 2016].
- Grotzinger, J.P., 2013. Analysis of surface materials by the Curiosity Mars rover. *Science (New York, N.Y.)*, 341(6153), p.1475. Available at: <http://science.sciencemag.org/content/341/6153/1475.abstract> [Accessed March 7, 2016].
- Grotzinger, J.P., Gupta, S., et al., 2015. Deposition, exhumation, and paleoclimate of an ancient lake deposit, Gale crater, Mars. *Science*, 350(6257). Available at: <http://science.sciencemag.org/content/350/6257/aac7575.full> [Accessed May 25, 2017].
- Grotzinger, J.P. et al., 2012. *Mars Science Laboratory Mission and Science Investigation*, Available at: <http://link.springer.com/10.1007/s11214-012-9892-2> [Accessed November 14, 2013].
- Grotzinger, J.P., Crisp, J.A. & Vasavada, A.R., 2015. Curiosity's Mission of Exploration at Gale Crater, Mars. *Elements*, 11(1), pp.19–26. Available at: <http://elements.geoscienceworld.org/content/11/1/19.abstract> [Accessed March 17, 2016].
- Gulick, V.C., 1998. Magmatic intrusions and a hydrothermal origin for fluvial valleys on Mars. *Journal of Geophysical Research: Planets*, 103(E8), pp.19365–19387. Available at: <http://doi.wiley.com/10.1029/98JE01321> [Accessed February 27, 2017].

- Gulick, V.C., 2001. Origin of the valley networks on Mars: a hydrological perspective. *Geomorphology*, 37(3), pp.241–268.
- Guo, J. et al., 2015. Variations of dose rate observed by MSL/RAD in transit to Mars. *Astronomy & Astrophysics*, 577, p.A58. Available at: <http://www.aanda.org/10.1051/0004-6361/201525680> [Accessed September 4, 2017].
- Gütlich, P., Bill, E. & Trautwein, A., 2011. *Mossbauer spectroscopy and transition metal chemistry : fundamentals and application*, Springer.
- Haberle, R.M. et al., 2014. Preliminary interpretation of the REMS pressure data from the first 100 sols of the MSL mission. *Journal of Geophysical Research: Planets*, 119(3), pp.440–453. Available at: <http://doi.wiley.com/10.1002/2013JE004488> [Accessed December 16, 2016].
- Hamilton, V. & Ruff, S.W., 2012. Distribution and characteristics of Adirondack-class basalt as observed by Mini-TES in Gusev crater, Mars and its possible volcanic source. *Icarus*, 218(2), pp.917–949. Available at: <http://www.sciencedirect.com/science/article/pii/S0019103512000267> [Accessed April 12, 2016].
- Hand, E., 2015. Planetary science. Plumes on Europa tease NASA mission planners. *Science (New York, N.Y.)*, 347(6225), pp.932–3. Available at: <http://science.sciencemag.org/content/347/6225/932.abstract> [Accessed May 20, 2016].
- Harris, J.K. et al., 2015. Remote detection of past habitability at Mars-analogue hydrothermal alteration terrains using an ExoMars Panoramic Camera emulator. *Icarus*, 252, pp.284–300. Available at: <http://www.sciencedirect.com/science/article/pii/S0019103515000445> [Accessed May 17, 2017].
- Harris, L. V., McHugh, M., et al., 2015. Avoiding misidentification of bands in planetary Raman spectra. *Journal of Raman Spectroscopy*, 46(10), pp.863–872. Available at: <http://doi.wiley.com/10.1002/jrs.4667> [Accessed July 14, 2017].
- Harris, L. V., Hutchinson, I.B., et al., 2015. Selection of Portable Spectrometers for Planetary Exploration: A Comparison of 532 nm and 785 nm Raman Spectroscopy of Reduced Carbon in Archean Cherts. *Astrobiology*, 15(6), pp.420–429. Available

- at: <http://online.liebertpub.com/doi/10.1089/ast.2014.1220> [Accessed December 26, 2016].
- Hartmann, W.K. & Neukum, G., 2001. Cratering Chronology and the Evolution of Mars. *Space Science Reviews*, 96(1/4), pp.165–194. Available at: <http://link.springer.com/10.1023/A:1011945222010> [Accessed February 27, 2017].
- Hassler, D. et al., 2014. Mars' Surface Radiation Environment Measured with the Mars Science Laboratory's Curiosity Rover. *Science*, 343(6169).
- Hassler, D. et al., 2012. The Radiation Assessment Detector (RAD) Investigation. *Space Science Reviews*, 170(1–4), pp.503–558. Available at: <http://link.springer.com/10.1007/s11214-012-9913-1> [Accessed November 19, 2013].
- Head, J.W. et al., 2003. Recent ice ages on Mars. *Nature*, 426(6968), pp.797–802. Available at: <http://www.ncbi.nlm.nih.gov/pubmed/14685228> [Accessed February 27, 2017].
- Head, J.W. et al., 1992. Venus volcanism: Classification of volcanic features and structures, associations, and global distribution from Magellan data. *Journal of Geophysical Research*, 97(E8), p.13153. Available at: <http://doi.wiley.com/10.1029/92JE01273> [Accessed December 15, 2016].
- Head, J.W., Kreslavsky, M.A. & Pratt, S., 2002. Northern lowlands of Mars: Evidence for widespread volcanic flooding and tectonic deformation in the Hesperian Period. *Journal of Geophysical Research*, 107(E1), p.5003. Available at: <http://doi.wiley.com/10.1029/2000JE001445> [Accessed February 27, 2017].
- Head, J.W. & Pratt, S., 2001. Extensive Hesperian-aged south polar ice sheet on Mars: Evidence for massive melting and retreat, and lateral flow and ponding of meltwater. *Journal of Geophysical Research: Planets*, 106(E6), pp.12275–12299. Available at: <http://doi.wiley.com/10.1029/2000JE001359> [Accessed February 27, 2017].
- Herkenhoff, K.E., 2000. Surface Ages and Resurfacing Rates of the Polar Layered Deposits on Mars. *Icarus*, 144(2), pp.243–253. Available at: <http://linkinghub.elsevier.com/retrieve/pii/S0019103599962875> [Accessed February 27, 2017].

- Hess, S.L., Henry, R.M. & Tillman, J.E., 1979. The seasonal variation of atmospheric pressure on Mars as affected by the south polar cap. *Journal of Geophysical Research*, 84(B6), p.2923. Available at: <http://doi.wiley.com/10.1029/JB084iB06p02923> [Accessed December 14, 2016].
- Hopkinson, G.R., 1993. Radiation-induced dark current increases in CCDs. In *RADECS 93. Second European Conference on Radiation and its Effects on Components and Systems (Cat. No.93TH0616-3)*. IEEE, pp. 401–408. Available at: <http://ieeexplore.ieee.org/document/316569/> [Accessed August 7, 2017].
- Howard, A.D., Moore, J.M. & Irwin, R.P., 2005. An intense terminal epoch of widespread fluvial activity on early Mars: 1. Valley network incision and associated deposits. *Journal of Geophysical Research*, 110(E12), p.E12S14. Available at: <http://doi.wiley.com/10.1029/2005JE002459> [Accessed February 27, 2017].
- Humayun, M. et al., 2013. Origin and age of the earliest Martian crust from meteorite NWA 7533. *Nature*, 503(7477), pp.513–6. Available at: <http://dx.doi.org/10.1038/nature12764> [Accessed April 21, 2016].
- Humphreys, E.R. & Niu, Y., 2009. On the composition of ocean island basalts (OIB): The effects of lithospheric thickness variation and mantle metasomatism. *Lithos*, 112(1–2), pp.118–136. Available at: <http://www.sciencedirect.com/science/article/pii/S002449370900187X> [Accessed April 4, 2016].
- Hynek, B.M. & Phillips, R.J., 2003. New data reveal mature, integrated drainage systems on Mars indicative of past precipitation. *Geology*, 31(9), p.757. Available at: <http://geology.gsapubs.org/cgi/doi/10.1130/G19607.1> [Accessed February 21, 2017].
- Ikeda, Y. et al., 2003. Primitive clasts in the Dar al Gani 319 polymict ureilite: Precursors of the ureilites. *Antartic Meteorite Research*, 16. Available at: <http://adsabs.harvard.edu/abs/2003AMR....16..105I> [Accessed April 26, 2016].
- Irvine, T.N. & Baragar, W.R.A., 1971. A Guide to the Chemical Classification of the Common Volcanic Rocks. *Canadian Journal of Earth Sciences*, 8(5), pp.523–548. Available at: <http://www.nrcresearchpress.com/doi/abs/10.1139/e71-055#.VOMA8fkrLmF> [Accessed May 23, 2016].
- Irwin, R.P. & Howard, A.D., 2002. Drainage basin evolution in Noachian Terra Cimmeria,

- Mars. *Journal of Geophysical Research*, 107(E7), p.5056. Available at: <http://doi.wiley.com/10.1029/2001JE001818> [Accessed February 21, 2017].
- Jackson, R.S. et al., 2016. ChemCam investigation of the John Klein and Cumberland drill holes and tailings, Gale crater, Mars. *Icarus*, 277, pp.330–341. Available at: <http://linkinghub.elsevier.com/retrieve/pii/S0019103516300902> [Accessed July 27, 2017].
- Jackson, R.S. et al., 2014. *ChemCam Investigation of the John Klein and Cumberland Drill Tailings*, Lunar and Planetary Institute. Available at: <http://adsabs.harvard.edu/abs/2014LPICo1791.1254J> [Accessed September 23, 2017].
- Jaffe, L.D., 1967. Lunar surface exploration by Surveyor spacecraft: Introduction. *Journal of Geophysical Research*, 72(2), pp.773–778. Available at: <http://doi.wiley.com/10.1029/JZ072i002p00773> [Accessed May 26, 2017].
- Jakosky, B. & Phillips, R.J., 2001. Mars' volatile and climate history. *Nature*, 412(6843), pp.237–244. Available at: <http://www.nature.com/doi/10.1038/35084184> [Accessed December 8, 2016].
- Jansen, F. et al., 2001. XMM-Newton observatory. *Astronomy and Astrophysics*, 365(1), pp.L1–L6. Available at: <http://www.edpsciences.org/10.1051/0004-6361:20000036> [Accessed December 13, 2016].
- Johnson, T. V. et al., 1983. Global multispectral mosaics of the icy Galilean satellites. *Journal of Geophysical Research: Solid Earth*, 88(B7), pp.5789–5805. Available at: <http://doi.wiley.com/10.1029/JB088iB07p05789> [Accessed December 16, 2016].
- Jorge, S.E. et al., 2005. Raman spectroscopy in astrobiology. *Analytical and Bioanalytical Chemistry*, 384(1), pp.100–113. Available at: <https://link.springer.com/content/pdf/10.1007%2Fs00216-005-0029-2.pdf> [Accessed December 13, 2013].
- Josset, J.-L. et al., 2012. CLUPI, a high-performance imaging system on the ESA-NASA rover of the 2018 ExoMars mission to discover biofabrics on Mars. *EGU General Assembly 2012, held 22-27 April, 2012 in Vienna, Austria.*, p.13616, 14, p.13616. Available at: <http://adsabs.harvard.edu/abs/2012EGUGA..1413616J> [Accessed May 18, 2017].
- Kargel, J., 2000. Europa's Crust and Ocean: Origin, Composition, and the Prospects for

- Life. *Icarus*, 148(1), pp.226–265. Available at: <http://www.sciencedirect.com/science/article/pii/S0019103500964716> [Accessed April 9, 2016].
- Kargel, J.S. et al., 1995. Evidence of ancient continental glaciation in the Martian northern plains. *Journal of Geophysical Research*, 100(E3), p.5351. Available at: <http://doi.wiley.com/10.1029/94JE02447> [Accessed February 27, 2017].
- Karlsson, H. et al., 1992. Water in SNC meteorites: evidence for a martian hydrosphere. *Science*, 255(5050), pp.1409–1411. Available at: <http://science.sciencemag.org/content/255/5050/1409.abstract> [Accessed April 28, 2016].
- Karunatillake, S. et al., 2006. Composition of northern low-albedo regions of Mars: Insights from the Mars Odyssey Gamma Ray Spectrometer. *Journal of Geophysical Research*, 112(E3), p.E03S05. Available at: <http://doi.wiley.com/10.1029/2006JE002675> [Accessed April 21, 2016].
- Kass, D. & Yung, Y., 1995. Loss of atmosphere from Mars due to solar wind-induced sputtering. *Science*, 268(5211).
- Kasting, J., 1993. Earth's early atmosphere. *Science*, 259(5097), pp.920–926. Available at: <http://science.sciencemag.org/content/259/5097/920.abstract> [Accessed December 21, 2015].
- Kasting, J.F. & Pollack, J.B., 1983. Loss of water from Venus. I. Hydrodynamic escape of hydrogen. *Icarus*, 53(3), pp.479–508. Available at: <http://www.sciencedirect.com/science/article/pii/0019103583902129> [Accessed May 24, 2016].
- Kawakatsu, Y. et al., 2012. An Orbit Plan toward AKATSUKI Venus Reencounter and Orbit Injection.
- Keldysh, M.V., 1977. Venus exploration with the Venera 9 and Venera 10 spacecraft. *Icarus*, 30(4), pp.605–625.
- Kerr, R.A., 1997. Geomicrobiology: Life Goes to Extremes in the Deep Earth--and Elsewhere? *Science*, 276(5313), pp.703–704. Available at: <http://science.sciencemag.org/content/276/5313/703.abstract> [Accessed March 18, 2016].
- Khurana, K.K. et al., 1998. Induced magnetic fields as evidence for subsurface oceans in

- Europa and Callisto. *Nature*, 395(6704), pp.777–80. Available at: <http://dx.doi.org/10.1038/27394> [Accessed April 14, 2016].
- Kieffer, H.H., Christensen, P.R. & Titus, T.N., 2006. CO<sub>2</sub> jets formed by sublimation beneath translucent slab ice in Mars' seasonal south polar ice cap. *Nature*, 442(7104), pp.793–796. Available at: <http://www.nature.com/doi/10.1038/nature04945> [Accessed December 9, 2016].
- Kivelson, M.G. et al., 2000. Galileo Magnetometer Measurements: A Stronger Case for a Subsurface Ocean at Europa. *Science*, 289(5483).
- Klein, H., Lederberg, J. & Rich, A., 1976. The Viking Mission search for life on Mars. .... Available at: [http://www.mars-exploration.co.uk/docs/Viking Mission Search For Life On Mars, 1976.pdf](http://www.mars-exploration.co.uk/docs/Viking%20Mission%20Search%20For%20Life%20On%20Mars,%201976.pdf) [Accessed December 18, 2015].
- Klein, H.P.H., 1979. The Viking mission and the search for life on Mars. *Reviews of Geophysics*, 17(7), p.1655. Available at: <http://doi.wiley.com/10.1029/RG017i007p01655> [Accessed December 18, 2015].
- Klingelhöfer, G., Morris, R. V., et al., 2003. Athena MIMOS II Mössbauer spectrometer investigation. *Journal of Geophysical Research: Planets*, 108(E12). Available at: <http://doi.wiley.com/10.1029/2003JE002138> [Accessed July 25, 2016].
- Klingelhöfer, G., Bernhardt, B., et al., 2003. The Miniaturized Mössbauer Spectrometer MIMOS II for Extraterrestrial and Outdoor Terrestrial Applications: A Status Report. In *Mössbauer Spectroscopy*. Dordrecht: Springer Netherlands, pp. 371–379. Available at: [http://link.springer.com/10.1007/978-94-010-0045-1\\_36](http://link.springer.com/10.1007/978-94-010-0045-1_36) [Accessed July 28, 2016].
- Kloprogge, J., Ruan, H. & Duong, L., 2001. FT-IR and Raman microscopic study at 293 K and 77 K of celestine, SrSO<sub>4</sub>, from the middle triassic limestone (Muschelkalk) in Winterswijk, The Netherlands. *Netherlands Journal of Geosciences*, 80(2), pp.41–47. Available at: <https://www.cambridge.org/core/journals/netherlands-journal-of-geosciences/article/ft-ir-and-raman-microscopic-study-at-293-k-and-77-k-of-celestine-srs04-from-the-middle-triassic-limestone-muschelkalk-in-winterswijk-the-netherlands/357B668034F32D6002F126F> [Accessed August 25, 2017].
- Kobayashi, T. et al., 2008. Determination of SiO<sub>2</sub> Raman spectrum indicating the transformation from coesite to quartz in Gföhl migmatitic gneisses in the

- Moldanubian Zone, Czech Republic. *Journal of Mineralogical and Petrological Sciences*, 103(2), pp.105–111. Available at: <http://joi.jlc.jst.go.jp/JST.JSTAGE/jmps/071020?from=CrossRef> [Accessed August 4, 2017].
- Koeppen, W.C. & Hamilton, V., 2008. Global distribution, composition, and abundance of olivine on the surface of Mars from thermal infrared data. *Journal of Geophysical Research*, 113(E5), p.E05001. Available at: <http://doi.wiley.com/10.1029/2007JE002984> [Accessed May 6, 2016].
- Korablev, O. et al., 2014. An Infrared Spectrometer at the Mast of ExoMars Rover. *40th COSPAR Scientific Assembly. Held 2-10 August 2014, in Moscow, Russia, Abstract B0.2-36-14.*, 40. Available at: <http://adsabs.harvard.edu/abs/2014cosp...40E1578K> [Accessed May 18, 2017].
- Korablev, O. et al., 2017. Science Investigation of the Atmospheric Chemistry Suite on Exomars TGO. *The Sixth International Workshop on the Mars Atmosphere: Modelling and observation...*, p.4402. Available at: <http://adsabs.harvard.edu/abs/2017mamo.conf.4402K> [Accessed August 26, 2017].
- Kozyrev, A.S. et al., 2009. Gamma-Rays and Neutron Spectrometers NS HEND -- Tool for Study of Phobos Surface Composition. *40th Lunar and Planetary Science Conference, (Lunar and Planetary Science XL), held March 23-27, 2009 in The Woodlands, Texas, id.1865*, 40.
- Krimigis, S.M. et al., 2003. Voyager 1 exited the solar wind at a distance of approximately 85 Au from the Sun. *Nature*, 426(6962), pp.45–8. Available at: <http://dx.doi.org/10.1038/nature02068> [Accessed April 29, 2016].
- Kuebler, K.E. et al., 2006. Extracting olivine (Fo–Fa) compositions from Raman spectral peak positions. *Geochimica et Cosmochimica Acta*, 70(24), pp.6201–6222.
- Lafuente, B. et al., 2015. *The power of databases: the RRUFF project*. In: *Highlights in Mineralogical Crystallography* T Armbruster and R M Danisi, ed., Berlin: W. De Gruyter. Available at: <http://rruff.info/about/downloads/HMC1-30.pdf> [Accessed September 7, 2017].
- Lamsal, N. & Angel, S., 2015. Deep-Ultraviolet Raman Measurements Using a Spatial Heterodyne Raman Spectrometer (SHRS). *Applied spectroscopy*, 69(5), pp.525–34.

- Available at: <http://www.ncbi.nlm.nih.gov/pubmed/25811967> [Accessed July 28, 2016].
- Lane, N., Allen, J.F. & Martin, W., 2010. How did LUCA make a living? Chemiosmosis in the origin of life. *BioEssays*, 32(4), pp.271–280. Available at: <http://doi.wiley.com/10.1002/bies.200900131> [Accessed September 20, 2017].
- Lange, R.D., 2008. Cassini-Huygens Mission Overview and Recent Science Results. In *2008 IEEE Aerospace Conference*. IEEE, pp. 1–10. Available at: <http://ieeexplore.ieee.org/document/4526259/> [Accessed December 13, 2016].
- Lange, R.G. & Carroll, W.P., 2008. Review of recent advances of radioisotope power systems. *Energy Conversion and Management*, 49(3), pp.393–401. Available at: <http://www.sciencedirect.com/science/article/pii/S0196890407003688> [Accessed September 13, 2017].
- Lanza, N.L. et al., 2015. Understanding the signature of rock coatings in laser-induced breakdown spectroscopy data. *Icarus*, 249, pp.62–73.
- Lebreton, J.-P. & Matson, D.L., 2003. The Huygens Probe: Science, Payload and Mission Overview. In *The Cassini-Huygens Mission*. Dordrecht: Springer Netherlands, pp. 59–100. Available at: [http://www.springerlink.com/index/10.1007/978-94-017-3251-2\\_2](http://www.springerlink.com/index/10.1007/978-94-017-3251-2_2) [Accessed December 15, 2016].
- Lefèvre, C.T. et al., 2011. Isolation of obligately alkaliphilic magnetotactic bacteria from extremely alkaline environments. *Environmental microbiology*, 13(8), pp.2342–50. Available at: <http://www.ncbi.nlm.nih.gov/pubmed/21605309> [Accessed March 18, 2016].
- Leroi, V., Bibring, J.-P. & Berthé, M., 2009. Micromega/IR: Design and status of a near-infrared spectral microscope for in situ analysis of Mars samples. *Planetary and Space Science*, 57(8), pp.1068–1075.
- Lewis, I.R. & Edwards, H.G.M., 2001. *Handbook of Raman spectroscopy: from the research laboratory to the process line*, Marcel Dekker.
- Lewis, J.S., 1968. An estimate of the surface conditions of Venus. *Icarus*, 8(1–3), pp.434–456. Available at: <http://www.sciencedirect.com/science/article/pii/0019103568900912> [Accessed May 24, 2016].
- Lissauer, J.J. & Pater, I. de, 2013. *Fundamental Planetary Science: Physics, Chemistry and*

- Habitability*, Cambridge University Press. Available at: [https://books.google.co.uk/books/about/Fundamental\\_Planetary\\_Science.html?id=NCnTPAAACAAJ&pgis=1](https://books.google.co.uk/books/about/Fundamental_Planetary_Science.html?id=NCnTPAAACAAJ&pgis=1) [Accessed April 8, 2016].
- Lopes, R.M.C. et al., 2007. Cryovolcanic features on Titan's surface as revealed by the Cassini Titan Radar Mapper. *Icarus*, 186(2), pp.395–412. Available at: <http://www.sciencedirect.com/science/article/pii/S0019103506003198> [Accessed April 14, 2016].
- Lopez-Reyes, G. et al., 2012. A simple statistical method for the pseudo-quantification of mineral phases within the ExoMars Raman RLS instrument. *GeoRaman*. Available at: [https://www.researchgate.net/profile/Aurelio\\_Sanz\\_Arranz/publication/282155774\\_A\\_simple\\_statistical\\_method\\_for\\_the\\_pseudo-quantification\\_of\\_mineral\\_phases\\_within\\_the\\_ExoMars\\_Raman\\_RLS\\_instrument/links/56056abe08aea25fce33395f.pdf](https://www.researchgate.net/profile/Aurelio_Sanz_Arranz/publication/282155774_A_simple_statistical_method_for_the_pseudo-quantification_of_mineral_phases_within_the_ExoMars_Raman_RLS_instrument/links/56056abe08aea25fce33395f.pdf) [Accessed September 21, 2017].
- López Reyes, G.E., 2015. Development of algorithms and methodological analyses for the definition of the operation mode of the Raman Laser Spectrometer instrument. Available at: <http://uvadoc.uva.es/handle/10324/17717> [Accessed September 11, 2017].
- Loubser, M. & Verryyn, S., 2008. Combining XRF and XRD analyses and sample preparation to solve mineralogical problems. *South African Journal of Geology*, 111(2–3), pp.229–238. Available at: <http://sajg.geoscienceworld.org/cgi/doi/10.2113/gssajg.111.2-3.229> [Accessed July 22, 2016].
- Mahaffy, P.R. et al., 2009. Sample Analysis at Mars (SAM) Instrument Suite for the 2011 Mars Science Laboratory. *40th Lunar and Planetary Science Conference, (Lunar and Planetary Science XL), held March 23-27, 2009 in The Woodlands, Texas, id.1088*, 40.
- Mahaffy, P.R. et al., 2012. The Sample Analysis at Mars Investigation and Instrument Suite. *Space Science Reviews*, 170(1–4), pp.401–478. Available at: <http://link.springer.com/10.1007/s11214-012-9879-z> [Accessed November 19, 2013].
- Le Maitre, R.W., 1989. A classification of igneous rocks and glossary of terms :

- recommendations of the International Union of Geological Sciences Subcommission on the Systematics of Igneous Rocks. *International Union of Geological Sciences, Subcommission on the Systematics of Igneous Rocks*. Available at: <http://www.sidalc.net/cgi-bin/wxis.exe/?IsisScript=FCL.xis&method=post&formato=2&cantidad=1&expresion=mfn=002567> [Accessed May 26, 2017].
- Malherbe, C., 2017. Cedric Malherbe, Department of Chemistry, University of Liege, sample collection.
- Malin, M.C. et al., 2005. The Mast Cameras and Mars Descent Imager (MARDI) for the 2009 Mars Science Laboratory. *36th Annual Lunar and Planetary Science Conference, March 14-18, 2005, in League City, Texas, abstract no.1214*, 36. Available at: <http://adsabs.harvard.edu/abs/2005LPI....36.1214M> [Accessed September 12, 2017].
- Mangold, N. et al., 2015. Chemical variations in Yellowknife Bay formation sedimentary rocks analyzed by ChemCam on board the Curiosity rover on Mars. *Journal of Geophysical Research: Planets*, 120(3), pp.452–482. Available at: <http://doi.wiley.com/10.1002/2014JE004681> [Accessed July 26, 2016].
- Mangold, N. et al., 2016. Composition of conglomerates analyzed by the Curiosity rover: Implications for Gale Crater crust and sediment sources. *Journal of Geophysical Research: Planets*, 121(3), pp.353–387. Available at: <http://doi.wiley.com/10.1002/2015JE004977> [Accessed May 26, 2016].
- Marinangeli, L. et al., 2007. An European XRD/XRF Instrument for the ExoMars Mission. *38th Lunar and Planetary Science Conference, (Lunar and Planetary Science XXXVIII), held March 12-16, 2007 in League City, Texas. LPI Contribution No. 1338*, p.1322, 38, p.1322.
- Marion, G.M. et al., 2003. The search for life on Europa: limiting environmental factors, potential habitats, and Earth analogues. *Astrobiology*, 3(4), pp.785–811. Available at: <http://online.liebertpub.com/doi/abs/10.1089/153110703322736105> [Accessed April 9, 2016].
- Marshall, C.P. et al., 2007. Carotenoid Analysis of Halophilic Archaea by Resonance Raman Spectroscopy. *Astrobiology*, 7(4), pp.631–643. Available at: <http://www.liebertonline.com/doi/abs/10.1089/ast.2006.0097> [Accessed

September 17, 2017].

- Martin, P. et al., 2007. Coronae of Parga Chasma, Venus. *Journal of Geophysical Research*, 112(E4), p.E04S03. Available at: <http://doi.wiley.com/10.1029/2006JE002758> [Accessed December 15, 2016].
- Mattingly, R. & May, L., 2011. Mars Sample Return as a campaign. In *2011 Aerospace Conference*. IEEE, pp. 1–13. Available at: <http://ieeexplore.ieee.org/document/5747287/> [Accessed December 8, 2016].
- Maurice, S. et al., 2016. ChemCam activities and discoveries during the nominal mission of the Mars Science Laboratory in Gale crater, Mars. *J. Anal. At. Spectrom.*, 31(4), pp.863–889. Available at: <http://xlink.rsc.org/?DOI=C5JA00417A> [Accessed March 31, 2016].
- Maurice, S. et al., 2007. Expected Performances of the ChemCam Instrument for the Mars Science Laboratory (MSL) Rover. *Lunar and Planetary Institute Science Conference Abstracts*, 38, p.1563. Available at: <http://adsabs.harvard.edu/abs/2007LPI....38.1563M> [Accessed November 7, 2013].
- Maurice, S. et al., 2012. The ChemCam Instrument Suite on the Mars Science Laboratory (MSL) Rover: Science Objectives and Mast Unit Description. *Space Science Reviews*, 170(1–4), pp.95–166. Available at: <http://link.springer.com/10.1007/s11214-012-9912-2> [Accessed November 7, 2013].
- Maurice, S. & Cousin, A., 2012. Laser Induced Breakdown Spectroscopy (LIBS) spot size at Stand-off distances with ChemCam. *43rd Lunar and Planetary Science Conference*, p.2899. Available at: <http://adsabs.harvard.edu/abs/2012LPI....43.2899M> [Accessed December 10, 2015].
- McCaughey, J.F. et al., 1972. Preliminary mariner 9 report on the geology of Mars. *Icarus*, 17(2), pp.289–327. Available at: <http://www.sciencedirect.com/science/article/pii/0019103572900036> [Accessed May 6, 2016].
- McCubbin, F.M. et al., 2008. Compositional diversity and stratification of the Martian crust: Inferences from crystallization experiments on the picrobasalt Humphrey from Gusev Crater, Mars. *Journal of Geophysical Research*, 113(E11), p.E11013.

- Available at: <http://doi.wiley.com/10.1029/2008JE003165> [Accessed May 5, 2016].
- McEwan, M.J. & Phillips, L.F., 1975. Chemistry of the atmosphere. *New York, Halsted Press, 1975. 309 p.* Available at: <http://adsabs.harvard.edu/abs/1975nyhp.book.....M> [Accessed May 26, 2017].
- McEwen, A.S. et al., 2011. Seasonal Flows on Warm Martian Slopes. *Science*, 333(6043).
- McKay, C.P., 2002. Planetary protection for a Europa surface sample return: The Ice Clipper mission. *Advances in Space Research*, 30(6), pp.1601–1605. Available at: <http://www.sciencedirect.com/science/article/pii/S0273117702004805> [Accessed April 14, 2016].
- McSween, H.Y. et al., 1999. Chemical, multispectral, and textural constraints on the composition and origin of rocks at the Mars Pathfinder landing site. *Journal of Geophysical Research: Planets*, 104(E4), pp.8679–8715. Available at: <http://doi.wiley.com/10.1029/98JE02551> [Accessed April 21, 2016].
- McSween, H.Y. et al., 2008. Mineralogy of volcanic rocks in Gusev Crater, Mars: Reconciling Mössbauer, Alpha Particle X-Ray Spectrometer, and Miniature Thermal Emission Spectrometer spectra. *Journal of Geophysical Research*, 113(E6), p.E06S04. Available at: <http://doi.wiley.com/10.1029/2007JE002970> [Accessed September 29, 2016].
- McSween, H.Y., 2002. The rocks of Mars, from far and near. *Meteoritics & Planetary Science*, 37(1), pp.7–25. Available at: <http://doi.wiley.com/10.1111/j.1945-5100.2002.tb00793.x> [Accessed April 28, 2016].
- McSween, H.Y., Grove, T.L. & Wyatt, M.B., 2003. Constraints on the composition and petrogenesis of the Martian crust. *Journal of Geophysical Research: Planets*, 108(E12). Available at: <http://doi.wiley.com/10.1029/2003JE002175> [Accessed May 27, 2016].
- McSween, H.Y., Labotka, T.C. & Viviano-Beck, C.E., 2015. Metamorphism in the Martian crust. *Meteoritics & Planetary Science*, 50(4), pp.590–603. Available at: <http://doi.wiley.com/10.1111/maps.12330> [Accessed May 5, 2016].
- McSween, H.Y. & Ruff, S.W., 2006. Alkaline volcanic rocks from the Columbia Hills, Gusev crater, Mars. *Journal of Geophysical Research: Planets*, 111(9), pp.1–15. Available at: <http://onlinelibrary.wiley.com/doi/10.1029/2006JE002698/full> [Accessed December 10, 2015].

- McSween, H.Y., Taylor, G.J. & Wyatt, M.B., 2009. Elemental composition of the Martian crust. *Science*, 324(5928), pp.736–739. Available at: <http://www.sciencemag.org/content/324/5928/736.short> [Accessed December 10, 2015].
- McSween, H.Y. & Treiman, A.H., 1998. Martian meteorites. *Reviews in Mineralogy and Geochemistry*, 36(1), p.6.1-653. Available at: <http://ring.geoscienceworld.org/content/36/1/6.1.short> [Accessed May 6, 2016].
- Melosh, H.J., 2003. Exchange of Meteorites (and Life?) Between Stellar Systems. *Astrobiology*, 3(1), pp.207–215. Available at: <http://www.liebertonline.com/doi/abs/10.1089/153110703321632525> [Accessed December 8, 2016].
- Melzer, C. et al., 2015. Mechanical Testing on the Core Sample Transportation Mechanism of the ExoMars 2018 Mission. *ESA Special*. Available at: <http://esmats.eu/esmatpapers/pastpapers/pdfs/2015/melzer.pdf> [Accessed September 21, 2017].
- Mezger, K., Debaille, V. & Kleine, T., 2012. Core Formation and Mantle Differentiation on Mars. *Space Science Reviews*, 174(1–4), pp.27–48. Available at: <http://link.springer.com/10.1007/s11214-012-9935-8> [Accessed April 28, 2016].
- Mezzacappa, A. et al., 2016. Application of distance correction to ChemCam laser-induced breakdown spectroscopy measurements. *Spectrochimica Acta Part B: Atomic Spectroscopy*, 120, pp.19–29.
- Ming, D.W. et al., 2008. Geochemical properties of rocks and soils in Gusev Crater, Mars: Results of the Alpha Particle X-Ray Spectrometer from Cumberland Ridge to Home Plate. *Journal of Geophysical Research*, 113(E12), p.E12S39. Available at: <http://doi.wiley.com/10.1029/2008JE003195> [Accessed May 5, 2016].
- Mitrofanov, I.G. et al., 2012. Dynamic Albedo of Neutrons (DAN) Experiment Onboard NASA's Mars Science Laboratory. *Space Science Reviews*, 170(1–4), pp.559–582. Available at: <http://link.springer.com/10.1007/s11214-012-9924-y> [Accessed November 19, 2013].
- Moore, J., 2001a. Hellas as a Possible Site of Ancient Ice-Covered Lakes on Mars. *Icarus*, 154(2), pp.258–276. Available at: <http://linkinghub.elsevier.com/retrieve/pii/S0019103501967363> [Accessed

- February 27, 2017].
- Moore, J., 2001b. Impact Features on Europa: Results of the Galileo Europa Mission (GEM). *Icarus*, 151(1), pp.93–111. Available at: <http://www.sciencedirect.com/science/article/pii/S0019103500965588> [Accessed April 14, 2016].
- Morris, R. V. et al., 2016. High-Temperature, Perhaps Silicic, Volcanism on Mars Evidenced by Tridymite Detection in High-SiO<sub>2</sub> Sedimentary Rock at Gale Crater, Mars. Available at: [http://oro.open.ac.uk/45422/1/High-Temperature%2C Perhaps Silicic%2C Volcanism on Mars Evidenced by Tridymite Detection in High-SiO<sub>2</sub> Sedimentary Rock at Gale Crater%2C Mars.pdf](http://oro.open.ac.uk/45422/1/High-Temperature%2C%20Perhaps%20Silicic%20Volcanism%20on%20Mars%20Evidenced%20by%20Tridymite%20Detection%20in%20High-SiO2%20Sedimentary%20Rock%20at%20Gale%20Crater%20Mars.pdf) [Accessed May 23, 2016].
- Morris, R. V. et al., 2006. Mössbauer mineralogy of rock, soil, and dust at Gusev crater, Mars: Spirit's journey through weakly altered olivine basalt on the plains and pervasively altered basalt in the Columbia Hills. *Journal of Geophysical Research: Planets*, 111(E2). Available at: <http://doi.wiley.com/10.1029/2005JE002584> [Accessed April 12, 2016].
- Motamedi, R. & Davies, G., 2010. Versatile Mars atmosphere simulation chamber used to test a combined Raman-LIBS instrument. *European Planetary Science Congress 2010*. Available at: <http://adsabs.harvard.edu/abs/2010epsc.conf..124M> [Accessed November 7, 2013].
- Le Mouélic, S. et al., 2015. The ChemCam Remote Micro-Imager at Gale crater: Review of the first year of operations on Mars. *Icarus*, 249, pp.93–107. Available at: <http://www.sciencedirect.com/science/article/pii/S0019103514002838> [Accessed December 10, 2015].
- Murchie, S., Science, C. & Teams, E., 2007. First Results from the Compact Reconnaissance Imaging Spectrometer for Mars (CRISM). *38th Lunar and Planetary Science Conference, (Lunar and Planetary Science XXXVIII), held March 12-16, 2007 in League City, Texas. LPI Contribution No. 1338, p.1472, 38, p.1472*.
- Murchie, S.L., Britt, D.T. & Pieters, C.M., 2014. The value of Phobos sample return. *Planetary and Space Science*, 102, pp.176–182.
- Murray, B., 1989. Voyager and the Grandest Tour Ever: Catching the Wave of the Century. *Engineering & Science*. Available at: <http://core.ac.uk/download/pdf/10705597.pdf> [Accessed May 25, 2017].

- Musselwhite, D.S. et al., 2005. Experimental petrology of the basaltic shergottite Yamato-980459: Implications for the thermal structure of the Martian mantle. *Meteoritics & Planetary Science Archives*, 41(9), pp.1271–1290. Available at: <https://journals.uair.arizona.edu/index.php/maps/article/view/15324> [Accessed May 5, 2016].
- Mustard, J.F. et al., 2008. Hydrated silicate minerals on Mars observed by the Mars Reconnaissance Orbiter CRISM instrument. *Nature*, 454(7202), pp.305–309. Available at: <http://www.nature.com/doi/10.1038/nature07097> [Accessed December 14, 2016].
- Mykytczuk, N.C.S. et al., 2013. Bacterial growth at -15 °C; molecular insights from the permafrost bacterium *Planococcus halocryophilus* Or1. *The ISME journal*, 7(6), pp.1211–26. Available at: <http://dx.doi.org/10.1038/ismej.2013.8> [Accessed March 10, 2016].
- Nachon, M. et al., 2014. Calcium sulfate veins characterized by ChemCam/Curiosity at Gale crater, Mars. *Journal of Geophysical Research: Planets*, 119(9), pp.1991–2016. Available at: <https://asu.pure.elsevier.com/en/publications/calcium-sulfate-veins-characterized-by-chemcamcuriosity-at-gale-c> [Accessed April 12, 2016].
- Navarro-González, R. et al., 2003. Mars-Like Soils in the Atacama Desert, Chile, and the Dry Limit of Microbial Life. *Science*, 302(5647). Available at: <http://science.sciencemag.org/content/302/5647/1018> [Accessed August 13, 2017].
- Nekvasil, H. et al., 2007. Alkalic parental magmas for chassignites? *Meteoritics & Planetary Science*, 42(6), pp.979–992. Available at: <http://doi.wiley.com/10.1111/j.1945-5100.2007.tb01145.x> [Accessed January 25, 2016].
- Nekvasil, H. et al., 2009. Linking the Chassigny meteorite and the Martian surface rock Backstay: Insights into igneous crustal differentiation processes on Mars. *Meteoritics & Planetary Science*, 44(6), pp.853–869. Available at: <http://doi.wiley.com/10.1111/j.1945-5100.2009.tb00773.x> [Accessed May 5, 2016].
- Nekvasil, H., 2004. The Origin and Evolution of Silica-saturated Alkalic Suites: an Experimental Study. *Journal of Petrology*, 45(4), pp.693–721. Available at:

- <http://petrology.oxfordjournals.org/content/45/4/693.abstract> [Accessed January 25, 2016].
- Neugebauer, M. & Snyder, C.W., 1966. Mariner 2 observations of the solar wind: 1. Average properties. *Journal of Geophysical Research*, 71(19), pp.4469–4484. Available at: <http://doi.wiley.com/10.1029/JZ071i019p04469> [Accessed April 29, 2016].
- Nicholls, I.A. & Ringwood, A.E., 1972. Production of silica-saturated tholeiitic magmas in island arcs. *Earth and Planetary Science Letters*, 17(1), pp.243–246. Available at: <http://www.sciencedirect.com/science/article/pii/0012821X72902828> [Accessed April 28, 2016].
- Noll, R. et al., 2001. Laser-induced breakdown spectrometry — applications for production control and quality assurance in the steel industry. *Spectrochimica Acta Part B: Atomic Spectroscopy*, 56(6), pp.637–649.
- Nyquist, L.E. et al., 2001. *Chronology and Evolution of Mars* R. Kallenbach, J. Geiss, & W. K. Hartmann, eds., Dordrecht: Springer Netherlands. Available at: <http://link.springer.com/10.1007/978-94-017-1035-0> [Accessed May 26, 2016].
- Ojha, L. et al., 2015. Spectral evidence for hydrated salts in recurring slope lineae on Mars. *Nature Geoscience*, 8(11), pp.829–832. Available at: <http://www.nature.com/doi/10.1038/ngeo2546> [Accessed December 14, 2016].
- Ollila, A.M. et al., 2014. Trace element geochemistry (Li, Ba, Sr, and Rb) using Curiosity's ChemCam: Early results for Gale crater from Bradbury Landing Site to Rocknest. *Journal of Geophysical Research: Planets*, 119(1), pp.255–285. Available at: <http://doi.wiley.com/10.1002/2013JE004517> [Accessed July 26, 2016].
- Osterloo, M.M. et al., 2008. Chloride-Bearing Materials in the Southern Highlands of Mars. *Science*, 319(5870).
- Owen, A. et al., 2015. Quantification of a distributive fluvial system: the Salt Wash DFS of the Morrison Formation, SW USA. *Journal of Sedimentary*. Available at: <http://jsedres.sepmonline.org/content/85/5/544.short> [Accessed September 21, 2017].
- Paige, D.A., 2005. Ancient Mars: Wet in Many Places. *Science*, 307(5715).
- Pain, C., Clarke, J.T. & Thomas, M., 2007. Inversion of relief on Mars. *Icarus*, 190(2),

- pp.478–491. Available at:  
<http://linkinghub.elsevier.com/retrieve/pii/S0019103507001376> [Accessed  
September 21, 2017].
- Papike, J.J. et al., 2013. Experimental and crystal chemical study of the basalt–eclogite transition in Mars and implications for martian magmatism. *Geochimica et Cosmochimica Acta*, 104, pp.358–376. Available at:  
<http://www.sciencedirect.com/science/article/pii/S0016703712006539> [Accessed  
April 28, 2016].
- Pappalardo, R.T. et al., 1998. Geological evidence for solid-state convection in Europa’s ice shell. *Nature*, 391(6665), pp.365–8. Available at:  
<http://dx.doi.org/10.1038/34862> [Accessed April 14, 2016].
- Parker, T.J. et al., 1993. Coastal geomorphology of the Martian northern plains. *Journal of Geophysical Research*, 98(E6), p.11061. Available at:  
<http://doi.wiley.com/10.1029/93JE00618> [Accessed February 27, 2017].
- Parker, T.J., Stephen Saunders, R. & Schneeberger, D.M., 1989. Transitional morphology in West Deuteronilus Mensae, Mars: Implications for modification of the lowland/upland boundary. *Icarus*, 82(1), pp.111–145. Available at:  
<http://linkinghub.elsevier.com/retrieve/pii/0019103589900274> [Accessed  
February 27, 2017].
- Pasquini, C., 2003. Near Infrared Spectroscopy: fundamentals, practical aspects and analytical applications. *Journal of the Brazilian Chemical Society*, 14(2), pp.198–219. Available at: [http://www.scielo.br/scielo.php?script=sci\\_arttext&pid=S0103-50532003000200006&lng=en&nrm=iso&tlng=en](http://www.scielo.br/scielo.php?script=sci_arttext&pid=S0103-50532003000200006&lng=en&nrm=iso&tlng=en) [Accessed January 2, 2017].
- Perminov, V.G., United States. National Aeronautics and Space Administration. Office of Policy and Plans. & United States. Office of Space Science., 1999. *The difficult road to Mars : a brief history of Mars exploration in the Soviet Union*, NASA History Division, Office of Policy and Plans.
- Pettijohn, F., 1957. Sedimentary rocks. Available at:  
<http://afrilib.odinafrica.org/handle/0/4009> [Accessed May 26, 2017].
- Phillips, C.B. & Pappalardo, R.T., 2014. Europa Clipper Mission Concept: Exploring Jupiter’s Ocean Moon. *Eos, Transactions American Geophysical Union*, 95(20), pp.165–167. Available at: <http://doi.wiley.com/10.1002/2014EO200002> [Accessed

- April 14, 2016].
- Phillips, R.J. et al., 2001. Ancient Geodynamics and Global-Scale Hydrology on Mars. *Science*, 291(5513).
- Pilles, E.A. et al., 2017. Implementation of Strategic Traverse Days During the CanMars 2016 Mars Sample Return Analogue Mission. *Lunar and Planetary Science Conference*, 48, p.2018. Available at: <https://www.hou.usra.edu/meetings/lpsc2017/eposter/2018.pdf> [Accessed August 25, 2017].
- Pilles, E.A. et al., 2017. To Hel and Back – Strategic Planning for The CanMars 2016 Mars Sample Return Analogue Mission. *LUNAR AND PLANETARY SCIENCE*, XLVIII, p.2022. Available at: <https://www.hou.usra.edu/meetings/lpsc2017/pdf/2022.pdf> [Accessed August 25, 2017].
- Pilorget, C. & Bibring, J.-P., 2014. Automated algorithms to identify and locate grains of specific composition for NIR hyperspectral microscopes: Application to the MicrOmega instrument onboard ExoMars. *Planetary and Space Science*, 99, pp.7–18.
- Plescia, J.B., 2003. Cerberus Fossae, Elysium, Mars: a source for lava and water. *Icarus*, 164(1), pp.79–95.
- Pollack, J.B., Toon, O.B. & Boese, R., 1980. Greenhouse models of Venus' High surface temperature, as constrained by Pioneer Venus measurements. *Journal of Geophysical Research*, 85(A13), p.8223. Available at: <http://doi.wiley.com/10.1029/JA085iA13p08223> [Accessed May 24, 2016].
- Poulet, F. et al., 2014. Mineral abundances at the final four curiosity study sites and implications for their formation. *Icarus*, 231, pp.65–76. Available at: <http://linkinghub.elsevier.com/retrieve/pii/S0019103513004971> [Accessed September 7, 2017].
- Poulet, F. et al., 2009. Quantitative compositional analysis of martian mafic regions using the MEx/OMEGA reflectance data. *Icarus*, 201(1), pp.84–101. Available at: <http://www.sciencedirect.com/science/article/pii/S0019103509000141> [Accessed May 6, 2016].
- Prakash, R. et al., 2008. *Mars Science Laboratory Entry, Descent, and Landing System Overview*, Available at: <http://ieeexplore.ieee.org/document/4526283/> [Accessed

- December 14, 2016].
- Quantin, C. et al., 2016. Oxia Planum, The Landing Site For Exomars 2018. *Lunar and Planetary*. Available at: <https://www.hou.usra.edu/meetings/lpsc2016/pdf/2863.pdf> [Accessed September 1, 2017].
- Quick, L.C. et al., 2013. Constraints on the detection of cryovolcanic plumes on Europa. *Planetary and Space Science*, 86, pp.1–9. Available at: <http://adsabs.harvard.edu/abs/2013P&SS...86....1Q> [Accessed June 2, 2016].
- Quintana, C. et al., 2016. RLS Instrument Radiometric Model: Instrument performance theoretical evaluation and experimental checks. *American Astronomical Society, DPS meeting #48, id.223.07*, 48. Available at: <http://adsabs.harvard.edu/abs/2016DPS....4822307Q> [Accessed September 5, 2017].
- Raman, C. V. & Krishnan, K.S., 1928. A New Type of Secondary Radiation. *Nature*, 501(121), p.3048. Available at: <http://www.uky.edu/~holler/raman.html>.
- Rampe, E.B. et al., 2017. *Mineralogy of an ancient lacustrine mudstone succession from the Murray formation, Gale crater, Mars*, Available at: <http://linkinghub.elsevier.com/retrieve/pii/S0012821X17302005> [Accessed June 12, 2017].
- Rampelotto, P.H. & Henrique, P., 2010. Resistance of Microorganisms to Extreme Environmental Conditions and Its Contribution to Astrobiology. *Sustainability*, 2(6), pp.1602–1623. Available at: <http://www.mdpi.com/2071-1050/2/6/1602/> [Accessed December 15, 2016].
- Rapin, W. et al., 2016. Hydration state of calcium sulfates in Gale crater, Mars: Identification of bassanite veins. *Earth and Planetary Science Letters*, 452, pp.197–205. Available at: <http://linkinghub.elsevier.com/retrieve/pii/S0012821X16304010> [Accessed July 27, 2017].
- Rennó, N.O. et al., 2009. Possible physical and thermodynamical evidence for liquid water at the Phoenix landing site. *Journal of Geophysical Research*, 114(E1), p.E00E03. Available at: <http://doi.wiley.com/10.1029/2009JE003362> [Accessed February 27, 2017].
- Rice, M., 2014. Geology of The Kimberley Waypoint, Gale Crater: Observations from

- orbit and MSL Curiosity. *2014 GSA Annual Meeting*, p.202. Available at: [https://gsa.confex.com/gsa/2014AM/finalprogram/abstract\\_249136.htm](https://gsa.confex.com/gsa/2014AM/finalprogram/abstract_249136.htm) [Accessed December 10, 2015].
- Richter, L. et al., 2015. Progress Report on Development of the Exomars 2018 Sample Processing and Distribution Subsystem (SPDS) and related OHB Sample Handling Studies. *ASTRA 2015*. Available at: [http://robotics.estec.esa.int/ASTRA/Astra2015/Papers/Session1A/95923\\_Richter.pdf](http://robotics.estec.esa.int/ASTRA/Astra2015/Papers/Session1A/95923_Richter.pdf) [Accessed July 25, 2016].
- Rogers, A.D. & Hamilton, V., 2015. Compositional provinces of Mars from statistical analyses of TES, GRS, OMEGA and CRISM data. *Journal of Geophysical Research: Planets*, 120(1), pp.62–91. Available at: <http://doi.wiley.com/10.1002/2014JE004690> [Accessed May 5, 2016].
- del Rosario Canchal, M. et al., 2017. Raman laser spectrometer optical head: qualification model assembly and integration verification. In J. Sasián & R. N. Youngworth, eds. *Optical System Alignment, Tolerancing, and Verification XI*. SPIE, p. 24. Available at: <https://www.spiedigitallibrary.org/conference-proceedings-of-spie/10377/2277003/Raman-laser-spectrometer-optical-head--qualification-model-assembly-and/10.1117/12.2277003.full> [Accessed September 21, 2017].
- Roth, L. et al., 2014. Transient Water Vapor at Europa’s South Pole. *Science*, 343(6167).
- Rothschild, L.J. & Mancinelli, R.L., 2001. Life in extreme environments. *Nature*, 409(6823), pp.1092–1101. Available at: <http://www.nature.com/doi/10.1038/35059215> [Accessed December 14, 2016].
- Ruff, S.W. & Christensen, P.R., 2002. Bright and dark regions on Mars: Particle size and mineralogical characteristics based on Thermal Emission Spectrometer data. *Journal of Geophysical Research: Planets*, 107(E12), pp.2-1-2–22. Available at: <http://doi.wiley.com/10.1029/2001JE001580> [Accessed December 14, 2016].
- Rull, F. et al., 2011. The Raman Laser Spectrometer (RLS) on the ExoMars 2018 Rover Mission. *42nd Lunar and Planetary Science Conference, held March 7-11, 2011 at The Woodlands, Texas. LPI Contribution No. 1608, p.2400*, 42, p.2400.
- Rull, F. et al., 2017. The Raman Laser Spectrometer for the ExoMars Rover Mission to Mars. *Astrobiology*. Available at:

- <http://online.liebertpub.com/doi/pdfplus/10.1089/ast.2016.1567> [Accessed August 8, 2017].
- Sagan, C., 1997. The Early Faint Sun Paradox: Organic Shielding of Ultraviolet-Labile Greenhouse Gases. *Science*, 276(5316), pp.1217–1221. Available at: <http://adsabs.harvard.edu/abs/1997Sci...276.1217S> [Accessed May 20, 2016].
- Sagan, C. & Fox, P., 1975. The canals of Mars: An assessment after Mariner 9. *Icarus*, 25(4), pp.602–612.
- Sallé, B. et al., 2004. Laser-Induced Breakdown Spectroscopy for Mars surface analysis: capabilities at stand-off distances and detection of chlorine and sulfur elements. *Spectrochimica Acta Part B: Atomic Spectroscopy*, 59(9), pp.1413–1422.
- Santos-Lleo, M. et al., 2009. The first decade of science with Chandra and XMM-Newton. *Nature*, 462(7276), pp.997–1004. Available at: <http://dx.doi.org/10.1038/nature08690> [Accessed April 29, 2016].
- Santos, A.R. et al., 2015. Petrology of igneous clasts in Northwest Africa 7034: Implications for the petrologic diversity of the martian crust. *Geochimica et Cosmochimica Acta*, 157, pp.56–85. Available at: <http://www.sciencedirect.com/science/article/pii/S0016703715001064> [Accessed April 16, 2016].
- Sarma, L.P., Prasad, P.S.R. & Ravikumar, N., 1998. Raman spectroscopic study of phase transitions in natural gypsum. *Journal of Raman Spectroscopy*, 29(9), pp.851–856. Available at: <http://doi.wiley.com/10.1002/%28SICI%291097-4555%28199809%2929%3A9%3C851%3A%3AAID-JRS313%3E3.0.CO%3B2-S> [Accessed August 4, 2017].
- Sautter, V. et al., 2014. Igneous mineralogy at Bradbury Rise: The first ChemCam campaign at Gale crater. *Journal of Geophysical Research: Planets*, 119(1), pp.30–46. Available at: <http://onlinelibrary.wiley.com/doi/10.1002/2013JE004472/full> [Accessed December 10, 2015].
- Sautter, V. et al., 2015. In situ evidence for continental crust on early Mars. *Nature Geoscience*, 8(8), pp.605–609. Available at: <http://dx.doi.org/10.1038/ngeo2474> [Accessed February 1, 2016].
- Schaber, G.G., Shoemaker, E.M. & Kozak, R.C., 1987. Surface age of venus: use of the terrestrial cratering record. *Sol. Syst. Res. (Engl. Transl.); (United States)*, 21:2.

- Schmidt, M.E. et al., 2013. APXS of First Rocks Encountered by Curiosity in Gale Crater: Geochemical Diversity and Volatile Element (K and ZN) Enrichment. Available at: <http://ntrs.nasa.gov/search.jsp?R=20130009734> [Accessed May 5, 2016].
- Schmidt, M.E. & Campbell, J.L., 2014. Geochemical diversity in first rocks examined by the Curiosity Rover in Gale Crater: Evidence for and significance of an alkali and volatile-rich igneous source. *Journal of Geophysical Research: Planets*, 119(1), pp.64–81. Available at: <http://onlinelibrary.wiley.com/doi/10.1002/2013JE004481/full> [Accessed December 10, 2015].
- Schmidt, M.E. & McCoy, T.J., 2010. The evolution of a heterogeneous Martian mantle: Clues from K, P, Ti, Cr, and Ni variations in Gusev basalts and shergottite meteorites. *Earth and Planetary Science Letters*, 296(1–2), pp.67–77. Available at: <http://www.sciencedirect.com/science/article/pii/S0012821X10002980> [Accessed May 5, 2016].
- Schubert, G. et al., 1980. Structure and circulation of the Venus atmosphere. *Journal of Geophysical Research*, 85(A13), p.8007. Available at: <http://doi.wiley.com/10.1029/JA085iA13p08007> [Accessed May 24, 2016].
- Schulze-Makuch, D. & Irwin, L.N., 2002. Reassessing the possibility of life on venus: proposal for an astrobiology mission. *Astrobiology*, 2(2), pp.197–202. Available at: <http://www.liebertonline.com/doi/abs/10.1089/15311070260192264> [Accessed May 24, 2016].
- Schulze, D.G., 1981. Identification of Soil Iron Oxide Minerals by Differential X-ray Diffraction1. *Soil Science Society of America Journal*, 45(2), p.437. Available at: <https://www.soils.org/publications/sssaj/abstracts/45/2/SS0450020437> [Accessed July 27, 2016].
- Schwenzer, S.P. et al., 2016. Modeling of sulphide environments on Mars. Available at: [http://oro.open.ac.uk/45419/1/Modeling\\_of\\_sulphide\\_environments\\_on\\_Mars\\_2016.pdf](http://oro.open.ac.uk/45419/1/Modeling_of_sulphide_environments_on_Mars_2016.pdf) [Accessed April 7, 2016].
- Segura, T.L. et al., 2002. Environmental Effects of Large Impacts on Mars. *Science*, 298(5600).
- Seiff, A. et al., 1985. Models of the structure of the atmosphere of Venus from the surface to 100 kilometers altitude. *Advances in Space Research*, 5(11), pp.3–58.

- Sharma, S.K. et al., 2003. Stand-off Raman spectroscopic detection of minerals on planetary surfaces. *Spectrochimica Acta Part A: Molecular and Biomolecular Spectroscopy*, 59(10), pp.2391–2407.
- Shearer, C.K. et al., 2008. Petrogenetic linkages among Martian basalts: Implications based on trace element chemistry of olivine. *Meteoritics & Planetary Science Archives*, 43(7), pp.1241–1258. Available at: <https://journals.uair.arizona.edu/index.php/maps/article/view/15617> [Accessed May 5, 2016].
- Shkuratov, Y. et al., 2013. Lunar surface traces of engine jets of Soviet sample return probes: The enigma of the Luna-23 and Luna-24 landing sites. *Planetary and Space Science*, 75, pp.28–36.
- Sicoli, G. et al., 2009. Gas chromatographic enantioseparation of unfunctionalized chiral alkanes: A challenge in separation science (overview, state of the art, and perspectives). *Chirality*, 21(1), pp.183–198. Available at: <http://doi.wiley.com/10.1002/chir.20638> [Accessed January 5, 2017].
- Silva, J.J.R.F. da. & Williams, R.J.P. (Robert J.P., 2001. *The biological chemistry of the elements : the inorganic chemistry of life*, Oxford University Press.
- Smith, B. et al., 2013. Venus In Situ Explorer Mission design using a mechanically deployed aerodynamic decelerator. In *2013 IEEE Aerospace Conference*. IEEE, pp. 1–18. Available at: <http://ieeexplore.ieee.org/document/6497176/> [Accessed December 14, 2016].
- Smith, D.E. et al., 2001. Mars Orbiter Laser Altimeter: Experiment summary after the first year of global mapping of Mars. *Journal of Geophysical Research: Planets*, 106(E10), pp.23689–23722. Available at: <http://doi.wiley.com/10.1029/2000JE001364> [Accessed June 5, 2017].
- Smith, M.R. et al., 1984. Petrogenesis of the SNC (shergottites, nakhlites, chassignites) meteorites: Implications for their origin from a large dynamic planet, possibly Mars. *Journal of Geophysical Research*, 89(S02), p.B612. Available at: <http://doi.wiley.com/10.1029/JB089iS02p0B612> [Accessed April 26, 2016].
- Smith, P.H. et al., 2009. H<sub>2</sub>O at the Phoenix Landing Site. *Science, Volume 325, Issue 5936, pp. 58- (2009).*, 325, p.58.
- Smrekar, S.E. et al., 2010. Recent Hotspot Volcanism on Venus from VIRTIS Emissivity

- Data. *Science*, 328(5978).
- Soderblom, L.A., Anderson, R.C. & Arvidson, R.E., 2004. Soils of Eagle Crater and Meridiani Planum at the Opportunity rover landing site. *Science*, 306(5702), pp.1723–1726. Available at: <http://www.sciencemag.org/content/306/5702/1723.short> [Accessed December 10, 2015].
- Soffen, G.A. & Snyder, C.W., 1976. The First Viking Mission to Mars. *Science*, 193(4255), pp.759–766. Available at: <http://www.sciencemag.org/cgi/doi/10.1126/science.193.4255.759> [Accessed June 5, 2017].
- Solomon, S.C. et al., 1992. Venus tectonics: An overview of Magellan observations. *Journal of Geophysical Research*, 97(E8), p.13199. Available at: <http://doi.wiley.com/10.1029/92JE01418> [Accessed December 14, 2016].
- Sotin, C., Head, J.W. & Tobie, G., 2002. Europa: Tidal heating of upwelling thermal plumes and the origin of lenticulae and chaos melting. *Geophysical Research Letters*, 29(8), pp.74-1-74-4. Available at: <http://doi.wiley.com/10.1029/2001GL013844> [Accessed April 14, 2016].
- Spulber, S.D. & Rutherford, M.J., 1983. The Origin of Rhyolite and Plagiogranite in Oceanic Crust: An Experimental Study. *Journal of Petrology*, 24(1), pp.1–25. Available at: <http://petrology.oxfordjournals.org/content/24/1/1.1.short> [Accessed May 5, 2016].
- Squyres, S.W. et al., 2003. Athena Mars rover science investigation. *Journal of Geophysical Research: Planets*, 108(E12). Available at: <http://doi.wiley.com/10.1029/2003JE002121> [Accessed December 15, 2016].
- Squyres, S.W., Grotzinger, J.P., et al., 2004. In Situ Evidence for an Ancient Aqueous Environment at Meridiani Planum, Mars. *Science*, 306(5702).
- Squyres, S.W. et al., 2006. Overview of the Opportunity Mars Exploration Rover Mission to Meridiani Planum: Eagle Crater to Purgatory Ripple. *Journal of Geophysical Research: Planets*, 111(E12), p.n/a-n/a. Available at: <http://doi.wiley.com/10.1029/2006JE002771> [Accessed December 14, 2016].
- Squyres, S.W. et al., 2007. Pyroclastic activity at Home Plate in Gusev Crater, Mars. *Science (New York, N.Y.)*, 316(5825), pp.738–42. Available at:

- <http://science.sciencemag.org/content/316/5825/738.abstract> [Accessed May 5, 2016].
- Squyres, S.W. et al., 2004. The Opportunity Rover's Athena science investigation at Meridiani Planum, Mars. *Science (New York, N.Y.)*, 306(5702), pp.1698–703. Available at: <http://www.ncbi.nlm.nih.gov/pubmed/15576602> [Accessed July 27, 2016].
- Squyres, S.W., Arvidson, R.E., et al., 2004. The Spirit Rover's Athena science investigation at Gusev Crater, Mars. *Science (New York, N.Y.)*, 305(5685), pp.794–9. Available at: <http://science.sciencemag.org/content/305/5685/794.abstract> [Accessed April 7, 2016].
- Squyres, S.W. & Kasting, J.F., 1994. Early Mars: How Warm and How Wet? *Science*, 265(5173), pp.744–749. Available at: <http://science.sciencemag.org/content/265/5173/744.abstract> [Accessed May 9, 2016].
- Stern, S.A. et al., 2016. New Horizons: Overview of Results From and Plans After the Exploration of The Pluto System. *American Astronomical Society, DPS meeting #48, id.103.01*, 48.
- Stetter, K.O., 1999. Extremophiles and their adaptation to hot environments. *FEBS Letters*, 452(1–2), pp.22–25. Available at: <http://www.sciencedirect.com/science/article/pii/S0014579399006638> [Accessed October 26, 2015].
- Stevenson, D.J., 2001. Jupiter and Its Moons. *Science*. Available at: <http://authors.library.caltech.edu/39163/> [Accessed April 29, 2016].
- Stolper, E. & Walke, D., 1980. Melt density and the average composition of basalt. *Contributions to Mineralogy and Petrology*, 74(1), pp.7–12.
- Stolper, E.M. et al., 2013. The petrochemistry of Jake\_M: a martian mugearite. *Science (New York, N.Y.)*, 341(6153), p.1239463. Available at: <http://www.ncbi.nlm.nih.gov/pubmed/24072927> [Accessed April 7, 2016].
- Stolper, E.M. & McSween, H.Y., 1979. Petrology and origin of the shergottite meteorites. *Geochimica et Cosmochimica Acta*, 43, pp.1475–1498. Available at: <http://www.sciencedirect.com/science/article/pii/001670377990142X> [Accessed December 10, 2015].

- Surkov, Y.A. et al., 2008. X-ray fluorescence spectrometry on the surface of Venus.
- Svedhem, H. et al., 2007. Venus Express—The first European mission to Venus. *Planetary and Space Science*, 55(12), pp.1636–1652.
- Symons, S., Symons & Sarah, 2012. Astronomy, Egyptian. In *The Encyclopedia of Ancient History*. Oxford, UK: Blackwell Publishing Ltd. Available at: <http://doi.wiley.com/10.1002/9781444338386.wbeah15046> [Accessed December 8, 2016].
- Szabó, T. et al., 2015. Reconstructing the transport history of pebbles on Mars. *Nature Communications*, 6, p.8366. Available at: <http://www.nature.com/doi/10.1038/ncomms9366> [Accessed December 9, 2016].
- Tanaka, K. L. et al., 1988. The resurfacing history of Mars - A synthesis of digitized, viking-based geology. IN: *Lunar and Planetary Science Conference*, pp.665–678. Available at: <http://adsabs.harvard.edu/abs/1988LPSC...18..665T> [Accessed May 20, 2016].
- Tanaka, K.L., Scott, D.H. & Kozak, R., 1987. Geologic Map of the Polar Regions of Mars.
- Taylor, G.J. et al., 2010. Mapping Mars geochemically. *Geology*, 38(2), pp.183–186. Available at: <http://geology.gsapubs.org/content/38/2/183.short> [Accessed May 5, 2016].
- Taylor, G.J., 2013. The bulk composition of Mars. *Chemie der Erde - Geochemistry*, 73(4), pp.401–420. Available at: <http://adsabs.harvard.edu/abs/2013ChEG...73..401T> [Accessed May 26, 2016].
- Thompson, L. M. et al., 2014. K-Rich Rocks at Gale, Dingo Gap to the Kimberley: An APXS Perspective. *Eighth International Conference on Mars*. Available at: <http://adsabs.harvard.edu/abs/2014LPICo1791.1433T> [Accessed May 27, 2016].
- Treiman, A.H. et al., 2016. Mineralogy, provenance, and diagenesis of a potassic basaltic sandstone on Mars: CheMin X-ray diffraction of the Windjana sample (Kimberley area, Gale Crater). *Journal of Geophysical Research: Planets*, 121(1), pp.75–106. Available at: <http://doi.wiley.com/10.1002/2015JE004932> [Accessed April 7, 2016].
- Treiman, A.H. & Filiberto, J., 2015. Geochemical diversity of shergottite basalts: Mixing and fractionation, and their relation to Mars surface basalts. *Meteoritics &*

- Planetary Science*, 50(4), pp.632–648. Available at: <http://doi.wiley.com/10.1111/maps.12363> [Accessed May 5, 2016].
- Usui, T., McSween, H.Y. & Clark, B., 2008. Petrogenesis of high-phosphorous Wishstone Class rocks in Gusev Crater, Mars. *Journal of Geophysical Research*, 113(E12), p.E12S44. Available at: <http://doi.wiley.com/10.1029/2008JE003225> [Accessed May 5, 2016].
- Vago, J. et al., 2013. → EXOMARS ESA's next step in Mars exploration. *ESA Bulletin*. Available at: [www.esa.int](http://www.esa.int) [Accessed December 14, 2016].
- Vago, J. et al., 2015. ESA ExoMars program: The next step in exploring Mars. *Solar System Research*, 49(7), pp.518–528. Available at: <http://link.springer.com/10.1134/S0038094615070199> [Accessed May 17, 2017].
- Vandenabeele, P. et al., 2000. Raman spectroscopic database of azo pigments and application to modern art studies. *Journal of Raman Spectroscopy*, 31(6), pp.509–517. Available at: <http://doi.wiley.com/10.1002/1097-4555%28200006%2931%3A6%3C509%3A%3AAID-JRS566%3E3.0.CO%3B2-0> [Accessed July 25, 2016].
- Vandenabeele, P., Edwards, H.G.M. & Luc, M., 2007. A Decade of Raman Spectroscopy in Art and Archaeology.
- Vaniman, D.T. et al., 2012. Ceramic ChemCam Calibration Targets on Mars Science Laboratory. *Space Science Reviews*, 170(1–4), pp.229–255. Available at: <http://link.springer.com/10.1007/s11214-012-9886-0> [Accessed September 5, 2016].
- Vaniman, D.T. et al., 2014. Mineralogy of a mudstone at Yellowknife Bay, Gale crater, Mars. *Science (New York, N.Y.)*, 343(6169), p.1243480. Available at: [http://authors.library.caltech.edu/42649/1/Vaniman\\_1243480\\_mineralogy\\_revised\\_Nov\\_final.pdf](http://authors.library.caltech.edu/42649/1/Vaniman_1243480_mineralogy_revised_Nov_final.pdf) [Accessed March 10, 2016].
- Vankeirsbilck, T. et al., 2002. Applications of Raman spectroscopy in pharmaceutical analysis. *TrAC Trends in Analytical Chemistry*, 21(12), pp.869–877.
- Varnali, T., Edwards, H.G.M. & Hargreaves, M.D., 2009. Scytonemin : molecular structural studies of a key extremophilic biomarker for astrobiology. *International Journal of Astrobiology*, 8(2), p.133.
- Vasavada, A.R., Gupta, S. & Team, M.S.L.S., 2016. The Ancient Habitability of Gale Crater,

- Mars, after Four Years of Exploration by Curiosity. *American Astronomical Society, DPS meeting #48, id.416.01, 48.*
- Vasavadaa, A.R. et al., 2017. Thermophysical properties along Curiosity's traverse in Gale crater, Mars, derived from the REMS ground temperature sensor. *Icarus*, 284, pp.372–386. Available at: <http://www.sciencedirect.com/science/article/pii/S001910351630344X?via%3Dihub> [Accessed September 20, 2017].
- Vaz, D. a. & Silvestro, S., 2014. Mapping and characterization of small-scale aeolian structures on Mars: An example from the MSL landing site in Gale Crater. *Icarus*, 230, pp.151–161. Available at: <http://www.sciencedirect.com/science/article/pii/S001910351300345X> [Accessed September 19, 2017].
- Venkatapathy, E. et al., 2016. Mars Sample Return Earth Entry Vehicle Design:can the Reliability Requirement Be Met by Emerging New Technologies?
- Wang, A., Wei, J., et al., 2015. A Compact Integrated Raman Spectrometer, CIRS, for Fine-Scale Definitive Mineralogy in Venus Explorations.
- Wang, A. et al., 2001. Characterization and comparison of structural and compositional features of planetary quadrilateral pyroxenes by Raman spectroscopy. *American Mineralogist*, 86(7–8), pp.790–806. Available at: <http://ammin.geoscienceworld.org/lookup/doi/10.2138/am-2001-0703> [Accessed July 26, 2016].
- Wang, A. et al., 2003. Development of the Mars microbeam Raman spectrometer (MMRS). *Journal of Geophysical Research*, 108(E1), p.5005. Available at: <http://doi.wiley.com/10.1029/2002JE001902> [Accessed January 5, 2017].
- Wang, A. et al., 2006. Sulfates on Mars: A systematic Raman spectroscopic study of hydration states of magnesium sulfates. *Geochimica et Cosmochimica Acta*, 70(24), pp.6118–6135. Available at: <http://linkinghub.elsevier.com/retrieve/pii/S0016703706020114> [Accessed August 2, 2017].
- Wang, A. et al., 2016. Two High Performance In Situ Raman Spectrometers for Landed Planetary Missions. *3rd International Workshop on Instrumentation for Planetary Mission, held 24-27 October, 2016 in Pasadena, California. LPI Contribution No.*

1980, *id.*4086, 1980.

- Wang, A., Freeman, J.J. & Jolliff, B.L., 2015. Understanding the Raman spectral features of phyllosilicates. *Journal of Raman Spectroscopy*, 46(10), pp.829–845. Available at: <http://doi.wiley.com/10.1002/jrs.4680> [Accessed September 8, 2017].
- Wang, H. & Ingersoll, A., 2002. Martian clouds observed by Mars Global Surveyor Mars Orbiter Camera. *Journal of Geophysical Research*, 107(E10), p.5078. Available at: <http://doi.wiley.com/10.1029/2001JE001815> [Accessed May 25, 2017].
- Webster, C.R. & Mahaffy, P.R., 2011. Determining the local abundance of Martian methane and its'  $^{13}\text{C}/^{12}\text{C}$  and D/H isotopic ratios for comparison with related gas and soil analysis on the 2011 Mars Science Laboratory (MSL) mission. *Planetary and Space Science*, 59(2), pp.271–283.
- Wei, J. et al., 2015. Autonomous soil analysis by the Mars Micro-beam Raman Spectrometer (MMRS) on-board a rover in the Atacama Desert: a terrestrial test for planetary exploration. *Journal of Raman Spectroscopy*, 46(10), pp.810–821. Available at: <http://doi.wiley.com/10.1002/jrs.4656> [Accessed January 4, 2017].
- Weiss, P. et al., 2011. Thermal drill sampling system onboard high-velocity impactors for exploring the subsurface of Europa. *Advances in Space Research*, 48(4), pp.743–754.
- Wetherill, G.W. & W., G., 1975. Late heavy bombardment of the moon and terrestrial planets. In: *Lunar Science Conference, 6th, Houston, Tex., March 17-21, 1975, Proceedings. Volume 2. (A78-46668 21-91) New York, Pergamon Press, Inc., 1975, p. 1539-1561.*, 6, pp.1539–1561.
- Whitaker, M. L., Nekvasil, H. & Lindsley, D.H., 2005. Potential Magmatic Diversity on Mars. *36th Annual Lunar and Planetary Science Conference*. Available at: <http://adsabs.harvard.edu/abs/2005LPI....36.1440W> [Accessed January 25, 2016].
- White, B.R., 1979. soil transport by winds on Mars. *Journal of Geophysical Research*, 84(B9), p.4643. Available at: <http://doi.wiley.com/10.1029/JB084iB09p04643> [Accessed December 14, 2016].
- Wiens, R.C. et al., 2013. Pre-flight calibration and initial data processing for the ChemCam laser-induced breakdown spectroscopy instrument on the Mars Science Laboratory rover. *Spectrochimica Acta Part B: Atomic Spectroscopy*, 82, pp.1–27. Available at: <http://adsabs.harvard.edu/abs/2013AcSpe..82....1W> [Accessed

December 11, 2013].

- Wiens, R.C. et al., 2012. The ChemCam Instrument Suite on the Mars Science Laboratory (MSL) Rover: Body Unit and Combined System Tests. *Space Science Reviews*, 170(1–4), pp.167–227. Available at: <http://link.springer.com/article/10.1007/s11214-012-9902-4> [Accessed November 7, 2013].
- Wiens, R.C. et al., 2016. The SuperCam Remote Sensing Instrument Suite for Mars 2020, p.1322.
- Wiens, R.C. & Maurice, S., 2015. ChemCam: Chemostratigraphy by the First Mars Microprobe. *Elements*, 11(1), pp.33–38. Available at: <http://elements.geoscienceworld.org/content/11/1/33.short> [Accessed May 9, 2016].
- Wilhelms, D.E. & Squyres, S.W., 1984. The martian hemispheric dichotomy may be due to a giant impact. *Nature*, 309(5964), pp.138–140. Available at: <http://www.nature.com/doi/10.1038/309138a0> [Accessed December 14, 2016].
- Williams, R.M.E. et al., 2013. Martian fluvial conglomerates at Gale crater. *Science (New York, N.Y.)*, 340(6136), pp.1068–72. Available at: <http://science.sciencemag.org/content/340/6136/1068.abstract> [Accessed April 5, 2016].
- Wilson, B.M., 2007. *Igneous Petrogenesis A Global Tectonic Approach*, Springer Science & Business Media. Available at: <https://books.google.com/books?hl=en&lr=&id=JR7UBwAAQBAJ&pgis=1> [Accessed April 21, 2016].
- Wilson, C.F., Zetterling, C.-M. & Pike, W.T., 2016. Venus Long-life Surface Package. Available at: <http://arxiv.org/abs/1611.03365> [Accessed December 14, 2016].
- Winkler, H.G.F., 1967. Definition and Types of Metamorphism. In *Petrogenesis of Metamorphic Rocks*. Berlin, Heidelberg: Springer Berlin Heidelberg, pp. 1–6. Available at: [http://www.springerlink.com/index/10.1007/978-3-662-00866-9\\_1](http://www.springerlink.com/index/10.1007/978-3-662-00866-9_1) [Accessed May 26, 2017].
- Withers, P. et al., 2015. Recovery and validation of Mars ionospheric electron density profiles from Mariner 9. *Earth, Planets and Space*, 67(1), p.194. Available at: <http://www.earth-planets-space.com/content/67/1/194> [Accessed December 7,

2016].

- Worth, R.J., Sigurdsson, S. & House, C.H., 2013. Seeding Life on the Moons of the Outer Planets via Lithopanspermia. *Astrobiology*, 13(12), pp.1155–1165. Available at: <http://online.liebertpub.com/doi/abs/10.1089/ast.2013.1028> [Accessed December 9, 2016].
- Wray, J.J., 2013. Gale crater: the Mars Science Laboratory/Curiosity rover landing site. *International Journal of Astrobiology*. Available at: [http://journals.cambridge.org/article\\_S1473550412000328](http://journals.cambridge.org/article_S1473550412000328) [Accessed June 5, 2017].
- Wray, J.J. et al., 2010. Identification of the Ca-sulfate bassanite in Mawrth Vallis, Mars. *Icarus*, 209(2), pp.416–421. Available at: <http://linkinghub.elsevier.com/retrieve/pii/S0019103510002198> [Accessed September 1, 2017].
- Wray, J.J. et al., 2013. Prolonged magmatic activity on Mars inferred from the detection of felsic rocks. *Nature Geoscience*, 6(12), pp.1013–1017. Available at: <http://dx.doi.org/10.1038/ngeo1994> [Accessed March 14, 2016].
- Yen, A.S. et al., 2005. An integrated view of the chemistry and mineralogy of martian soils. *Nature*, 436(7047), pp.49–54. Available at: <http://www.nature.com/doi/10.1038/nature03637> [Accessed July 27, 2016].
- Yingst, R.A. et al., 2013. Characteristics of pebble- and cobble-sized clasts along the Curiosity rover traverse from Bradbury Landing to Rocknest. *Journal of Geophysical Research: Planets*, 118(11), pp.2361–2380. Available at: <http://doi.wiley.com/10.1002/2013JE004435> [Accessed December 16, 2016].
- Yoder, H.S. & Tilley, C.E., 1962. Origin of Basalt Magmas: An Experimental Study of Natural and Synthetic Rock Systems. *Journal of Petrology*, 3(3), pp.342–532. Available at: <http://petrology.oxfordjournals.org/content/3/3/342.short> [Accessed April 12, 2016].
- Young, K.E. et al., 2016. A review of the handheld X-ray fluorescence spectrometer as a tool for field geologic investigations on Earth and in planetary surface exploration. *Applied Geochemistry*, 72, pp.77–87.
- Young, R.E., 1998. The Galileo probe mission to Jupiter: Science overview. *Journal of Geophysical Research: Planets*, 103(E10), pp.22775–22790. Available at:

- <http://doi.wiley.com/10.1029/98JE01051> [Accessed December 12, 2016].
- Zimmer, M.M. et al., 2010. The Role of Water in Generating the Calc-alkaline Trend: New Volatile Data for Aleutian Magmas and a New Tholeiitic Index. *Journal of Petrology*, 51(12), pp.2411–2444. Available at: <http://petrology.oxfordjournals.org/content/early/2010/11/18/petrology.egq062.full> [Accessed March 21, 2016].
- Zipfel, J. et al., 2011. Bounce Rock-A shergottite-like basalt encountered at Meridiani Planum, Mars. *Meteoritics & Planetary Science*. Available at: <http://doi.wiley.com/10.1111/j.1945-5100.2010.01127.x> [Accessed May 5, 2016].
- Zurek, R. et al., 2016. Ongoing Mars Missions: Extended Mission Plans. *American Astronomical Society, DPS meeting #48, id.123.12*, 48.
- Zurek, R.W., 1982. Martian great dust storms: An update. *Icarus*, 50(2), pp.288–310.

# Appendix 1 Technology Readiness Levels

Technology Readiness Levels or TRLs indicate how close an instrument is to being ready for Space applications. A TRL of 9 indicates an instrument has already flown on a mission. Below are NASA's TRL system, The European Space Agency uses a broadly similar system. The higher a technique's TRL the easier it is to adapt to a new mission.

**TRL 1** – Basic principles observed and reported

**TRL 2** – Technology concept and/or application formulated

**TRL 3** – Analytical experimental critical function and/or characteristic proof of concept

**TRL 4** – Component and/or breadboard validation in laboratory environment

**TRL 5** – Component and/or breadboard validation in relevant environment

**TRL 6** – System/Subsystem model or prototype demonstration in relevant environment (ground or space)

**TRL 7** – System prototype in a space environment

**TRL 8** – Actual system completed and “flight qualified” through test and demonstration (ground or space)

**TRL 9** – Actual system is “flight proven” through successful mission operations.

## **Appendix 2 Geological definitions**

Aeolian – Features associated with wind processes

ChemCam target – Target selected from MastCam images. Typically grids of spots (usually 3 x 3) are used for series of 30 LIBS observations

Clasts – Fragment of rock

Conglomerate – Sedimentary rock composed of smaller pre-existing minerals and rocks cemented together

Crystallisation – The processes through which minerals form in rocks

Cumulates – Igneous rock formed from the accumulation of the crystals in magma

Diagenesis – The process of a sedimentary rock changing from one type to another at relatively low temperatures and pressures

Effusive – Formed from a molten rock solidifying

Endmember – Composition of the most extreme points on a compositional trend

Extrusive – Rocks formed on the surface

Felsic – Rocks richer in silica, aluminium and alkali

Float rock – Rock transported from their original location

Fluvial – Features associated with flowing water

Fractionation – The process of a rocks changing composition via the removal of a mineral

Hawaiite – Olivine-rich basalt named for lavas on Hawaii

Intrusive – Rocks formed below the surface

Lithology – Description of an outcrop's visible characteristics

Mafic – Rocks richer in iron and magnesium

Mid Ocean Ridge Basalt – (MORB) Basalt formed from geologically active areas in the ocean where magma reaches the surface and crystallises

Mugearite – Basalt containing olivine and the feldspar oligoclase

Oceanic Island Basalt – (OIB) Basalts found on volcanic islands separate from plate boundaries

Outcrop – Bedrock exposed on the surface

Petrogenesis – Study of the origin of igneous rocks

Picritic basalts – Basalts rich in olivine

Regolith – Loose young material over the surface of rock

Tharsis – Equatorial volcanic plateau on Mars

Tholeiitic – One of two major igneous rock series